Faculdade de Engenharia da Universidade do Porto
Departamento de Engenharia Mecânica e Gestão Industrial

# Modeling the Dynamic Behavior of Laminate Structures with Cork Compounds

João de Deus Santos Silva Daniel Lopes

Porto, Março de 2008

FACULDADE DE ENGENHARIA DA UNIVERSIDADE DO PORTO
Departamento de Engenharia Mecânica e Gestão Industrial

# Modeling the Dynamic Behavior of Laminate Structures with Cork Compounds

João de Deus Santos Silva Daniel Lopes

Licenciado em Engenharia Mecânica
pela Faculdade de Engenharia da Universidade do Porto

Dissertação de Mestrado apresentada à
Faculdade de Engenharia da Universidade do Porto
para obtenção do grau de Mestre em Engenharia Mecânica

Trabalho realizado sob a supervisão
do Professor Doutor José Fernando Dias Rodrigues
do Departamento de Engenharia Mecânica e Gestão Industrial
da Faculdade de Engenharia da Universidade do Porto

Porto, Março de 2008

# Acknowledgments

To professor José Fernando Dias Rodrigues, for the guidance and help he has given me during the development of this this thesis, his support and contribution were fundamental during the whole work.

To professor Jorge Humberto Oliveira Seabra, for all the thrust and support he has given me and for providing me the opportunity to work in the Centro de Tribologia e Manutenção Industrial (CETRIB).

To professor Rui Moreira for his help and advice in the experimental part of this work.

To colleague César Vasques for all the help he gave me in this work, the discussion of several issues with him were very important.

To all my colleagues and friends of the Faculdade de Engenharia da Universidade do Porto (FEUP) and Instituto de Engenharia Mecânica e Gestão Industrial (INEGI).

To Instituto de Engenharia Mecânica e Gestão Industrial (INEGI), for the scholarship it has given me and for giving me the resources necessary to perform this work.

Finally, a sincere thank to all my family and friends, specially my mother Gena and sister Mariana who had always unconditionally supported me, providing me a never ending help. Without them none of this work would have been possible.

# Resumo

Neste trabalho de dissertação apresenta-se um estudo numérico e experimental sobre o comportamento dinâmico de estruturas laminadas com camadas de aglomerado de cortiça actuando estas camadas como tratamentos passivos de amortecimento. Apresenta-se uma revisão sobre as diferentes configurações de tratamentos passivos bem como dos modelos numéricos descritos na literatura para simular o comportamento de estruturas laminadas com este tipo de tratamentos. Apresenta-se também uma descrição da estrutura celular e propriedades da cortiça, nomeadamente no que diz respeito à sua capacidade de amortecimento, a qual faz deste material biológico um excelente material para ser usado como tratamento passivo de amortecimento. Por forma a estabelecer um modelo numérico representativo de estruturas laminadas com camadas de aglomerado de cortiça é necessário caracterizar as propriedades dinâmicas, dependentes da frequência, deste material. Por forma a identificar estas propriedades, dois métodos experimentais, descritos nesta dissertação, foram aplicados na identificação das propriedades dinâmicas de vários aglomerados de cortiça, disponíveis comercialmente, com diferentes parâmetros de formulação (tamanho de grão e densidade). Um dos referidos métodos permitiu identificar o módulo de ganho de corte bem como o factor de perda a partir das funções de resposta em frequência de um sistema com um grau de liberdade, enquanto que o outro permitiu identificar o módulo de ganho extensional e o factor de perda dos aglomerados de cortiça a partir das funções de resposta em frequência de um sistema com dois graus de liberdade semi-definido. Por forma a simular numericamente estruturas em viga e placa laminadas que incluam camadas viscoelásticas de aglomerado de cortiça, é necessário estabelecer um modelo de grande exactidão, capaz de representar a elevada deformação de corte presente nas camadas laminadas da estrutura. Nesta dissertação são formulados dois elementos finitos multi-camada layerwise, um de viga com dois nós e outro de placa com quatro nós. Ambos os elementos finitos de viga e placa foram formulados de acordo com uma teoria layerwise parcial, por forma a incluir um número arbitrário de camadas sendo que as camadas da estrutura tanto podem ter propriedades viscoelásticas como elásticas. Com o objectivo de validar os modelos numéricos que usam os elementos finitos formulados, um conjunto de vigas sandwich e placas sandwich com núcleos de aglomerado de cortiça foram preparadas usando os aglomerados de cortiça cujas propriedades foram identificadas. Um conjunto de funções de resposta em frequência foram medidas para cada viga e placa sandwich, sendo o comportamento dinâmico destas, caracterizado através de análise modal, tendo sido obtidas as suas frequências e formas naturais. As referidas estruturas sandwich foram então simuladas usando os elementos finitos formulados e incluindo no modelo numérico as propriedades do aglomerado de cortiça identificadas. As funções de resposta em frequência directas foram então geradas com o modelo numérico através do procedimento de análise directa em frequência. Resultados obtidos por simulação numérica foram então comparados com os resultados obtidos experimentalmente, revelando não só a boa representatividade dos modelos numéricos gerados com elementos finitos formulados bem como a exactidão das propriedades identificadas para os aglomerados de cortiça.

# Abstract

In this dissertation, a numerical and experimental study about the dynamic behavior of beam and plate laminate structures with a cork compound layer acting as a passive damping treatment is presented. A revision about the commonly used configurations of passive damping treatments is presented and the numerical models referred in the literature used to simulated the dynamic behavior of laminate structures with these type of treatments are described. The cork cellular structure and remarkable properties are presented, namely its damping capability which makes this biologic material an excellent material to be used as a passive damping treatment. To establish a representative numerical model of laminate structures with cork compound layers it is necessary to accurately characterize the cork compound frequency dependent dynamic properties. Therefore, in order to identify these properties, two different experimental procedures, described in this dissertation, were applied in order to identify the dynamic properties of several cork compounds, available commercially, with different formulation parameters (grain size and density). One of the referred procedures allowed identifying the shear storage modulus and loss factor from the frequency response functions measured from a single degree of freedom system, while the other allowed identifying the extensional storage modulus and loss factor of cork compounds from the frequency response functions measured from a two degree of freedom semidefinite system. To numerically simulate the dynamic behavior of the beam and plate laminate structures complying cork compound viscoelastic layers, an accurate model, capable of representing the high deformation shear pattern inside the laminate layers is required. In this dissertation, a multilayer layerwise beam finite element, with two nodes, and a multilayer layerwise plate finite element, with four nodes, were formulated. Both beam and plate finite elements hereby presented were formulated according to a partial layerwise theory, in order to include an arbitrary number of layers as well as to include both viscoelastic and elastic layers. To validate the numerical models using the formulated elements a set of sandwich beams and sandwich plates with cork compound cores were prepared using the cork compounds which properties have been identified. Several frequency response functions were measured for each sandwich beam and sandwich plate, being the dynamic behavior of the referred structures characterized through modal analysis, being obtained the structures natural frequencies and mode shapes. The referred sandwich structures were then simulated using the formulated finite elements and including in the numerical model the identified cork compound properties. The driving point frequency response functions were generated with the numerical model through the direct frequency analysis procedure. Results from numerical simulations were compared to the ones obtained exerimentally, revealing not only the good representativity of the numerical models generated with the formulated finite elements as well as the accuracy of the identified cork compound properties.

# Contents

# List of Figures

# List of Tables

# Nomenclature

**Subscripts and superscripts**

| | |
|---|---|
| $\gamma$ | subscript indicating a shear component |
| $\varepsilon$ | subscript indicating an extensional component |
| $b$ | subscript indicating the bottom face of a layer |
| $e$ | superscript used when a vector or matrix refers to the element |
| $i$ | subscript representing a general counter for the element nodes |
| $k$ | subscript representing a general counter for the layer numbers |
| $n$ | subscript representing the total number of layers |
| $t$ | subscript indicating the top face of a layer |

**Geometric properties**

| | |
|---|---|
| $A_s$ | section area |
| $h$ | section thickness |

**Mathematical operators**

| | |
|---|---|
| $(\ddot{\bullet})$, $\partial^2 (\bullet) / \partial t^2$ | second derivative in order to time |
| $\delta (\bullet)$ | variation of a quantity $(\bullet)$ |
| $(\dot{\bullet})$, $\partial (\bullet) / \partial t$ | first derivative in order to time |
| $[\bullet]^{\mathrm{T}}$ | transpose of a matrix |

**Scalar variables**

| | |
|---|---|
| $\alpha(\omega)$ | receptance function |
| $\bar{E}(\omega)$ | complex extensional modulus |
| $\bar{G}(\omega)$ | complex shear modulus |
| $\bar{K}$ | frequency dependent complex stiffness of a *sdof* system |

$\bar{X}$ amplitude and phase of the generalized degree of freedom of a *sdof* system

$\eta(\omega)$ loss factor

$\gamma$ shear strains

$\omega$ circular frequency [rad/s]

$\Pi^K$ kinetic energy

$\Pi^P$ potential energy

$\upsilon$ *Poisson's* coefficient

$\varepsilon$ extensional strains

$A(\omega)$ accelerance function

$E$ *Young's* modulus

$E(\omega)$ extensional storage modulus

$F$ amplitude of the force of a *sdof* system

$f(t)$ time dependent force of a *sdof* system

$G$ elastic shear modulus

$G(\omega)$ shear storage modulus

$M$ mass of a *sdof* system

$T(\omega)$ transmissibility function

$u(x,t)$ displacement in the $x$-axis direction

$W$ work of external forces

$w(x,t)$ displacement in the $z$-axis direction

$x(t)$ generalized degree of freedom of a *sdof* system

$\mathcal{M}(\omega)$ apparent mass function

$\mathcal{Z}(\omega)$ dynamic stiffness function

**Vector variables**

$\{\sigma\}$ stress field of the finite element

$\{\mathbf{u}\}$ displacement field of the finite element

$\{\varepsilon\}$ strain field of the finite element

$\{d\}$ generalized displacement field

$\{d^e\}$ generalized displacement field of the element

$\{d_i^e\}$ vector of the element displacements at node $i$

$\{F^e\}$ element force vector

**Matrix variables**

$[B]$ deformation matrix

$[B_\gamma]$ shear deformation matrix

$[B_\varepsilon]$ extensional deformation matrix

$[J]$ inertia matrix

$\left[K_\gamma^e\right]$ element shear stiffness matrix

$[K_\varepsilon^e]$ element extensional stiffness matrix

$[L_k]$ location matrix of layer $k$

$[M^e]$ element mass matrix

$[N]$ interpolation functions matrix

$[\mathcal{L}]$ matrix of the differential operators

$[\mathcal{L}_\gamma]$ matrix of the shear differential operators

$[\mathcal{L}_\varepsilon]$ matrix of the extensional differential operators

$[D]$ elasticity matrix

# Chapter 1

# Introduction

Recent developments on structural engineering, powered by the aim of achieving greater objectives, led to the construction of more efficient structures allowing to overcome challenges which in the past seemed to be unreachable. Part of this evolution has been done with the introduction of brand new materials, with very particular properties, and new production and assembling processes which allowed building more efficient and lighter structures which are, for instance, very important in the demanding aerospace industry.

The use of new stiffer and lighter materials with very low damping capability in structural applications makes them very fragile when submitted to the continuous action of external and internal dynamic excitation sources. In some cases, the vibration energy can lead the structure to collapse or limit its utility.

These effects are more evident in large structures, like bridges, where natural frequencies, and consequently large structural motion amplitudes, are verified at very low frequency values inducing an excessive and uncontrolled structural vibration. Even being not so evident, small structures like aircraft panels, suffer from the same effects if the structure does not have a big enough damping capability.

Most of the collapses of structures are due to fatigue failures caused by a dynamic loading or an impact. Therefore, if the structure damping capability is not able to dissipate the vibration energy introduced by these loads, the useful life period of the structure as well as its safety level will be dramatically reduced and can lead it to collapse.

Essentially, there are three technical solutions to reduce the effects of vibration phenomena in engineering structures. One technique is to eliminate the source of vibration or eliminate its effects, for instance, when it is wanted to eliminate a structural born noise by creating a secondary source which eliminates the primary noise. The second technique is to eliminate the vibration transmission from the vibration source to the structure without eliminating the source, just isolating it. The third technique is to minimize the amplitudes of the structural vibration when the excitation frequencies are closer to the natural frequencies of the structure. More generally, the vibration control methods can be distinguished into passive, active or hybrid methods.

Passive techniques of structural vibration damping are based on the integration of new materials on the original structure, which have higher damping capabilities. When these materials are coupled to the structure they introduce a passive damping effect because no external action is used to control the structure vibration. Commonly, polymeric viscoelastic materials are used to provide this effect.

Active techniques consist of controlling the structure vibration on every time instant using actuators which act over the structure according to a command law in order to minimize and control the vibration measured on some points of the structure. These measurements can be made based on a reference or are obtained by sensors located on the structure. Usually these sensors and actuators are piezoelectric materials which are glued to the structure.

Hybrid control technique consist of a combination of active and passive techniques. Being the piezoelectric actuators, which will perform the active control, attached to structure by a viscoelastic layer which will perform the passive control of vibrations.

In this work, the main focus will be on the passive vibration control which, on the following, will be more detailed.

## 1.1 Passive Damping Treatments

Within all the passive damping mechanisms, the distributed and the localized damping treatments using viscoelastic materials play an important role [1] due to its simple application on the structure, its reduced cost and the reduced structural modification introduced by them.

A general analysis on the viscoelastic passive damping treatments has been made by Nakra [2] on what concerns their configuration and the effects they have on the structure dynamic behavior. A chronological evolution of the passive damping treatments, their origin and future has been made by Jones [3]. Johnson [4] made a compared analysis of the main configurations of passive damping treatments evidencing their advantages and inconveniences. Other publications by Nashif, Jones and Henderson [5] are fully dedicated to this subject.

Although these type of materials are structurally not very efficient due to its low stiffness, they exhibit an excellent dissipation capability which results from its molecular structure.

The use of viscoelastic materials in passive vibration control is then possible due to its excellent damping capability which is a result of the material molecular structure. These materials have the ability to dissipate large amounts of deformation energy to the exterior on the form of heat. This effect results from the interaction of their long reticulated molecular chains when excited cyclically and continuously. This capability allowed to use these materials as isolators on many structures like bridges, buildings or aircrafts and land vehicles, reducing structural vibration as well as noise radiation [6–8].

### 1.1.1 Unconstrained Layer Damping

Unconstrained superficial treatments, as the one depicted in figure 1.1, are obtained by simply applying a layer of viscoelastic material on the surface of the structure which vibration is to be controlled. This type of configuration has a relatively low cost and a very easy application procedure.

However, with this configuration the deformation imposed by the vibrating structure to the viscoelastic layer is not very high and is essentially an extension-compression deformation. Therefore, for this type of treatment to be effective, it requires very thick viscoelastic layers. Actually, it has been verified that the efficiency of this treatments increases significantly with the thickness of the viscoelastic layer until this one reaches a thickness that is twice the one of the structure [9, 10]. Above this value the damping effectiveness remains approximately constant unjustifying the use of thicker viscoelastic layers [11].

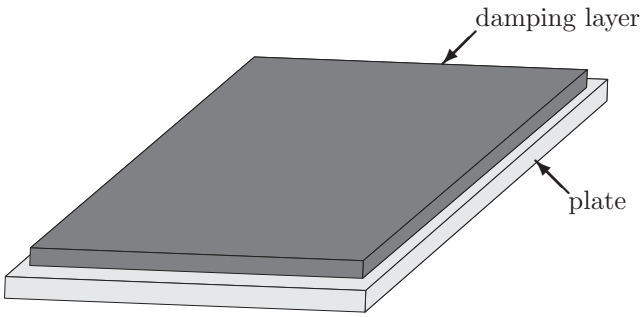


**Figure 1.1:** Unconstrained layer damping on a plate.

Besides the influence of the referred thickness ratio, this treatments efficiency increases as the ratio between the viscoelastic material storage modulus and the structure extensional modulus gets higher, being therefore used, in unconstrained layer damping, viscoelastic materials with a high storage modulus, like plasticized PVC [5].

Generally, this type of treatments are not very efficient because they introduce large changes in the original structure mass and stiffness due to the need of applying very thick viscoelastic layers with a very high storage modulus material, but despite that, they are a quite cheap solution of passive vibration control as well as thermal and acoustic isolation of a structure.

### 1.1.2 Constrained Layer Damping

The application of a restraining layer over the viscoelastic layer applied on the structure surface will induce in the viscoelastic layer a significant increase on its shear deformation. This treatment configuration allows to obtain very effective damping treatments with low thickness viscoelastic layers, usually lower than 0.5mm. In figure 1.2 is generally depicted an example of a constrained layer damping treatment.

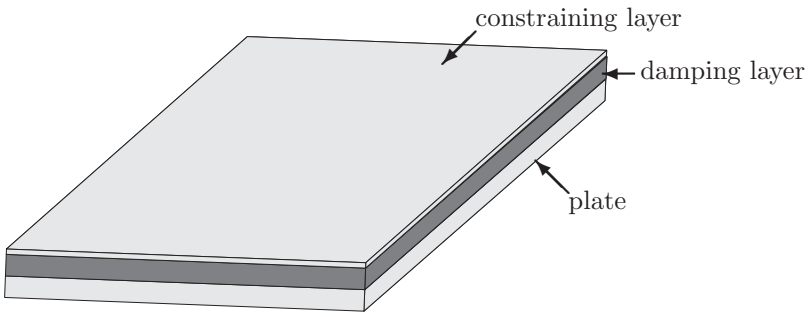


**Figure 1.2:** Constrained layer damping on a plate.

The restriction layer will protect the viscoelastic material from the external environment as well as will increase the shear strain it suffers, allowing to use thinner viscoelastic layers with a higher *Young's* modulus [10].

Despite this treatment efficiency, numerical modeling of this type of structures is not very simple and requires a special attention due to the high shear deformation patterns induced in the dissipation layer due to the existence of a restriction layer. Usually, the viscoelastic materials

applied have a low storage modulus, so it can be promoted its shear deformation. This is why these treatments present a very high efficiency with a low addition of mass and stiffness due to the low thickness of the applied materials.

Constrained layer damping treatments are very easy to apply and some commercial products can be found which are usually ready to be used on the structure surface. These products are made of a polymeric layer with the viscoelastic material and a constraining layer usually made out of aluminum or stainless steel [9].

### 1.1.3 Integrated Layer Damping

Integrated layer damping treatment consists on the application of a viscoelastic material in the core layer of a sandwich structure, in order to maximize the dissipative layer damping capability. This type of structure is generally depicted in figure 1.3 as a sandwich plate structure with a dissipative core.

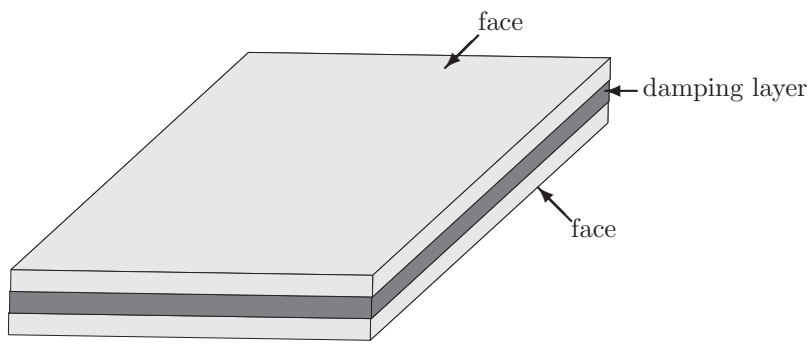


**Figure 1.3:** Integrated layer damping on a plate.

With this type of configuration, the shear strain to which the viscoelastic layer is submitted is the highest when compared to the previously referred damping treatments. This fact is due to the central position of the dissipative layer on the structure neutral axis, amplifying the shear strains in the treatment layer.

Actually, the integrated layer damping treatment is a very effective passive vibration control method. Despite that, while the previously referred configurations are suitable as a corrective procedure, being usually applied after the assembling of the whole structure, the integrated layer damping has to be applied into some parts of the structure prior to the assembling and final production process of the final structure.

## 1.2 Cork as an Engineering Natural Material

Natural cork is a material with a remarkable combination of properties that have been for long time used in various applications like fishing boats, shoe soles, tool handlers and wine bottle sealers. The first known written reference to cork seems to be from Plinius the Old in 77 a.C. [12] who described the cork tree as a small plant which only useful product that can be obtained from it is its bark. Later on Plutarcus, in 100 a.C, refers the use of cork in the building process of roman boats. Additionally, cork played a very important role in the history of science because the first microscopic observations, performed in 1664 by the optic microscope inventor Robert

Hooke, were made on thin sheets of natural cork allowing him to be the first to describe the structure of a living being and to introduce the term cell. Cork is commonly used after its first industrial treatment in fishing boats, shoe soles, tool handles and bottle sealers, also being this kind of applications of cork the older known ones. In this kind of applications only first quality cork is used and a lot of material that can not be reused in the aforementioned applications results from the cut of the cork boards. After 1900, in the United States of America, the cork compound was invented [12] and expanded the whole cork industry, allowing to use this material resultant from the cork first processing as well as lower quality cork produced from younger trees. Additionally, this new material created a new challenge to engineering, raising new questions about its properties, its influence when used in engineering structures, its producing methods and its applications possibilities.

Cork is obtained from the bark of Quercus suber, a species of oak that grows mainly in Mediterranean countries. Cork is described as a homogeneous tissue of thin-walled closed prismatic cells, regularly arranged, without inter cellular spaces. Such prismatic cells (pentagonal or hexagonal) are packed in columns parallel to the radial direction of the tree. The cellular walls are composed of a lignin middle lamelae (27%), a thicker secondary layer with alternate lamelae of suberin (45%), polysaccharides (12%), waxes (6%) and tannins (6%) [13]. The cellular structure of cork is responsible for its singular properties, such as low density, high thermal and acoustic insulation and chemical resistance [12].

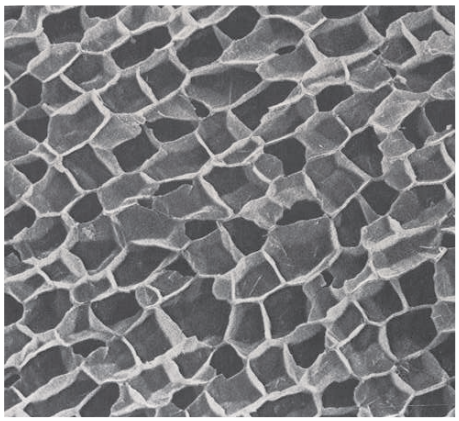

**Figure 1.4:** Cork cellular structure.

Cork is removed from the tree in the form of boards through tangential and longitudinal cuts on the tree bark. Usually, three types of cork can be distinguished according to the growth generation of the tree. The first generation one is known as *virgin cork* and is removed in the first 20 to 30 years of the tree life, when its diameter is between 20-25cm. This type of cork has an irregular surface and can only be used in the production of cork compounds. The second generation cork is known as *secondary cork* and this one does not possesses yet enough quality to be used as primary product, being therefore, essentially used in cork compound production. The third generation of cork, named *amadia cork*, is extracted when the tree is between 40 to 50 years old and corresponds to cork with a good quality that can be directly used to obtain products such as bottle sealers. From this point, *amadia cork* can be extracted from the tree every 10 years until the tree death when it is about 100 to 150 years and has a diameter between 60-100cm. Boards of *amadia cork* are submerged into boiling water and compacted prior to

being process and obtained the final product.

To produce cork compounds, *virgin cork*, *secondary cork* and left overs of the production process of *amadia cork* are used. There are essentially two types of cork compounds, the *black cork compounds* and the *white cork compounds*. The *black cork compounds*, also called *pure cork compounds*, are only made out of cork pieces with dimensions between 1 to 5 cm which, in its production process, are compressed and placed in an autoclave where are treated with water vapor. The compression strength can be varied to obtain different densities in the final product. When the water vapor temperature rises above 300°C the cork compound becomes very dark and this is why they are called *black cork compounds*. On the other hand, *white cork compounds* are completely different materials and much more recent than *black cork compounds*. *White cork compounds* are produced by bonding cork grains, with sizes between 1 to 15 mm, with a synthetic bonding material. The cork grains are mixed with the synthetic bonding material and this mixture is afterwords molded or extruded continuously allowing the bonding material to cure so it can be obtained the final product.

Naturally, in engineering applications, cork is not commonly used in the state it has when it is removed from the tree. In order to maximize the referred capabilities of cork the material is subjected to an industrial process complying a few stages. First of all, the cork bark is used to produce objects like bottle sealer or shoe soles which do not require a very difficult transformation process.

It seems that cork compounds can also be used in sandwich structures, assuring an increasing of the structure damping capability, with possible applications on aeronautic fuselages and land vehicle chassis. This is why cork compound is an excellent material to be used as a *passive free layer damping* (PFLD) or a *passive constrained layer damping* (PCLD) treatments. Its significant low density, large useful temperature range, durability and resistance are important issues that justify the growing interest on these materials.

## 1.3 Modeling and Characterization of Viscoelastic Materials

The development of physically representative models of the viscoelastic materials and the characterization of their properties is a fundamental step when designing structures with passive damping treatments.

The difficulty on the experimental determination of the viscoelastic material mechanical properties, due to its high sensitivity to temperature and frequency dependence, presents one of the up most complex and critical steps while developing and designing efficient passive damping treatments. The representation of these properties throughout physical models is also one of the main problems raised in a passive damping treatment design.

In the middle of the $20^{th}$ century, a growing interest on the evaluation and description of the polymeric viscoelastic materials was verified [9, 14], being made a strong effort toward the understanding of the dissipative mechanism and the characterization of the viscoelastic material behavior. The experimental methodologies to characterize the dynamic behavior of viscoelastic materials remained the same since then, being nowadays used the same techniques as the ones developed at that time, having although evolved the results verification methods using more powerful numerical tools and methods to achieve it. Myklestad [9] presented for the first time, the concept of complex modulus as an approach to model the viscoelastic material mechanical behavior. By then, to represent the dynamic behavior of viscoelastic materials was

normally used a set of rheological models obtained from a combination of discrete elastic and viscous elements. The Maxwell and Voight are the simplest and most commonly known models [9, 14, 15]. Additionally, a combination of these models [11] has been used, allowing a more accurate physical representation of the behavior of the viscoelastic material. Even tough, to conveniently represent the complex modulus of a material along a frequency range it is necessary to use a model with a considerably large number of parameters.

The introduction of the fractionary derivatives concept on the representation of the viscoelastic material behavior was made by Bagley and Torvic [16, 17]. Throughout this model, it becomes possible to describe the viscoelastic behavior of a material in a broad frequency range with a single derivative term. This model is nowadays commonly used in the analysis of passive damping treatments.

More recently, alternative models have been proposed in order to allow the transient analysis of systems with viscoelastic damping. These models formulation is based on the inclusion of a set of additional variables representing the variation of the material properties with frequency. The *Anelastic Displacement Fields* (ADF) model, proposed by Lesieutre [18, 19] introduces the effect of the properties frequency variation using a set of additional anelastic variables. Other model is the *Golla-Hughes-McTavish* (GHM) [20] where a set of additional oscillators is used to represent the viscoelastic effect. Wagner and Adhikari [21] presented a comparative analysis between the different viscoelastic damping models including their space state formalism and their application.

## 1.4 Numerical Modeling of Layered Structures

The most common method to simulate the static and dynamic behavior of structures is the finite element method. In this method, the application of variational principles or the weighted residues method leads to matrices which represent each individual element and can be inserted in a global matrix to obtain a representation of the whole structure. The result of the application of the finite element method is a spatial model described by a set of nodes each one with several degrees of freedom, allowing to numerically obtain the desired solution for a given problem.

Modeling viscoelastic materials in damped continuous systems, such as beams or plates, with the finite element method arises some specific issues that have to be considered. It is necessary to consider that the viscoelastic material properties vary in frequency and temperature, therefore, these two variables have to be considered in the simulation. Additionally, it is necessary to select the model to describe the viscoelastic material, considering the simulation objective, as well as the kind of solution it is supposed to be obtained.

To understand and study the behavior of a layered structure with viscoelastic based passive damping treatments, a representative and accurate numerical model is required. Due to the high shear deformation pattern developed inside the viscoelastic layer in a laminated structure, the classical laminate theories are not adequate to accurately describe it [22]. One way to model layered structures, with viscoelastic layers, using the finite element method consists on applying stratified conventional elements, representing individually each layer [23–25]. Although these models represent quite accurately the structure deformation pattern, they are computationally very demanding. To overcome these drawbacks, the well known *layerwise* theory, based on a piecewise description of the displacement field [26–28], has been considered as a promising approach, evidencing a good accuracy in the simulation of the damping layer effects as published

in [29–32]. Despite the obtained good results, some of the published models suffer from lack of generalization being some of them built considering strictly a three layered structure.

*Layerwise* theories are developed by assuming continuity of the displacements field over the laminate thickness [26]. As a consequence of that, the displacement components are continuous through the laminate but its derivatives with respect to the thickness coordinate may be not at several points through the thickness. *Layerwise* displacement fields represent more accurately the moderate to severe cross-sectional wrapping associated with the deformation of thick laminates.

The displacement-based *layerwise* theories can be divided in two classes [26] as follows:

- Partial *layerwise* theories - which use *layerwise* expansions for the in-plane displacement components but not the transverse displacement component;
- Full *layerwise* theories - that use expansions for all three displacement components.

The use of partial and full *layerwise* theories in laminated beams and plates is widely accepted because they allow in-plane displacements to vary in a *layerwise* manner, giving a good representation of its zigzag behavior through the thickness of the laminate. This zigzag behavior is more pronounced for thick laminates where the transverse shear modulus changes abruptly through the thickness.

The finite element method, with a *layerwise* theory based finite element, is the most common procedure to numerically simulate layered structures. Despite that fact, a main drawback of this approach is verified when trying to simulate the structural behavior at mid and high frequencies which will demand an increase on the number of elements associated with a reduction on their dimensions as the frequency range to be analyzed increases, requiring more powerful computational resources. The solution to overcome this problems is to use wave based theories which accurately describe the wave motion in a continuum solid [33] allowing to easily convert the problem from the time to the frequency domain. One of the existing methods is the Statistical Energy Analysis (SEA) [34], which is a non element-based, probabilistic technique capable to predict the structure averaged energy levels. Although the good accuracy provided by this method for high frequencies, it is unable to give results at different locations on the domain and, in the mid-frequency range, some of the assumptions that are necessary for its application are not verified, such as high modal density. An element based alternative method to simulate the dynamic behavior of a structure at high frequencies is the Spectral Element Method (SEM) which is a wave based method [35] where the element stiffness matrix is frequency dependent assuring a good accuracy even at high frequencies with a small algebraic dimension problem.

## 1.5 Objective of the Thesis

Cork compound insulation properties are well known and make it one of the best materials to be used as insulator. Despite this fact, the cork compound dynamic properties and specially its viscoelastic characteristics are scarcely known and have not been deeply investigated.

The use of damping treatments to increase structural damping is one of the most widely used methods to improve a structure dynamic behavior. Nowadays, the automobile and aeronautical industry apply these kind of surface treatments regularly when structural vibration control is required. The most common materials used in layered damping treatments are synthetic, polymeric materials which are very difficult to recycle due to the bonding of these type of materials

to the host structure. Cork compound, as a traditionally insulator material, can present an alternative to these synthetic materials due to its high damping characteristics and because it eliminates the recycling problem. To better understand the capability of cork compound to be used as a passive damping treatment, it is necessary to accurately know the dynamic properties of cork compound.

This thesis aims to obtain the dynamic properties, namely the storage modulus and loss factor, of several commercially available cork compounds with different formulation parameters in order to inspect their properties frequency dependence and therefore verify the cork compound viscoelastic properties characterizing the material.

Additionally, the performance of the cork compound in a real structure is to be tested. Therefore, the dynamic behavior of a set of beam and plate test samples, in a three layered sandwich configuration with cork compound cores, will be analyzed. The frequency response functions of the structures will be obtained and throughout experimental modal analysis the structures modal parameters such as natural frequencies, mode shapes and modal damping ratios will be obtained.

Another objective of this thesis is to formulate a beam and plate finite element based on a partial *layerwise* theory. Both finite elements are programed in a finite element routine allowing to simulate the real structures with cork compound layers. To simulate the beam and plate structures, the cork compound dynamic properties are inserted in the finite element model using the Complex Modulus Approach (CMA) and the response evaluation is performed in the frequency domain using the *Direct Frequency Analysis* (DFA) procedure. In the case of the plate finite element, two strategies will be implemented to avoid shear locking problems, one is to use biharmonic interpolation functions, another is to use a *Mixed Interpolation of Tensorial Components* (MITC) [9].

In order to allow high frequency simulation of layered structures, a beam spectral element will be developed.

## 1.6 Organization of the Thesis

This thesis begins with an introductory chapter, chapter 1, where a revision of the state of the art is performed and a summary of the contents of the thesis is presented. A brief introduction of the approached subjects is as well presented.

In chapter 2, a detailed determination of the cork compound dynamic properties is performed. Previous studies have been made in order to investigate cork compound properties [13], but these were experimental determinations made at the very low constant frequency of 1 Hz which is meaningless if the material is to be used in demanding dynamical applications. Therefore, given the lack of data relative to the dynamic properties of cork compound, in order to give a more real approach to a further finite element simulation, a determination procedure, based on the work developed by Moreira [9], Moreira and Dias Rodrigues [36], was used to determine the cork compound dynamic properties. With this procedure, it was possible to obtain the shear storage modulus as well as the material loss factor [37], in both shear and extension.

In chapter 3, a *layerwise* beam element was formulated considering two translational displacements for each element layer. This element is representative of laminate structures in which one of the laminate layers is made out of cork compound implying that the material dynamic properties were included in the formulated element. The element was also formulated in order to

be possible to include it in a finite element method routine developed in Matlab® programming language.

In chapter 4, the experimental tests performed on a set of three layered sandwich beams with cork compound cores and two aluminum plies are presented. Different cork compounds with different thicknesses, granulometry and density were used and these parameters influence on the system dynamic properties was investigated. To obtain the system characteristics a modal identification procedure [38] was used, assisted by the Matlab® SDT® toolbox. The experimental results obtained were afterwords compared to the ones obtained from the numerical simulation using the finite element method.

In chapter 5, numerical results were obtained, using the beam finite element developed in chapter 3. To verify the physical representativity of the finite element, the sandwich beam analyzed in chapter 4 was simulated, and using a direct frequency analysis and the cork compound properties determined in chapter 2, the driving point FRFs were predicted and compared to the measured ones in chapter 4.

The beam element developed in chapter 3 was then extended to a plate element, formulated in chapter 6, in order to further allow a deeper investigation on the influence of the treatment properties on a plate like structure dynamic behavior. In Moreira [9], Moreira and Dias Rodrigues [36], the element displacement approach has been made considering for each layer rotational displacements. In this thesis, the plate element has been formulated considering translational displacements instead of the rotational ones. Similarly to the beam element, the plate element was developed according to a partial *layerwise* theory so it was representative of the subject laminate structure. The plate element is therefore a multilayer, multimaterial element. The element was also developed in order to be included in a Matlab® finite element routine.

In chapter 7 experimental tests were performed on three sandwich plates each having a different cork compound core with two aluminum plies. The effects of the cork compound core were investigated, and a modal identification procedure was performed on the measured FRFs.

In chapter 8 the plate finite element formulated in chapter 6 was used to simulate the plate structures tested in chapter 7, including the cork compound dynamic properties obtained in chapter 2. The predicted driving point FRFs are then compared to the ones measured in chapter 7.

In chapter 9 the spectral element method is presented as a case study to approach the high frequency problem. Some simple examples are solved and a beam spectral element is formulated, being the results, as well as the dimension of the spectral problem compared with the finite element solution.

In chapter 10 some conclusions are drawn from the developed work.

# Chapter 2

# Cork Compound Properties

## 2.1 Introduction

When designing an engineering structure it is fundamental to know the properties of every material used in it, specially if the structure is to be submitted to extreme situations or if it has to be designed with low safety coefficients due to weight restrictions for instance. Cork compound is the key material of this study, as it is applied to laminate sandwich beams and plates which will, further on, be the subject of the experimental tests and numerical simulations.

In this study, the analysis of the dynamic behavior of structures with cork compound will be performed. Therefore, it is essential to correctly obtain the dynamic properties of this material, namely its frequency dependent storage modulus and loss factor [39] due to the cork compound viscoelastic behavior [12, 13].

To obtain these properties, two experimental methodologies are presented and applied. One to identify the shear storage modulus and loss factor, properties described in the ASTM norm [37], and other to identify the extensional storage modulus and loss factor of different commercially available cork compounds, allowing to investigate the frequency dependence of these properties. Additionally, the effects of cork compound formulation parameters on the complex modulus are also investigated by testing compounds with different densities, grain sizes and thicknesses.

## 2.2 Shear Properties of Cork Compound

The experimental characterization methodology is based on the evaluation of the effects of the cork compound element, which represents the stiffness and damping, on the response of a dynamic system. For this purpose, it was adopted a direct approach similarly to the described by Kergourlay and Balmés [40], and by Allen [39], by using a discrete mass-complex stiffness dynamic system. The complex modulus was then directly identified from the frequency response functions measured on the experimental setup [9, 36].

### 2.2.1 Analytical model

The analytical model used for the identification procedure is based on the characterization of a complex stiffness spring of a single degree of freedom system represented in figure 2.1.

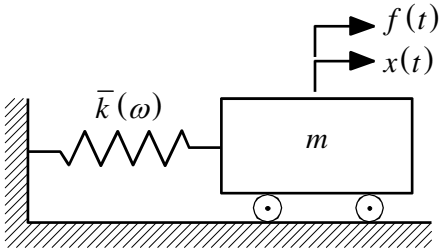


**Figure 2.1:** Single degree of freedom analytical model.

The differential equation of motion for this single degree of freedom system, excited by the force $f(t)$ , is defined as:

$$M\ddot{x}(t) + \bar{K}(\omega)\, x(t) = f(t) \tag{2.1}$$

where $M$ represents the system mass, $\bar{K}(\omega)$ the frequency dependent spring complex stiffness, $x(t)$ the mass displacement and $\ddot{x}(t)$ the time second derivative.

Assuming an harmonic excitation $f(t) = Fe^{j\omega t}$ with amplitude $F$ and frequency $\omega$ , the system response will also be harmonic, $x(t) = \bar{X}(\omega)\, e^{j\omega t}$, with amplitude and phase given by $\bar{X}(\omega)$, allowing equation (2.1) to be rewritten as:

$$\left[-\omega^2 M + \bar{K}(\omega)\right] \bar{X}(\omega) = F \tag{2.2}$$

Therefore, the receptance and accelerance frequency response functions [38] of the dynamic system can be defined as:

$$\alpha(\omega) = \frac{\bar{X}(\omega)}{F} = \frac{1}{-\omega^2 M + \bar{K}(\omega)} \qquad \text{(Receptance)} \tag{2.3}$$

$$A(\omega) = \frac{-\omega^2 \bar{X}(\omega)}{F} = \frac{\omega^2}{\omega^2 M - \bar{K}(\omega)} \qquad \text{(Accelerance)} \tag{2.4}$$

The stiffness complex function of the test sample can be directly determined either through the inverse of the receptance function (dynamic stiffness $\mathcal{Z}(\omega)$), or the inverse of the accelerance function (apparent mass $\mathcal{M}(\omega)$):

$$\bar{K}(\omega) = \omega^2 M + \mathcal{Z}(\omega) \qquad \text{(Dynamic stiffness)} \tag{2.5}$$

$$\bar{K}(\omega) = \omega^2 M - \omega^2 \mathcal{M}(\omega) \qquad \text{(Apparent mass)} \tag{2.6}$$

In a dynamic system where the stiffness element is deformed in shear, the complex shear modulus $\bar{G}(\omega)$ is related with the complex stiffness function as follows,

$$\bar{G}(\omega) = G(\omega)\,(1 + j\eta(\omega)) = \bar{K}(\omega)\,\frac{h}{A_s} \tag{2.7}$$

where $\eta(\omega)$ represents the material loss factor and $G(\omega)$ the shear storage modulus. The geometric parameters $A_s$ and $h$ represent, respectively, the test sample shear area and its thickness.

### 2.2.2 Experimental setup

The experimental setup simulates a single degree of freedom system using one sample of the cork compound that is deformed in shear.

#### Experimental assembly

The proposed experimental assembly, capable of representing a single degree of freedom system, and which will be used along the identification process, is depicted in figure 2.2.

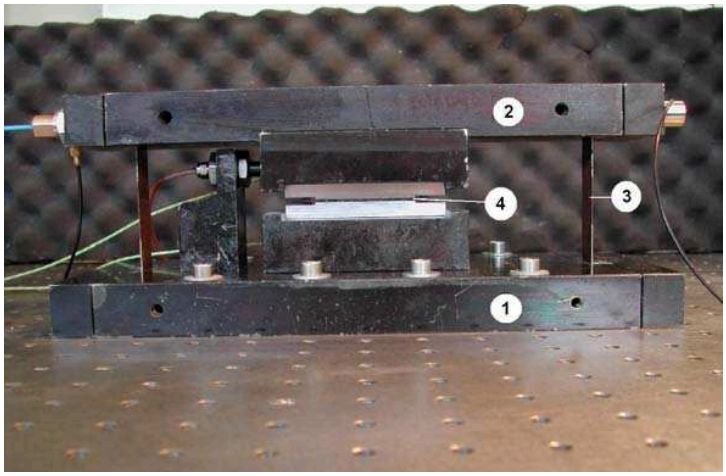


**Figure 2.2:** Experimental assembly.

This assembly consists of a rigidly fixed base plate (1) and a moving upper plate (2) representing the moving mass. The cork compound test sample (4) is placed between two rigid blocks, as depicted in figure 2.3, and connected to each plate. The cork compound sample represents the complex stiffness of the discrete dynamic system. Additionally, two very thin spring steel blades (3), clamped at both ends of the moving and fixed plate, introduce a very low stiffness into the system and provide the necessary restraining condition to minimize effect of spurious degrees of freedom, getting the system more close to a single degree of freedom one.

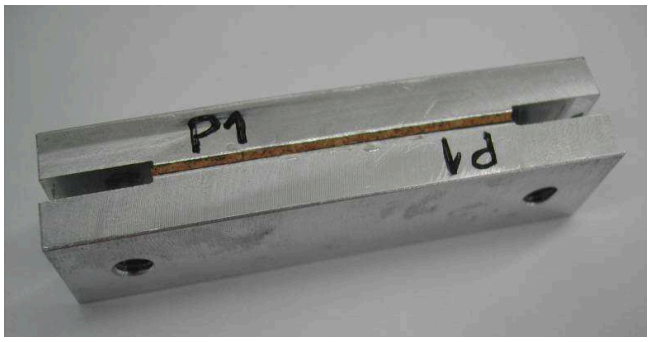


**Figure 2.3:** Test sample.

The excitation force is applied by the electromagnetic shaker (LDS-201), connected to one

side of the moving upper plate by a stinger, and it is measured with a piezoelectric force transducer (B&K-8200). The system's response is measured in terms of acceleration on the opposite side of the moving plate by a piezoelectric accelerometer (B&K-4371) as well as by a proximity probe (Philips-PR6423) that measures the relative displacement between the moving plate and the fixed one, where it is mounted, as depicted in figure 2.4.

The excitation force signal type is random and is generated by the FFT spectral analyzer (B&K-2035) generator module and amplified by the power amplifier (LDS-PA25E). The signal conditioning and the frequency response functions determination are also performed by the referred spectral analyzer.

The electromagnetic shaker and the experimental assembly are rigidly fixed to the surface of a granite block (figure 2.4) which is supported by four silicone rubber pads in order to minimize the effects of the rigid body modes of the assembly.

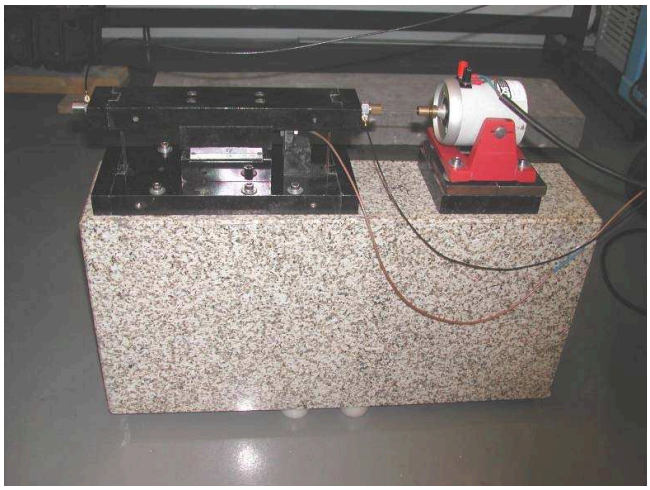

**Figure 2.4:** Experimental setup.

### Material samples

The experimental tests were performed for three different cork compound samples, that have been named P1, P2 and P3, with different grain sizes and densities as illustrated in figure 2.5.

**(a)** Specimen P1. **(b)** Specimen P2. **(c)** Specimen P3.

**Figure 2.5:** Cork compound samples.

The shear storage modulus and loss factor were computed for the referred three different

test samples which characteristics are listed in table 2.1.

**Table 2.1:** Test samples characteristics.

| Name | Thickness [mm] | Mass [g] | Area [mm$^2$] | Density | Grain |
|---|---|---|---|---|---|
| P1 | 1.2 | 63 | 997.67 | high | fine (0.5-2mm) |
| P2 | 1.2 | 63 | 1006.83 | low | fine (0.5-1mm) |
| P3 | 1.2 | 63 | 993.79 | high | coarse (2-4mm) |

The measurements were performed at a room temperature of approximately 25$^o$C. In the table 2.2, the relation between the test samples used to characterize the cork compound material and the cork compound type is shown.

**Table 2.2:** Test samples characteristics.

| Name | Cork compound type |
|---|---|
| P1 | 8123 |
| P2 | 8003 |
| P3 | 8303 |

Therefore, the characterization of these cork compounds will allow to perform further simulations which can then include the frequency dependent cork compound properties.

### 2.2.3 Results

A set of four accelerance frequency response functions (FRFs) and a set of four receptance FRFs were measured for each specimen. For each set of FRFs, two of them were measured in bandwidth [0-400]Hz and the other two in the bandwidth [200-400]Hz. The referred FRFs are depicted in appendix A, where figure A.1(a), figure A.2(a) and figure A.3(a) show the accelerance FRFs measured, respectively, for specimens P1, P2 and P3, while figure A.1(b), figure A.2(b) and figure A.3(b) represent the receptance ones.

Using equations (2.5)-(2.7) and the measured receptance and accelerance FRFs, the complex shear modulus was identified, and from it, the shear storage modulus and the loss factor of each test sample were calculated. Figures 2.6(a) and 2.6(b) represent the distribution, along the frequency analysis range, of the shear storage modulus and loss factor, computed from measured accelerances and receptances of Sample P1. The same properties obtained for P1 are reproduced in the following figures 2.7 for sample P2 and figures 2.8 for sample P3.

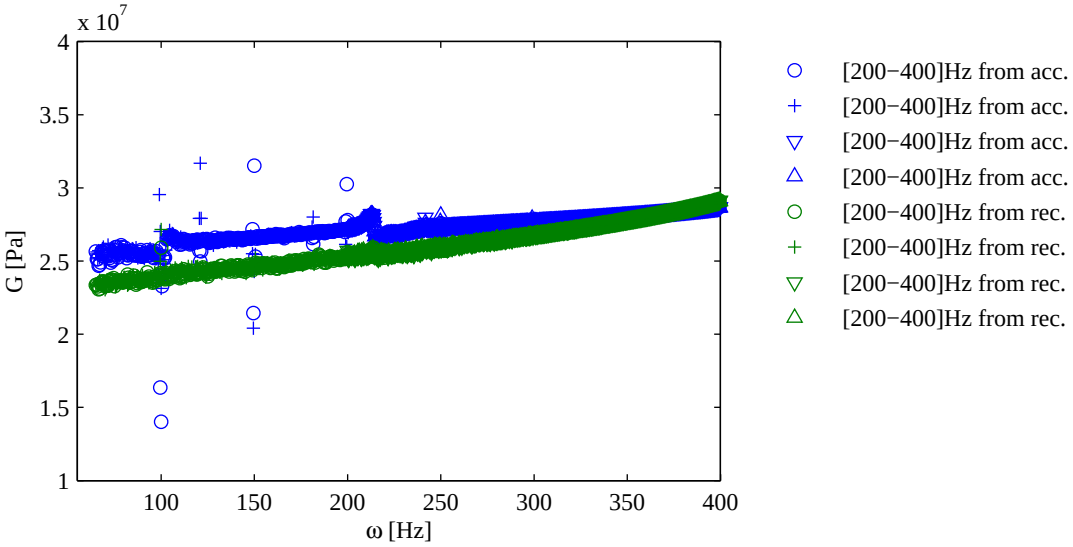


**(a)** $G(\omega)$ identified from receptances and accelerances.

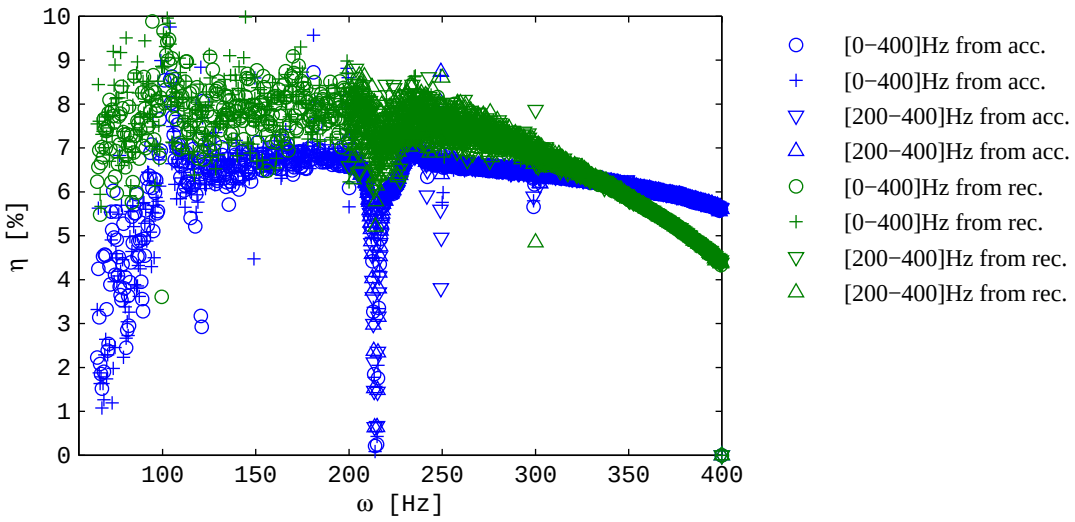


**(b)** $\eta(\omega)$ identified from receptances and accelerances.

**Figure 2.6:** Identified shear storage modulus and loss factor of sample P1.

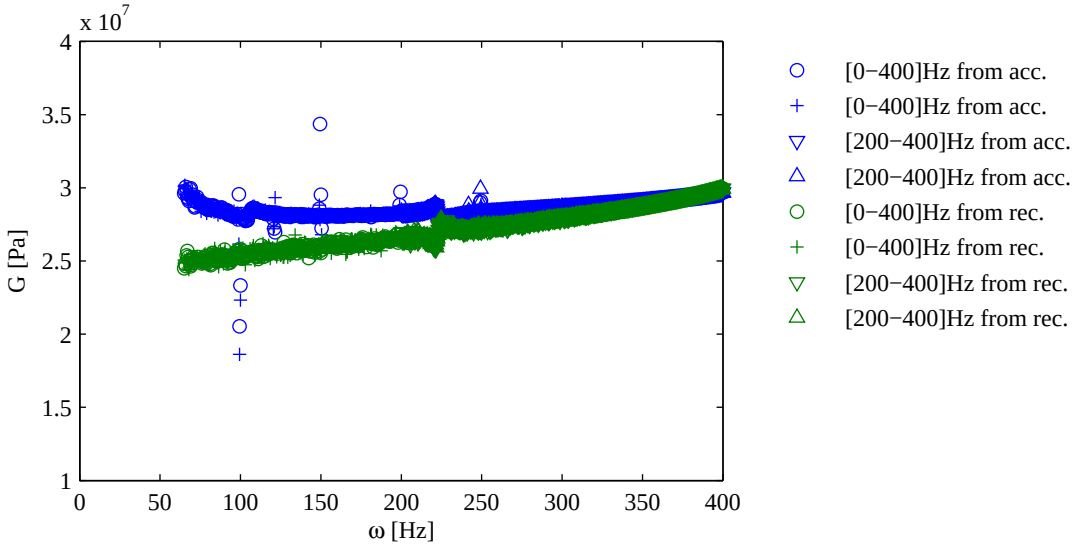


**(a)** $G(\omega)$ identified from receptances and accelerances.

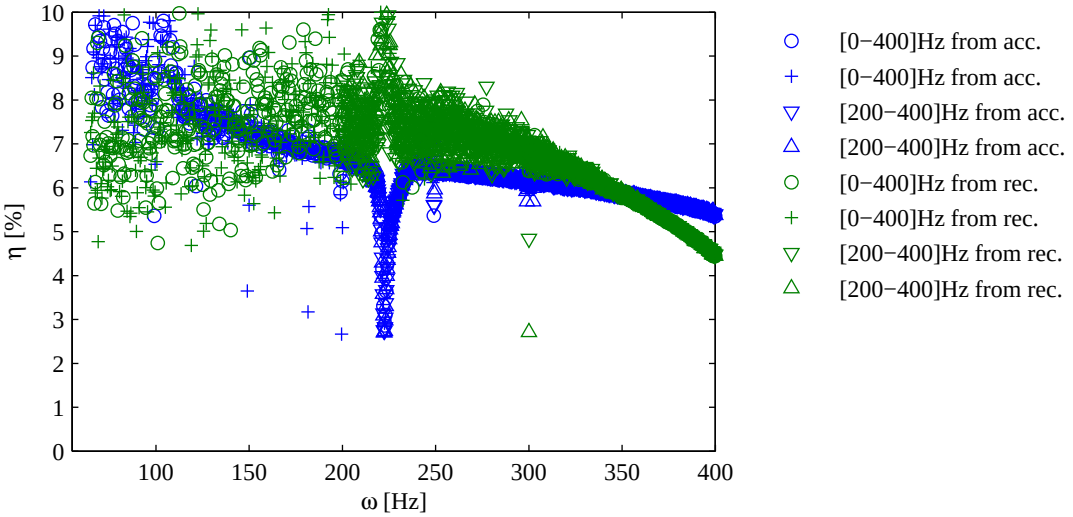


**(b)** $\eta(\omega)$ identified from receptances and accelerances.

**Figure 2.7:** Identified shear storage modulus and loss factor of sample P2.

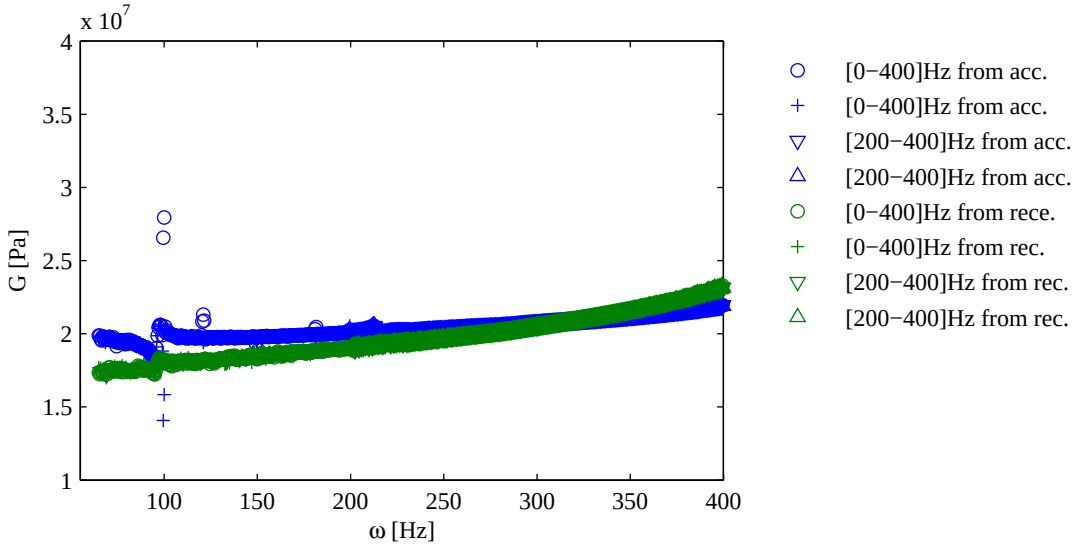


**(a)** $G(\omega)$ identified from receptances and accelerances.

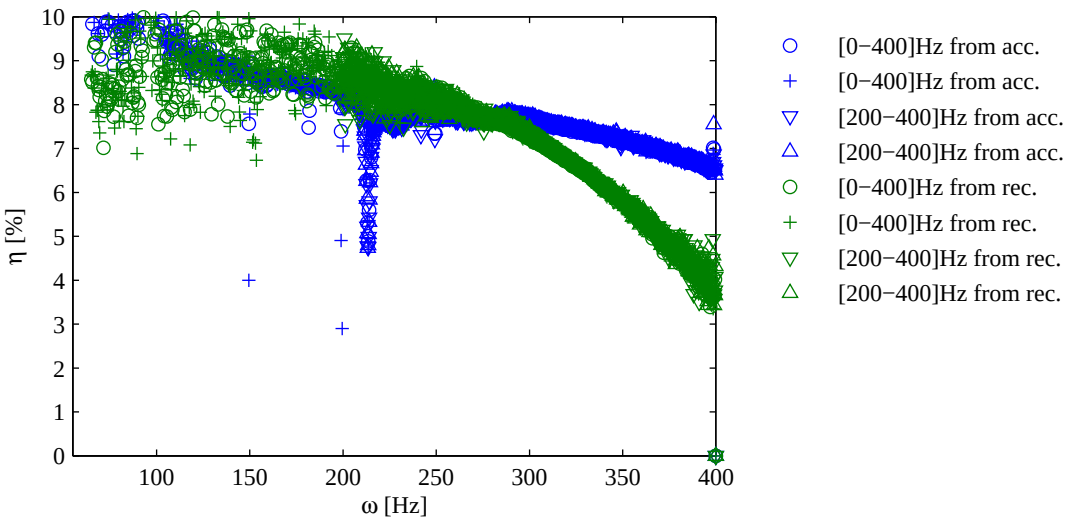


**(b)** $\eta(\omega)$ identified from receptances and accelerances.

**Figure 2.8:** Identified shear storage modulus and loss factor of sample P3.

### 2.2.4 Discussion

At the low frequency band, measured FRFs are affected by the presence of the rigid body modes and some measurement noise, which enhances oscillation of shear storage modulus and loss factors values at those low frequencies. Furthermore, as the identification procedure is very sensitive to measurement noise, the experimental procedure needs to be improved in order to enhance the quality of the results in the low frequency range. On the other hand, the distribution of the results in the frequency range [200-400] is smooth and shows a well defined tendency along frequency, which demonstrates that measurements and the identification methodology are consistent.

From the obtained results, one can see that the grain size influences the shear storage modulus while it has a little influence on the loss factor values, as it can be seen in the results for specimens P1 and P3, figures 2.6 and 2.8. Moreover, it can be seen that in the frequency band of analysis both the shear storage modulus and the loss factor of cork compounds present frequency dependence. Although this frequency dependence is not very accentuated, it reveals, as expected, a viscoelastic behavior of these materials.

## 2.3 Extensional Properties of Cork Compound

To obtain the extensional properties of cork compound, a semi-definite two degrees of freedom system was set up where the cork compound represents the stiffness element connecting the two degrees of freedom. The transmissibilities and accelerances of this system were measured, and directly from them, the dynamic properties of the material were identified.

### 2.3.1 Analytical model

In this alternative, a system with two degrees of freedom is considered. This system, as depicted in figure 2.9, complies two concentrated masses, where mass $m$ is driven by the excitation $f(t)$. The system two degrees of freedom are $x(t)$ for mass $m$ and $x_0(t)$ for mass $M$. The spring element with stiffness $\bar{K}$ represents the cork compound test sample and from it the material properties will be obtained.

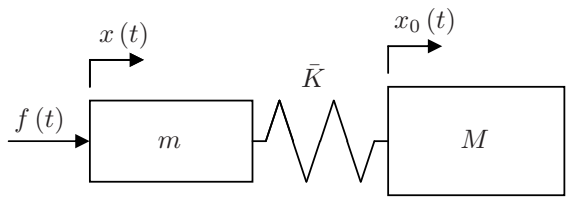


**Figure 2.9:** Two degrees of freedom analytical model.

The system of differential equations which describe the system motion is defined as:

$$\begin{cases} m\ddot{x}(t) + \bar{K}\left(x(t) - x_0(t)\right) = f(t) \\ M\ddot{x}_0(t) + \bar{K}\left(x_0(t) - x(t)\right) = 0 \end{cases} \tag{2.8}$$

As it has been done previously, assuming an harmonic excitation $f(t) = Fe^{j\omega t}$ with amplitude $F$ and frequency $\omega$ , the system steady responses will also have to be harmonic, therefore $x(t) = \bar{X}(\omega)\, e^{j\omega t}$ and $x_0(t) = \bar{X}_0(\omega)\, e^{j\omega t}$, with phasors $\bar{X}(\omega)$ and $\bar{X}_0(\omega)$, allowing expression (2.8) to be rewritten as

$$\begin{cases} \left(-\omega^2 m + \bar{K}\right)\bar{X} - \bar{K}\bar{X}_0 = F \\ \left(-\omega^2 M + \bar{K}\right)\bar{X}_0 - \bar{K}\bar{X} = 0 \end{cases} \tag{2.9}$$

Manipulating the algebraic system of equations (2.9), the following frequency response functions [38], accelerance and transmissibility, of the two degrees of freedom semi-definite system

can be obtained:

$$T(\omega) = \frac{\bar{X}_0(\omega)}{\bar{X}(\omega)} = \frac{\bar{K}}{-\omega^2 M + \bar{K}} \qquad \text{(Transmissibility)} \tag{2.10}$$

$$A(\omega) = \frac{-\omega^2 \bar{X}(\omega)}{F} = \frac{\omega^2 M - \bar{K}}{\omega^2 M m + (M+m)\bar{K}} \qquad \text{(Accelerance)} \tag{2.11}$$

The stiffness $\bar{K}$ which is related to the material dynamic properties, can be determined from both expressions (2.10) and (2.11) as follows,

$$\bar{K}(\omega) = \frac{-\omega^2 M T(\omega)}{1 - T(\omega)} \qquad \text{(from Transmissibility)} \tag{2.12}$$

$$\bar{K}(\omega) = \frac{\omega^2 M (1 - mA(\omega))}{1 - (M+m) A(\omega)} \qquad \text{(from Accelerance)} \tag{2.13}$$

In a dynamic system where the stiffness element is deformed in extension, the complex extensional modulus $\bar{E}(\omega)$ is related with the complex stiffness function as follows

$$\bar{E}(\omega) = E(\omega)(1 + j\eta(\omega)) = \bar{K}(\omega)\frac{h}{A_e} \tag{2.14}$$

where $\eta(\omega)$ represents the material loss factor and $E(\omega)$ the extensional storage modulus. The geometric parameters $A_e$ and $h$ represent, respectively, the test sample extensional area and its thickness.

### 2.3.2 Experimental setup

The experimental setup presented in this section aims to simulate the analytical semi-definite two degrees of freedom system, described in the previous section, where the cork compound test sample acts as the system stiffness connecting the two masses (degrees of freedom).

#### Experimental assembly

The proposed experimental assembly, capable of representing a semi-definite two degrees of freedom system, and which will be used along the cork compound properties identification process, is represented in figure 2.10a.

This assembly has a moving mass (1), which represents mass $m$ in the previously described analytical model, and another moving mass (3), representing mass $M$. The assembly will be suspended from a frame structure, using hooks (4), to assure a semi-definite system with its rigid body mode. The cork compound test sample (2) is placed between the two masses, representing the system stiffness and damping.

The cork compound test sample was fixed to two aluminum cylinders as depicted in figure 2.10b using epoxy resin assuring a rigid connection between the cork compound and the moving components.

The excitation force was applied by the electromagnetic shaker (LDS-401). The excitation force and acceleration of the degree of freedom $x(t)$ associated with mass $m$ were measured with the impedance head (B&K8001-285). The response $x_0(t)$ of mass $M$ was also measured in terms of acceleration on the extreme side of mass $M$ by a piezoelectric accelerometer (B&K4371-430).

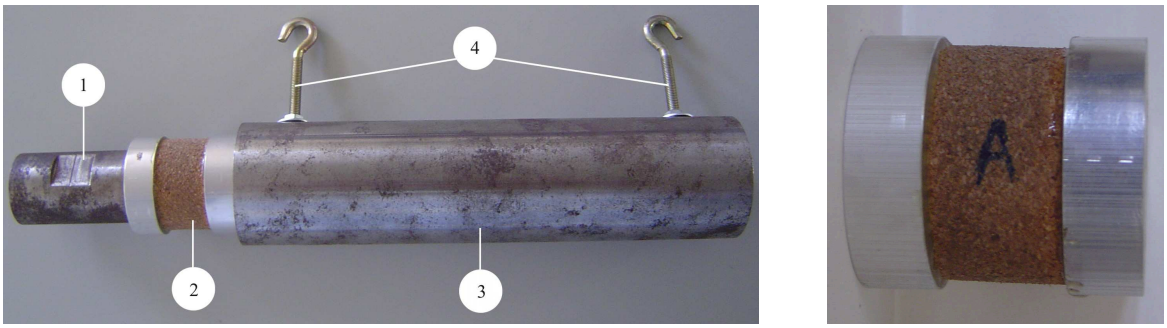


**(a)** Experimental assembly. **(b)** Test sample.

**Figure 2.10:** Experimental assembly and test sample.

The electromagnetic shaker and the experimental assembly were suspended from two independent frame structures to allow a more efficient alignment between the shaker and the experimental assembly, as depicted in figure 2.11, assuring that the movement of the assembly would only be made in its axial direction.

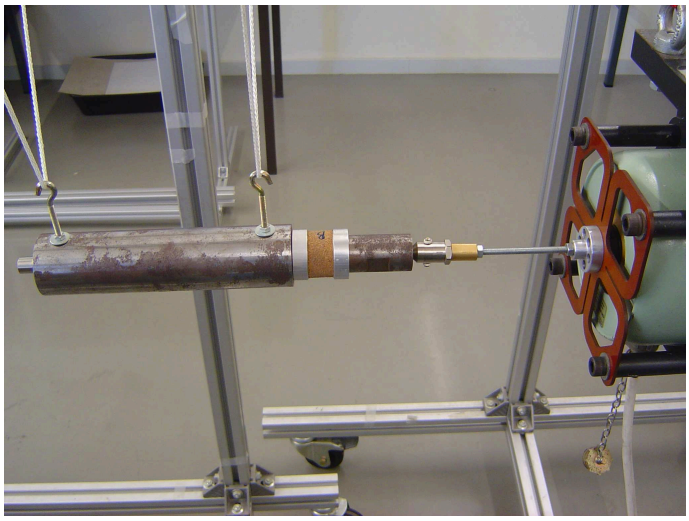

**Figure 2.11:** Experimental setup.

With the measurement of the excitation force and the acceleration of $x(t)$ from the transducer B&K8001-285, it becomes possible to obtain the accelerance analytically described by equation (2.11). Furthermore, with the acceleration of the degree of freedom $x(t)$, obtained with the transducer B&K8001-285, and the acceleration of the degree of freedom $x_0(t)$, obtained with the transducer B&K4371-430, it is possible to determine the transmissibility function that was previously established in equation (2.10).

The excitation force signal used was random and was generated by the FFT spectral analyzer (B&K-2035) generator module and amplified by the power amplifier (LDS-PA100E). The signal conditioning and the described frequency response functions determination were also performed by the referred spectral analyzer.

### Material samples

The experimental tests were performed on four different cork compound samples, that have been named A, B, C and D, with different grain sizes and densities as it can be observed in figure 2.12.

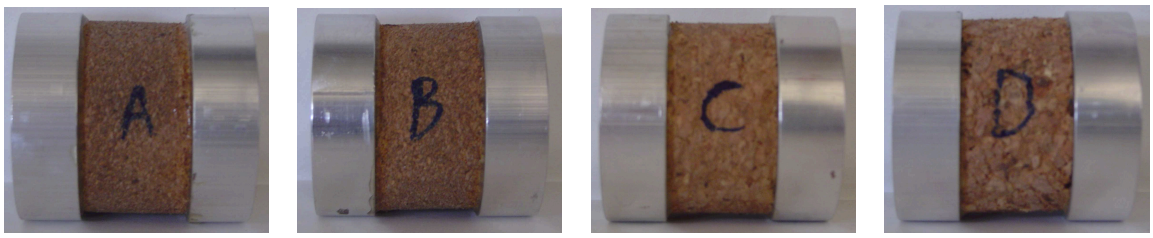


**(a)** Specimen A **(b)** Specimen B **(c)** Specimen C **(d)** Specimen D

**Figure 2.12:** Cork compound samples.

The detailed properties of the four test samples are listed in the following table 2.3.

**Table 2.3:** Test samples characteristics.

| Sample | Thickness [mm] | Mass [g] | Area [mm$^2$] | Density | Grain |
|---|---|---|---|---|---|
| A | 20 | 63 | 997.67 | low | fine (0.5-2mm) |
| B | 20 | 63 | 1006.83 | high | fine (0.5-1mm) |
| C | 20 | 63 | 993.79 | high | coarse (2-4mm) |
| D | 20 | 63 | 993.79 | low | coarse (2-4mm) |

The measurements were performed at a room temperature of approximately 25$^o$C. Test samples described in table 2.3 are of cork compounds of types which will further on be used in beam and plate structures which shall be subject of an experimental modal analysis and numerical simulation. In the table 2.4, the relation between the test samples name and their commercial reference is presented.

**Table 2.4:** Test samples commercial reference.

| Sample | Commercial reference |
|---|---|
| A | 8003 |
| B | 8123 |
| C | 8303 |
| D | 8002 |

Therefore, the characterization of these cork compounds will allow to perform further simulations which can then include the frequency dependent cork compound properties.

### 2.3.3 Results

For each test sample, an accelerance and a transmissibility function was measured. These FRFs are presented in appendix A, and from them, using equations (2.12)-(2.13), the complex stiffness of the two degree of freedom model was determined, allowing to obtain, using (2.14), the extensional storage $E(\omega)$ modulus and loss factor $\eta(\omega)$ of each test sample. In figure 2.13a is presented the obtained extensional storage modulus of Sample A, identified from the measured accelerance and transmissibility, and in figure 2.13b is presented the obtained loss factor, from the accelerance and transmissibility, of Sample A. The same type of results are presented for Sample B in figure 2.14, for Sample C in figure 2.15 and for Sample D in figure 2.16.

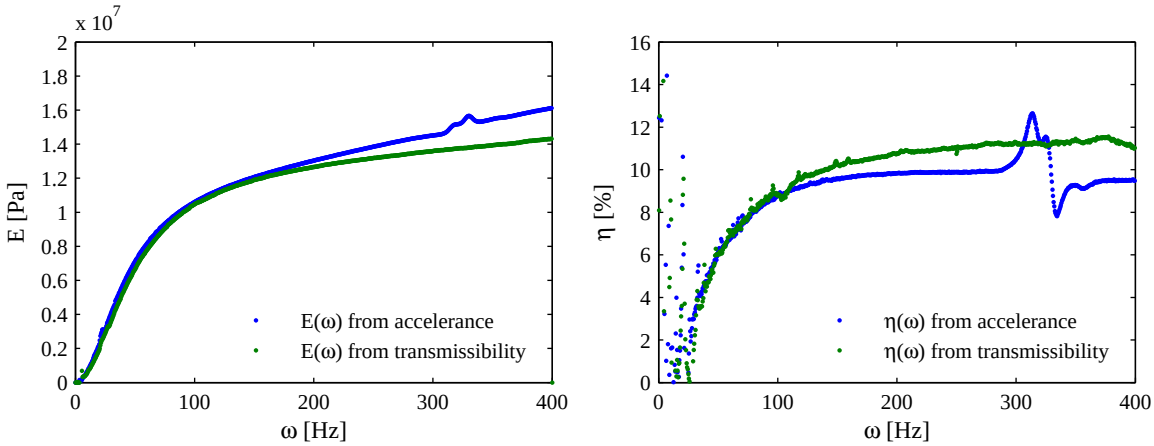


**(a)** Identified $E(\omega)$ from accelerance and transmissibility

**(b)** Identified $\eta(\omega)$ from accelerance and transmissibility

**Figure 2.13:** Extensional storage modulus and loss factor of Sample A.

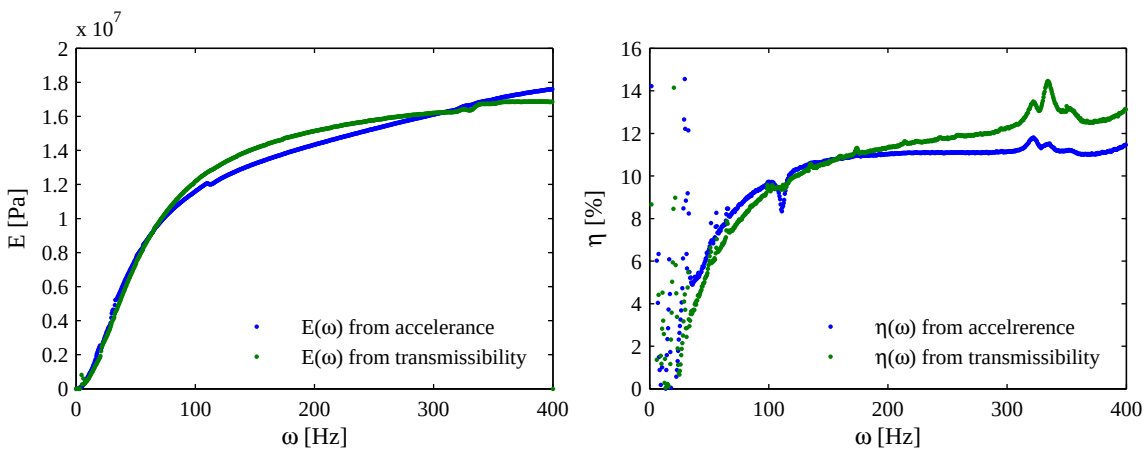


**(a)** Identified $E(\omega)$ from accelerance and transmissibility

**(b)** Identified $\eta(\omega)$ from accelerance and transmissibility

**Figure 2.14:** Extensional storage modulus and loss factor of Sample B.

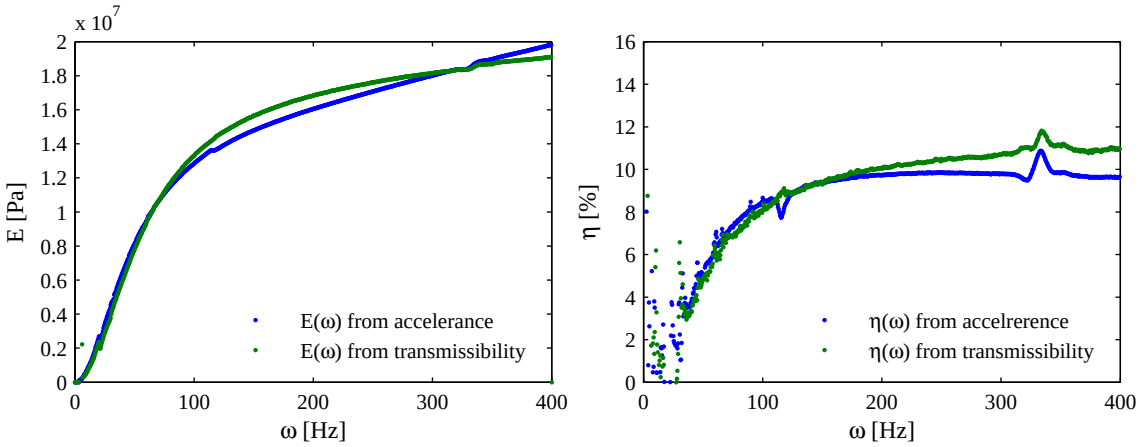


**(a)** Identified $E(\omega)$ from accelerance and transmissibility

**(b)** Identified $\eta(\omega)$ from accelerance and transmissibility

**Figure 2.15:** Extensional storage modulus and loss factor of Sample C.

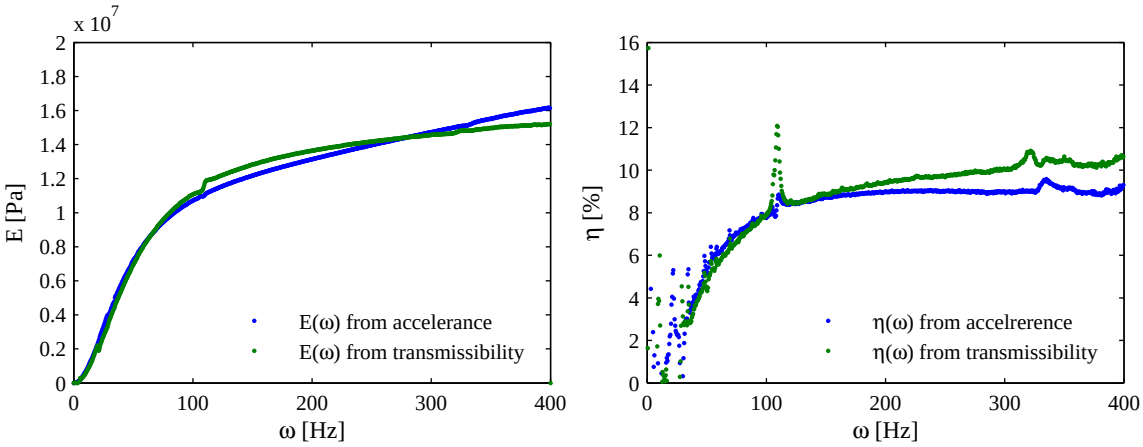


**(a)** Identified $E(\omega)$ from accelerance and transmissibility

**(b)** Identified $\eta(\omega)$ from accelerance and transmissibility

**Figure 2.16:** Extensional storage modulus and loss factor of Sample D.

### 2.3.4 Discussion

In figure 2.17 and figure 2.18, the properties obtained for all test samples are plotted together allowing a better comparison of the values obtained for the different test samples.

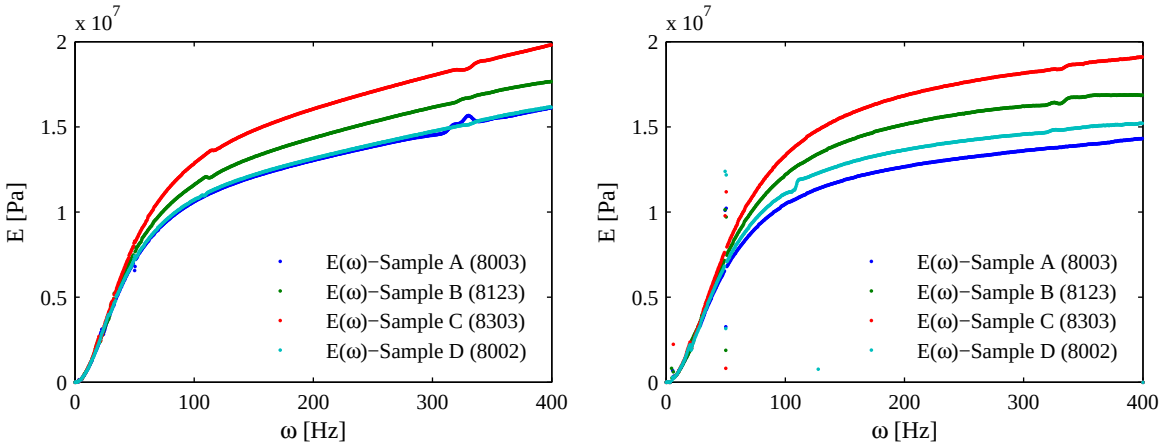


**(a)** $E(\omega)$ identified from accelerances **(b)** $E(\omega)$ identified from transmissibilities

**Figure 2.17:** Extensional storage modulus of all test samples.

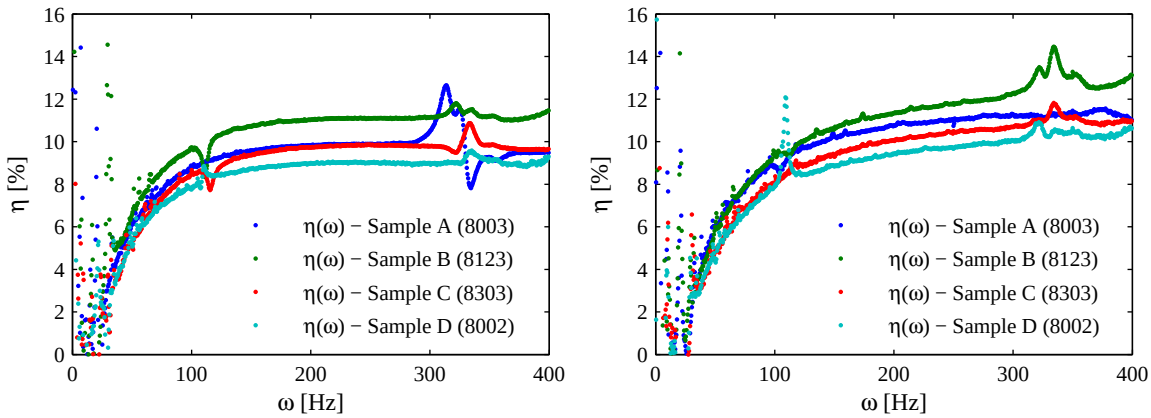


**(a)** $\eta(\omega)$ identified from accelerances **(b)** $\eta(\omega)$ identified from transmissibilities

**Figure 2.18:** Loss factor of of all test samples.

Figure 2.17 shows the values of $E(\omega)$ of all test samples obtained from accelerances and transmisibilities. Comparing figure 2.17a and figure 2.17b, it is possible to see that both values of $E(\omega)$, obtained from accelerances and transmissibilities, show the same tendency along the frequency although at frequencies higher than 300Hz the values obtained from transmissibilities appear to be lower than the ones obtained from accelerances. When comparing the values of $E(\omega)$ for the different test samples it is possible to see that the samples with high density present a higher extensional storage modulus than the samples with low density with the same grain size, the values of $E(\omega)$ of sample B (cork 8123, high density, fine grain) are higher than the ones of sample A (cork 8003, low density, fine grain) and the same is verified when comparing sample C (cork 8303, high density, coarse grain) with sample D (cork 8002, low density, coarse grain). Comparing sample B with sample C, both low density cork, B having fine grain size

while C having coarse grain size, it is possible to see, from figure 2.17a and figure 2.17b that the values of $E(\omega)$ of test sample C are higher that the values of test sample B, evidencing that an higher storage modulus might be associated with a coarse grain size. The same conclusions can be drawn on what concerns sample A and D referring to figure 2.17b.

From figure 2.18 it can be seen that the values of $\eta(\omega)$ obtained from accelerances and transmissibilities show approximately the same behavior along the frequency. When comparing sample B (cork 8123, high density, fine grain) with sample A (cork 8003, low density, fine grain) it is possible to see that the loss factor values, along the frequency range, of sample A are lower than the ones obtained for sample B. The same can be observed when comparing the loss factor of sample D (cork 8002, low density, coarse grain) with the loss factor of sample C (cork 8303, high density, coarse grain). The loss factor values obtained for sample D are lower than the values obtained for sample C, suggesting that the high composite cork compounds provide a higher loss factor along the frequency granting an higher damping. From figure 2.18 it is also possible to see that fine grain size cork compounds are associated with higher values of the loss factor.

## 2.4 Conclusion

In this chapter, two different methodologies have been presented in order to identify the dynamic properties of cork compounds based on a Complex Modulus Analysis(CMA). The first established methodology allowed obtaining the shear storage modulus and loss factor from the frequency response functions of a single degree of freedom system where the test sample represents the system complex stiffness. The second methodology permitted obtaining the extensional storage modulus and loss factor of cork compounds from the accelerance and transmissibility frequency response functions of a semi-definite two degrees of freedom system.

The developed experimental setups provided the frequency dependent shear and extensional storage modulus as well as the loss factors for different, commercially available, cork compounds which values are essential for a better understanding of the material dynamic behavior, which was little known, and for design purposes of passive damping treatments which are a possible application of this type of materials.

The obtained results enhance the frequency dependence of cork compounds dynamic properties, as well as the influence of its grain size and density on the shear storage modulus, extensional storage modulus and loss factor of the material.

# Chapter 3

# Layerwise Beam Finite Element

## 3.1 Introduction

In this chapter, the *layerwise* beam finite element is formulated in order to be integrated in a finite element routine and to perform with it simulations of sandwich beam structures. To formulate the element, a general domain displacement field will be defined and the strains and stresses will be derived from it. The *layerwise* theory hereby used is a partial *layerwise* theory in which *layerwise* expansions of the in-plane displacements are used, being assured the continuity of displacements in the layer interfaces as depicted in figure 3.1. On what concerns the displacement in the out of plane direction, it is considered to be constant for all layers.

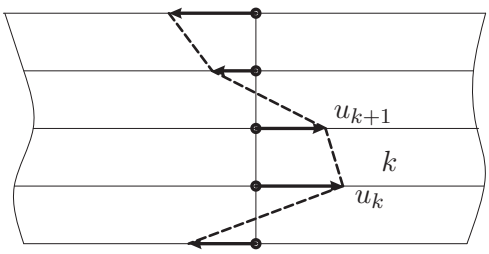


**Figure 3.1:** Beam in-plane displacements based on a partial *layerwise* theory.

The expressions for the potential strain and kinetic energy as well as for the virtual work of the external forces will be established. To derive the element equation of motion, as well as its mass and stiffness matrices, the Hamilton's principle will be used. It is worth mentioning that the element stiffness matrix has been partitioned in its extensional and shear components, so that the stiffness matrix could be selectively integrated in order to avoid shear locking.

## 3.2 Displacement field

The sandwich beam displacement vector of a generic single layer is described by the displacement field

$$\{\mathbf{u}\} = \left\{ \begin{array}{c} u(x,z,t) \\ w(x,z,t) \end{array} \right\} \tag{3.1}$$

where the in-plane displacement $u(x,z,t)$ is described by two in-plane generalized displacements, $u_t(x,t)$ and $u_b(x,t)$ which are space $(x)$ and time $(t)$ dependent, as follows,

$$u\left(x,z,t\right)=\frac{u_t\left(x,t\right)+u_b\left(x,t\right)}{2}+z\frac{u_t\left(x,t\right)-u_b\left(x,t\right)}{h} \tag{3.2}$$

The transverse displacement is considered to be constant for each layer through the thickness which means that a partial *layerwise* theory is used,

$$w(x,z,t)=w(x,t) \tag{3.3}$$

The previously described displacements are hereby represented in figure 3.2.

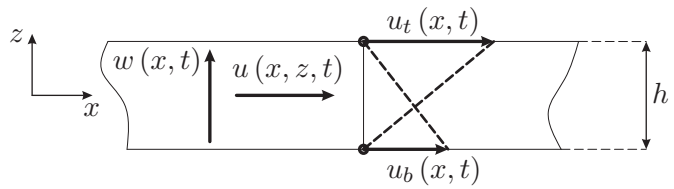


**Figure 3.2:** Single layer beam displacements.

## 3.3 Strain field

Having the displacement field characterized, it follows describing the sandwich beam strain field, which will be given by

$$\{\varepsilon\}=\left\{\begin{array}{c}\varepsilon_{xx}\\ \gamma_{xz}\end{array}\right\} \tag{3.4}$$

As it is suggested by expression (3.4), the strain field can be divided into two components, one characterizing extensional deformations represented by $\varepsilon_{xx}$ and other shear ones, represented by $\gamma_{xz}$.

### 3.3.1 Extensional

The extensional component of the strain field is represented by $\epsilon_{xx}$ which has the following relation to the displacement:

$$\varepsilon_{xx}=\frac{\partial u\left(x,z,t\right)}{\partial x} \tag{3.5}$$

Deriving (3.2) in order to $x$ and substituting it into (3.5):

$$\begin{aligned}\varepsilon_{xx}=\frac{\partial u}{\partial x} &= \frac{1}{2}\left(\frac{\partial u_t}{\partial x}+\frac{\partial u_b}{\partial x}\right)+\frac{z}{h}\left(\frac{\partial u_t}{\partial x}-\frac{\partial u_b}{\partial x}\right)\\ &= \left(\frac{1}{2}+\frac{z}{h}\right)\frac{\partial u_t}{\partial x}+\left(\frac{1}{2}-\frac{z}{h}\right)\frac{\partial u_b}{\partial x}\end{aligned} \tag{3.6}$$

The extensional strain in expression (3.6) can be expressed in a matrix form, taking the following aspect:

$$\varepsilon_{xx}=\left[\begin{array}{ccc}0 & \left(\frac{1}{2}-\frac{z}{h}\right)\frac{\partial}{\partial x} & \left(\frac{1}{2}+\frac{z}{h}\right)\frac{\partial}{\partial x}\end{array}\right]\left\{\begin{array}{c}w\\ u_b\\ u_t\end{array}\right\} \tag{3.7}$$

### 3.3.2 Shear

The other component of the strain field is the shear one and is represented by $\gamma_{xz}$ which is related to the displacement by the following expression,

$$\gamma_{xz} = \frac{\partial u(x,z,t)}{\partial z} + \frac{\partial w(x,t)}{\partial x} \tag{3.8}$$

Deriving expression (3.2) in order to $z$ and (3.3) to $x$ and substituting them into (3.8), it is obtained,

$$\gamma_{xz} = \frac{\partial u}{\partial z} + \frac{\partial w}{\partial x} = \frac{u_t - u_b}{h} + \frac{\partial w(x,t)}{\partial x} \tag{3.9}$$

In a matrix form, expression (3.9) can be written as follows,

$$\gamma_{xz} = \begin{bmatrix} \frac{\partial}{\partial x} & -\frac{1}{h} & \frac{1}{h} \end{bmatrix} \begin{Bmatrix} w \\ u_b \\ u_t \end{Bmatrix} \tag{3.10}$$

### 3.3.3 Total Strain Field

The total strain field defined in (3.4) can then be expressed as,

$$\{\varepsilon\} = \begin{Bmatrix} \varepsilon_{xx} \\ \gamma_{xz} \end{Bmatrix} = \begin{bmatrix} 0 & \left(\frac{1}{2} - \frac{z}{h}\right)\frac{\partial}{\partial x} & \left(\frac{1}{2} + \frac{z}{h}\right)\frac{\partial}{\partial x} \\ \frac{\partial}{\partial x} & -\frac{1}{h} & \frac{1}{h} \end{bmatrix} \begin{Bmatrix} w \\ u_b \\ u_t \end{Bmatrix} \tag{3.11}$$

## 3.4 Stress field

As plane strain is considered, the stresses are defined as

$$\{\sigma\} = \begin{Bmatrix} \sigma_{xx} \\ \tau_{xz} \end{Bmatrix} \tag{3.12}$$

which are related with the strains according to the following constitutive law

$$\{\sigma\} = [\mathcal{D}]\{\varepsilon\} \tag{3.13}$$

where $[D]$ represents the elasticity matrix and is defined as

$$[\mathcal{D}] = \begin{bmatrix} E & 0 \\ 0 & G \end{bmatrix} \tag{3.14}$$

where $E$ is the material *Young's* Modulus and $G$ is the shear modulus which is given by

$$G = \frac{E}{2(1+\nu)} \tag{3.15}$$

where $\nu$ is the *Poisson's* coefficient.

## 3.5 Potential strain energy

The potential strain energy is defined by the following integral extended over the volume $\Omega$:

$$\Pi^P = \frac{1}{2}\int_\Omega \{\varepsilon\}^{\mathrm{T}}\{\sigma\}\, d\Omega \tag{3.16}$$

Substituting (3.13) into (3.16) will result in

$$\Pi^P = \frac{1}{2}\int_\Omega \{\varepsilon\}^{\mathrm{T}}[\mathcal{D}]\{\varepsilon\}\, d\Omega \tag{3.17}$$

Performing the matrix multiplication of the integral argument of equation (3.17) one will obtain

$$\Pi^P = \frac{1}{2}\int_\Omega \varepsilon_{xx}E\varepsilon_{xx}\, d\Omega + \frac{1}{2}\int_\Omega \gamma_{xz}G\gamma_{xz}\, d\Omega \tag{3.18}$$

Expression (3.18) denotes the partition of the potential strain energy into an extensional and a shear component.

### 3.5.1 Extensional

The extensional component of the total potential strain energy, according to (3.18), will then be given by:

$$\Pi^{P_\varepsilon} = \frac{1}{2}\int_\Omega \varepsilon_{xx}E\varepsilon_{xx}\, d\Omega \tag{3.19}$$

where the strain $\varepsilon_{xx}$ has been previously described by (3.6). Then, replacing (3.6) into equation (3.19) will lead to:

$$\begin{aligned}\Pi^{P_\varepsilon} &= \frac{1}{2}\int_\Omega \left(\left(\frac{1}{2}+\frac{z}{h}\right)\frac{\partial u_t}{\partial x} + \left(\frac{1}{2}-\frac{z}{h}\right)\frac{\partial u_b}{\partial x}\right)E\left(\left(\frac{1}{2}+\frac{z}{h}\right)\frac{\partial u_t}{\partial x} + \left(\frac{1}{2}-\frac{z}{h}\right)\frac{\partial u_b}{\partial x}\right)d\Omega \\ &= \frac{1}{2}\int_\Omega \left(\frac{1}{2}+\frac{z}{h}\right)\frac{\partial u_t}{\partial x}E\left(\frac{1}{2}+\frac{z}{h}\right)\frac{\partial u_t}{\partial x}d\Omega + \frac{1}{2}\int_\Omega \left(\frac{1}{2}-\frac{z}{h}\right)\frac{\partial u_b}{\partial x}E\left(\frac{1}{2}-\frac{z}{h}\right)\frac{\partial u_b}{\partial x}d\Omega \\ &+\frac{1}{2}2\int_\Omega \left(\frac{1}{2}+\frac{z}{h}\right)\frac{\partial u_t}{\partial x}E\left(\frac{1}{2}-\frac{z}{h}\right)\frac{\partial u_b}{\partial x}d\Omega\end{aligned} \tag{3.20}$$

Expanding each integral from expression (3.20) one obtains,

$$\begin{aligned}\Pi^{P_\varepsilon} &= \frac{1}{2}\int_\Omega \frac{\partial u_t}{\partial x}E\left(\frac{1}{2}+\frac{z}{h}\right)^2\frac{\partial u_t}{\partial x}d\Omega + \frac{1}{2}\int_\Omega \frac{\partial u_b}{\partial x}E\left(\frac{1}{2}-\frac{z}{h}\right)^2\frac{\partial u_b}{\partial x}d\Omega \\ &+\frac{1}{2}2\int_\Omega \left(\frac{1}{2}+\frac{z}{h}\right)\frac{\partial u_t}{\partial x}E\left(\frac{1}{2}-\frac{z}{h}\right)\frac{\partial u_b}{\partial x}d\Omega\end{aligned} \tag{3.21}$$

Integrating expression (3.21) in order to the width direction $y$,

$$\begin{aligned}\Pi^{P_\varepsilon} &= \frac{1}{2}b\int_\ell\int_z \frac{\partial u_t}{\partial x}E\left(\frac{1}{2}+\frac{z}{h}\right)^2\frac{\partial u_t}{\partial x}dzdx+\frac{1}{2}b\int_\ell\int_z \frac{\partial u_b}{\partial x}E\left(\frac{1}{2}-\frac{z}{h}\right)^2\frac{\partial u_b}{\partial x}dzdx\\ &+ \frac{1}{2}2b\int_\ell\int_z\left(\frac{1}{2}+\frac{z}{h}\right)\frac{\partial u_t}{\partial x}E\left(\frac{1}{2}-\frac{z}{h}\right)\frac{\partial u_b}{\partial x}dzdx \qquad (3.22)\end{aligned}$$

where $b$ represents the beam width. Expanding (3.22) will result into

$$\begin{aligned}\Pi^{P_\varepsilon} &= \frac{1}{2}b\int_\ell\int_z \frac{\partial u_t}{\partial x}E\left(\frac{1}{2}\right)^2\frac{\partial u_t}{\partial x}dzdx+\frac{1}{2}b\int_\ell\int_z \frac{\partial u_t}{\partial x}E\left(\frac{z}{h}\right)^2\frac{\partial u_t}{\partial x}dzdx\\ &+ \underbrace{\frac{1}{2}b\int_\ell\int_z 2\frac{\partial u_t}{\partial x}E\frac{z}{h}\frac{1}{2}\frac{\partial u_t}{\partial x}dzdx}_{=0}+\frac{1}{2}b\int_\ell\int_z \frac{\partial u_b}{\partial x}E\left(\frac{1}{2}\right)^2\frac{\partial u_b}{\partial x}dzdx\\ &+ \frac{1}{2}b\int_\ell\int_z \frac{\partial u_b}{\partial x}E\left(\frac{z}{h}\right)^2\frac{\partial u_b}{\partial x}dzdx-\underbrace{\frac{1}{2}b\int_\ell\int_z 2\frac{\partial u_b}{\partial x}E\frac{z}{h}\frac{1}{2}\frac{\partial u_b}{\partial x}dzdx}_{=0}\\ &+ \frac{1}{2}2b\int_\ell\int_z \frac{\partial u_t}{\partial x}E\left(\frac{1}{2}\right)^2\frac{\partial u_b}{\partial x}dzdx-\underbrace{\frac{1}{2}2b\int_\ell\int_z \frac{\partial u_t}{\partial x}E\frac{1}{2}\frac{z}{h}\frac{\partial u_b}{\partial x}dzdx}_{=0}\\ &+ \underbrace{\frac{1}{2}2b\int_\ell\int_z \frac{\partial u_t}{\partial x}E\frac{1}{2}\frac{z}{h}\frac{\partial u_b}{\partial x}dzdx}_{=0}-\frac{1}{2}2b\int_\ell\int_z \frac{\partial u_t}{\partial x}E\left(\frac{z}{h}\right)^2\frac{\partial u_b}{\partial x}dzdx \qquad (3.23)\end{aligned}$$

Integrals refered to be zero in expression (3.23) correspond to integrations of odd functions respecting to $z$ in a symmetric integration interval $\left[-\frac{h}{2},\frac{h}{2}\right]$ which complies the layer thickness, which result into zero.

Then, integrating (3.23) in order to the thickness direction $z$ within the interval $\left[-\frac{h}{2},\frac{h}{2}\right]$ will lead to

$$\begin{aligned}\Pi^{P_\varepsilon} &= \frac{1}{2}b\int_\ell \frac{\partial u_t}{\partial x}E\frac{h}{4}\frac{\partial u_t}{\partial x}dx+\frac{1}{2}b\int_\ell \frac{\partial u_t}{\partial x}E\frac{1}{h^2}\frac{h^3}{12}\frac{\partial u_t}{\partial x}dx\\ &+ \frac{1}{2}b\int_\ell \frac{\partial u_b}{\partial x}E\frac{h}{4}\frac{\partial u_b}{\partial x}dx+\frac{1}{2}b\int_\ell \frac{\partial u_b}{\partial x}E\frac{1}{h^2}\frac{h^3}{12}\frac{\partial u_b}{\partial x}dx\\ &+ \frac{1}{2}2b\int_\ell \frac{\partial u_t}{\partial x}E\frac{h}{4}\frac{\partial u_b}{\partial x}dx-\frac{1}{2}2b\int_\ell \frac{\partial u_t}{\partial x}E\frac{1}{h^2}\frac{h^3}{12}\frac{\partial u_b}{\partial x}dx \qquad (3.24)\end{aligned}$$

After rearranging expression (3.24), it results into,

$$\begin{aligned}\Pi^{P_\varepsilon} &= \frac{1}{2}b\int_\ell \frac{\partial u_t}{\partial x}E\left(\frac{h}{4}+\frac{h}{12}\right)\frac{\partial u_t}{\partial x}dx+\frac{1}{2}b\int_\ell \frac{\partial u_b}{\partial x}E\left(\frac{h}{4}+\frac{h}{12}\right)\frac{\partial u_b}{\partial x}dx \\ &+ \frac{1}{2}2b\int_\ell \frac{\partial u_t}{\partial x}E\left(\frac{h}{4}-\frac{h}{12}\right)\frac{\partial u_b}{\partial x}dx \end{aligned} \tag{3.25}$$

Finally, equation (3.25) will resume to

$$\Pi^{P_\varepsilon} = \frac{1}{2}b\int_\ell \frac{\partial u_t}{\partial x}E\frac{h}{3}\frac{\partial u_t}{\partial x}dx+\frac{1}{2}b\int_\ell \frac{\partial u_b}{\partial x}E\frac{h}{3}\frac{\partial u_b}{\partial x}dx+\frac{1}{2}2b\int_\ell \frac{\partial u_t}{\partial x}E\frac{h}{6}\frac{\partial u_b}{\partial x}dx \tag{3.26}$$

In a matrix form, expression (3.26) can also be written as follows,

$$\Pi^{P_\varepsilon} = \frac{1}{2}b\int_\ell \begin{Bmatrix} w \\ \frac{\partial u_b}{\partial x} \\ \frac{\partial u_t}{\partial x} \end{Bmatrix}^{\mathrm{T}} E\begin{bmatrix} 0 & 0 & 0 \\ 0 & \frac{h}{6} & \frac{h}{3} \\ 0 & \frac{h}{3} & \frac{h}{6} \end{bmatrix}\begin{Bmatrix} w \\ \frac{\partial u_b}{\partial x} \\ \frac{\partial u_t}{\partial x} \end{Bmatrix}dx \tag{3.27}$$

Equation (3.27) can be expressed in terms of displacements according to

$$\begin{Bmatrix} w \\ \frac{\partial u_b}{\partial x} \\ \frac{\partial u_t}{\partial x} \end{Bmatrix} = [\mathcal{L}_\varepsilon]\{d\} \tag{3.28}$$

where $[\mathcal{L}_\varepsilon]$ is the differential operators matrix defined as

$$[\mathcal{L}_\varepsilon] = \begin{bmatrix} 1 & 0 & 0 \\ 0 & \frac{\partial}{\partial x} & 0 \\ 0 & 0 & \frac{\partial}{\partial x} \end{bmatrix} \tag{3.29}$$

With the above definition from (3.28), expression (3.26) or (3.27) can be written in the compact form

$$\Pi^{P_\varepsilon} = \frac{1}{2}b\int_\ell \left([\mathcal{L}_\varepsilon]\{d\}\right)^{\mathrm{T}}[D_\varepsilon][\mathcal{L}_\varepsilon]\{d\}\,dx \tag{3.30}$$

where the elasticity matrix $[D_\varepsilon]$ is defined as

$$[D_\varepsilon] = E\begin{bmatrix} 0 & 0 & 0 \\ 0 & \frac{h}{6} & \frac{h}{3} \\ 0 & \frac{h}{3} & \frac{h}{6} \end{bmatrix} \tag{3.31}$$

### 3.5.2 Shear

The shear component of the total potential strain energy, according to (3.18), will then be given by:

$$\Pi^{P_\gamma} = \frac{1}{2}\int_\Omega \gamma_{xz}G\gamma_{xz}\,d\Omega \tag{3.32}$$

Substituting $\gamma_{xz}$ from (3.8) into expression (3.32) it will be obtained:

$$\begin{aligned}\Pi^{P_\gamma} &= \frac{1}{2}\int_\Omega \left(\left(\frac{u_t-u_b}{h}\right)+\frac{\partial w}{\partial x}\right) G \left(\left(\frac{u_t-u_b}{h}\right)+\frac{\partial w}{\partial x}\right) d\Omega \\ &= \frac{1}{2}\int_\Omega \left(\frac{u_t-u_b}{h}\right) G \left(\frac{u_t-u_b}{h}\right) d\Omega + \frac{1}{2}\int_\Omega \frac{\partial w}{\partial x} G \frac{\partial w}{\partial x} d\Omega \\ &\quad + \frac{1}{2} 2 \int_\Omega \left(\frac{u_t-u_b}{h}\right) G \frac{\partial w}{\partial x} d\Omega \end{aligned} \tag{3.33}$$

Expanding each integral from expression (3.33) and integrating in order to $y$ one shall obtain:

$$\begin{aligned}\Pi^{P_\gamma} &= \frac{1}{2} b \int_\ell \int_z \left(\frac{u_t-u_b}{h}\right) G \left(\frac{u_t-u_b}{h}\right) dz dx + \frac{1}{2} b \int_\ell \int_z \frac{\partial w}{\partial x} G \frac{\partial w}{\partial x} dz dx \\ &\quad + \frac{1}{2} 2 b \int_\ell \int_z \left(\frac{u_t-u_b}{h}\right) G \frac{\partial w}{\partial x} dz dx \end{aligned} \tag{3.34}$$

where $b$ is the beam width. Then, integrating expression (3.34) in order to $z$, it comes,

$$\begin{aligned}\Pi^{P_\gamma} &= \frac{1}{2} b \int_\ell \left(\frac{u_t-u_b}{h}\right) Gh \left(\frac{u_t-u_b}{h}\right) dx + \frac{1}{2} b \int_\ell \frac{\partial w}{\partial x} Gh \frac{\partial w}{\partial x} dx \\ &\quad + \frac{1}{2} 2 b \int_\ell \left(\frac{u_t-u_b}{h}\right) Gh \frac{\partial w}{\partial x} dx \end{aligned} \tag{3.35}$$

After rearranging expression (3.35), it results into:

$$\begin{aligned}\Pi^{P_\gamma} &= \frac{1}{2} b \int_\ell \frac{u_t}{h} Gh \frac{u_t}{h} dx + \frac{1}{2} b \int_\ell \frac{u_b}{h} Gh \frac{u_b}{h} dx \\ &\quad - \frac{1}{2} b \int_\ell 2 \frac{u_t}{h} Gh \frac{u_b}{h} dx + \frac{1}{2} b \int_\ell 2 \frac{u_t}{h} Gh \frac{\partial w}{\partial x} dx \\ &\quad - \frac{1}{2} b \int_\ell 2 \frac{u_b}{h} Gh \frac{\partial w}{\partial x} dx + \frac{1}{2} b \int_\ell \frac{\partial w}{\partial x} Gh \frac{\partial w}{\partial x} dx \end{aligned} \tag{3.36}$$

The shear potential energy given by (3.36) can be represented as follows

$$\Pi^{P_\gamma} = \frac{1}{2} b \int_\ell \left(\frac{\partial w}{\partial x} + \frac{u_t}{h} - \frac{u_b}{h}\right) Gh \left(\frac{\partial w}{\partial x} + \frac{u_t}{h} - \frac{u_b}{h}\right) dx \tag{3.37}$$

Then assuming that

$$\begin{aligned}\left(\frac{\partial w}{\partial x} + \frac{u_t}{h} - \frac{u_b}{h}\right) &= \begin{bmatrix} \frac{\partial}{\partial x} & -\frac{1}{h} & \frac{1}{h} \end{bmatrix} \begin{Bmatrix} w \\ u_b \\ u_t \end{Bmatrix} \\ &= [\mathcal{L}_\gamma]\{d\} \end{aligned} \tag{3.38}$$

and considering the shear elasticity matrix as

$$[D_\gamma] = Gh \tag{3.39}$$

the expression (3.37) can be written in the matrix form as follows,

$$\Pi^{P_\gamma} = \frac{1}{2} b \int_\ell \left( [\mathcal{L}_\gamma] \{d\} \right)^{\mathrm{T}} [D_\gamma] [\mathcal{L}_\gamma] \{d\} \, dx \tag{3.40}$$

## 3.6 Kinetic energy

From expressions (3.2) and (3.3), the displacements derivatives with respect to the time $t$ will come as:

$$\frac{\partial u(x,t)}{\partial t} = \dot{u}(x,t) = \frac{\dot{u}_t(x,t) + \dot{u}_b(x,t)}{2} + z \frac{\dot{u}_t(x,t) - \dot{u}_b(x,t)}{h} \tag{3.41}$$

$$\frac{\partial w(x,t)}{\partial t} = \dot{w}(x,t) \tag{3.42}$$

Then, the single layer kinetic energy can be expressed by the following integral over the volume $\Omega$:

$$\Pi^K = \frac{1}{2} \int_\Omega \left( \frac{\dot{u}_t + \dot{u}_b}{2} + z \frac{\dot{u}_t - \dot{u}_b}{h} \right) \rho \left( \frac{\dot{u}_t + \dot{u}_b}{2} + z \frac{\dot{u}_t - \dot{u}_b}{h} \right) d\Omega + \frac{1}{2} \int_\Omega \dot{w} \rho \dot{w} d\Omega \tag{3.43}$$

Expanding (3.43) it is obtained:

$$\begin{aligned} \Pi^K &= \frac{1}{2} \int_\Omega \left( \frac{1}{2} + \frac{z}{h} \right) \dot{u}_t \rho \left( \frac{1}{2} + \frac{z}{h} \right) \dot{u}_t d\Omega + \frac{1}{2} \int_\Omega \left( \frac{1}{2} - \frac{z}{h} \right) \dot{u}_b \rho \left( \frac{1}{2} - \frac{z}{h} \right) \dot{u}_b d\Omega \\ &+ \frac{1}{2} 2 \int_\Omega \left( \frac{1}{2} + \frac{z}{h} \right) \dot{u}_t \rho \left( \frac{1}{2} - \frac{z}{h} \right) \dot{u}_b d\Omega + \frac{1}{2} \int_\Omega \dot{w} \rho \dot{w} d\Omega \end{aligned} \tag{3.44}$$

After rearranging (3.44), it comes,

$$\begin{aligned} \Pi^K &= \frac{1}{2} \int_\Omega \dot{u}_t \rho \left( \frac{1}{2} + \frac{z}{h} \right)^2 \dot{u}_t d\Omega + \frac{1}{2} \int_\Omega \dot{u}_b \rho \left( \frac{1}{2} - \frac{z}{h} \right)^2 \dot{u}_b d\Omega \\ &+ \frac{1}{2} 2 \int_\Omega \left( \frac{1}{2} + \frac{z}{h} \right) \dot{u}_t \rho \left( \frac{1}{2} - \frac{z}{h} \right) \dot{u}_b d\Omega + \frac{1}{2} \int_\Omega \dot{w} \rho \dot{w} d\Omega \end{aligned} \tag{3.45}$$

Integrating (3.45) in order to $y$ yields,

$$\begin{aligned} \Pi^K &= \frac{1}{2} b \int_\ell \int_z \dot{u}_t \rho \left( \frac{1}{2} + \frac{z}{h} \right)^2 \dot{u}_t dz dx + \frac{1}{2} b \int_\ell \int_z \dot{u}_b \rho \left( \frac{1}{2} - \frac{z}{h} \right)^2 \dot{u}_b dz dx \\ &+ \frac{1}{2} 2 b \int_\ell \int_z \left( \frac{1}{2} + \frac{z}{h} \right) \dot{u}_t \rho \left( \frac{1}{2} - \frac{z}{h} \right) \dot{u}_b dz dx + \frac{1}{2} b \int_\ell \int_z \dot{w} \rho \dot{w} dz dx \end{aligned} \tag{3.46}$$

where $b$ represents the beam width. Then, expanding (3.46) one will obtain:

$$\begin{aligned}
\Pi^K &= \frac{1}{2}b\int_\ell\int_z \dot{u}_t\rho\left(\frac{1}{2}\right)^2\dot{u}_t dzdx + \frac{1}{2}b\int_\ell\int_z \dot{u}_t\rho\left(\frac{z}{h}\right)^2\dot{u}_t dzdx \\
&+ \underbrace{\frac{1}{2}b\int_\ell\int_z 2\dot{u}_t\rho\frac{z}{h}\frac{1}{2}\dot{u}_t dzdx}_{=0} + \frac{1}{2}b\int_\ell\int_z \dot{u}_b\rho\left(\frac{1}{2}\right)^2\dot{u}_b dzdx \\
&+ \frac{1}{2}b\int_\ell\int_z \dot{u}_b\rho\left(\frac{z}{h}\right)^2\dot{u}_b dzdx - \underbrace{\frac{1}{2}b\int_\ell\int_z 2\dot{u}_b\rho\frac{z}{h}\frac{1}{2}\dot{u}_b dzdx}_{=0} \\
&+ \frac{1}{2}2b\int_\ell\int_z \dot{u}_t\rho\left(\frac{1}{2}\right)^2\dot{u}_b dzdx - \underbrace{\frac{1}{2}2b\int_\ell\int_z \dot{u}_t\rho\frac{1}{2}\frac{z}{h}\dot{u}_b dzdx}_{=0} \\
&+ \underbrace{\frac{1}{2}2b\int_\ell\int_z \dot{u}_t\rho\frac{1}{2}\frac{z}{h}\dot{u}_b dzdx}_{=0} - \frac{1}{2}2b\int_\ell\int_z \dot{u}_t\rho\left(\frac{z}{h}\right)^2\dot{u}_b dzdx \\
&+ \frac{1}{2}b\int_\ell\int_z \dot{w}\rho\dot{w}dzdx
\end{aligned} \tag{3.47}$$

Integrals referred to be zero in expression (3.47) correspond to integrations of odd functions respecting to $x$ in a symmetric integration interval, which result into zero. Then, integrating (3.47) in order to $z$ will lead to

$$\begin{aligned}
\Pi^K &= \frac{1}{2}b\int_\ell \dot{u}_t\rho\frac{h}{4}\dot{u}_t dx + \frac{1}{2}b\int_\ell \dot{u}_t\rho\frac{1}{h^2}\frac{h^3}{12}\dot{u}_t dx + \frac{1}{2}b\int_\ell \dot{u}_b\rho\frac{h}{4}\dot{u}_b dzdx \\
&+ \frac{1}{2}b\int_\ell \dot{u}_b\rho\frac{1}{h^2}\frac{h^3}{12}\dot{u}_b dx + \frac{1}{2}2b\int_\ell \dot{u}_t\rho\frac{h}{4}\dot{u}_b dx \\
&- \frac{1}{2}2b\int_\ell \dot{u}_t\rho\frac{1}{h^2}\frac{h^3}{12}\dot{u}_b dx + \frac{1}{2}b\int_\ell \dot{w}\rho h\dot{w}dx
\end{aligned} \tag{3.48}$$

By grouping identical terms, the last expression simplifies into,

$$\begin{aligned}
\Pi^K &= \frac{1}{2}b\int_\ell \dot{u}_t\rho\left(\frac{h}{4}+\frac{h}{12}\right)\dot{u}_t dx + \frac{1}{2}b\int_\ell \dot{u}_b\rho\left(\frac{h}{4}+\frac{h}{12}\right)\dot{u}_b dx \\
&+ \frac{1}{2}2b\int_\ell \dot{u}_t\rho\left(\frac{h}{4}-\frac{h^3}{12}\right)\dot{u}_b dx + \frac{1}{2}b\int_\ell \dot{w}\rho h\dot{w}dx
\end{aligned} \tag{3.49}$$

Performing the sums in expression (3.49), it will lead to:

$$\begin{aligned}\Pi^K &= \frac{1}{2}b\int_\ell \dot{u}_t\rho\frac{h}{3}\dot{u}_t dx + \frac{1}{2}b\int_\ell \dot{u}_b\rho\frac{h}{3}\dot{u}_b dx + \frac{1}{2}2b\int_\ell \dot{u}_t\rho\frac{h}{6}\dot{u}_b dx \\ &+ \frac{1}{2}b\int_\ell \dot{w}\rho h\dot{w} dx \end{aligned} \tag{3.50}$$

In matrix form, expression (3.50) can be written as:

$$\Pi^K = \frac{1}{2}b\int_\ell \left\{ \begin{array}{ccc} \dot{w} & \dot{u}_b & \dot{u}_t \end{array} \right\} \rho \left[ \begin{array}{ccc} h & 0 & 0 \\ 0 & \frac{h}{6} & \frac{h}{3} \\ 0 & \frac{h}{3} & \frac{h}{6} \end{array} \right] \left\{ \begin{array}{c} \dot{w} \\ \dot{u}_b \\ \dot{u}_t \end{array} \right\} dx \tag{3.51}$$

Expressing the derivatives of the displacement vector as

$$\left\{\dot{d}\right\} = \left\{ \begin{array}{c} \dot{w} \\ \dot{u}_b \\ \dot{u}_t \end{array} \right\} \tag{3.52}$$

and considering the inertia matrix $[J]$ defined by

$$[J] = \rho \left[ \begin{array}{ccc} h & 0 & 0 \\ 0 & \frac{h}{6} & \frac{h}{3} \\ 0 & \frac{h}{3} & \frac{h}{6} \end{array} \right] \tag{3.53}$$

equation (3.50) will become

$$\Pi^K = \frac{1}{2}b\int_\ell \left\{\dot{d}\right\}^{\mathrm{T}} [J] \left\{\dot{d}\right\} dx \tag{3.54}$$

## 3.7 Virtual work of surface forces

If each layer surface of the laminate beam is subjected to several normal distributed loads, then the virtual work $\delta W$ done by those external loadings will be given by

$$\delta W = \int_S \{\delta d\}^{\mathrm{T}} \{q\} dS \tag{3.55}$$

where $\{q\}$ represents the net normal loading and $S$ is the surface area where distributed loads are applied.

## 3.8 Variational formulation

To obtain the variational form of the laminated beam equations of motion, including boundary conditions, the Hamilton's principle was used.

The Hamilton's principle states that:

$$\int_{t_1}^{t_2} \delta\left(\Pi^K - \Pi^P\right) dt + \int_{t_1}^{t_2} \delta W = 0 \tag{3.56}$$

where $\Pi^K$ and $\Pi^P$ are respectively the total kinetic and potential energy and $\delta W$ is the virtual work done by external forces.

Substituting the total kinetic energy from (3.54), the total potential strain energy from the sum of (3.30) and (3.40), and the work done by external forces from (3.55), it will be obtained

$$\begin{aligned}\int_{t_1}^{t_2} \delta \Bigg( & \frac{1}{2} b \int_{\ell} \left( \left\{ \dot{d} \right\} \right)^{\mathrm{T}} [J] \left\{ \dot{d} \right\} dx - \frac{1}{2} b \int_{\ell} \left( [\mathcal{L}_{\varepsilon}] \{d\} \right)^{\mathrm{T}} [D_{\varepsilon}] [\mathcal{L}_{\varepsilon}] \{d\} \, dx \\ & - \frac{1}{2} b \int_{\ell} \left( [\mathcal{L}_{\gamma}] \{d\} \right)^{\mathrm{T}} [D_{\gamma}] [\mathcal{L}_{\gamma}] \{d\} \, dx \Bigg) dt + \int_{t_1}^{t_2} \left( \int_{S} \{\delta d\}^{\mathrm{T}} \{q\} \, dS \right) dt = 0 \end{aligned} \tag{3.57}$$

Integrating by parts expression (3.56) will lead to

$$\begin{aligned} & \frac{1}{2} b \int_{\ell} \left( \{\delta d\} \right)^{\mathrm{T}} [J] \left\{ \dot{d} \right\} dx \Bigg|_{t_1}^{t_2} - \int_{t_1}^{t_2} \left( \frac{1}{2} b \int_{\ell} \left( \{\delta d\} \right)^{\mathrm{T}} [J] \left\{ \ddot{d} \right\} dx \right) dt \\ + & \int_{t_1}^{t_2} \left( -\frac{1}{2} b \int_{\ell} \left( [\mathcal{L}_{\varepsilon}] \{\delta d\} \right)^{\mathrm{T}} [D_{\varepsilon}] [\mathcal{L}_{\varepsilon}] \{d\} \, dx - \frac{1}{2} b \int_{\ell} \left( [\mathcal{L}_{\gamma}] \{\delta d\} \right)^{\mathrm{T}} [D_{\gamma}] [\mathcal{L}_{\gamma}] \{d\} \, dx \right) dt \\ + & \int_{t_1}^{t_2} \left( \int_{S} \{\delta d\}^{\mathrm{T}} \{q\} \, dS \right) dt = 0 \end{aligned} \tag{3.58}$$

The first term from expression (3.58) becomes zero because all the paths pass through fixed end points. Then,

$$\begin{aligned} \int_{t_1}^{t_2} \Bigg( & -\frac{1}{2} b \int_{\ell} \left( \{\delta d\} \right)^{\mathrm{T}} [J] \left\{ \ddot{d} \right\} dx - \frac{1}{2} b \int_{\ell} \left( [\mathcal{L}_{\varepsilon}] \{\delta d\} \right)^{\mathrm{T}} [D_{\varepsilon}] [\mathcal{L}_{\varepsilon}] \{d\} \, dx \\ & - \frac{1}{2} b \int_{\ell} \left( [\mathcal{L}_{\gamma}] \{\delta d\} \right)^{\mathrm{T}} [D_{\gamma}] [\mathcal{L}_{\gamma}] \{d\} \, dx + \int_{S} \{\delta d\}^{\mathrm{T}} \{q\} \, dS \Bigg) dt = 0 \end{aligned} \tag{3.59}$$

As equation (3.59) must be zero for any arbitrary $\{\delta d\}$ within the time interval $[t_1, t_2]$, equation (3.59) must become

$$\begin{aligned} & \underbrace{\frac{1}{2} b \int_{\ell} \left( \{\delta d\} \right)^{\mathrm{T}} [J] \left\{ \ddot{d} \right\} dx}_{\text{Inertia component}} + \underbrace{\frac{1}{2} b \int_{\ell} \left( [\mathcal{L}_{\varepsilon}] \{\delta d\} \right)^{\mathrm{T}} [D_{\varepsilon}] [\mathcal{L}_{\varepsilon}] \{d\} \, dx}_{\text{Extensional Stiffness component}} \\ & + \underbrace{\frac{1}{2} b \int_{\ell} \left( [\mathcal{L}_{\gamma}] \{\delta d\} \right)^{\mathrm{T}} [D_{\gamma}] [\mathcal{L}_{\gamma}] \{d\} \, dx}_{\text{Shear Stiffness component}} - \underbrace{\int_{S} \{\delta d\}^{\mathrm{T}} \{q\} \, dS}_{\text{External Force component}} = 0 \end{aligned} \tag{3.60}$$

Finally, equation (3.60) represents the variational formulation of a single generic beam layer.

## 3.9 Finite element formulation

### 3.9.1 Single layer element

The variational formulation described in the previous section was made for a general domain with a single layer based on the described displacement field. Next, the general domain referred will be divided in a finite number of elements for which the variational formulation obtained is also valid.

The single layer beam finite element will have two nodes, having each node three degrees of freedom, two in the $x$ axis direction $u_b$ (on the bottom of the layer) and $u_t$ (on the top of the layer), and one degree of freedom in the z axis direction $w$, as represented in figure 3.3.

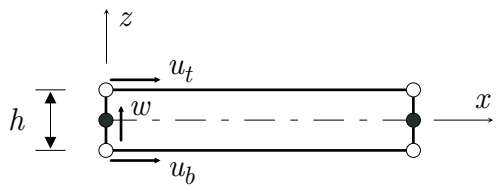


**Figure 3.3:** Single layer beam element displacements.

Considering, as referred, two node elements and linear interpolation functions like the ones represented in figure 3.4, each layer displacements along the element can be computed by interpolating each node displacement with the referred functions.

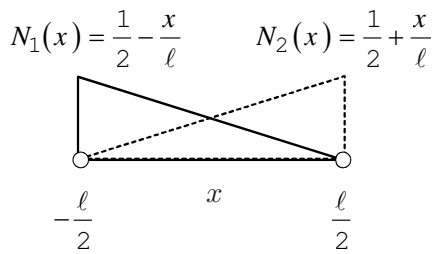


**Figure 3.4:** Element interpolation functions.

The displacements vector for node $i$ of the element is given by

$$\{d_i^e\} = \left\{ \begin{array}{ccc} w_i & u_{b_i} & u_{t_i} \end{array} \right\}^{\mathrm{T}} \tag{3.61}$$

Therefore, the element nodal displacements vector will be described as

$$\{d^e\} = \left\{ \begin{array}{cc} \{d_1^e\} & \{d_2^e\} \end{array} \right\}^{\mathrm{T}} \tag{3.62}$$

Then, the displacements within the element, $\{d\} = \left\{ \begin{array}{ccc} w & u_b & u_t \end{array} \right\}^{\mathrm{T}}$, can be expressed as a function of the element node displacements $\{d^e\}$ as:

$$\{d\} = \sum_{i=1}^{2} N_i\left(x\right)\{d_i^e\} \tag{3.63}$$

where $N_i(x)$, with $i = 1, 2$, are the so-called shape functions which are represented in figure 3.4. Naturally, expression (3.63) can also be written in matrix form, becoming

$$\{d\} = [N]\{d^e\} \tag{3.64}$$

where $[N]$ is the shape function matrix defined as

$$[N] = \begin{bmatrix} N_1 & 0 & 0 & N_2 & 0 & 0 \\ 0 & N_1 & 0 & 0 & N_2 & 0 \\ 0 & 0 & N_1 & 0 & 0 & N_2 \end{bmatrix} \tag{3.65}$$

Inserting the displacements given by (3.64) into the variational form (3.60) restrained to the element domain, the elemental discrete variational form will be obtained,

$$\begin{aligned} &\frac{1}{2}b\int_\ell \left\{\delta\ddot{d}^e\right\}^{\mathrm{T}}[N]^{\mathrm{T}}[J][N]\left\{\ddot{d}^e\right\}dx + \frac{1}{2}b\int_\ell \{\delta d^e\}^{\mathrm{T}}[N]^{\mathrm{T}}[\mathcal{L}_\varepsilon]^{\mathrm{T}}[D_\varepsilon][\mathcal{L}_\varepsilon][N]\{d^e\}\,dx \\ &\quad + \frac{1}{2}b\int_\ell \{\delta d^e\}^{\mathrm{T}}[N]^{\mathrm{T}}[\mathcal{L}_\gamma]^{\mathrm{T}}[D_\gamma][\mathcal{L}_\gamma][N]\{d^e\}\,dx - \int_S \{\delta d^e\}^{\mathrm{T}}[N]^{\mathrm{T}}\{f^e\}\,dS = 0 \end{aligned} \tag{3.66}$$

According to the above equation, the deformation matrices can be defined as:

- for the extensional stiffness component

$$\begin{aligned} [B_\varepsilon] &= [\mathcal{L}_\varepsilon][N] \\ &= \begin{bmatrix} 1 & 0 & 0 \\ 0 & \frac{\partial}{\partial x} & 0 \\ 0 & 0 & \frac{\partial}{\partial x} \end{bmatrix}\begin{bmatrix} N_1 & 0 & 0 & N_2 & 0 & 0 \\ 0 & N_1 & 0 & 0 & N_2 & 0 \\ 0 & 0 & N_1 & 0 & 0 & N_2 \end{bmatrix} \\ &= \begin{bmatrix} N_1 & 0 & 0 & N_2 & 0 & 0 \\ 0 & \frac{\partial N_1}{\partial x} & 0 & 0 & \frac{\partial N_2}{\partial x} & 0 \\ 0 & 0 & \frac{\partial N_1}{\partial x} & 0 & 0 & \frac{\partial N_2}{\partial x} \end{bmatrix} \end{aligned} \tag{3.67}$$

- for the shear stiffness component

$$\begin{aligned} [B_\gamma] &= [\mathcal{L}_\gamma][N] \\ &= \begin{bmatrix} \frac{\partial}{\partial x} & \frac{1}{h} & -\frac{1}{h} \end{bmatrix}\begin{bmatrix} N_1 & 0 & 0 & N_2 & 0 & 0 \\ 0 & N_1 & 0 & 0 & N_2 & 0 \\ 0 & 0 & N_1 & 0 & 0 & N_2 \end{bmatrix} \\ &= \begin{bmatrix} \frac{\partial N_1}{\partial x} & \frac{N_1}{h} & -\frac{N_2}{h} & \frac{\partial N_2}{\partial x} & \frac{N_2}{h} & -\frac{N_2}{h} \end{bmatrix} \end{aligned} \tag{3.68}$$

Then, equation (3.66) can be rewritten, resulting into

$$\begin{aligned} &\frac{1}{2}b\int_\ell \{\delta d^e\}^{\mathrm{T}}[N]^{\mathrm{T}}[J][N]\left\{\ddot{d}^e\right\}dx + \frac{1}{2}b\int_\ell \{\delta d^e\}^{\mathrm{T}}[B_\varepsilon]^{\mathrm{T}}[D_\varepsilon][B_\varepsilon]\{d^e\}\,dx \\ &\quad + \frac{1}{2}b\int_\ell \{\delta d^e\}^{\mathrm{T}}[B_\gamma]^{\mathrm{T}}[D_\gamma][B_\gamma]\{d^e\}\,dx - \int_S \{\delta d^e\}^{\mathrm{T}}[N]^{\mathrm{T}}\{f^e\}\,dS = 0 \end{aligned} \tag{3.69}$$

By factorizing $\{\delta d^e\}$, equation (3.69) can be rearranged into

$$\{\delta d^e\}^{\mathrm{T}} \left( \frac{1}{2} b \int_{\ell} [N]^{\mathrm{T}} [J] [N] \, dx \right) \left\{ \ddot{d}^e \right\} + \{\delta d^e\}^{\mathrm{T}} \left( \frac{1}{2} b \int_{\ell} [B_\varepsilon]^{\mathrm{T}} [D_\varepsilon] [B_\varepsilon] \, dx \right) \{d^e\}$$
$$+ \{\delta d^e\}^{\mathrm{T}} \left( \frac{1}{2} b \int_{\ell} [B_\gamma]^{\mathrm{T}} [D_\gamma] [B_\gamma] \, dx \right) \{d^e\} - \{\delta d^e\}^{\mathrm{T}} \left( \int_{S} [N]^{\mathrm{T}} \{f^e\} \, dS \right) = 0 \tag{3.70}$$

Now, for the generic layer beam element, from expression (3.70), the following elemental matrices can be defined:

- the mass matrix $[M^e] = \frac{1}{2} b \int_{\ell} [N]^{\mathrm{T}} [J] [N] \, dx$
- the extensional stiffness matrix $[K^e_\varepsilon] = \frac{1}{2} b \int_{\ell} [B_\varepsilon]^{\mathrm{T}} [D_\varepsilon] [B^e_\varepsilon] \, dx$
- the shear stiffness matrix $\left[K^e_\gamma\right] = \frac{1}{2} b \int_{\ell} [B_\gamma]^{\mathrm{T}} [D_\gamma] [B_\gamma] \, dx$
- the force vector $\{F^e\} = \int_{S} [N]^{\mathrm{T}} \{f^e\} \, dS$

Equation (3.70) can then be rewritten, resulting into

$$\{\delta d^e\}^{\mathrm{T}} [M^e] \left\{ \ddot{d}^e \right\} + \{\delta d^e\}^{\mathrm{T}} [K^e_\varepsilon] \{d^e\} + \{\delta d^e\}^{\mathrm{T}} \left[K^e_\gamma\right] \{d^e\} - \{\delta d^e\}^{\mathrm{T}} \{F^e\} = 0 \tag{3.71}$$

### 3.9.2 Multilayer element

Until now, a generic one layer element has been treated and its discrete variational has been obtained. However, a more generalized approach is required to model a laminate beam. Therefore, the single layer formulation needs to be generalized for a multilayer beam. So, from now on, a subscript $k$ will be added, refering to the generic $k^{th}$ layer. Then, equation (3.71) can be rewritten as

$$\{\delta d^e\}^{\mathrm{T}}_k [M^e]_k \left\{ \ddot{d}^e \right\}_k + \{\delta d^e\}^{\mathrm{T}}_k [K^e_\varepsilon]_k \{d^e\}_k + \{\delta d^e\}^{\mathrm{T}}_k \left[K^e_\gamma\right]_k \{d^e\}_k - \{\delta d^e\}^{\mathrm{T}}_k \{F^e\}_k = 0 \tag{3.72}$$

As a *layerwise* approximation was assumed for the in-plane displacements, the discrete variational statement of equation (3.72) can be generalized for a multilayer element with $n$ layers. Therefore, for each generic layer $k$, the degrees of freedom can be related to the upper and lower layer displacements as represented in figure 3.5.

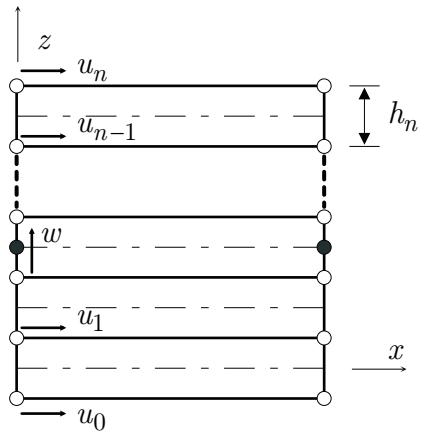


**Figure 3.5:** Layer degrees of freedom assembly.

According to figure 3.5, the degrees of freedom of the element node $i$ on a $n$ layer structure will be given by

$$\{d_i^e\}_n = \left\{ \begin{array}{ccccccccc} w_i & u_{0_i} & u_{1_i} & u_{2_i} & \cdots & u_{(k-1)_i} & u_{k_i} & \cdots & u_{(n-1)_i} & u_{n_i} \end{array} \right\}^{\mathrm{T}} \tag{3.73}$$

Then, the element degrees of freedom vector for a $n$ layer domain will be

$$\{d^e\}_n = \left\{ \begin{array}{cc} \{d_1^e\}_n & \{d_2^e\}_n \end{array} \right\}^{\mathrm{T}} \tag{3.74}$$

Given the degrees of freedom vector for a generic layer $k$, previously described in (3.62), these degrees of freedom can be related to the degrees of freedom of a $n$ layer element (3.74) according to

$$\{d^e\}_k = [L]_k \{d^e\}_n \tag{3.75}$$

where matrix $[L]_k$ represents a location matrix which, for the generic layer $k$, it is given by the composition of two matrices $[L_i]_k$, one for each node,

$$[L]_k = \left[ \begin{array}{cc} [L_1]_k & [L_2]_k \end{array} \right] \tag{3.76}$$

being each $[L_i]_k$ matrix described as:

$$[L_i]_n = \left[ \begin{array}{cccccccccc} 1 & 0 & 0 & 0 & \cdots & 0 & 0 & \cdots & 0 & 0 \\ 0 & 0 & 0 & 0 & \cdots & 1 & 0 & \cdots & 0 & 0 \\ 0 & 0 & 0 & 0 & \cdots & 0 & 1 & \cdots & 0 & 0 \end{array} \right] \tag{3.77}$$

Then, relation (3.75) can be inserted into (3.72), which can be adapted to comply an arbitrary number of layers $n$, becoming:

$$\begin{aligned} &\{\delta d^e\}_n^{\mathrm{T}} \sum_{k=1}^{n} \left( [L]_k^T [M^e]_k [L]_k \right) \left\{ \ddot{d}^e \right\}_n + \{\delta d^e\}_n^{\mathrm{T}} \sum_{k=1}^{n} \left( [L]_k^T [K_\varepsilon^e]_k [L]_k \right) \{d^e\}_n \\ &+ \{\delta d^e\}_n^{\mathrm{T}} \sum_{k=1}^{n} \left( [L]_k^T \left[K_\gamma^e\right]_k [L]_k \right) \{d^e\}_n - \{\delta d^e\}_n^{\mathrm{T}} \sum_{k=1}^{n} \left( [L]_k^T \{F^e\}_k \right) = 0 \end{aligned} \tag{3.78}$$

From equation (3.78), the elemental matrices of a $n$ layer element are:

- mass matrix

$$[M^e]_n = \sum_{k=1}^{n} \left( [L]_k^{\mathrm{T}} [M^e]_k [L]_k \right) \tag{3.79}$$

- extensional stiffness matrix

$$[K_\varepsilon^e]_n = \sum_{k=1}^{n} \left( [L]_k^{\mathrm{T}} [K_\varepsilon^e]_k [L]_k \right) \tag{3.80}$$

- shear stiffness matrix

$$\left[K_\gamma^e\right]_n = \sum_{k=1}^{n} \left( [L]_k^{\mathrm{T}} \left[K_\gamma^e\right]_k [L]_k \right) \tag{3.81}$$

- external forces vector

$$\{F^e\}_n = \sum_{k=1}^{n} \left( [L]_k^{\mathrm{T}} \{F^e\}_k \right) \tag{3.82}$$

As equation (3.78) must be fulfilled for any $\{\delta d^e\}_n$, then it yields to

$$[M^e]_n \left\{\ddot{d}^e\right\}_n + [K_\varepsilon^e]_n \{d^e\}_n + \left[K_\gamma^e\right]_n \{d^e\}_n = \{F^e\}_n \tag{3.83}$$

Finally, summing the extensional and shear stiffness matrices will result into

$$[M^e]_n \left\{\ddot{d}^e\right\}_n + [K^e]_n \{d^e\}_n = \{F^e\}_n \tag{3.84}$$

which is the equation of motion of a multilayer *layerwise* beam element.

## 3.10 Global assembly of the finite elements

Having defined the equation of motion of a multilayer beam element, equation (3.84), the global assembly of the elements to model a multilayer beam structure can now be made using a standard element assembly procedure widely documented and described [41, 42]. The equation of motion for the global structure will be obtained assembling each element equation of motion resulting

$$[M] \left\{\ddot{d}\right\} + [K(\omega)] \{d\} = \{F\} \tag{3.85}$$

where $[K(\omega)]$ and $[M]$ are, respectively, the global mass and stiffness matrices and $\{d\}$ and $\{F\}$ are the global displacement and force vector.

## 3.11 Direct frequency analysis procedure

The system of equations of motion of a multilayer finite element model is given by

$$[M]\left\{\ddot{d}\right\}+[K]\{d\}=\{F\} \tag{3.86}$$

where vectors $\{d\}$ and $\{F\}$ represent respectively the time dependent responses and excitation forces of FE degrees of freedom .

In equation (3.86) all the layers of the finite element model are considered to be elastic, but, if the finite element model has any viscoelastic layer, like a cork compound layer, the stiffness matrix has to be divided into two parcels, one respecting to the elastic layers and other respecting to the viscoelastic layers. Therefore, the system of equations of motion of the finite element model with purely viscoelastic damping layers and elastic layers can be rewritten as

$$[M]\left\{\ddot{d}\right\}+\left([K]+\left[\bar{K}\left(j\omega\right)\right]\right)\{d\}=\{F\} \tag{3.87}$$

where $[M]$ is the mass matrix, $[K]$ is the stiffness matrix of the elastic layers and $\left[\bar{K}\left(j\omega\right)\right]$ is the frequency dependent stiffness matrix of the viscoelastic layers.

Using Equation (3.87) as it is, the frequency dependent stiffness matrix definition implies that its use and analysis can only be performed in the frequency domain, based on the Complex Modulus Approach (CMA), where the material properties of the stiffness matrix of the viscoelastic layers are defined for each discrete frequency value.

Assuming that the system excitation is harmonic, it can therefore be characterized by an amplitudes vector $\left\{\bar{F}\right\}$ and a single excitation frequency $\omega$ as follows

$$\{F\}=\left\{\bar{F}\right\}e^{j\omega t} \tag{3.88}$$

The system response in steady state shall also be harmonic with the same frequency $\omega$ of the excitation force,

$$\{d\}=\left\{\bar{d}\left(j\omega\right)\right\}e^{j\omega t} \tag{3.89}$$

Replacing expressions (3.88) and (3.89) into equation (3.87) results into

$$\left[[K]+\left[\bar{K}\left(j\omega\right)\right]-\omega^2\left[M\right]\right]\left\{\bar{d}\left(j\omega\right)\right\}=\left\{\bar{F}\right\} \tag{3.90}$$

The FRF (frequency response function), for a displacement measured in the $o^{th}$ DOF and a load applied in the $i^{th}$ DOF, can be obtained by solving (3.90) for different values of frequency $\omega_l$,

$$\left[[K]+\left[\bar{K}\left(j\omega_l\right)\right]-\omega^2\left[M\right]\right]\left\{\bar{d}\left(j\omega_l\right)\right\}=\left\{\bar{F}_i\right\} \tag{3.91}$$

where $\left\{\bar{F}_i\right\}$ is the force vector with all elements equal to zero except the $i^{th}$ component and $\left\{\bar{d}\left(j\omega_l\right)\right\}$ is the resulting complex response vector (amplitudes and phases), obtained at frequency $\omega_l$. Therefore, the receptance FRF $H_{oi}\left(j\omega_l\right)$ value at frequency $\omega_l$ will be given by

$$H_{oi}\left(j\omega_l\right)=\frac{\bar{d}_o\left(j\omega_l\right)}{\bar{F}_i} \tag{3.92}$$

where $\bar{F}_i$ is the amplitude of the load input and $\bar{d}_o\left(j\omega_l\right)$ is the displacement response extracted from the $o^{th}$ DOF of vector $\left\{\bar{d}\left(j\omega_l\right)\right\}$.

Finally, the FRF can be generated from the results of many discrete frequency calculations of equation (3.91), in which the complex stiffness matrix of the viscoelastic layers is re-calculated for each frequency value of the discrete frequency range $\omega = \omega_1, \omega_2, \omega_3 \ldots \omega_l$, as represented in figure 3.6.

The direct frequency analysis (DFA) method is therefore a frequency domain method where the frequency response model can be generated in a straightforward manner from the results of many discrete frequency calculations of the equations of motion, in which the complex stiffness matrix of the viscoelastic layers is re-calculated for each frequency value of the desired discrete frequency range.

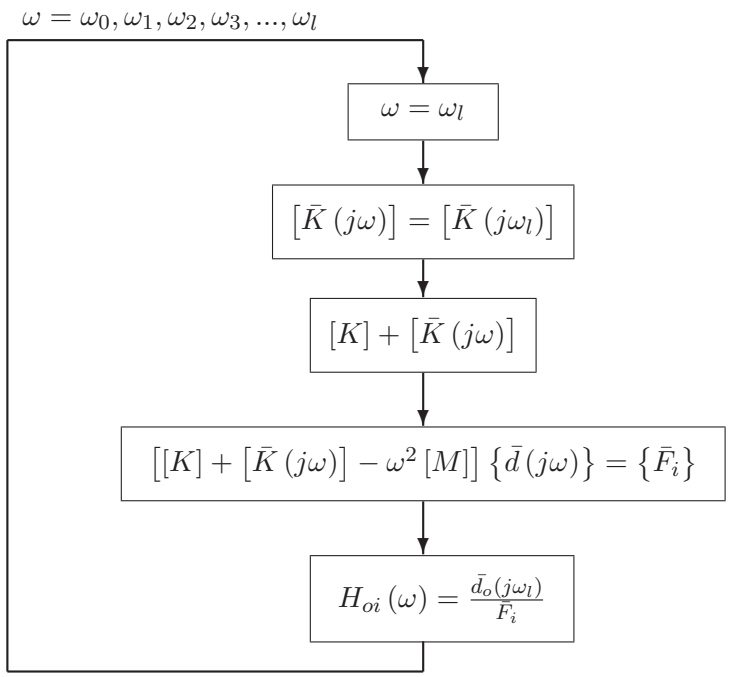


**Figure 3.6:** Direct frequency analysis algorithm diagram.

The main disadvantage of this method is its heavy computational cost and the time it takes to perform a full analysis due to the need to solve a linear and complex system of equations with the dimension of the spatial model for each frequency cycle.

# Chapter 4

# Sandwich Beams with Cork Compound Cores: Experimental Results

## 4.1 Introduction

The experimental study has been focused on the use of modal analysis to characterize the dynamic behavior of sandwich structures composed of two aluminum beams with a cork compound core. The main objective of this experimental study is to determine the cork compound influence on the structure dynamic response and use the measured data to further validate the developed multilayer beam finite element. To achieve it, several sandwich beams with different cork compound cores have been tested and its results were compared.

## 4.2 Characterization of the test samples

On the following sections, the sandwich beams as well as the properties of the different cork compounds used are described.

### 4.2.1 Description of the test samples

The test samples are sandwich beams with a cork compound core and two aluminum plies as schematically depicted in figure 4.1.The cork compound core thickness is represented by $e$ and takes different values for each cork compound type.

The principal dimensions of the test samples, as depicted in figure 4.1, are :

- length $\ell$: 745 mm
- width $b$: 40 mm
- thickness $h$: $[3 + e + 3]$ mm

Eight test samples have been prepared with different cork compound cores, and another one has been prepared without cork compound core so it could be used as a reference test sample.

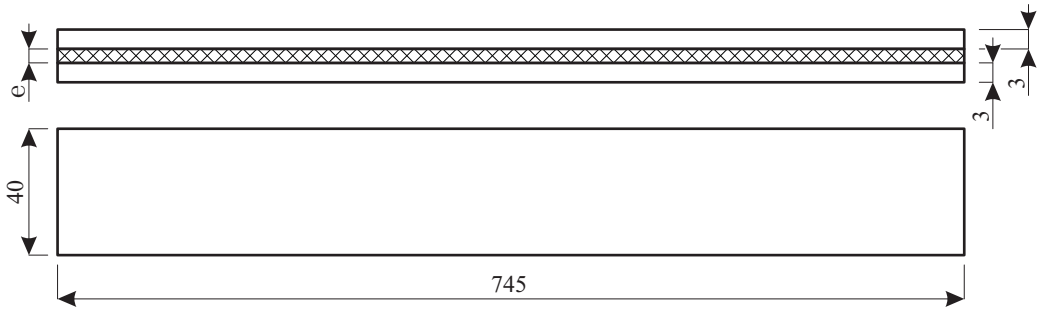


**Figure 4.1:** Schematic drawing of the test samples.

In the table 4.1, on the next page, the most relevant properties of the cork compounds used on each test sample are presented.

### 4.2.2 Preparation of the test samples

The test samples preparation process involves the gluing of its constitutive parts in order to obtain the referred sandwich structure depicted in figure 4.1. Therefore, the following preparation steps were followed:

1. The two aluminum beams were sandpapered in order to obtain a good gluing surface on the beams;

2. The two beams were cleaned with acetone;

3. The cork compound was cut out with the beams width and length dimensions from a big sheet of it;

4. The cork compound was glued to the aluminum beams, using epoxy resign as glue, forming a sandwich structure.

## 4.3 Experimental modal analysis

The experimental modal analysis was implemented by measuring a set of frequency response functions and identifying the modal parameters. The identification procedure was performed by the modal analysis function of the Matlab® toolbox SDT®.

### 4.3.1 Experimental setup

To achieve free boundary conditions, the beams were suspended from a frame structure by two nylon cables. The chosen configuration restrains the structure in-plane motion while allowing it to move in the direction normal to the structure plane, as it can be seen in figure 4.2.

The testing beam was excited with an electromagnetic shaker (LDS-201) at one point, being at that same point measured the exciting force with a piezoelectric force transducer (B&K-8203).

**Table 4.1:** Test samples characteristics.

| Sample Name | Sample Description | Core | Core Description | Equivalent Extensional Sample (Chapter 2) | Equivalent Shear Sample (Chapter 2) | Core thickness $e$ $[mm]$ |
|---|---|---|---|---|---|---|
| Beam 0 | Two glued aluminium beams without cork compound core | - | - | - | - | - |
| Beam 1 | Two aluminium beam plies with a cork compound core | 8123 | • small grain<br>• high density | Sample B | Sample P1 | 0.8 |
| Beam 2 | Two aluminium beam plies with a cork compound core | 8123 | • small grain<br>• high density | Sample B | Sample P1 | 1.2 |
| Beam 3 | Two aluminium beam plies with a cork compound core | 8003 | • small grain<br>• low density | Sample A | Sample P2 | 0.8 |
| Beam 4 | Two aluminium beam plies with a cork compound core | 8003 | • small grain<br>• low density | Sample A | Sample P2 | 1.2 |
| Beam 5 | Two aluminium beam plies with a cork compound core | 8303 | • coarse grain<br>• high density | Sample C | Sample P3 | 0.8 |
| Beam 6 | Two aluminium beam plies with a cork compound core | 8303 | • coarse grain<br>• high density | Sample C | Sample P3 | 1.2 |
| Beam 7 | Two aluminium beam plies with a cork compound core | 8002 | • coarse grain<br>• low density | Sample D | - | 0.8 |
| Beam 8 | Two aluminium beam plies with a cork compound core | 8002 | • coarse grain<br>• low density | Sample D | - | 1.2 |

**Figure 4.2:** Assembled experimental setup.

The exciter was connected to the beam by a thin rod made out of steel, allowing an high axial stiffness but a low bending stiffness connection, assuring a good directional control of the excitation force. This connection can be seen in figure 4.3.

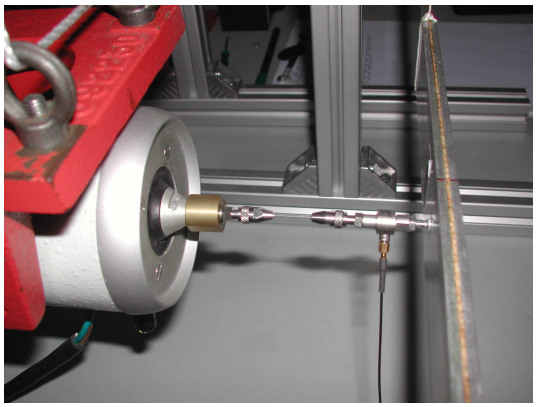

**Figure 4.3:** Connection between stinger and the beam test sample.

The shaker (LDS-201) was suspended by four nylon cables connected to a frame structure separated to the one from which was suspended the test sample in order to assure that no reaction force was transmitted to the testing structure.

The excitation force signal is generated by the generator module of the analyzer (B&K-2035) and sent to the power amplifier (LDS-PA25E) which finally actuates the electromagnetic shaker.

The beam response was measured in velocity, by the laser vibrometer (Polytec-OFV303) using the vibrometer controller (Polytec-OFV3001) as depicted in figure 4.4, on each point of the measuring mesh, being afterwords derived in the analyzer (B&K-2035) to obtain the response acceleration.

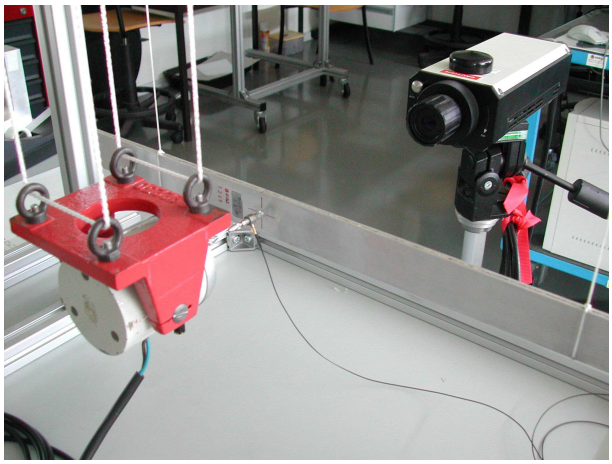

**Figure 4.4:** Laser velocity measurement.

The responses were measured in 11 points uniformly distributed along each test sample where were placed reflective stickers to allow the response measurement with the vibrometer laser head (Polytec-OFV303), as depicted in figure 4.5. The excitation force was applied at the point number 7 also represented in the measurement mesh depicted by figure 4.5.

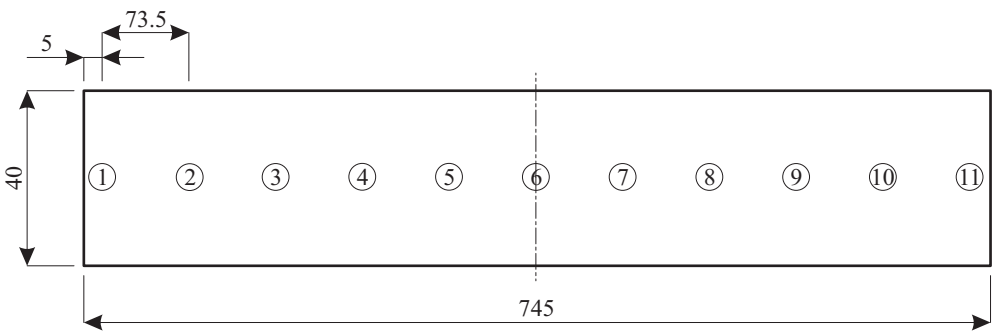


**(a)** measuring mesh schematic drawing.

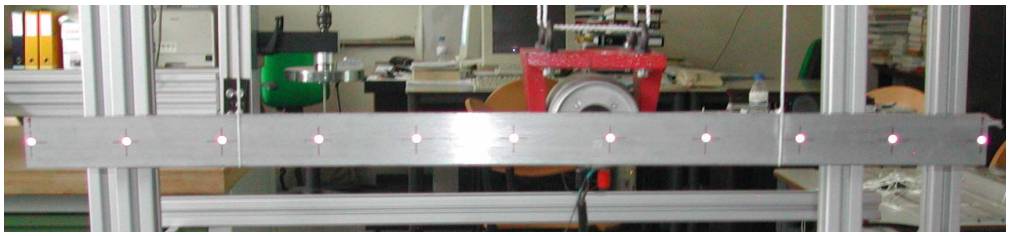

**(b)** real measuring mesh mesh picture.

**Figure 4.5:** Measuring mesh of each beam test sample.

To measure the response and the excitation, and to estimate the frequency response functions (FRFs) between the measuring points and the excitation point, an FFT analyzer (B&K-2035) was used. The measurements were made in a frequency range between 0 Hz and 400 Hz.

From the measured FRFs, a multi degree of freedom technique (MDOF) was used to estimate the modal parameters. The "Least Squares Complex Exponential" time domain algorithm was used to identify the poles (values of the natural frequencies and damping), being the residues determined afterwords using the "Least Squares Frequency Domain" algorithm [43].

Finally, a set of modes were obtained, which include estimations for the natural frequencies, loss factors and modeshapes. In the analysed frequency range, $[0 - 400]$ Hz, three modes for each test sample were identified.

The software used to obtain the modal parameters for the eight test samples and the reference one was the Matlab® toolbox SDT® and the LMS CADA-PC [43].

### 4.3.2 Measured FRFs

For each test sample a set of 11 accelerance FRFs were measured corresponding to each measuring point. In this section, only the measured driving point FRF of each test sample is shown. The other measured FRFs are presented in Appendix B. In figure 4.6 to figure 4.14, the driving point FRF (point 7) of the test samples, Beam 0 to Beam 8, are shown in the frequency bandwidth $[0 - 400]$ Hz.

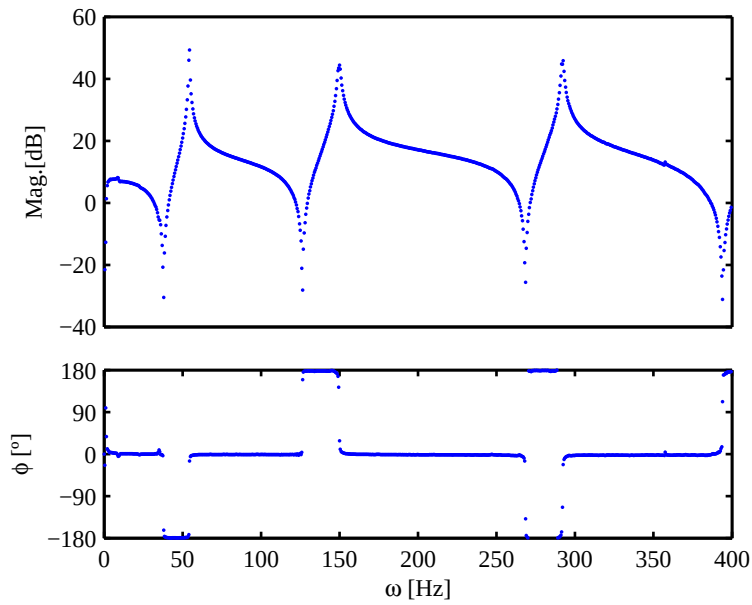


**Figure 4.6:** Driving point accelerance FRF of Beam 0.

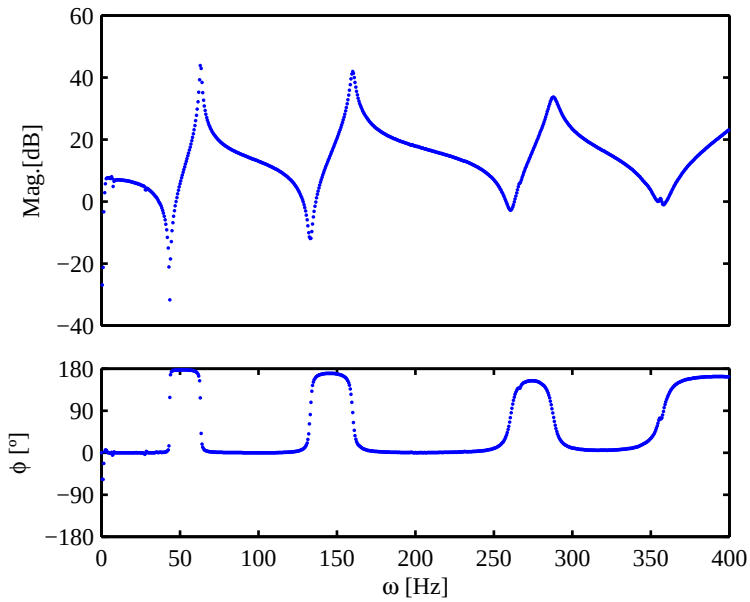


**Figure 4.7:** Driving point accelerance FRF of Beam 1.

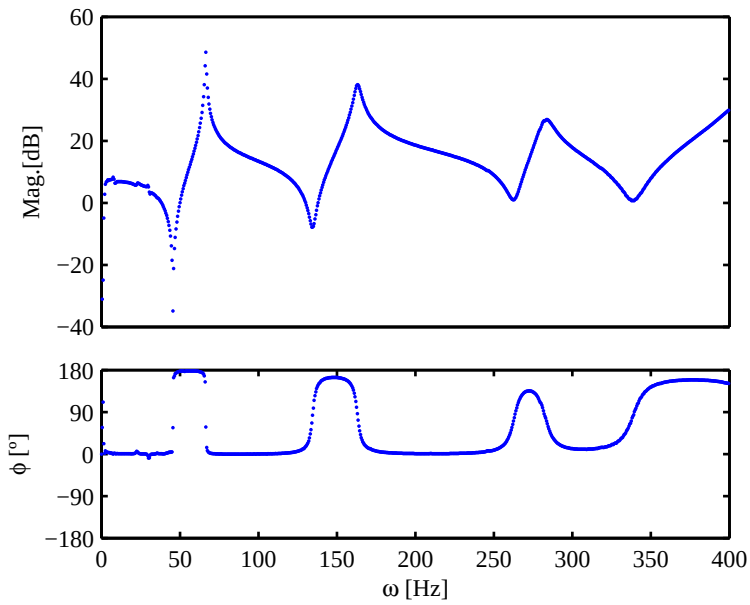


**Figure 4.8:** Driving point accelerance FRF of Beam 2.

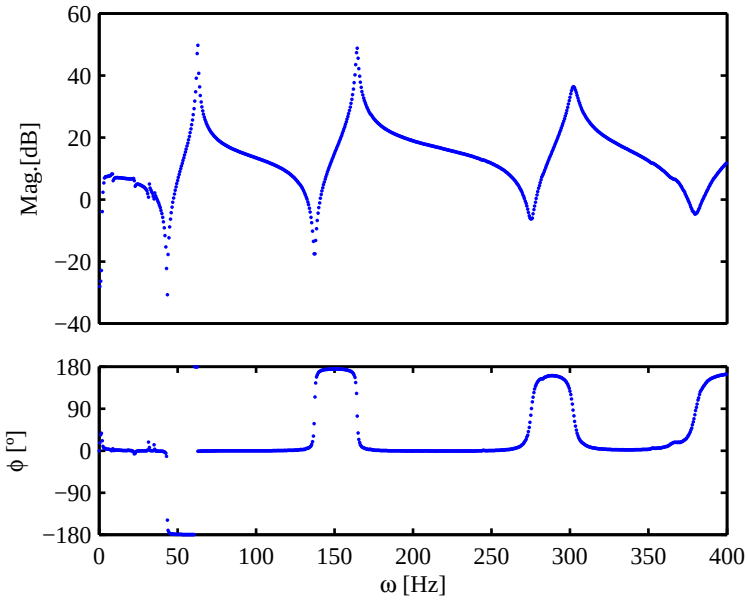


**Figure 4.9:** Driving point accelerance FRF of Beam 3.

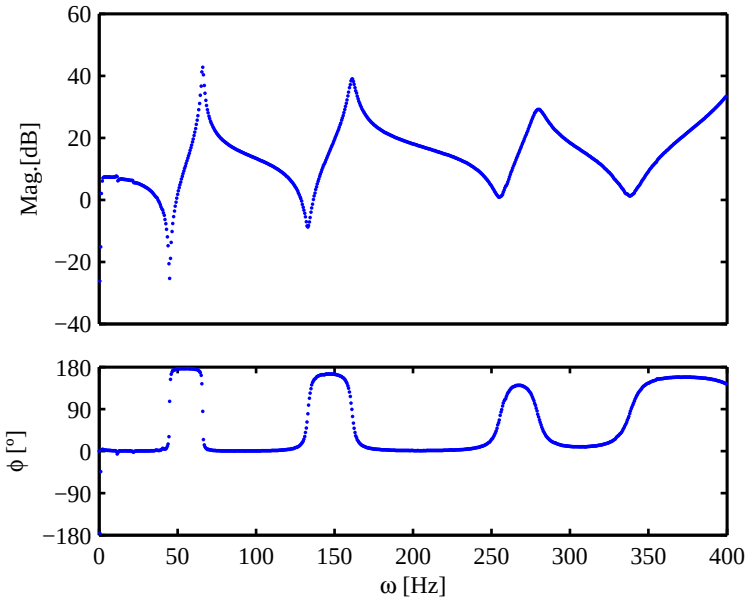


**Figure 4.10:** Driving point accelerance FRF of Beam 4.

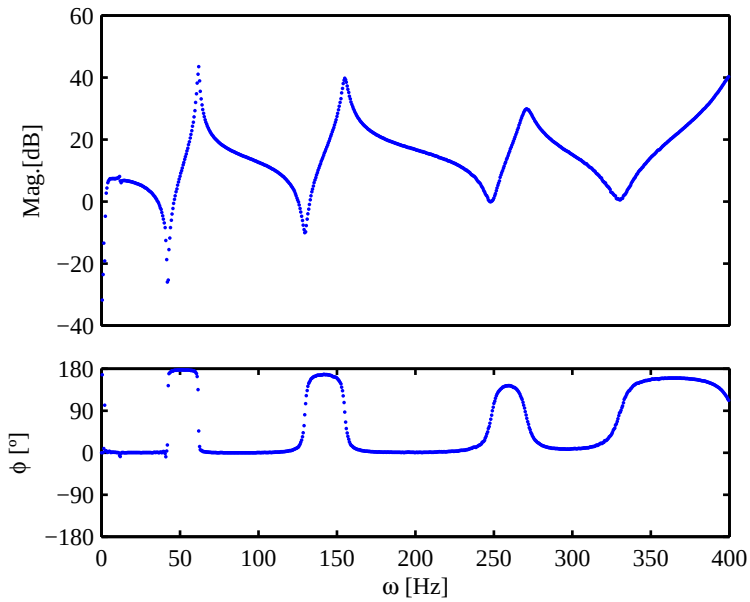


**Figure 4.11:** Driving point accelerance FRF of Beam 5.

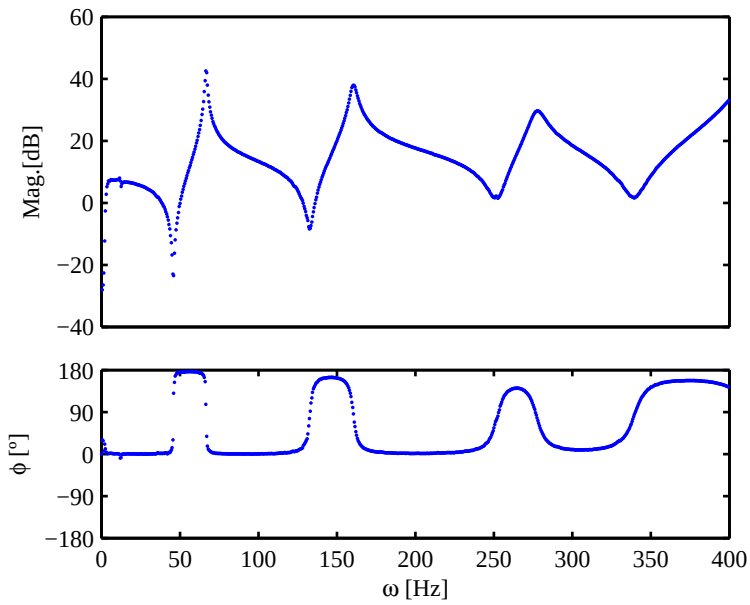


**Figure 4.12:** Driving point accelerance FRF of Beam 6.

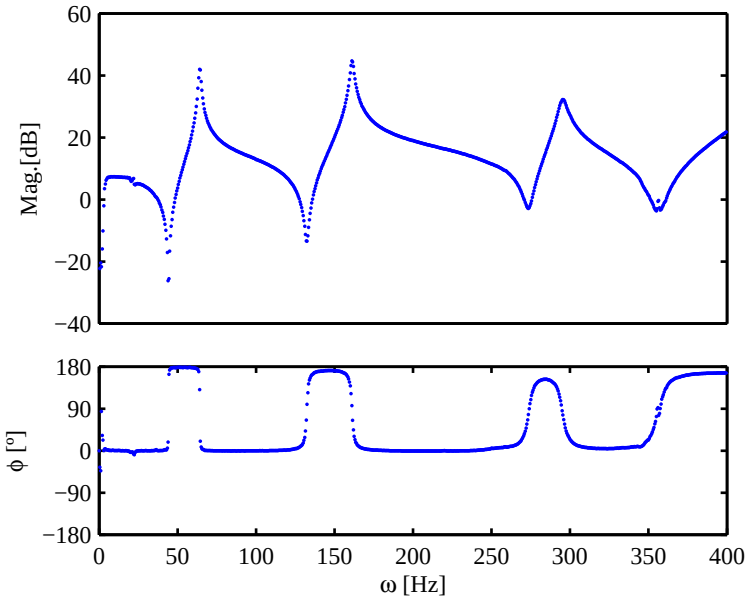


**Figure 4.13:** Driving point accelerance FRF of Beam 7.

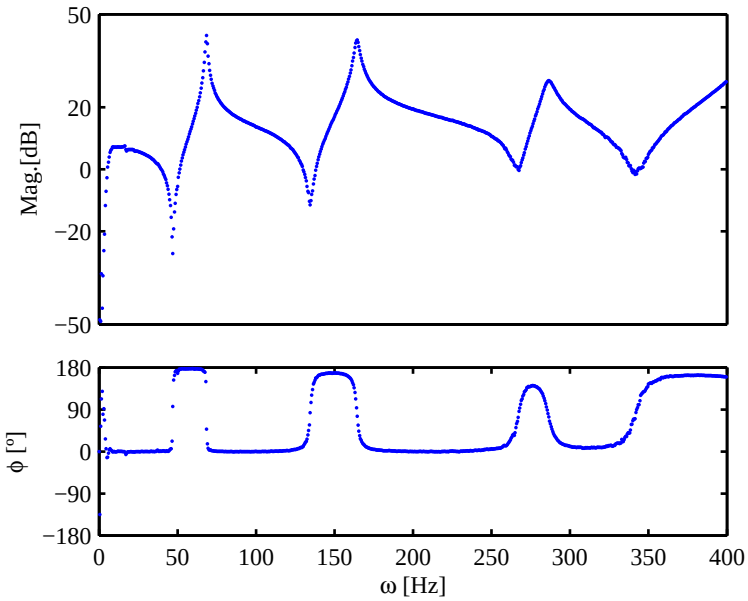


**Figure 4.14:** Driving point accelerance FRF of Beam 8.

### 4.3.3 Discussion of the measurements

As it can be seen from the measured FRFs, for all the test samples three modes can be clearly found in the bandwidth $[0 - 400]$ Hz.

## 4.4 Modal identification

With the set of measured frequency response functions (FRFs), a modal model can now be identified in order to describe the acquired information. Then, it becomes necessary to use estimation techniques like curve fitting to approximate the modal model to the acquired information, and therefore obtain the modal parameters of the system.

The curve fitting technique is a method with the following main stages:

1. Definition of a frequency range to perform the analysis;

2. Identification of the poles and each mode natural frequency;

3. Choice of physical model;

4. Estimation of the residues vectors representing the mode shapes;

5. Validation of the identified modal model.

In the identification process, the Modal Indicator Function (MIF) and Sum (SUM) function were obtained. The MIF function shows in which frequency the modes will probably exist, if they exist. When this function drops abruptly at a specific frequency, denotes a possible natural mode at that same frequency.

To perform the identification process, in a first stage, a multi degree of freedom (MDOF) technique, which uses the "Least Squares Complex Exponential" time domain algorithm, was applied in order to determine the natural frequencies and damping values for each mode. In a second stage, the residues were identified with a "Least Squares Frequency Domain" technique.

The validation of the identified modal model was performed by comparing the measured driving point FRF with the synthesized one and by using the Modal Assurance Criterion (MAC), which cross correlates a mode shape for one pole against the mode shape of all other poles. If the identified model is valid, there should be little or no correlation between mode shapes.

Next, for each test sample, some results of the above outlined modal analysis procedure are presented, namely the MIF and SUM functions, the comparison between the measured and the synthesized driving point FRF, the identified mode shapes and the MAC matrix.

The natural frequencies and loss factors are presented in table 4.2 and table 4.3 for all test samples.

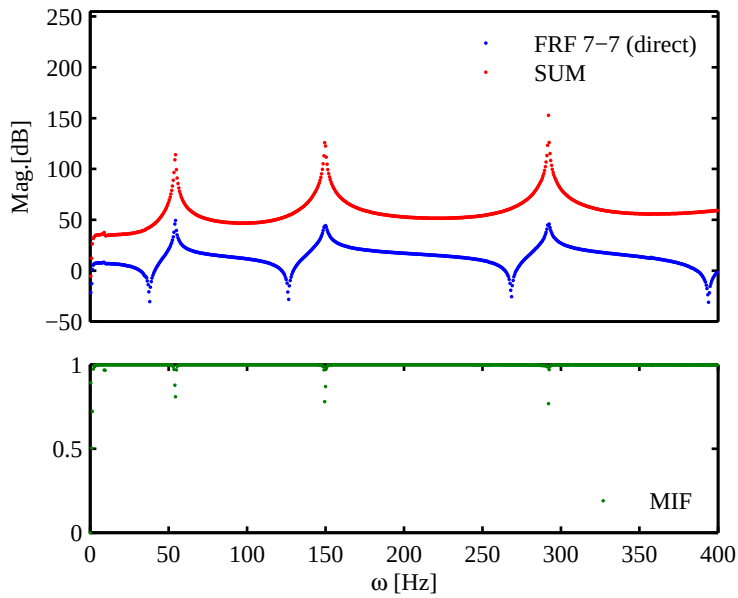


**Figure 4.15:** SUM and MIF of Beam 0 test sample.

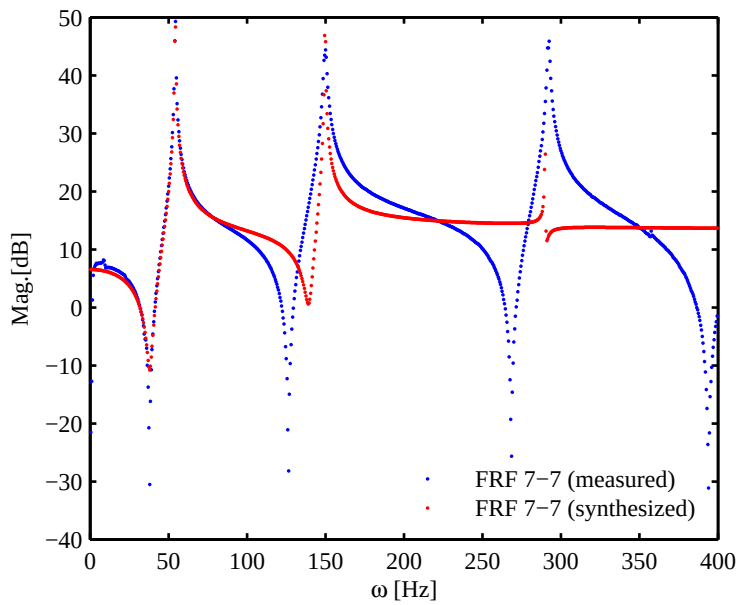


**Figure 4.16:** Synthesized and measured FRFs of Beam 0 test sample.

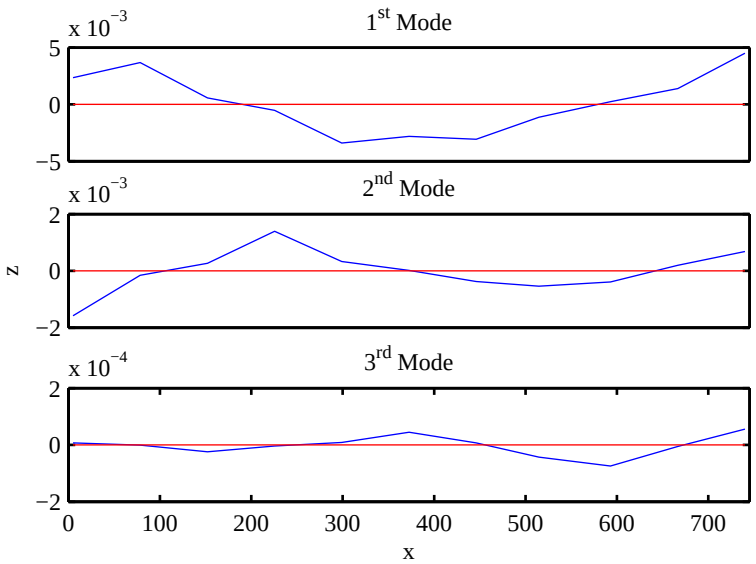


**Figure 4.17:** Estimated mode shapes of Beam 0 test sample.

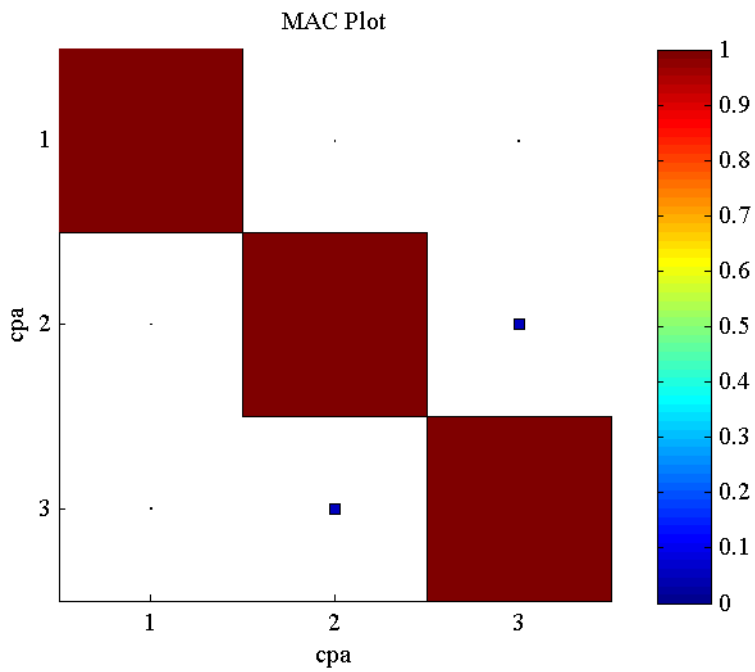


**Figure 4.18:** MAC plot for test sample Beam 0.

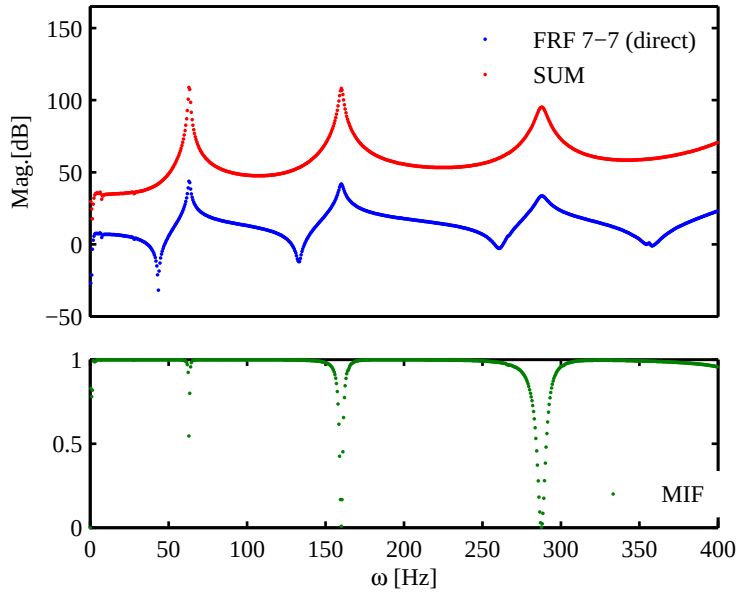


**Figure 4.19:** SUM and MIF of Beam 1 test sample.

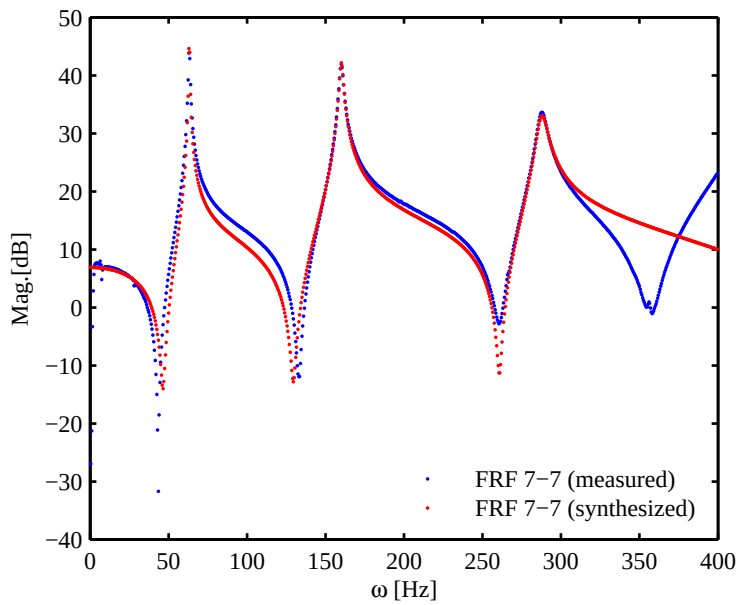


**Figure 4.20:** Synthesized and measured FRFs of Beam 1 test sample.

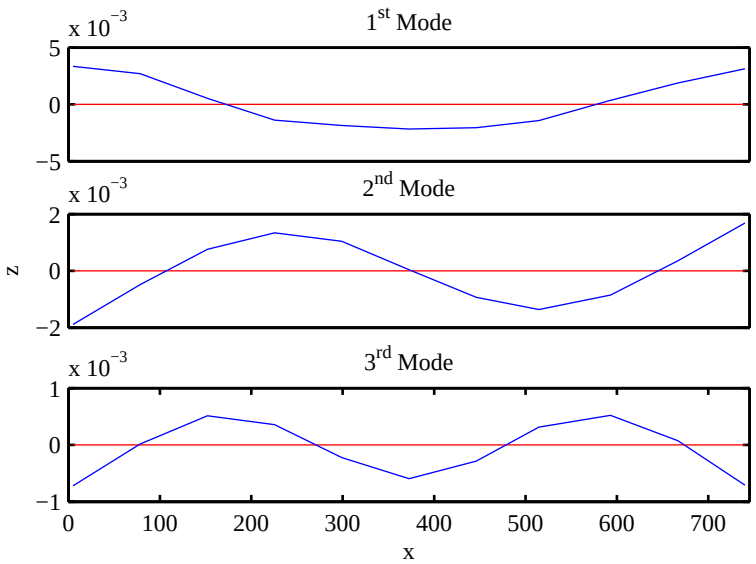


**Figure 4.21:** Estimated mode shapes of Beam 1 test sample.

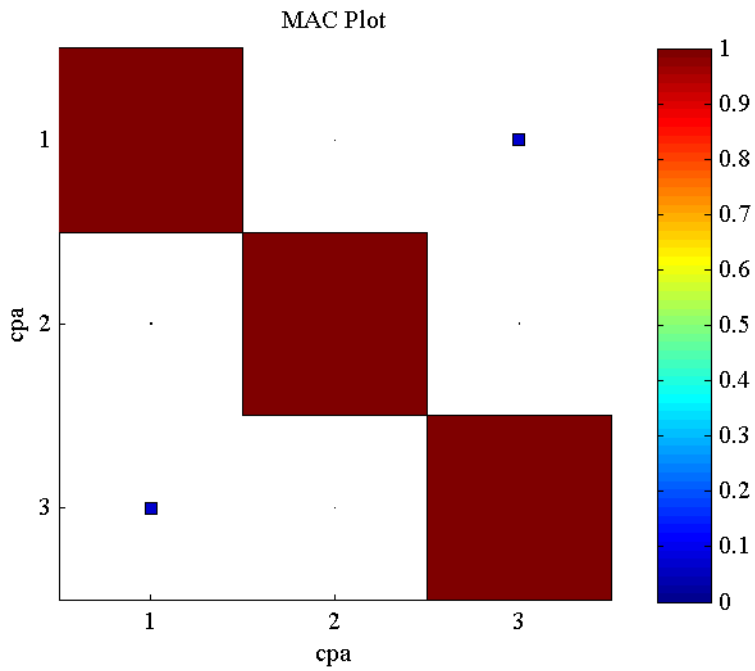


**Figure 4.22:** MAC plot for Beam 1 test sample.

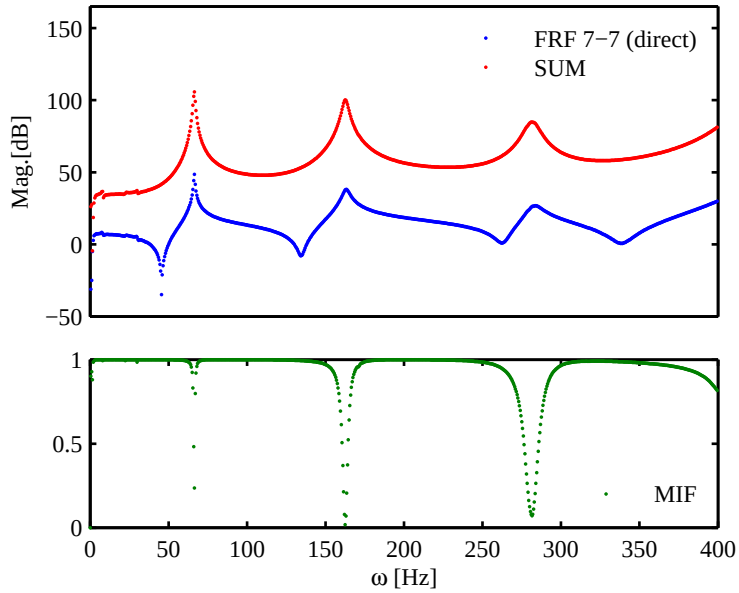


**Figure 4.23:** SUM and MIF of Beam 2 test sample.

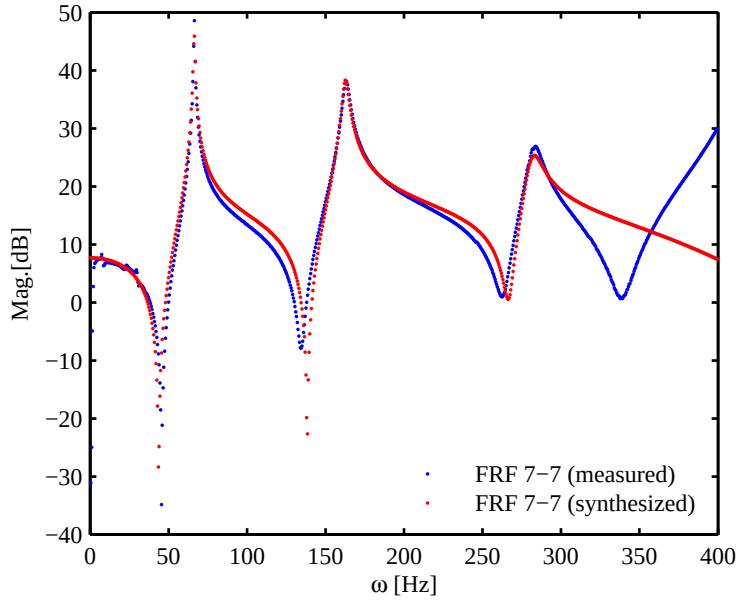


**Figure 4.24:** Synthesized and measured FRFs of Beam 2 test sample.

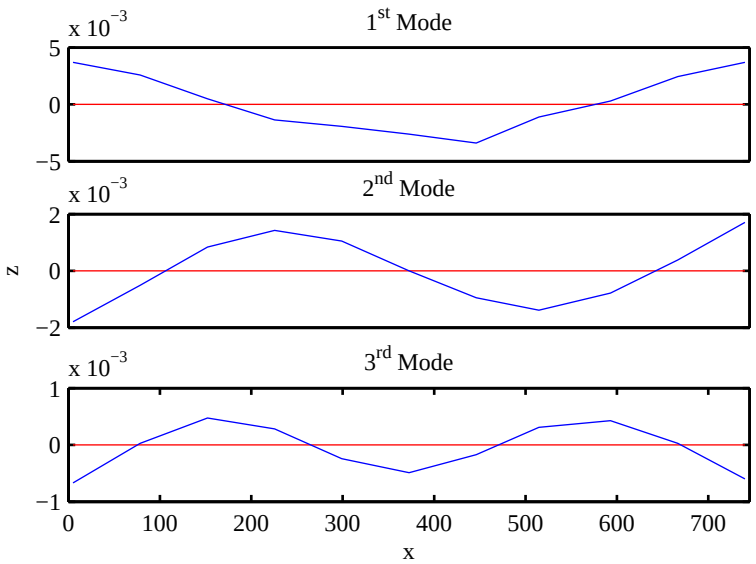


**Figure 4.25:** Estimated mode shapes of Beam 2 test sample.

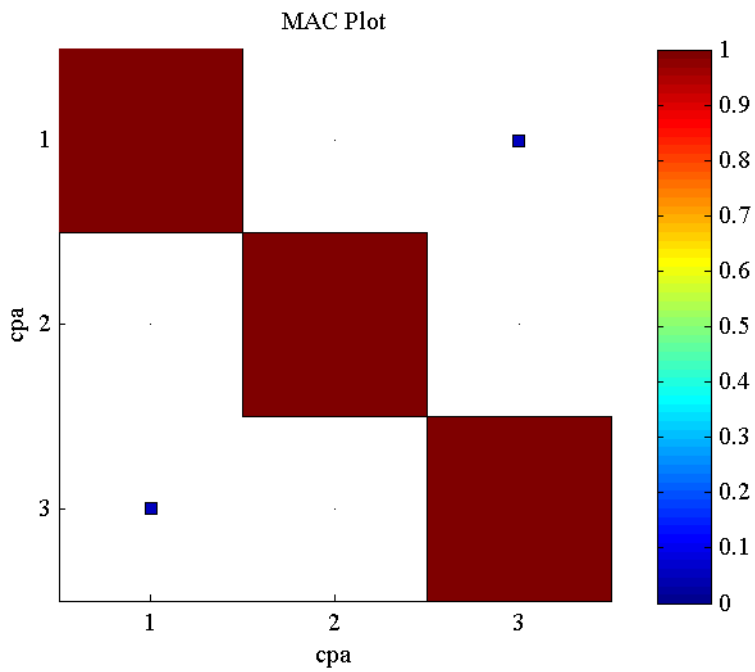


**Figure 4.26:** MAC plot for Beam 2 test sample.

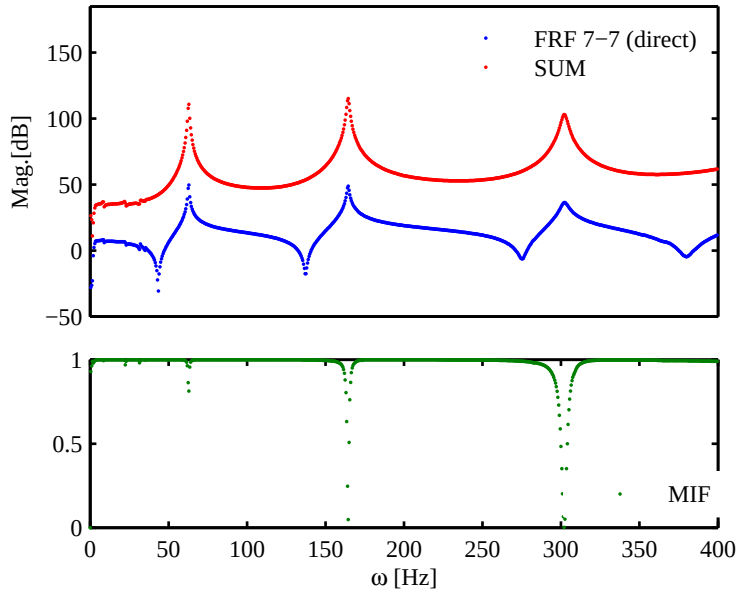


**Figure 4.27:** SUM and MIF of Beam 3 test sample.

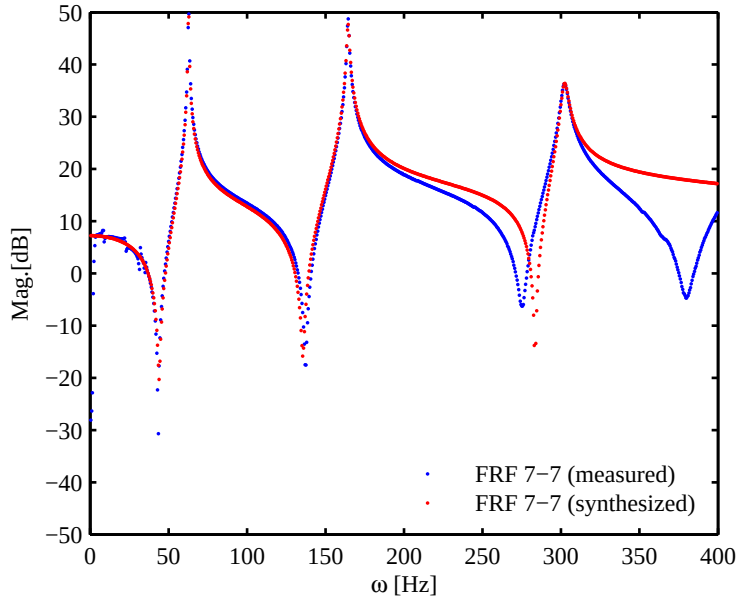


**Figure 4.28:** Synthesized and measured FRFs of Beam 3 test sample.

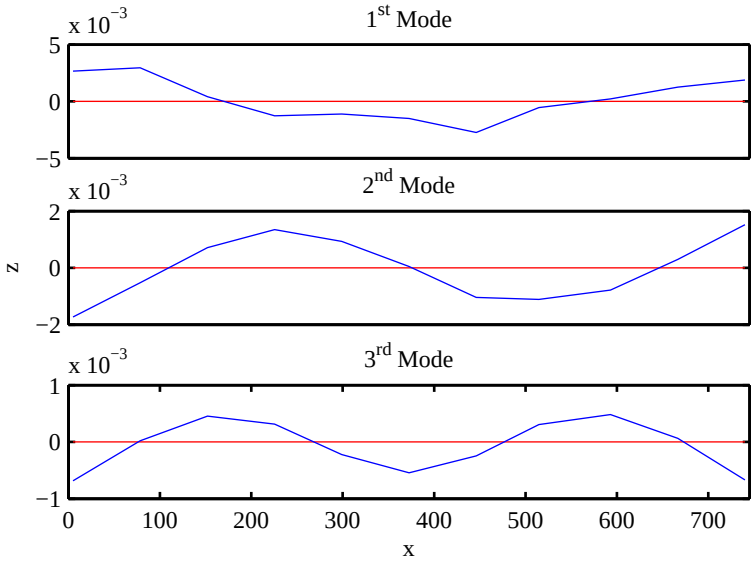


**Figure 4.29:** Estimated mode shapes of Beam 3 test sample.

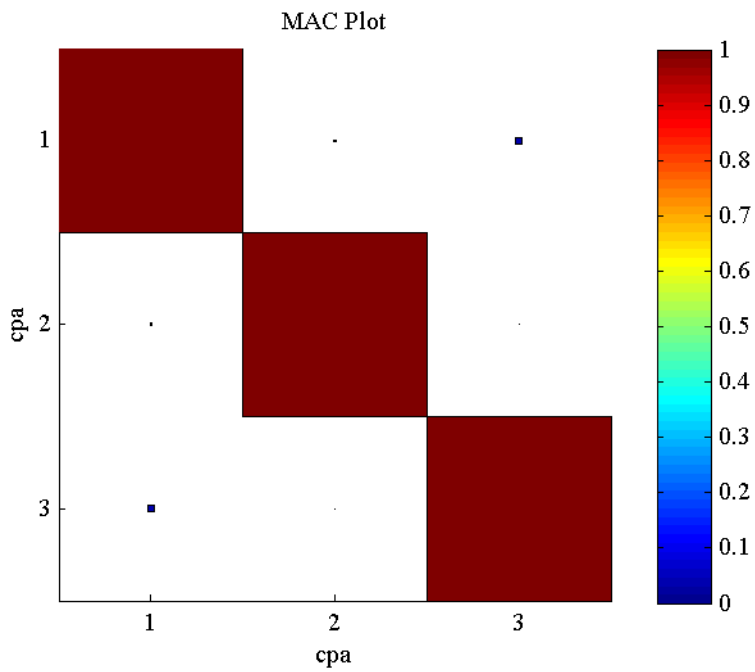


**Figure 4.30:** MAC plot for Beam 3 test sample.

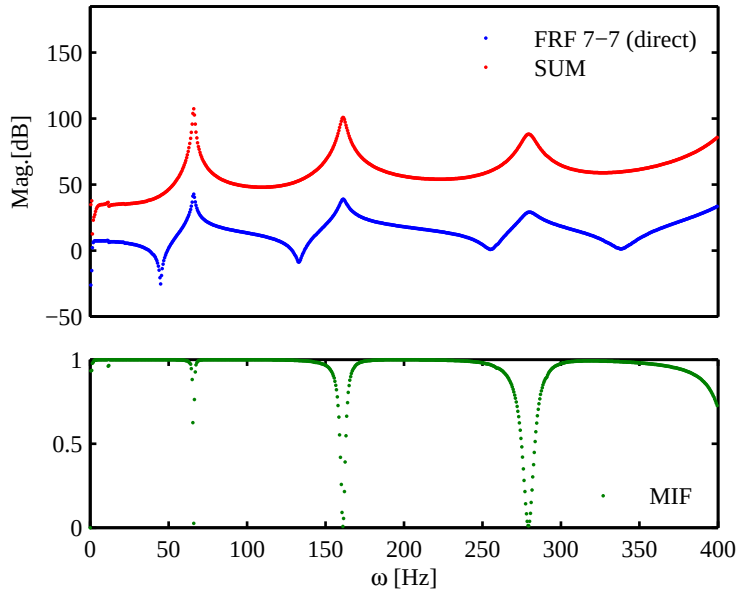


**Figure 4.31:** SUM and MIF of Beam 4 test sample.

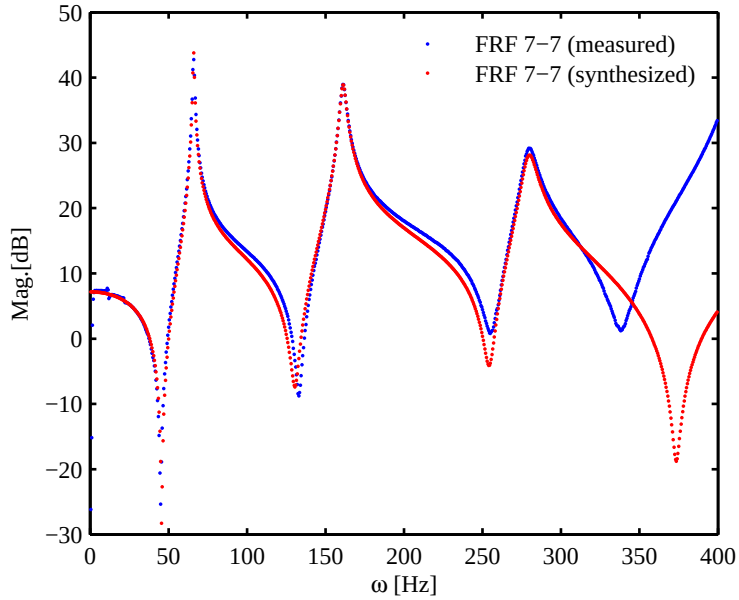


**Figure 4.32:** Synthesized and measured FRFs of Beam 4 test sample.

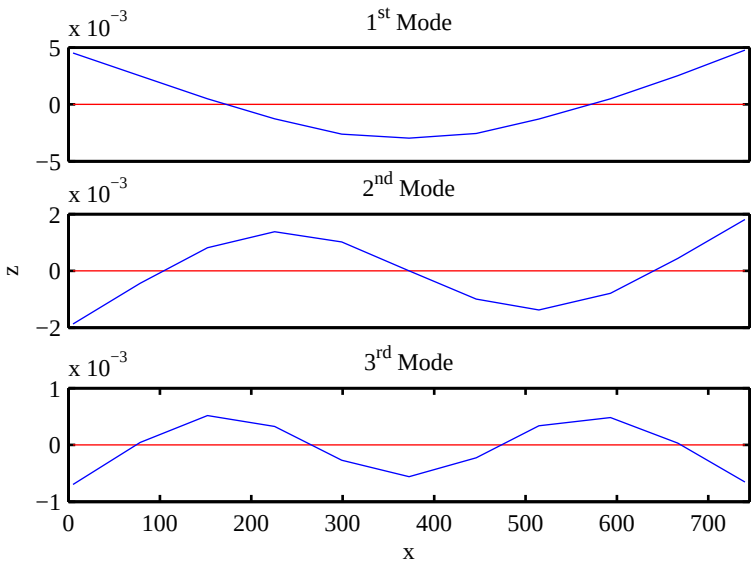


**Figure 4.33:** Estimated mode shapes of Beam 4 test sample.

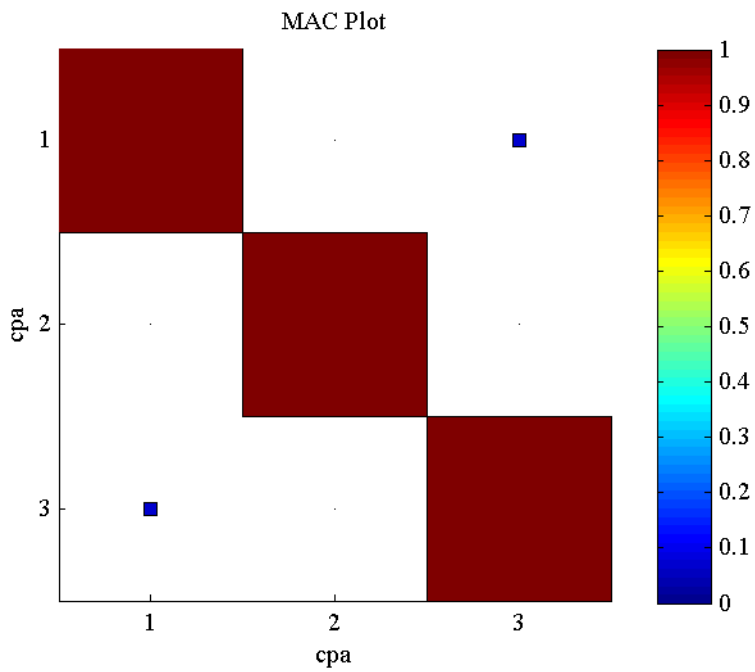


**Figure 4.34:** MAC plot for Beam 4 test sample.

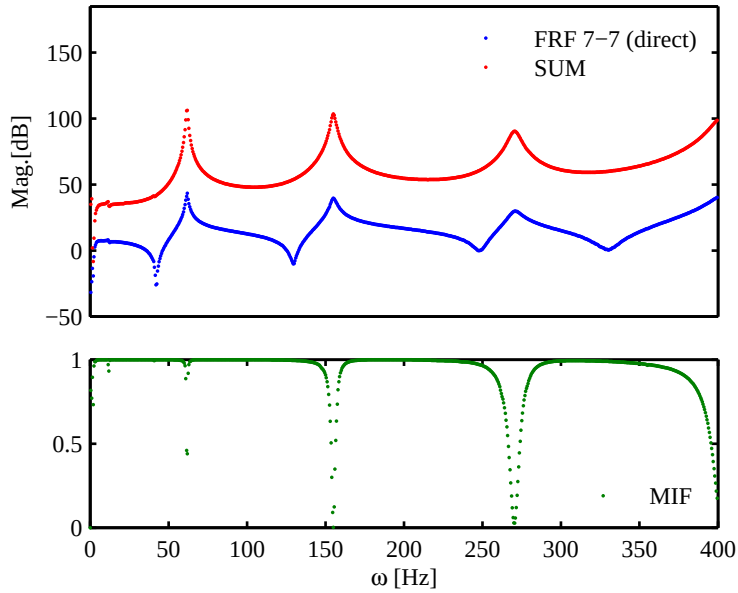


**Figure 4.35:** SUM and MIF of Beam 5 test sample.

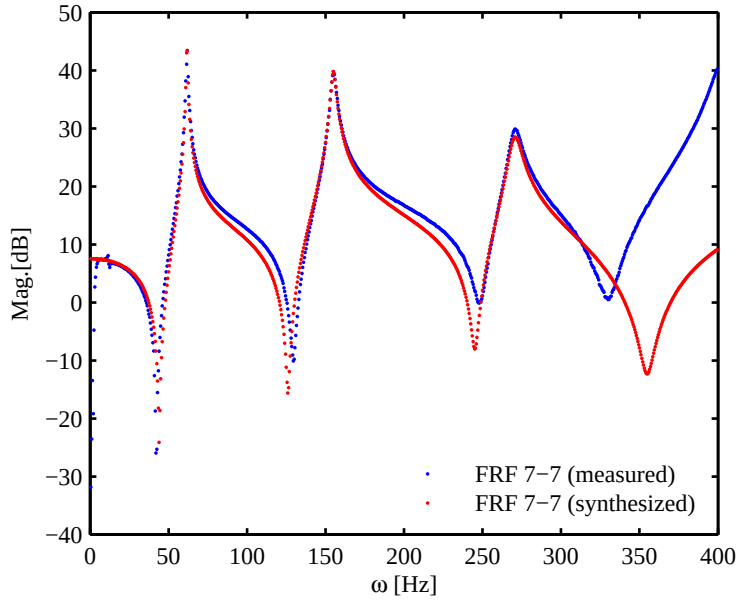


**Figure 4.36:** Synthesized and measured FRFs of Beam 5 test sample.

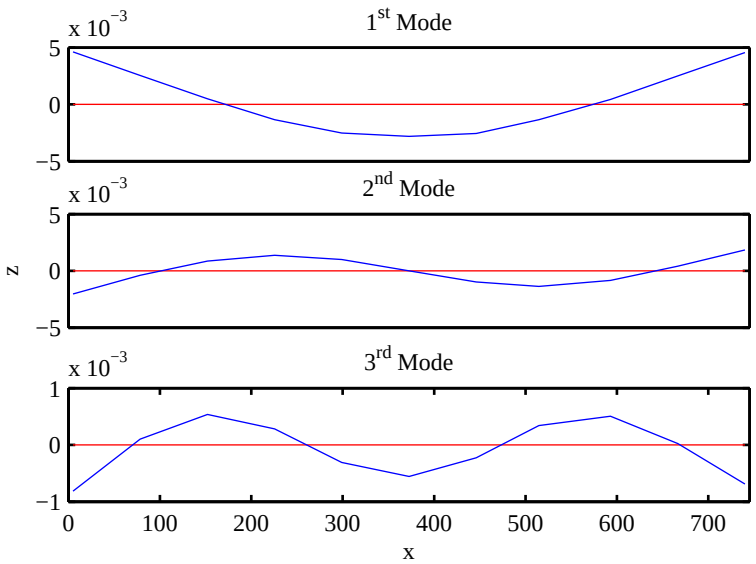


**Figure 4.37:** Estimated mode shapes of Beam 5 test sample.

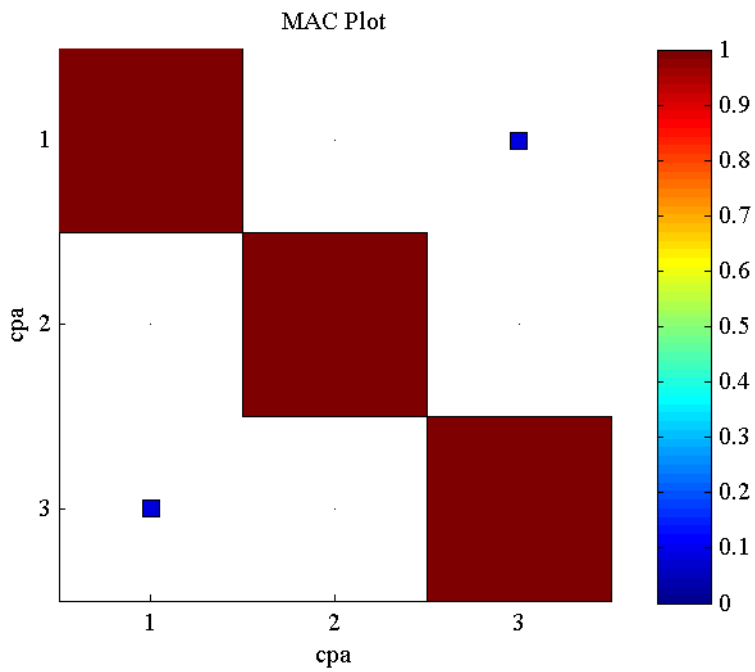


**Figure 4.38:** MAC plot for Beam 5 test sample.

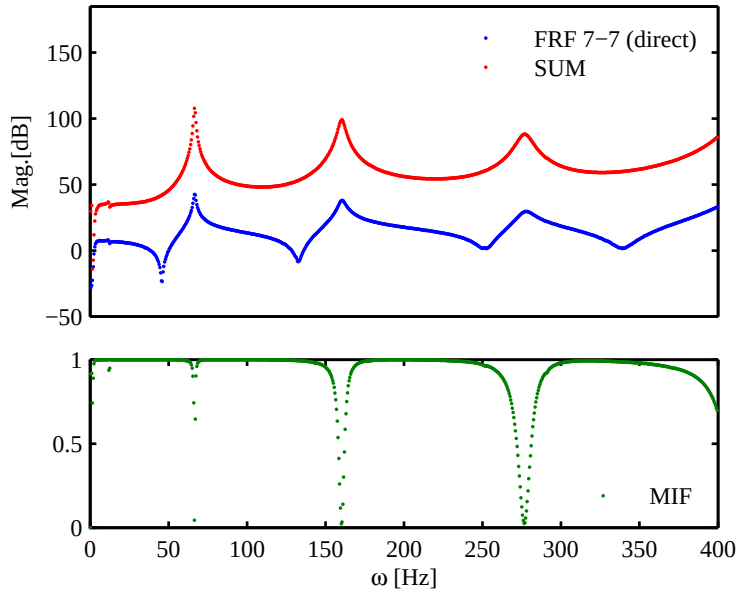


**Figure 4.39:** SUM and MIF of Beam 6 test sample.

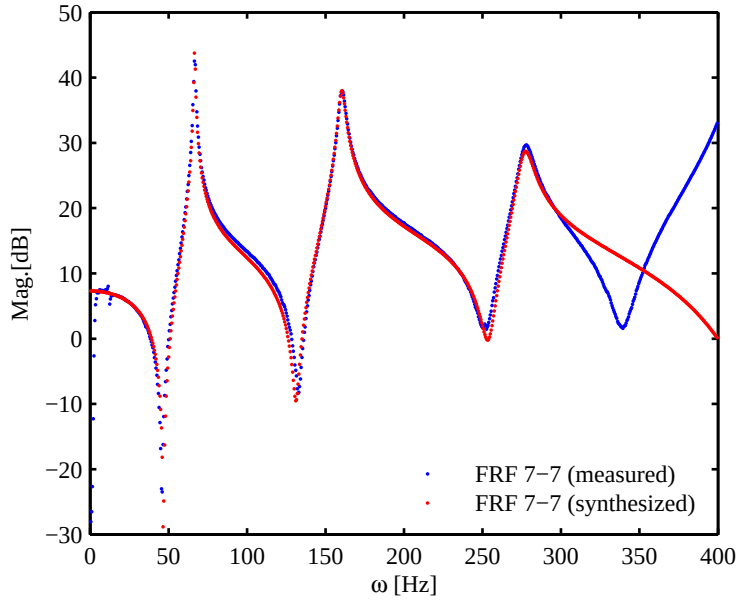


**Figure 4.40:** Synthesized and measured FRFs of Beam 6 test sample.

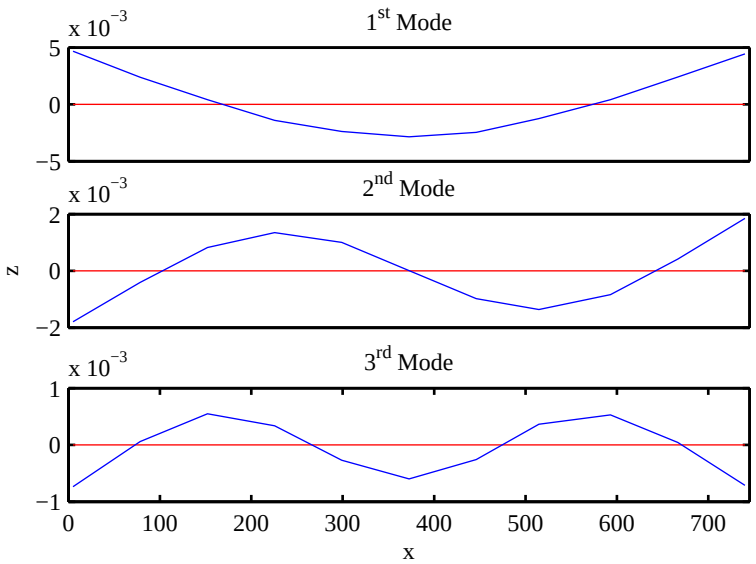


**Figure 4.41:** Estimated mode shapes of Beam 6 test sample.

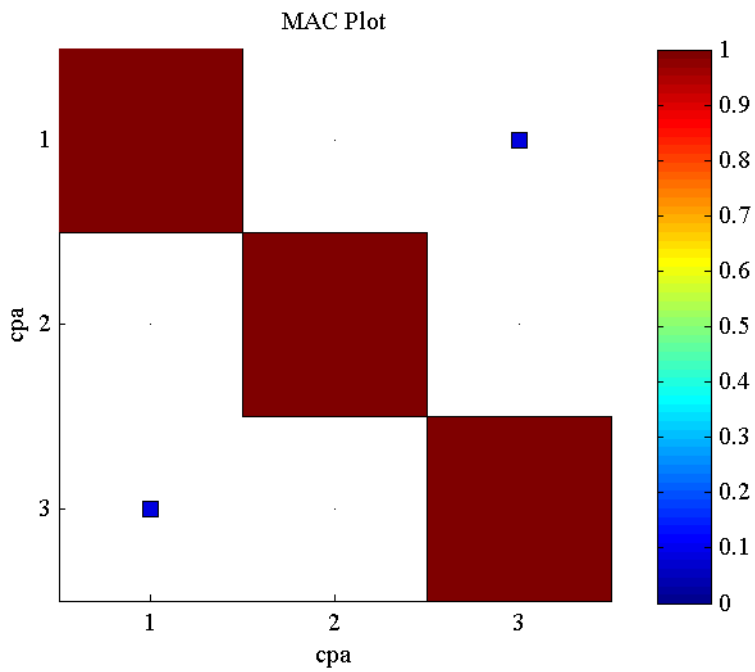


**Figure 4.42:** MAC plot for Beam 6 test sample.

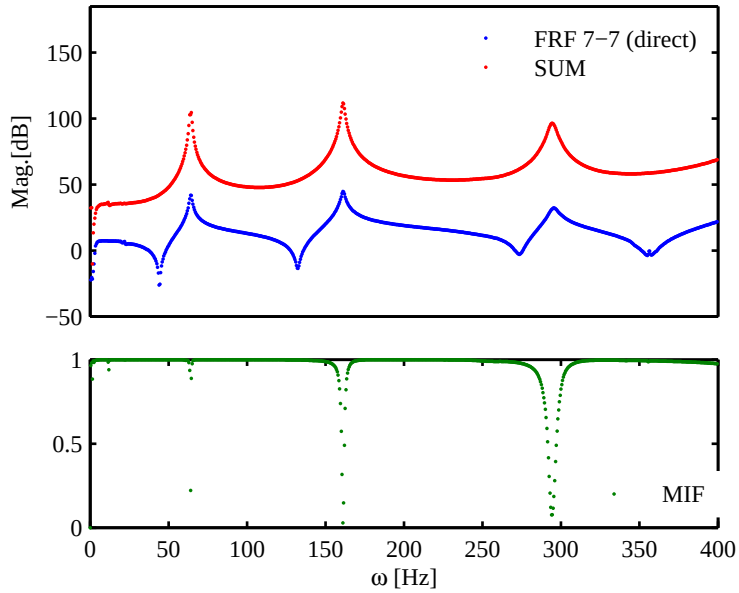


**Figure 4.43:** SUM and MIF of Beam 7 test sample.

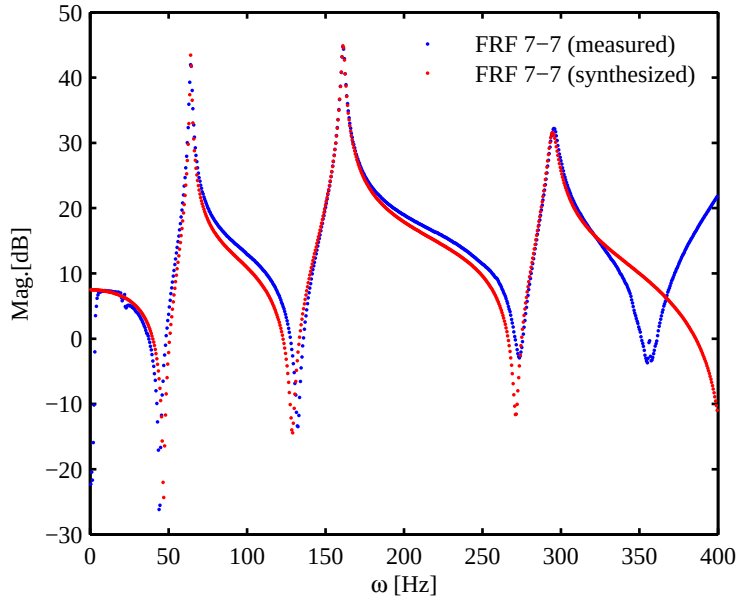


**Figure 4.44:** Synthesized and measured FRFs of Beam 7 test sample.

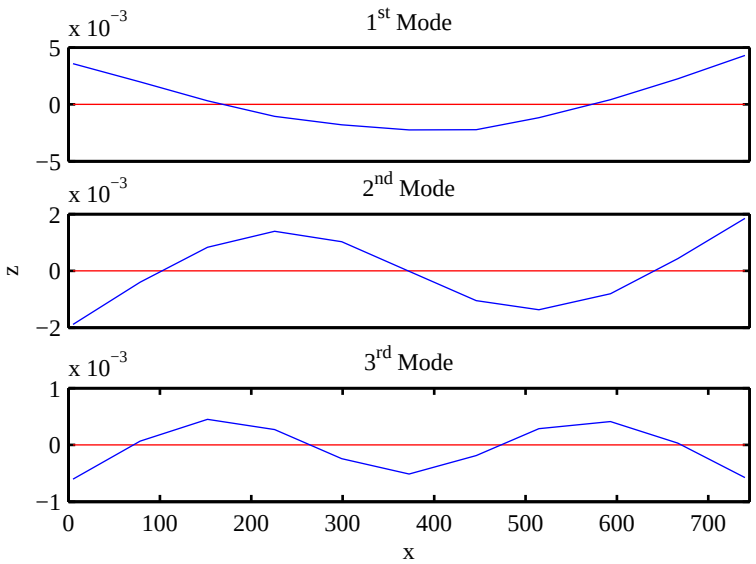


**Figure 4.45:** Estimated mode shapes of Beam 7 test sample.

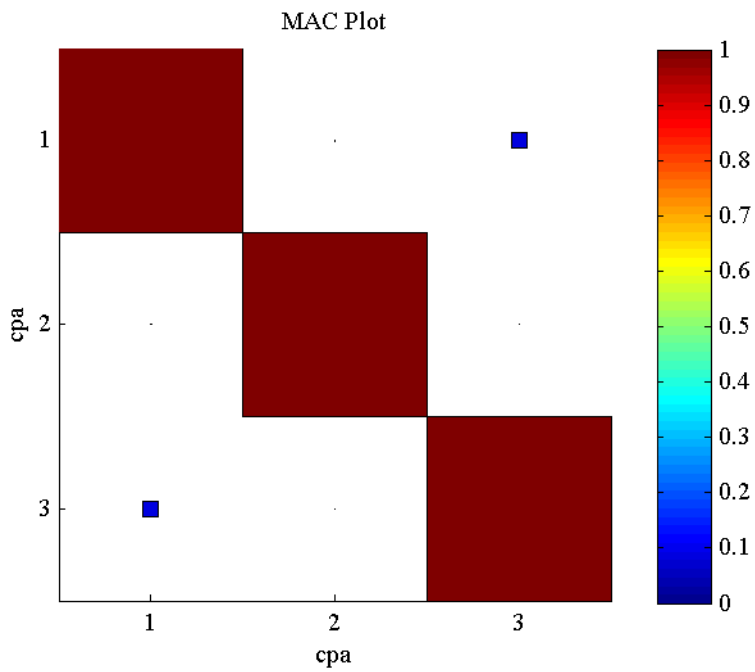


**Figure 4.46:** MAC plot for Beam 7 test sample.

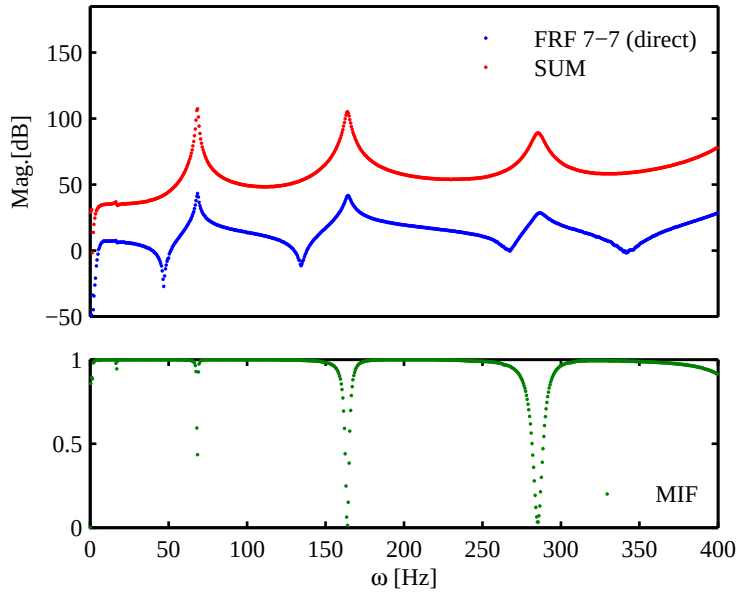


**Figure 4.47:** SUM and MIF of Beam 8 test sample.

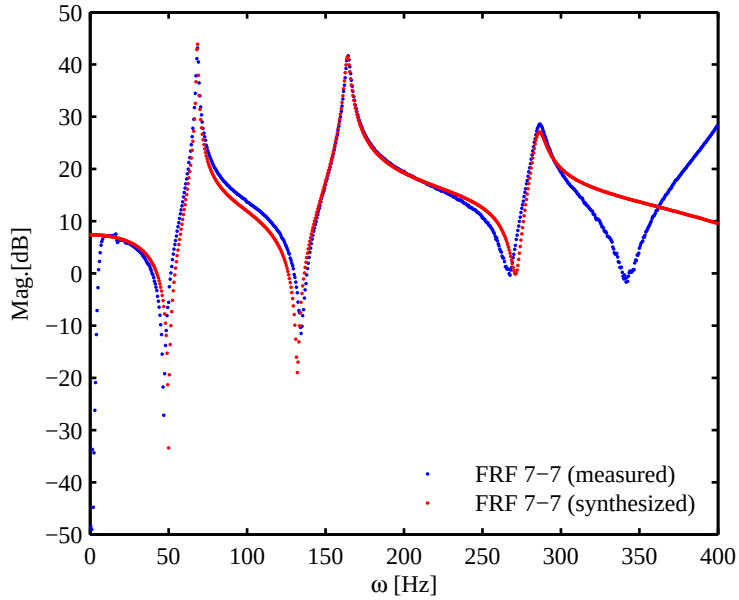


**Figure 4.48:** Synthesized and measured FRF of Beam 8 test sample.

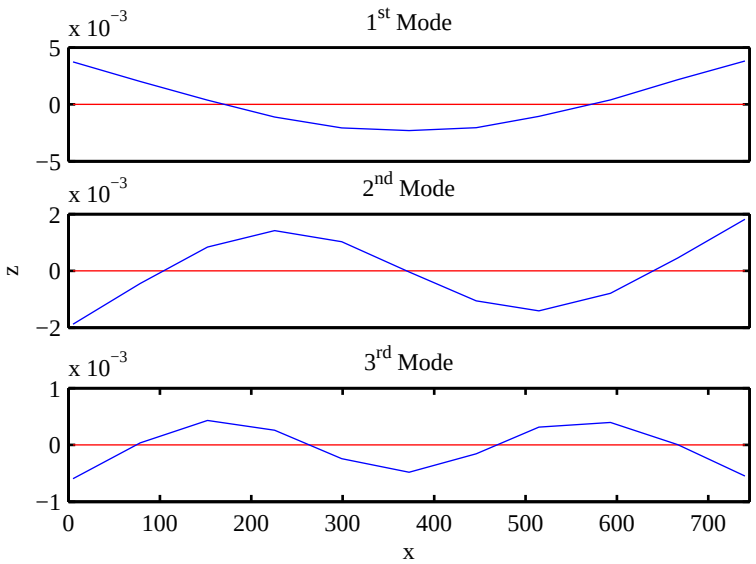


**Figure 4.49:** Estimated mode shapes of Beam 8 test sample.

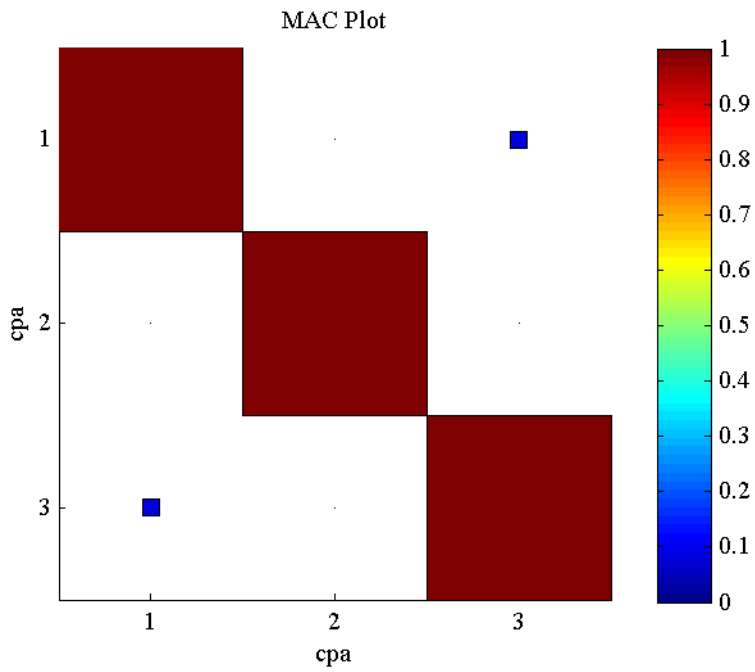


**Figure 4.50:** MAC plot for Beam 8 test sample.

## 4.5 Discussion of modal identification results

From the above presented results of the modal identification it can generally be said that, for all test samples:

- three modes were clearly identified by both MIF and SUM functions;
- the synthesized driving point FRF shows a good accordance with the measured one, which validates the identification procedure;
- the identified mode shapes are the ones expected in a free-free boundary conditions beam;
- the MAC matrix shows a perfectly uncoupling between modes, which also validates the identification procedure.

In order to further analyze the experimental results obtained from modal identification, a comparison between the natural frequencies and loss factors obtained for each test sample was made and is presented in the next section.

### 4.5.1 Comparison of natural frequencies and loss factors

The experimental analysis has been made for eight different test samples in the frequency range between 0 Hz and 400 Hz. The obtained natural frequencies and loss factors are summarized in table 4.2 and table 4.3.

**Table 4.2:** Natural frequencies of all test samples.

| Sample Name | Natural Frequencies [Hz] | | |
|---|---|---|---|
| | $1^{st}$ mode | $2^{nd}$ mode | $3^{rd}$ mode |
| Beam 0 | 54.283 | 149.727 | 289.839 |
| Beam 1 | 63.230 | 160.035 | 287.706 |
| Beam 2 | 66.320 | 162.579 | 281.631 |
| Beam 3 | 62.766 | 164.376 | 302.152 |
| Beam 4 | 65.945 | 161.145 | 279.433 |
| Beam 5 | 61.756 | 154.994 | 270.455 |
| Beam 6 | 66.585 | 160.279 | 276.770 |
| Beam 7 | 64.170 | 161.157 | 294.424 |
| Beam 8 | 68.281 | 163.914 | 285.393 |

**Table 4.3:** Loss factors of all test samples.

| Sample Name | Loss Factor $\eta$[%] | | |
|---|---|---|---|
| | $1^{st}$ mode | $2^{nd}$ mode | $3^{rd}$ mode |
| Beam 0 | 0.22 | 0.08 | 0.02 |
| Beam 1 | 0.62 | 1.46 | 2.26 |
| Beam 2 | 1.34 | 2.36 | 3.58 |
| Beam 3 | 0.18 | 0.88 | 1.40 |
| Beam 4 | 1.38 | 2.28 | 3.16 |
| Beam 5 | 1.12 | 1.94 | 2.90 |
| Beam 6 | 1.32 | 2.50 | 3.36 |
| Beam 7 | 1.08 | 1.20 | 1.82 |
| Beam 8 | 0.94 | 1.84 | 2.62 |

In order to clearly visualize the differences between natural frequencies and loss factors of the test samples, these are represented in bar plots in figure 4.51 and figure 4.52.

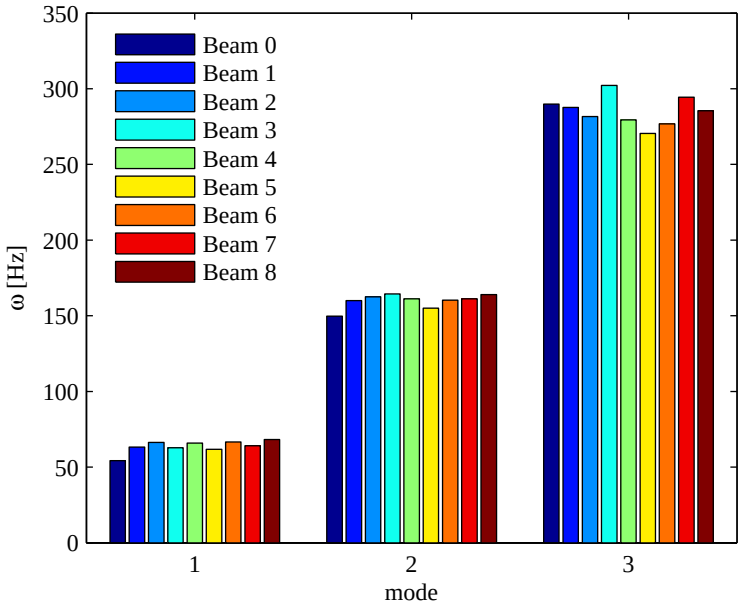


**Figure 4.51:** Natural frequencies of all test samples.

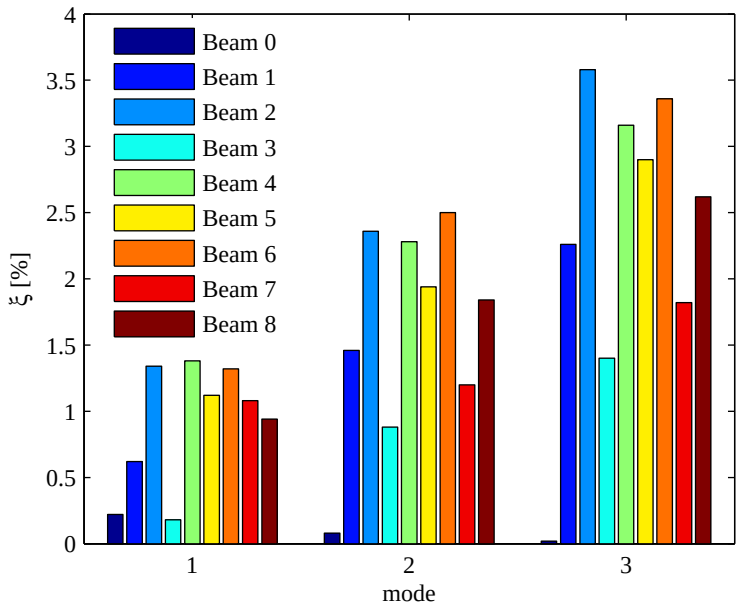


**Figure 4.52:** Loss factors of all test samples.

### 4.5.2 Conclusion

From the schematized results shown in figure 4.51 and figure 4.52, it is possible to conclude that:

- the introduction of the cork compound enlarges the structure damping property; that effect can be seen comparing Beam 0, which has no cork compound core, to the other test samples;
- the differences between the natural frequencies, from one test sample to another, are smaller than the differences obtained for the loss factors; therefore, the cork compound core influences more the structure damping performance than the other mechanical properties of the structure, namely the stiffness and mass;
- in all the test samples, the higher the mode, the bigger the loss factor is, showing the viscoelastic behaviour of the cork compound;
- comparing Beam 1 to Beam 2, which have the same cork compound core type but with different thicknesses, it is possible to see that the loss factor of Beam 2 is bigger than the one from Beam 1. The same effect is verified when comparing Beam 3 to Beam 4, Beam 5 to Beam 6 and Beam 7 to Beam 8, allowing to conclude that the bigger the cork compound thickness is, the bigger the loss factor will be;
- the cork compound cores with small grain and high density (8123 and 8303) like the ones used in Beam 1, Beam 2, Beam 5 and Beam 6 present a loss factor bigger than the loss factors obtained for Beam 2, Beam 4, Beam 7 and Beam 8 which cork compounds were small grain and low density ones (8003 and 8002).

# Chapter 5

# Sandwich Beams with Cork Compound Cores: Numerical Results

## 5.1 Introduction

This chapter is devoted to the validation of the developed multilayer beam finite element. Firstly, a comparison between analytical results from the *Euler-Bernoulli* beam theory and numerical results obtained with the developed finite element is done. Afterwords, a comparison between experimental results obtained in chapter 4 and the finite element results for the same sandwich beams is presented and some conclusions are drawn.

## 5.2 Multilayer beam element validation

Element validation is an important step in formulating a new element because it assures the element efficiency and shows how physically representative the element is. In order to validate the beam element formulated in chapter 3, a single layer beam was analysed and the obtained mode shapes and natural frequencies were compared with the analytical ones obtained by *Euler-Bernoulli* theory.

### 5.2.1 Natural frequencies and mode shapes analysis of a single layer beam

The most simple test to immediately verify the representativity of a finite element is using it to simulate a simple beam structure with different boundary conditions and compare the results obtained, namely natural frequencies and mode shapes, with the well described analytical ones. Therefore, a simple aluminum beam with properties and geometric characteristics presented in table 5.1 was simulated with a finite element model which characteristics are described in the same table, using the formulated beam element in a single layer configuration for different boundary conditions.

**Table 5.1:** Characteristics of the aluminum beam.

| Aluminum properties | | Beam geometry | | FE model | |
|---|---|---|---|---|---|
| *Young's* modulus | $E = 69.5$ GPa | Thickness | $h = 3$ mm | $N^{br}$ of elements | 20 |
| *Poisson's* ratio | $\nu = 0.3$ | Width | $b = 40$ mm | $N^{br}$ of layers | 1 |
| | | Length | $\ell = 745$ mm | | |

In table 5.2 the first four natural frequencies of the aluminum beam are presented, computed using the formulated element, for three different boundary conditions: free-free, simply supported and clamped-free beam boundaries. The computed natural frequencies (table 5.2) using the formulated beam element can also be compared to the ones computed analytically [44, 45], allowing to verify the validity of the approximation using the formulated element.

**Table 5.2:** Natural frequencies [Hz] of the beam for different boundary conditions.

| | Free-Free | | Simply Supported | | Clamped-Free | |
|---|---|---|---|---|---|---|
| Mode | FEM | Analytic | FEM | Analytic | FEM | Analytic |
| 1 | 28.2431 | 27.9273 | 12.4502 | 12.4121 | 4.4231 | 3.103 |
| 2 | 78.667 | 77.5757 | 50.2621 | 49.6485 | 27.8795 | 27.9273 |
| 3 | 156.7607 | 152.0484 | 114.8533 | 111.709 | 78.9584 | 77.5757 |
| 4 | 265.063 | 251.3453 | 208.7034 | 198.5938 | 157.5216 | 152.0484 |

Additionally, the first three mode shapes of the referred aluminum beam were predicted with the formulated element. Figure 5.1 depicts the first three mode shapes of the beam with free-free boundary conditions, figure 5.2 depict the same mode shapes for the same beam with simply supported boundary conditions and in figure 5.3 are represented the first three mode shapes for the clamped-free boundary conditions. For the different boundary conditions the computed mode shapes reproduce the ones predicted analytically in the literature [45].

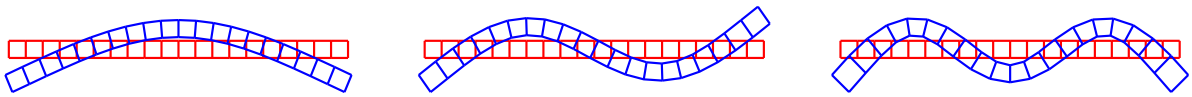

**(a)** $1^{st}$ mode. **(b)** $2^{nd}$ mode. **(c)** $3^{rd}$ mode.

**Figure 5.1:** Aluminum beam predicted mode shapes with free-free boundaries.

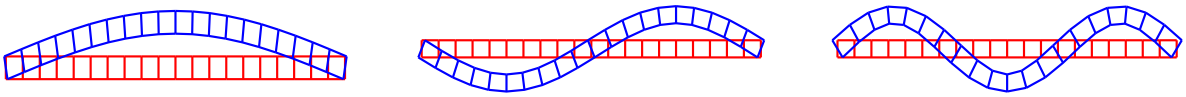

**(a)** $1^{st}$ mode. **(b)** $2^{nd}$ mode. **(c)** $3^{rd}$ mode.

**Figure 5.2:** Aluminum beam predicted mode shapes with simply supported boundaries.

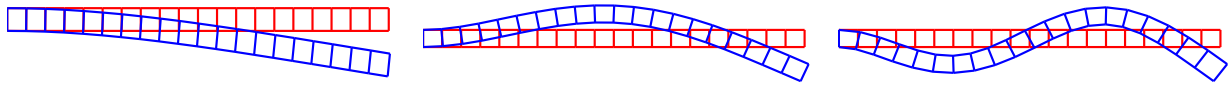

**(a)** $1^{st}$ mode. **(b)** $2^{nd}$ mode. **(c)** $3^{rd}$ mode.

**Figure 5.3:** Aluminum beam predicted mode shapes with clamped-free boundaries.

### 5.2.2 Convergence analysis

Another test was to compare the natural frequencies, obtained using the formulated beam element with different mesh sizes and number of layers, for a beam with free boundary conditions, made out of aluminum with physical properties and geometry identical to the ones referred in table 5.1. The natural frequencies were therefore computed with the formulated beam element in a 1 layer, 2 layers, 3 layers and 6 layers configuration, maintaining the beam thickness (all layers have the same thickness) and using different mesh sizes from 11 elements to 500 elements in the mesh.

The obtained results are graphically represented in figure 5.4 in which the convergence of results to the analytical solution, for the first three natural frequencies, is notorious with the mesh refinement.

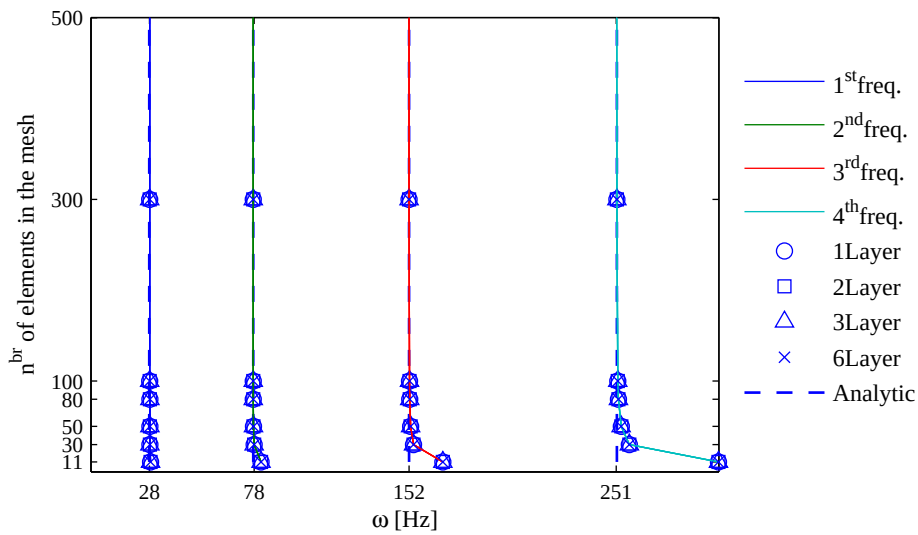


**Figure 5.4:** Element convergence with mesh refinement and layer refinement.

The convergence of results with the previously explained layer refinement cannot be seen from figure 5.4. Therefore in table 5.3 the values obtained for the natural frequencies are presented for three particular mesh sizes, with 11 elements, 30 element and 100 elements, using the formulated beam element in a 1 layer, 2 layers and 3 layers configuration.

**Table 5.3:** Natural frequencies [Hz] of the beam for different meshes and number of layers.

| Mode | Analytic | FEM (11 elements) | | | |
|---|---|---|---|---|---|
| | | 1 layer | 2 layers | 3 layers | 6 layers |
| 1 | 27.9273 | 28.48865 | 28.48865 | 28.48859 | 28.48855 |
| 2 | 77.5757 | 81.26400 | 81.26400 | 81.26333 | 81.26283 |
| 3 | 152.0484 | 168.15980 | 168.15980 | 168.15661 | 168.15422 |
| Mode | Analytic | FEM (30 elements) | | | |
| | | 1 layer | 2 layers | 3 layers | 6 layers |
| 1 | 27.9273 | 28.18332 | 28.18332 | 28.18326 | 28.18321 |
| 2 | 77.5757 | 78.04486 | 78.04486 | 78.04424 | 78.04377 |
| 3 | 152.0484 | 154.10309 | 154.10309 | 154.10042 | 154.09841 |
| Mode | Analytic | FEM (100 elements) | | | |
| | | 1 layer | 2 layers | 3 layers | 6 layers |
| 1 | 27.9273 | 28.13964 | 28.13964 | 28.13958 | 28.13954 |
| 2 | 77.5757 | 77.59301 | 77.59301 | 77.59239 | 77.59193 |
| 3 | 152.0484 | 152.19168 | 152.19168 | 152.18907 | 152.18711 |

Additionally, a comparison between two integration methods using the finite element method was made. In the symbolic type of integration, a symbolic integration of the membrane, bending and shear components has been made using the Matlab® Symbolic Toolbox. On the other hand, the numerical integration has been made using the Gauss integration method with just 1 integration point to integrate the shear component of the stiffness matrix, while using 2 integration points to integrate the membrane and bending components of the stiffness matrix.

The first three natural frequencies were computed for three different beam lengths such as $\ell = 7.45$ mm, $\ell = 74.5$ mm and $\ell = 745$ mm all with thickness $e = 3$ mm and made of aluminum with the same physical properties as the ones described in table 5.1. For all different lengths a constant number of 50 elements was used. The results for the natural frequencies of the two integration methods, in order to the aspect ratio $\lambda = \frac{e}{\ell}$ are depicted in figure 5.5 and described in table 5.4.

**Table 5.4:** Natural frequencies [Hz] for different aspect ratios and integration types.

| Mode | Aspect ratio $\lambda$ | | | | | |
|---|---|---|---|---|---|---|
| | 1/250 | | 1/25 | | 1/2.5 | |
| | Numeric | Symbolic | Numeric | Symbolic | Numeric | Symbolic |
| 1 | 28.15261 | 91.15236 | 2800.075 | 2929.305 | 201150.540 | 201230.891 |
| 2 | 77.72698 | 251.52230 | 7656.862 | 8005.952 | 339932.685 | 339932.685 |
| 3 | 152.75672 | 493.87939 | 14843.639 | 15508.059 | 392708.256 | 392808.375 |

From the results presented in table 5.4 and depicted in figure 5.5, it is possible to identify that the shear locking phenomena can be avoided using a reduced numerical integration for the shear component of the stiffness matrix. As the beam gets thiner, the shear energy is not accurately described when the symbolic integration method of the shape functions is used. Meanwhile, when using the Gauss integration method reduced to 1 integration point for the shear component of the stiffness matrix, a more realistic solution is obtained. Therefore, for

all the numerical solutions obtained with FEM, from now on, are all obtained using reduced integration of the shear stiffness matrix.

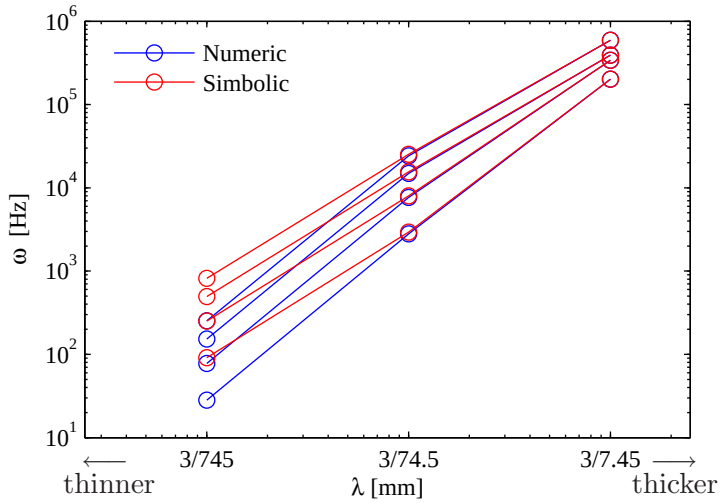


**Figure 5.5:** Element test for shear locking phenomena.

## 5.3 Numerical simulation of experimental tests

For the numerical simulation, the beam element formulated in chapter 3 was included in a finite element routine, written in Matlab® programming language. In this section, the numerical simulation of the sandwich beams with cork compound cores, analysed in chapter 4, which geometry is recalled in figure 5.6, is performed and the comparison of the obtained numerical results with the measured experimentally is made.

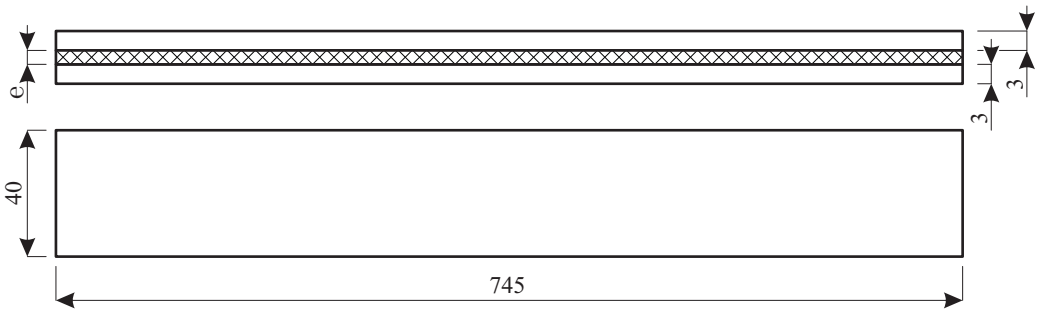


**Figure 5.6:** Beams measurement mesh.

In the experimental tests, the frequency response functions obtained were accelerances and were measured at several points of the sandwich beams. In figure 5.7 the measuring mesh of the test samples, also previously described in chapter 4, is now recalled.

The excitation force was applied at point number 7, and the FRFs were measured for all 11 points. In this section, a comparison has been made between the direct FRF (obtained at

the excitation point) measured experimentally and the one obtained using the finite element method with the layerwise beam element previously formulated in chapter 3.

To obtain the direct FRF, the sandwich beams with 745 mm length were divided into 149 elements, allowing node number 91 to be placed at the location of point 7, approximately 446 mm from the left side of the test sample as shown in figure 5.7.

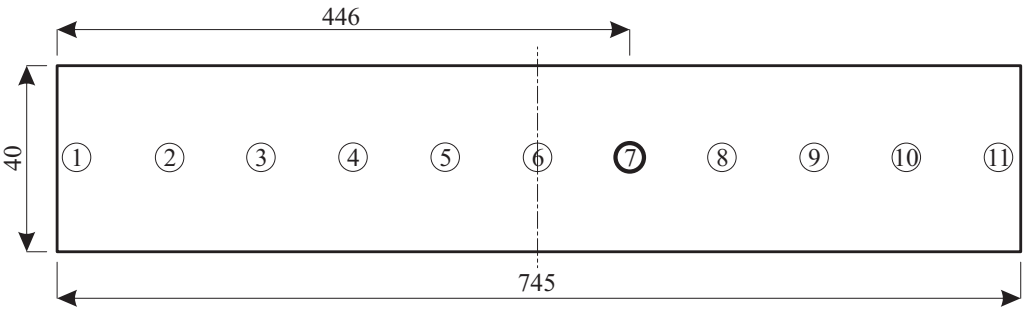


**Figure 5.7:** Beams measurement mesh.

For the sandwich beams cores, the cork compounds dynamic properties identified in chapter 2 were introduced in the finite element model through the complex modulus and the predicted FRFs were generated according to direct frequency analysis procedure described in chapter 3.

**Table 5.5:** Beam test samples description (summary of table 4.1, chapter 4).

| Sample Name | Cork Compound Core Ref. (Chap. 2) | Shear test sample Ref. (Chap. 2) | Core Thickness [mm] | Plies Material and Properties |
|---|---|---|---|---|
| Beam 0 | - | - | - | |
| Beam 1 | 8123 | P1 | 0.8 | For all Beams, |
| Beam 2 | 8123 | P1 | 1.2 | Aluminum Plies |
| Beam 3 | 8003 | P2 | 0.8 | $E = 69.5$ GPa |
| Beam 4 | 8003 | P2 | 1.2 | $\mu = 0.3$ |
| Beam 5 | 8303 | P3 | 0.8 | $\rho = 2700$ Kg/m$^3$ |
| Beam 6 | 8303 | P3 | 1.2 | |

In the following pages, a comparison between the FEM predicted FRFs and the experimental ones is shown for each test sample.

### 5.3.1 FEM predicted and experimental FRFs

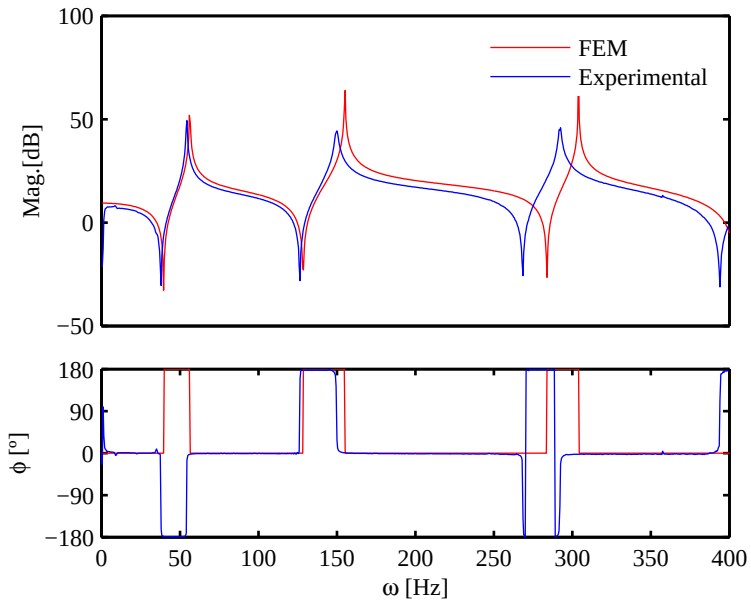


**Figure 5.8:** Comparison between FEM and experimental results of Beam 0.

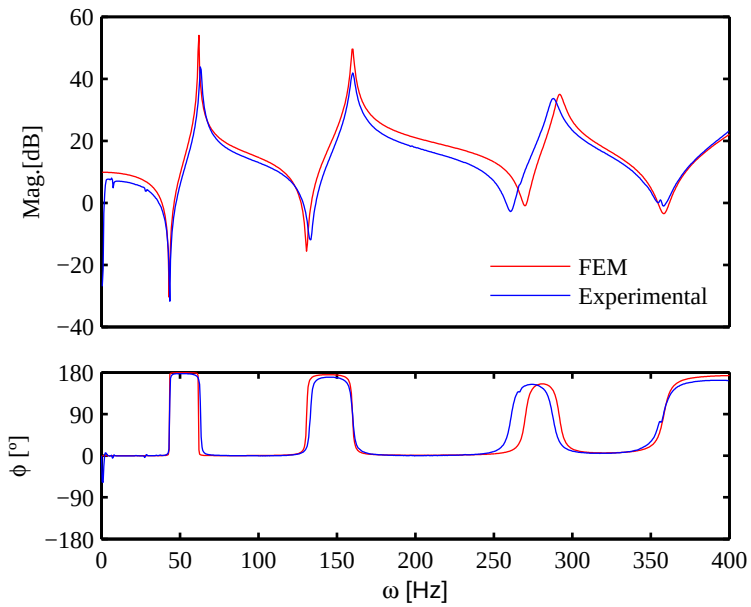


**Figure 5.9:** Comparison between FEM and experimental results of Beam 1.

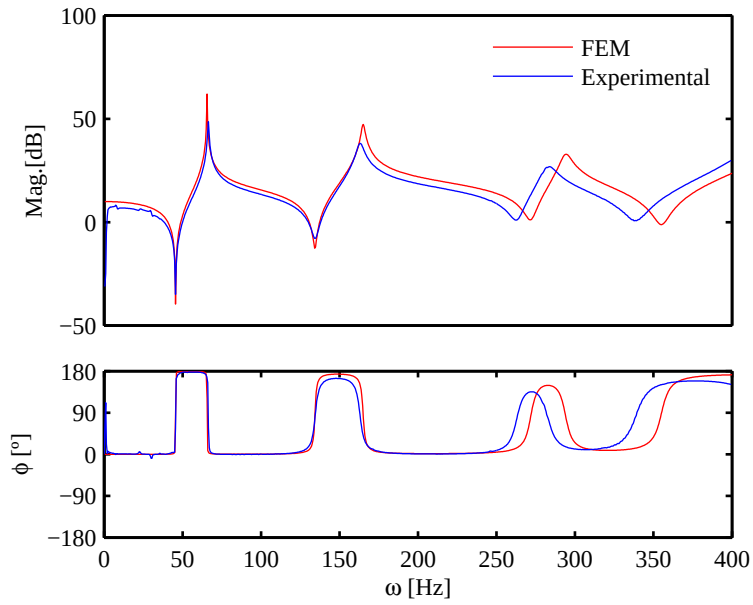


**Figure 5.10:** Comparison between FEM and experimental results of Beam 2.

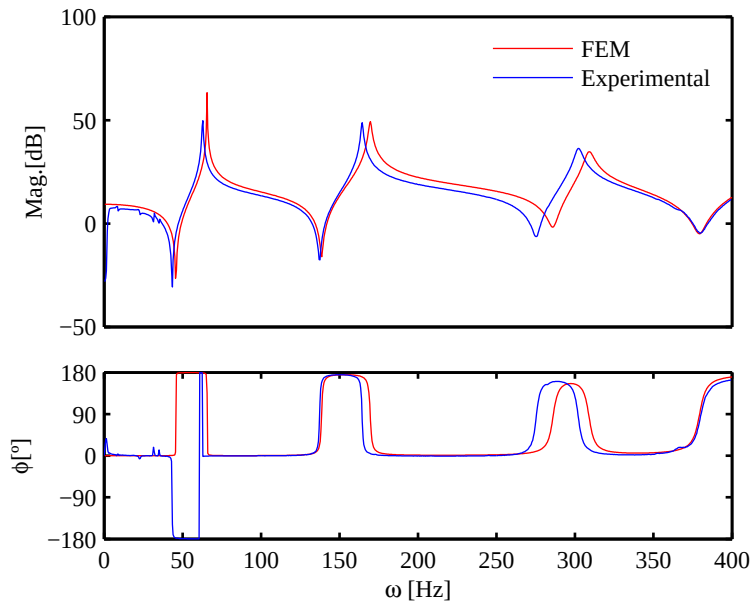


**Figure 5.11:** Comparison between FEM and experimental results of Beam 3.

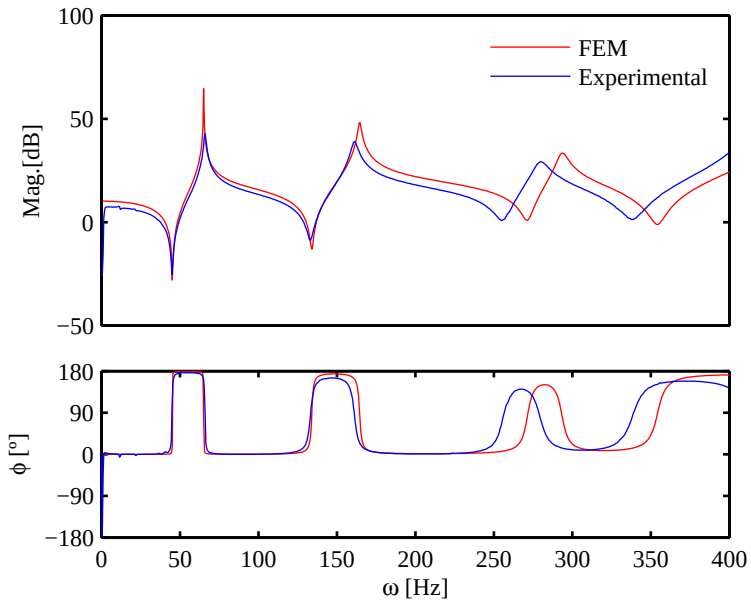


**Figure 5.12:** Comparison between FEM and experimental results of Beam 4.

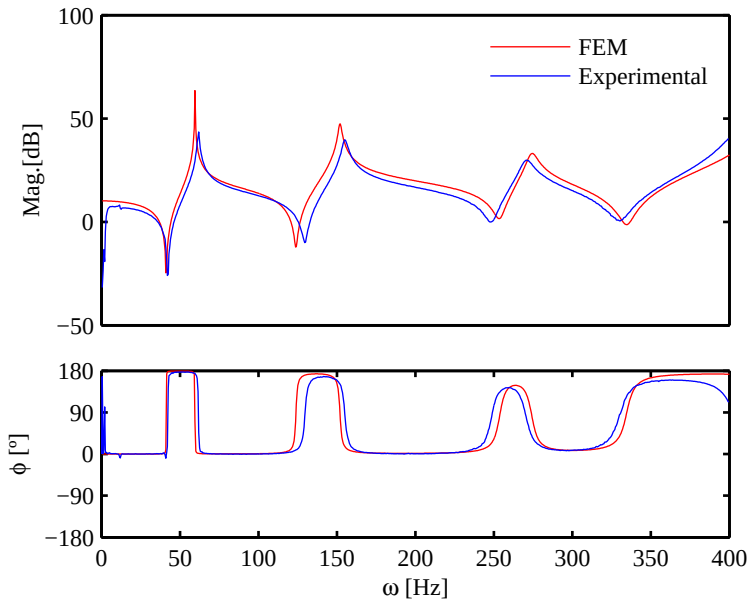


**Figure 5.13:** Comparison between FEM and experimental results of Beam 5.

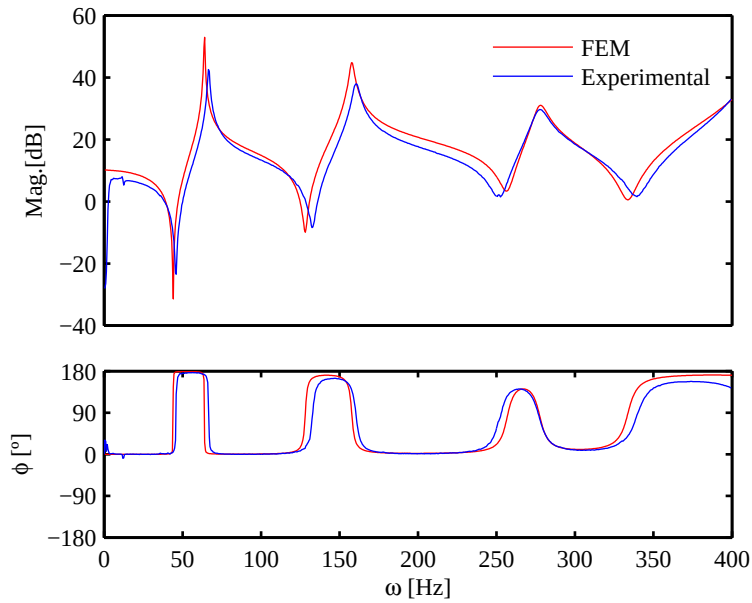


**Figure 5.14:** Comparison between FEM and experimental results of Beam 6.

### 5.3.2 Discussion of the numerical results

As can be seen from figure 5.8 to figure 5.14, for all test samples, the three modes obtained in experimental results were also obtained when simulating the sandwich beams by a finite element model with the developed multilayer beam finite element. It is possible to see that for the first two modes, the FRFs obtained from numerical simulation are very close to the ones obtained experimentally while for the third mode the FRFs obtained numerically present bigger values. The third peak appears at a higher frequency than the verified experimentally, which could be a consequence of incorrect material properties inserted in the finite element method. The natural frequencies, identified as the frequencies for which peak values occur (peak-picking), of the measured and predicted FRFs, presented in table 5.6, also reveal the referred accordance between numerical and experimental results, which has been previously verified by a simple visual inspection of the FRF plots.

**Table 5.6:** Natural frequencies [Hz] of the beam test samples.

| | $\omega_1$ | | $\omega_2$ | | $\omega_3$ | |
|---|---|---|---|---|---|---|
| Sample | Experimental | FEM | Experimental | FEM | Experimental | FEM |
| Beam 0 | 54.5 | 56.1 | 150.0 | 155.2 | 292.5 | 303.9 |
| Beam 1 | 63.0 | 62.1 | 160.0 | 160.2 | 288.0 | 291.9 |
| Beam 2 | 66.5 | 65.6 | 163.0 | 165.2 | 284.5 | 294.4 |
| Beam 3 | 63.0 | 65.2 | 164.5 | 169.7 | 302.5 | 308.9 |
| Beam 4 | 66.0 | 65.1 | 161.0 | 164.7 | 279.5 | 293.9 |
| Beam 5 | 62.0 | 59.6 | 155.0 | 152.2 | 271.0 | 273.8 |
| Beam 6 | 66.5 | 53.0 | 161.0 | 157.7 | 278.0 | 277.8 |

It has been remarked in chapter 2 that the cork compound properties vary with frequency

and the identified properties have presented instable values for some measured frequencies. Therefore, an error in the properties identification is most likely the cause of the third mode verified deviation.

The comparison between numerical and experimental results has been hereby made by visual inspection and determination of the FRFs peak values associated to the natural frequencies. However, there are some correlation strategies to quantify the approximation degree of a numerical solution to an experimental measurement, that has not been used.

# Chapter 6

# Layerwise Plate Finite Element

## 6.1 Introduction

In this chapter, a *layerwise* plate finite element is formulated in order to be integrated in a finite element routine and to perform with it simulations of sandwich plates with a cork compound core. The *layerwise* theory hereby used in the plate element formulation is a partial *layerwise* theory in which *layerwise* expansions of the in-plane plate displacements are used, being assured the continuity of displacements in the layer interfaces as depicted in figure 6.1. On what concerns the displacement in the out of plane direction, it is considered to be constant for all layers.

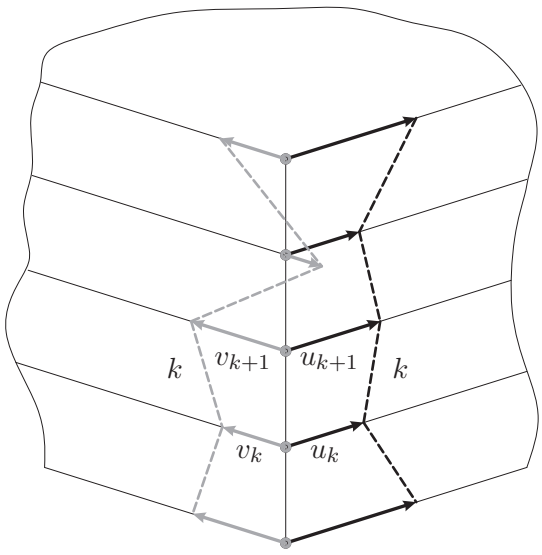


**Figure 6.1:** Plate in-plane displacements based on a partial *layerwise* theory.

From the general domain displacement field defined, the strains and stresses are derived from it. Expressions for the potential and kinetic energy are established and virtual work of the external forces is obtained. To derive the plate finite element equation of motion as well as its mass and stiffness matrices, the Hamilton's principle is used. It is important to mention that the element stiffness matrix is partitioned in its membrane, bending and shear components

allowing to analyze the shear locking phenomena and avoid resultant numerical errors.

## 6.2 Displacement field

Considering a generic layer of a multilayer plate, its displacement field $\{\mathbf{u}\}$ can be described by

$$\{\mathbf{u}\,(x,y,z,t)\} = \left\{ \begin{array}{ccc} u\,(x,y,z,t) & v\,(x,y,z,t) & w\,(x,y,t) \end{array} \right\} \tag{6.1}$$

where $u$ and $v$ represent the plate in-plane displacements and $w$ is the transverse displacement. For the in-plane displacements, considering as degrees of freedom the top and bottom displacements, as depicted in figure 6.2, the displacement field will result in

$$\{\mathbf{u}\} = \left\{ \begin{array}{c} u \\ v \\ w \end{array} \right\} = \left\{ \begin{array}{c} \frac{u_t+u_b}{2} + z\frac{u_t-u_b}{h} \\ \frac{v_t+v_b}{2} + z\frac{v_t-v_b}{h} \\ w \end{array} \right\} \tag{6.2}$$

From equation (6.2) it should be noticed that:

- the condition $w\,(x,y,t) = w$ represents the non-smashing condition of the plate;
- the continuity condition between layers is established directly from the displacements formulation.

The displacements described in 6.2 are represented in figure 6.2

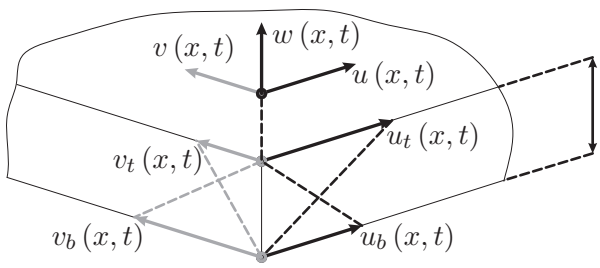


**Figure 6.2:** Plate displacement field.

Therefore, the kinematic model of the generic layer takes into account, besides the kinematic model developed according to the thick plate theory, the displacement field on the interface $\left(z_{k-1} = \frac{1}{2}h_{k-1}\right)$ with the previous layer.

The displacement field from (6.2) can be expressed as a matrix operation:

$$\{\mathbf{u}\} = [\mathcal{N}]\,\{d\} \tag{6.3}$$

where the vector $\{d\}$ is

$$\{d\} = \left\{ \begin{array}{ccccc} w & u_b & v_b & u_t & v_t \end{array} \right\}^T \tag{6.4}$$

representing the generalized displacements vector, and the matrix $[\mathcal{N}]$ is

$$[\mathcal{N}] = \left[ \begin{array}{ccccc} 0 & \left(\frac{1}{2}-\frac{z}{h}\right) & 0 & \left(\frac{1}{2}+\frac{z}{h}\right) & 0 \\ 0 & 0 & \left(\frac{1}{2}-\frac{z}{h}\right) & 0 & \left(\frac{1}{2}+\frac{z}{h}\right) \\ 1 & 0 & 0 & 0 & 0 \end{array} \right] \tag{6.5}$$

## 6.3 Strain field

The strain field $\{\varepsilon\}$ for a generic layer is composed by the strains as follows

$$\{\varepsilon\} = \left\{ \begin{array}{ccccc} \varepsilon_{xx} & \varepsilon_{yy} & \gamma_{xy} & \gamma_{xz} & \gamma_{yz} \end{array} \right\}^T \tag{6.6}$$

which can be defined as

$$\varepsilon_{xx} = \frac{\partial u}{\partial x} \tag{6.7a}$$

$$\varepsilon_{yy} = \frac{\partial v}{\partial y} \tag{6.7b}$$

$$\gamma_{xy} = \frac{\partial u}{\partial y} + \frac{\partial v}{\partial x} \tag{6.7c}$$

$$\gamma_{xz} = \frac{\partial u_k}{\partial z} + \frac{\partial w}{\partial x} \tag{6.7d}$$

$$\gamma_{yz} = \frac{\partial v}{\partial z} + \frac{\partial w}{\partial x} \tag{6.7e}$$

According to the displacements field described by equation (6.2), and expressions (6.7), the strain field $\{\varepsilon\}$ will come as

$$\varepsilon_{xx} = \left(\frac{1}{2} + \frac{z}{h}\right)\frac{\partial u_t}{\partial x} + \left(\frac{1}{2} - \frac{z}{h}\right)\frac{\partial u_b}{\partial x} \tag{6.8a}$$

$$\varepsilon_{yy} = \left(\frac{1}{2} + \frac{z}{h}\right)\frac{\partial v_t}{\partial y} + \left(\frac{1}{2} - \frac{z}{h}\right)\frac{\partial v_b}{\partial y} \tag{6.8b}$$

$$\begin{aligned} \gamma_{xy} \quad = \quad & \left(\frac{1}{2} + \frac{z}{h}\right)\frac{\partial u_t}{\partial y} + \left(\frac{1}{2} - \frac{z}{h}\right)\frac{\partial u_b}{\partial y} \\ & + \left(\frac{1}{2} + \frac{z}{h}\right)\frac{\partial v_t}{\partial x} + \left(\frac{1}{2} - \frac{z}{h}\right)\frac{\partial v_b}{\partial x} \end{aligned} \tag{6.8c}$$

$$\gamma_{xz} = \frac{1}{h}u_t - \frac{1}{h}u_b + \frac{\partial w}{\partial x} \tag{6.8d}$$

$$\gamma_{xz} = \frac{1}{h}v_t - \frac{1}{h}v_b + \frac{\partial w}{\partial y} \tag{6.8e}$$

### 6.3.1 Deformation Matrix

According to equations (6.7), the strain vector $\{\varepsilon\}$ can be obtained from the displacement vector $\{\mathbf{u}\}$, by pre-multiplying it by a matrix of differential operators $[\mathcal{L}]$

$$\{\varepsilon\} = [\mathcal{L}]\,\{\mathbf{u}\} \tag{6.9}$$

where the matrix $[\mathcal{L}]$ is defined as:

$$[\mathcal{L}] = \begin{bmatrix} \frac{\partial}{\partial x} & 0 & 0 \\ 0 & \frac{\partial}{\partial y} & 0 \\ \frac{\partial}{\partial y} & \frac{\partial}{\partial x} & 0 \\ \frac{\partial}{\partial z} & 0 & \frac{\partial}{\partial x} \\ 0 & \frac{\partial}{\partial z} & \frac{\partial}{\partial y} \end{bmatrix} \tag{6.10}$$

According to (6.3), the generic layer displacement field is obtained using the generalized displacement vector $\{d\}$ which contains the plate degrees of freedom. Therefore, the strain field can be directly related to the generalized displacement vector by multiplying it to the deformation matrix $[\mathcal{B}]$

$$\{\varepsilon\} = [\mathcal{B}]\,\{d\} \tag{6.11}$$

being $\{d\}$ the generalized displacements vector previously defined in (6.4).

The deformation matrix can then be obtained through the following matrix multiplication

$$[\mathcal{B}] = [\mathcal{L}]\,[\mathcal{N}] \tag{6.12}$$

which results in

$$[\mathcal{B}] = \begin{bmatrix} 0 & \left(\frac{1}{2} - \frac{z}{h}\right)\frac{\partial}{\partial x} & 0 & \left(\frac{1}{2} + \frac{z}{h}\right)\frac{\partial}{\partial x} & 0 \\ 0 & 0 & \left(\frac{1}{2} - \frac{z}{h}\right)\frac{\partial}{\partial y} & 0 & \left(\frac{1}{2} + \frac{z}{h}\right)\frac{\partial}{\partial y} \\ 0 & \left(\frac{1}{2} - \frac{z}{h}\right)\frac{\partial}{\partial y} & \left(\frac{1}{2} - \frac{z}{h}\right)\frac{\partial}{\partial y} & \left(\frac{1}{2} + \frac{z}{h}\right)\frac{\partial}{\partial x} & \left(\frac{1}{2} + \frac{z}{h}\right)\frac{\partial}{\partial x} \\ \frac{\partial}{\partial x} & -\frac{1}{h} & 0 & \frac{1}{h} & 0 \\ \frac{\partial}{\partial y} & 0 & -\frac{1}{h} & 0 & \frac{1}{h} \end{bmatrix} \tag{6.13}$$

Inspecting expression (6.13), matrix $[\mathcal{B}]$ can be considered to be composed by three sub-matrices as schematically shown bellow

$$[\mathcal{B}] = \begin{bmatrix} [\mathcal{B}]^M + [\mathcal{B}]^B \\ [\mathcal{B}]^S \end{bmatrix} \tag{6.14}$$

where:

- $[\mathcal{B}]^M$, with 1/2 in evidence, is the membrane deformation matrix:

$$[\mathcal{B}]^M = \frac{1}{2}\begin{bmatrix} 0 & \frac{\partial}{\partial x} & 0 & \frac{\partial}{\partial x} & 0 \\ 0 & 0 & \frac{\partial}{\partial y} & 0 & \frac{\partial}{\partial y} \\ 0 & \frac{\partial}{\partial y} & \frac{\partial}{\partial y} & \frac{\partial}{\partial x} & \frac{\partial}{\partial x} \end{bmatrix} \tag{6.15a}$$

- $[\mathcal{B}]^B$, with $z/h$ in evidence, is the bending deformation matrix:

$$[\mathcal{B}]^B = \frac{z}{h}\begin{bmatrix} 0 & -\frac{\partial}{\partial x} & 0 & \frac{\partial}{\partial x} & 0 \\ 0 & 0 & -\frac{\partial}{\partial y} & 0 & \frac{\partial}{\partial y} \\ 0 & -\frac{\partial}{\partial y} & -\frac{\partial}{\partial y} & \frac{\partial}{\partial x} & \frac{\partial}{\partial x} \end{bmatrix} \tag{6.15b}$$

- $[\mathcal{B}]^S$ is the shear deformation matrix:

$$[\mathcal{B}]^S = \begin{bmatrix} \frac{\partial}{\partial x} & -\frac{1}{h} & 0 & \frac{1}{h} & 0 \\ \frac{\partial}{\partial y} & 0 & -\frac{1}{h} & 0 & \frac{1}{h} \end{bmatrix} \tag{6.15c}$$

## 6.4 Stress field

The stress field to which the generic layer is submitted is determined using its strain field, being that relationship the constitutive law of the material. Therefore, and still considering the generic layer, the stress field is described by the vector:

$$\{\sigma\} = \left\{ \begin{array}{ccccc} \sigma_{xx} & \sigma_{yy} & \tau_{xy} & \tau_{xz} & \tau_{yz} \end{array} \right\}^T \tag{6.16}$$

### 6.4.1 Elasticity matrix

The relationship between the strain field (6.6) and the stress field (6.16) can then be obtained using the material constitutive law, which, considering an isotropic material and that the plate deformation takes place on the linear elastic regime of the material, can be described as

$$\{\sigma\} = [\mathcal{D}]\{\varepsilon\} \tag{6.17}$$

where matrix $[\mathcal{D}]$ is defined as

$$[\mathcal{D}] = \begin{bmatrix} [\mathcal{D}]^{MB} & [0] \\ [0] & [\mathcal{D}]^S \end{bmatrix} \tag{6.18}$$

and the sub-matrices $[\mathcal{D}]^{MB}$ and $[\mathcal{D}]^S$ represent respectively the membrane and bending matrix and the shear matrix, which are described bellow

- membrane and bending matrix

$$[\mathcal{D}]^{MB} = \frac{E}{1-\nu^2} \begin{bmatrix} 1 & \nu & 0 \\ \nu & 1 & 0 \\ 0 & 0 & \frac{1-\nu}{2} \end{bmatrix} \tag{6.19a}$$

- shear matrix

$$[\mathcal{D}]^S = \frac{E}{2(1-\nu)} \begin{bmatrix} 1 & 0 \\ 0 & 1 \end{bmatrix} \tag{6.19b}$$

## 6.5 Potential energy

The internal potential strain energy of the system is defined by the integral over the volume as

$$\Pi^P = \frac{1}{2} \int_\Omega \{\varepsilon\}^T \{\sigma\} \, d\Omega \tag{6.20}$$

Replacing the stress vector in (6.20) by (6.17) allows rewriting the equation as

$$\Pi^P = \tfrac{1}{2} \int_{\Omega} \{\varepsilon\}^T [\mathcal{D}] \{\varepsilon\} \, d\Omega \tag{6.21}$$

The volume integral from expression (6.21) can be replaced by a double integral extended to the plate area $A$ and a simple integral extended to the thickness $h_k$, being possible to analytically calculate the last one. Then, expression (6.21) will result in

$$\Pi^P = \frac{1}{2} \int_A \int_z \{\varepsilon\}^T [\mathcal{D}] \{\varepsilon\} \; dz \, dA \tag{6.22}$$

where $A$ is the two dimensional space defined by the coordinates $x, y (A \subset \mathbb{R})$ and $z \in \left[-\frac{h}{2}, \frac{h}{2}\right]$. This manipulation is possible because it has been assumed a constant thickness along $x$ and $y$ directions.

Substituting the relation from (6.11), being $[\mathcal{B}]$ defined as in (6.13), the potential energy (6.22) can be rewritten as

$$\Pi^P = \frac{1}{2} \int_A \int_z \{d\}^T [\mathcal{B}]^T [\mathcal{D}] [\mathcal{B}] \{d\} \; dz \, dA \tag{6.23}$$

As previously described in (6.14), matrix $[\mathcal{B}]$ can be subdivided into $[\mathcal{B}]^M$, $[\mathcal{B}]^B$ and $[\mathcal{B}]^S$ (6.15a)-(6.15c). And matrix $[\mathcal{D}]$ (6.18) can also be subdivided into $[\mathcal{D}]^{MB}$ and $[\mathcal{D}]^S$ given in (6.19a)-(6.19b). Then, according to this, the potential energy integral from (6.23) can be divided into the sum of three components

$$\begin{aligned} \Pi^P \;=\; & \frac{1}{2} \int_A \int_z \{d\}^T \; [\mathcal{B}]^{M\;T} [\mathcal{D}]^{MB} [\mathcal{B}]^M \{d\} \; dz \, dA \\ & + \frac{1}{2} \int_A \int_z \{d\}^T \; [\mathcal{B}]^{B\;T} [\mathcal{D}]^{MB} [\mathcal{B}]^B \{d\} \; dz \, dA \\ & + \frac{1}{2} \int_A \int_z \{d\}^T \; [\mathcal{B}]^{S\;T} [\mathcal{D}]^S [\mathcal{B}]^S \{d\} \; dz \, dA \end{aligned} \tag{6.24}$$

Then, the integrals form (6.24) can be analytically computed in order to $z$, resulting into

$$\begin{aligned} \Pi^P \;=\; & \frac{1}{2} \int_A \{d\}^T \; \left[\hat{\mathcal{B}}\right]^{M\;T} \left[\hat{\mathcal{D}}\right]^M \left[\hat{\mathcal{B}}\right]^M \{d\} \; dA \\ & + \frac{1}{2} \int_A \{d\}_k^T \; \left[\hat{\mathcal{B}}\right]^{B\;T} \left[\hat{\mathcal{D}}\right]^B \left[\hat{\mathcal{B}}\right]^B \{d\} \; dA \\ & + \frac{1}{2} \int_A \{d\}^T \; \left[\hat{\mathcal{B}}\right]^{S\;T} \left[\hat{\mathcal{D}}\right]^S \left[\hat{\mathcal{B}}\right]^S \{d\} \; dA \end{aligned} \tag{6.25}$$

where the new deformation matrices obtained are

- membrane deformation matrix $\left[\hat{\mathcal{B}}\right]^M = 2\left[\mathcal{B}\right]^M$;
- bending deformation matrix $\left[\hat{\mathcal{B}}\right]^B = \frac{h}{z}\left[\mathcal{B}\right]^B$;
- shear deformation matrix $\left[\hat{\mathcal{B}}\right]^S = \left[\mathcal{B}\right]^S$.

And the new elasticity matrices are

- membrane elasticity matrix $\left[\hat{\mathcal{D}}\right]^M = \frac{h}{4}\left[\mathcal{D}\right]^{MB}$;
- bending elasticity matrix $\left[\hat{\mathcal{D}}\right]^B = \frac{h}{12}\left[\mathcal{D}\right]^{MB}$;
- shear elasticity matrix $\left[\hat{\mathcal{D}}\right]^S = h\left[\mathcal{D}\right]^S$.

## 6.6 Velocity field

The velocity field for a generic layer can be obtained by deriving the displacement field from (6.2), in order to time, being obtained

$$\{\dot{\mathbf{u}}\} = \left\{ \begin{array}{c} \dot{u} \\ \dot{v} \\ \dot{w} \end{array} \right\} = \left\{ \begin{array}{c} \frac{\dot{u}_t+\dot{u}_b}{2} + z\frac{\dot{u}_t-\dot{u}_b}{h} \\ \frac{\dot{v}_t+\dot{v}_b}{2} + z\frac{\dot{v}_t-\dot{v}_b}{h} \\ \dot{w} \end{array} \right\} \tag{6.26}$$

Using matrix $[\mathcal{N}]$, which relates the displacement field with the generalized displacements vector $\{d\}$, the velocity field can be obtained as a matrix multiplication

$$\{\dot{\mathbf{u}}\} = [\mathcal{N}]\left\{\dot{d}\right\} \tag{6.27}$$

where $\left\{\dot{d}\right\} = \left\{ \begin{array}{ccccc} \dot{u}_b & \dot{v}_b & \dot{u}_t & \dot{v}_t & \dot{w} \end{array} \right\}$, representing the time derivative of the generalized displacements vector.

## 6.7 Kinetic energy

The system kinetic energy is obtained by computing the following integral

$$\Pi^K = \frac{1}{2}\int_{\Omega} \{\dot{\mathbf{u}}\}^T [\mathcal{J}] \{\dot{\mathbf{u}}\}\, d\Omega \tag{6.28}$$

where $\{\dot{\mathbf{u}}\}$ and $[\mathcal{J}]$ represent, respectively the velocity field and the system inertia matrix.

Similarly to the calculation for the potential energy, the integral (6.28) extended to the domain $\Omega$ can be divided into a double integral extended to the area $A$ and a simple integral extended to the thickness $h$. Therefore, (6.28) can be rewritten into

$$\Pi^K = \frac{1}{2}\int_{A}\int_{z} \{\dot{\mathbf{u}}\}^T [\mathcal{J}] \{\dot{\mathbf{u}}\}\, dzdA \tag{6.29}$$

where the velocity field $\{\dot{\mathbf{u}}\}$ is the one defined in (6.26) and the matrix $[\mathcal{J}]$ is the inertia matrix, being represented by

$$[\mathcal{J}] = \begin{bmatrix} \rho & 0 & 0 \\ 0 & \rho & 0 \\ 0 & 0 & \rho \end{bmatrix} \tag{6.30}$$

with $\rho$ representing the generic layer material density.

Replacing the velocity field into expression (6.29) by its relation with the derivative of the generalized displacements (6.27), the kinetic energy can be rewritten as

$$\Pi^K = \frac{1}{2} \int_A \int_z \left\{\dot{d}\right\}^T [\mathcal{N}]^T [\mathcal{J}] [\mathcal{N}] \left\{\dot{d}\right\} dzdA \tag{6.31}$$

Expression (6.31) can also be rewritten as

$$\Pi^K = \frac{1}{2} \int_A \int_z \left\{\dot{d}\right\}^T [J] \left\{\dot{d}\right\} dzdA \tag{6.32}$$

being the matrix $[J]$ defined by

$$[J] = [\mathcal{N}]^T [\mathcal{J}] [\mathcal{N}] \tag{6.33}$$

Then, analytically computing the integral in order to $z$, the kinetic energy expression can be rewritten as

$$\Pi^K = \frac{1}{2} \int_A \left\{\dot{d}\right\}^T \left[\hat{J}\right] \left\{\dot{d}\right\} dA \tag{6.34}$$

where the modified inertia matrix $\left[\hat{J}\right]$, results from the performed analytical integration within the interval $\left[-\frac{h}{2}, \frac{h}{2}\right]$ and is defined by

$$\left[\hat{J}\right] = \rho h \begin{bmatrix} 1 & 0 & 0 & 0 & 0 \\ 0 & \frac{1}{3} & 0 & \frac{1}{6} & 0 \\ 0 & 0 & \frac{1}{3} & 0 & \frac{1}{6} \\ 0 & \frac{1}{6} & 0 & \frac{1}{3} & 0 \\ 0 & 0 & \frac{1}{6} & 0 & \frac{1}{3} \end{bmatrix} \tag{6.35}$$

## 6.8 Virtual work of surface forces

If the external face layers of the sandwich plates are loaded by a transverse distributed load, $\{q\}$, then the virtual work $\delta W$ done by this external load shall be given by

$$\delta W = \int_S \{\delta d\}^T \{q\} \, dS \tag{6.36}$$

where $S$ is the surface area of the distributed load and $\{\delta d\}$ is the virtual displacement.

## 6.9 Variational formulation

In the derivation of the variational, equivalent to the governing differential equations, as well as the natural boundary conditions, the Hamilton's principle is adopted, being described by

$$\delta \int_{t_1}^{t_2} \left(\Pi^K - \Pi^P\right) dt + \int_{t_1}^{t_2} \delta W dt = 0 \tag{6.37}$$

where $\Pi_n^K$ and $\Pi_n^P$ are, respectively, the kinetic and potential strain energies of the system and $\delta W$ is the virtual work done by the external forces.

Introducing equations (6.25), (6.34) and (6.36) into (6.37) leads to

$$\begin{aligned}\int_{t_1}^{t_2} \Bigg( & \frac{1}{2}\int_A \left\{\delta\dot{d}\right\}^T \left[\hat{J}\right] \left\{\dot{d}\right\} dA - \frac{1}{2}\int_A \{\delta d\}^T \left[\hat{\mathcal{B}}\right]^{M\ T} \left[\hat{\mathcal{D}}\right]^{MB} \left[\hat{\mathcal{B}}\right]^{M} \{d\}\, dA \\ & -\frac{1}{2}\int_A \{\delta d\}^T \left[\hat{\mathcal{B}}\right]^{B\ T} \left[\hat{\mathcal{D}}\right]^{MB} \left[\hat{\mathcal{B}}\right]^{B} \{d\}\, dA - \frac{1}{2}\int_A \{\delta d\}^T \left[\hat{\mathcal{B}}\right]^{S\ T} \left[\hat{\mathcal{D}}\right]^{S} \left[\hat{\mathcal{B}}\right]^{S} \{d\}\, dA \\ & + \int_S \{\delta d\}^T \{q\}\, dS \Bigg) dt = 0\end{aligned} \tag{6.38}$$

Integrating by parts the first component of equation (6.38) will lead into

$$\begin{aligned}\frac{1}{2}\int_A \{\delta d\}^T \left[\hat{J}\right] \left\{\dot{d}\right\} dA\Bigg|_{t_1}^{t_2} - \int_{t_1}^{t_2} \Bigg( & \frac{1}{2}\int_A \{\delta d\}^T \left[\hat{J}\right]_k \left\{\ddot{d}\right\} dA \\ & + \frac{1}{2}\int_A \{\delta d\}^T \left[\hat{\mathcal{B}}\right]^{M\ T} \left[\hat{\mathcal{D}}\right]^{MB} \left[\hat{\mathcal{B}}\right]^{M} \{d\}\, dA + \frac{1}{2}\int_A \{\delta d\}^T \left[\hat{\mathcal{B}}\right]^{B\ T} \left[\hat{\mathcal{D}}\right]^{MB} \left[\hat{\mathcal{B}}\right]^{B} \{d\}\, dA \\ & + \frac{1}{2}\int_A \{\delta d\}^T \left[\hat{\mathcal{B}}\right]^{S\ T} \left[\hat{\mathcal{D}}\right]^{S} \left[\hat{\mathcal{B}}\right]^{S} \{d\}\, dA + \int_S \{\delta d\}^T \{q\}\, dS \Bigg) dt = 0\end{aligned} \tag{6.39}$$

As the first term from equation (6.39) is zero, expression (6.39) will then become

$$\begin{aligned}\int_{t_1}^{t_2} \Bigg( & \frac{1}{2}\int_A \{\delta d\}^T \left[\hat{J}\right] \left\{\ddot{d}\right\} dA + \frac{1}{2}\int_A \{\delta d\}^T \left[\hat{\mathcal{B}}\right]^{M\ T} \left[\hat{\mathcal{D}}\right]^{MB} \left[\hat{\mathcal{B}}\right]^{M} \{d\}\, dA \\ & + \frac{1}{2}\int_A \{\delta d\}^T \left[\hat{\mathcal{B}}\right]^{B\ T} \left[\hat{\mathcal{D}}\right]^{MB} \left[\hat{\mathcal{B}}\right]^{B} \{d\}\, dA + \frac{1}{2}\int_A \{\delta d\}^T \left[\hat{\mathcal{B}}\right]^{S\ T} \left[\hat{\mathcal{D}}\right]^{S} \left[\hat{\mathcal{B}}\right]^{S} \{d\}\, dA \\ & - \int_S \{\delta d\}^T \{q\}\, dS \Bigg) dt = 0\end{aligned} \tag{6.40}$$

Since equation (6.40) must be satisfied for an arbitrary $\{\delta d\}$ within the time interval from $t_1$ to $t_2$, meaning that it must be zero for all kinematic admissible displacement fields with fixes

values at $t_1$ and $t_2$. That can only be verified if the terms integrated in order to time $t$ in expression (6.40) are also zero throughout the time interval. Then, the variational or the weak form of the governing differential equation can be expressed in matrix notation as

$$\begin{aligned}
&\frac{1}{2}\int_A \{\delta d\}^T \left[\hat{J}\right] \left\{\ddot{d}\right\} dA + \frac{1}{2}\int_A \{\delta d\}^T \left[\hat{\mathcal{B}}\right]^{M\ T} \left[\hat{\mathcal{D}}\right]^{MB} \left[\hat{\mathcal{B}}\right]^{M} \{d\}\ dA \\
&\quad + \frac{1}{2}\int_A \{\delta d\}^T \left[\hat{\mathcal{B}}\right]^{B\ T} \left[\hat{\mathcal{D}}\right]^{MB} \left[\hat{\mathcal{B}}\right]^{B} \{d\}\ dA + \frac{1}{2}\int_A \{\delta d\}^T \left[\hat{\mathcal{B}}\right]^{S\ T} \left[\hat{\mathcal{D}}\right]^{S} \left[\hat{\mathcal{B}}\right]^{S} \{d\}\ dA \\
&\quad = \int_S \{\delta d\}^T \{q\}\, dS
\end{aligned} \tag{6.41}$$

Finally, equation (6.41) represents then the variational formulation of the problem equations of motion.

## 6.10 Finite element formulation

The finite element method is a numerical technique to solve problems related to the behavior of physical systems. It is a particularly accurate method for problems with complex and irregular geometries due to the domain discretization into simple and regular subdomains, called finite elements, within which the problem solution becomes more simple.

The finite element formulation more often used in solid mechanics problems acts directly over the displacement field. This is defined inside the finite element by interpolating, using interpolation functions, the values of the dependent variable, which in this case are the components of generalized displacement vector $\{d^e\}$, on the element nodes. Therefore, the problem is reduced to a system of linear equations, where the unknowns are the components of the generalized displacement field.

### 6.10.1 Single layer plate element

The previously established and described formulation, assuming a singe layer plate configuration, is applied, using a 4 node quadrilateral element. The single layer plate finite element has four nodes, having each node five degrees of freedom, two in the x axis direction $u_b$ (on the bottom of the layer) and $u_t$ (on the top of the layer), another two in the y axis direction $v_b$ (on the bottom of the layer) and $v_t$ (on the top of the layer) and one degree of freedom in the z axis direction $w$, as represented in figure 6.3.

The plate element is three dimensional and described in the global cartesian axes $(X, Y, Z)$, being its stiffness and mass matrices computed in the local cartesian axes $(x, y, z)$, where the plane $x-y$ is coplanar with the element face. This element, when described in natural coordinates $(\xi, \eta, \zeta)$, assumes the configuration of a square with two times the unit side length. It is also assumed that the nodes are numbered counterclockwise.

The redefinition of the element in the natural coordinate space simplifies the construction of the interpolation functions as well as the numerical integration processes as, for example, the quadrature *Gauss-Legendre* method.

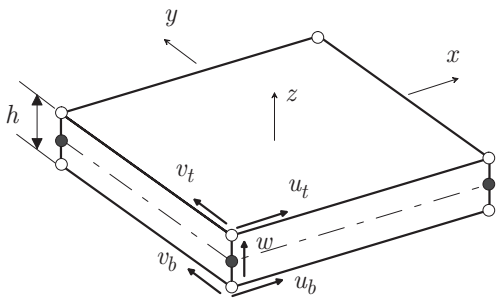


**Figure 6.3:** Single layer plate element displacements.

### Geometric interpolation of the displacement field

The spacial representation of the element in the natural coordinates $(\xi, \eta, \zeta)$ allows a simpler mathematical treatment. However, it is necessary to define a transformation process of the finite element geometry between the cartesian coordinate system $(x, y, z)$ and the natural coordinate system $(\xi, \eta, \zeta)$. This transformation can be done using a geometric approximation, by using the interpolation functions, which allow the calculation of the cartesian coordinates $(x, y)$ of any point within the element from its natural coordinates $(\xi, \eta)$ and the cartesian coordinates of the element nodes

$$x(\xi, \eta) = \sum_{i=1}^{4} N_i(\xi, \eta)\, x_i \tag{6.42a}$$

$$y(\xi, \eta) = \sum_{i=1}^{4} N_i(\xi, \eta)\, y_i \tag{6.42b}$$

where $x_i$ and $y_i$ represent the cartesian coordinates of the element nodes and $N_i(\xi, \eta)$ are the geometric interpolation functions of the finite element, usually known as shape functions.

Besides the element geometry, it is also required an interpolation of the problem variables. That interpolation can be done with the same interpolation functions as the ones used in the geometric interpolation, being therefore the element an isoparametric one. Then, being each node $i$ defined by its nodal coordinates $(x_i, y_i)$ and the respective degrees of freedom vector $\{d_i^e\} = \left\{ \begin{array}{ccccc} w_i & u_{b_i} & v_{b_i} & u_{t_i} & v_{t_i} \end{array} \right\}^T$, then, the generalized displacement vector within the element:

$$\{d\} = \left\{ \begin{array}{ccccc} w & u_b & v_b & u_t & v_t \end{array} \right\}^T \tag{6.43}$$

can be computed from the nodal degrees of freedom by applying interpolation relationships identical to the ones from (6.42), like:

$$\{d\} = \sum_{i=1}^{4} N_i(\xi, \eta)\, \{d^e\} \tag{6.44}$$

where the vector $\{d_i^e\}$ is defined as:

$$\{d^e\} = \left\{ \begin{array}{cccc} \{d_1^e\} & \{d_2^e\} & \{d_3^e\} & \{d_4^e\} \end{array} \right\}^T \tag{6.45}$$

representing the element nodal degrees of freedom.

### Shape function matrix

Then, according to (6.45) and (6.43), expression (6.44) can be expressed in matrix form as

$$\{d\} = [N]\{d^e\} \tag{6.46}$$

where matrix $[N]$, usually called by shape function matrix, is defined as:

$$[N] = \left[\begin{array}{ccc|ccc|ccc|ccc} \ddots & & & \ddots & & & \ddots & & & \ddots & & \\ & N_1 & & & N_2 & & & N_3 & & & N_4 & \\ & & \ddots & & & \ddots & & & \ddots & & & \ddots \end{array}\right] \tag{6.47}$$

### Bilinear shape functions

The shape functions are normally simple polynomial functions, which should satisfy the continuity conditions within the element and allow a correct approximation of the interpolated variable, based on the values that it assumes on the respective nodes. Usually, for a 4 node element, bilinear shape functions are applied like the following

$$N_i = \frac{1}{4}\left(1 + \xi_i\xi\right)\left(1 + \eta_i\eta\right) \tag{6.48}$$

which derivatives in order to $\xi$ and $\eta$ are

$$\frac{\partial N_i}{\partial \xi} = \frac{1}{4}\xi_i\left(1 + \eta_i\eta\right) \tag{6.49a}$$

$$\frac{\partial N_i}{\partial \eta} = \frac{1}{4}\eta_i\left(1 + \xi_i\xi\right) \tag{6.49b}$$

The nodal parameters $\xi_i$ and $\eta_i$ define the shape functions and its derivatives for each one of the element nodes. This parameters are shown in table 6.1.

**Table 6.1:** Nodal parameters of the 4 node quadrilateral element shape functions.

| Node | 1 | 2 | 3 | 4 |
|---|---|---|---|---|
| $\xi_i$ | -1 | 1 | 1 | -1 |
| $\eta_i$ | -1 | -1 | 1 | 1 |

### Biharmonic shape functions

Additionally, a different type of interpolation functions can be used looking forward to obtain better results, therefore, the biharmonic shape functions [9] can be applied, having those the following aspect

$$N_i^{BH} = \left[\frac{1}{2} - \frac{2}{4-\pi}\left[\frac{\pi}{4}\xi_i\xi - cos\left(\frac{\pi}{4}\left(1-\xi_i\xi\right)\right) + sin\left(\frac{\pi}{4}\left(1-\xi_i\xi\right)\right)\right]\right] \times \\ \left[\frac{1}{2} - \frac{2}{4-\pi}\left[\frac{\pi}{4}\eta_i\eta - cos\left(\frac{\pi}{4}\left(1-\eta_i\eta\right)\right) + sin\left(\frac{\eta}{4}\left(1-\eta_i\eta\right)\right)\right]\right] \tag{6.50}$$

where the parameters $\xi_i$ and $\eta_i$ are also given by table 6.1.

This set of interpolation functions is particularly interesting due to having its derivatives null on the element borders.

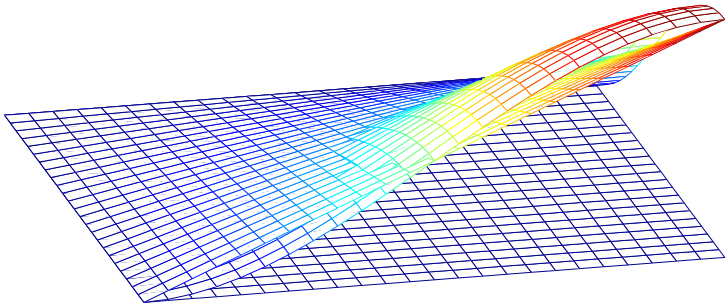

**Figure 6.4:** Comparison between a bilinear and a biharmonic interpolator function.

Figure 6.4 plots a comparison between the bilinear and biharmonic shape functions, showing the weight distribution of both interpolation functions within each element and the derivative continuity of the biharmonic shape function between contiguous elements.

### Weak form finite element discretization

With the relationship between the displacements within the element, with the displacements in the element nodes, is now possible to obtain the weak form of the finite element discretization by introducing the relation from (6.46) into the variational expression from (6.41), being obtained

$$\begin{aligned}
&\frac{1}{2}\int_A \{\delta d^e\}^T [N]^T \left[\hat{J}\right] [N] \left\{\ddot{d}^e\right\} dA \\
&\quad + \frac{1}{2}\int_A \{\delta d^e\}^T [N]^T \left[\hat{\mathcal{B}}\right]^{M\ T} \left[\hat{\mathcal{D}}\right]^{MB} \left[\hat{\mathcal{B}}\right]^{M} [N] \{d^e\}\ dA \\
&\quad + \frac{1}{2}\int_A \{\delta d^e\}^T [N]^T \left[\hat{\mathcal{B}}\right]^{B\ T} \left[\hat{\mathcal{D}}\right]^{MB} \left[\hat{\mathcal{B}}\right]^{B} [N] \{d^e\}\ dA \\
&\quad + \frac{1}{2}\int_A \{\delta d^e\}^T [N]^T \left[\hat{\mathcal{B}}\right]^{S\ T} \left[\hat{\mathcal{D}}\right]^{S} \left[\hat{\mathcal{B}}\right]^{S} [N] \{d^e\}\ dA \\
&\quad = \int_S \{\delta d^e\}^T [N]^T \{q\}\, dS
\end{aligned} \tag{6.51}$$

From equation (6.51), the following definitions can be adopted

- the finite element membrane deformation matrix $[B]^M = \left[\hat{\mathcal{B}}\right]^M [N]$
- the finite element bending deformation matrix $[B]^B = \left[\hat{\mathcal{B}}\right]^B [N]$

- the finite element shear deformation matrix $[B]^S = \left[\hat{\mathcal{B}}\right]^S [N]$

Becoming equation (6.51)

$$\frac{1}{2}\int_A \{\delta d^e\}^T [N]^T \left[\hat{J}\right] [N] \left\{\ddot{d}^e\right\} dA + \frac{1}{2}\int_A \{\delta d^e\}^T \ [B]^{M\ T} \left[\hat{\mathcal{D}}\right]^{MB} [B]^M \{d^e\} \ dA$$
$$+\frac{1}{2}\int_A \{\delta d^e\}^T \ [B]^{B\ T} \left[\hat{\mathcal{D}}\right]^{MB} [B]^B \{d^e\} \ dA + \frac{1}{2}\int_A \{\delta d_i^e\}^T \ [B]^{S\ T} \left[\hat{\mathcal{D}}\right]^S [B]^S \{d^e\} \ dA$$
$$= \int_S \{\delta d^e\}^T [N]^T \{q\} \, dS \tag{6.52}$$

From equation (6.52) it can be defined

- the mass matrix as $[M^e] = \frac{1}{2}\int_A [N]^T \left[\hat{J}\right] [N] \, dA$
- the membrane stiffness matrix $[K^e]^M = \frac{1}{2}\int_A \ [B]^{M\ T} \left[\hat{\mathcal{D}}\right]^{MB} [B]^M \ dA$
- the bending stiffness matrix $[K^e]^B = \frac{1}{2}\int_A \ [B]^{B\ T} \left[\hat{\mathcal{D}}\right]^{MB} [B]^B \ dA$
- the shear stiffness matrix $[K^e]^S = \frac{1}{2}\int_A \ [B]^{S\ T} \left[\hat{\mathcal{D}}\right]^S [B]^S \ dA$
- the nodal forces vector $\{F^e\} = \int_S [N]^T \{q\} \, dS$

Equation (6.52) can then be modified into

$$\{\delta d^e\}^T [M^e] \left\{\ddot{d}^e\right\} + \{\delta d^e\}^T [K^e]^M \{d^e\}$$
$$+ \{\delta d^e\}^T [K^e]^B \{d^e\} + \{\delta d^e\}^T [K^e]^S \{d^e\} = \{\delta d^e\}^T \{F^e\} \tag{6.53}$$

The generic layer stiffness matrix can be defined as the sum of the membrane, bending and shear matrices as

$$[K^e] = [K^e]^M + [K^e]^B + [K^e]^S \tag{6.54}$$

allowing rewritting equation (6.53) as

$$\{\delta d^e\}^T [M^e] \left\{\ddot{d}^e\right\} + \{\delta d^e\}^T [K^e] \{d^e\} = \{\delta d^e\}^T \{F^e\} \tag{6.55}$$

### 6.10.2 Multilayer plate element

To this moment, the finite element formulation has been made considering a generic single layer, ignoring any layers above and below. Let's now say that this generic single layer is the layer number $k$ of a multilayer element and refer to it as generic layer $k$.

With the obtained variational for a generic single layer plate, it is now possible to generalize equation (6.55) to a multilayer configuration plate. Therefore, the next step will be to generalize the expressions for the $k^{th}$ layer. Therefore, equation (6.55) can now be rewritten as

$$\{\delta d^e\}_k^T [M^e]_k \left\{\ddot{d}^e\right\}_k + \{\delta d^e\}_k^T [K^e]_k \{d^e\}_k = \{\delta d^e\}_k^T \{F^e\}_k \tag{6.56}$$

where $k$ respects to the referred generic layer.

As a *layerwise* approximation was assumed for the in-plane plate displacements, the discrete variational statement of equation (6.56) can be generalized for a multilayer plate element with $n$ layers. Therefore, for each generic layer $k$, the displacements (degrees of freedom) can be related to the upper and lower layer displacements as represented in figure 6.5.

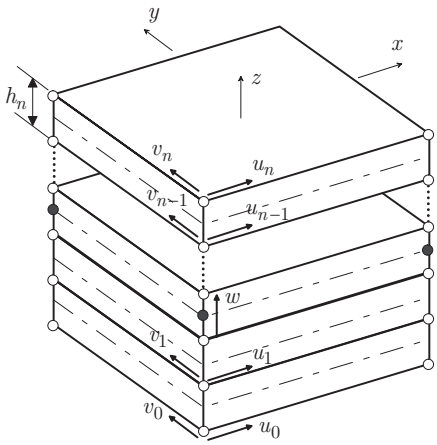


**Figure 6.5:** Plate element layers assembly.

According to figure 6.5, the generalized displacements for a $n$ layer domain can be expressed as

$$\{d\}_n = \left\{ \begin{array}{cccccccccccccccc} w & u_0 & v_0 & u_1 & v_1 & \cdots & u_{k-1} & v_{k-1} & u_k & v_k & \cdots & u_{n-1} & v_{n-1} & u_n & v_n \end{array} \right\}^T \tag{6.57}$$

Then, at element node $i$, the nodal displacement vector will be

$$\{d_i^e\}_n = \left\{ \begin{array}{cccccc} w_i & u_{0_i} & v_{0_i} & u_{1_i} & v_{1_i} & \cdots & u_{n_i} & v_{n_i} \end{array} \right\}^T \tag{6.58}$$

The element displacement vector of all nodes will be

$$\{d^e\}_n = \left\{ \begin{array}{cccc} \{d_1^e\}_n & \{d_2^e\}_n & \{d_3^e\}_n & \{d_4^e\}_n \end{array} \right\}^T \tag{6.59}$$

The generalized element displacements for the $k^{th}$ layer, defined at (6.45), can be derived from the $n$ layer displacements (6.59) by

$$\{d^e\}_k = [L]_k \{d^e\}_n \tag{6.60}$$

where matrix $[L]_k$ represents a location matrix and its given for a $k^{th}$ layer by the composition of four matrices $[L_i]_k$

$$[L]_k = \left[ \begin{array}{cccc} [L_1]_k & [L_2]_k & [L_3]_k & [L_4]_k \end{array} \right] \tag{6.61}$$

being each $[L_i]_k$ matrix described by

$$[L_i]_k = \begin{bmatrix} 1 & 0 & 0 & 0 & 0 & \cdots & 0 & 0 & 0 & 0 & \cdots & 0 & 0 & 0 & 0 \\ 0 & 0 & 0 & 0 & 0 & \cdots & 1 & 0 & 0 & 0 & \cdots & 0 & 0 & 0 & 0 \\ 0 & 0 & 0 & 0 & 0 & \cdots & 0 & 1 & 0 & 0 & \cdots & 0 & 0 & 0 & 0 \\ 0 & 0 & 0 & 0 & 0 & \cdots & 0 & 0 & 1 & 0 & \cdots & 0 & 0 & 0 & 0 \\ 0 & 0 & 0 & 0 & 0 & \cdots & 0 & 0 & 0 & 1 & \cdots & 0 & 0 & 0 & 0 \end{bmatrix} \tag{6.62}$$

Then,expression (6.56) defined for a generic $k^{th}$ layer, can be adapted for an arbitrary number of layers $n$ becoming

$$\begin{aligned} &\{\delta d^e\}_n^T \sum_{k=1}^{n} \left( [L]_k^T [M^e]_k [L]_k \right) \left\{ \ddot{d}^e \right\}_n \\ &\quad + \{\delta d^e\}_n^T \sum_{k=1}^{n} \left( [L]_k^T [K^e]_k [L]_k \right) \{d^e\}_k = \{\delta d^e\}_n^T \sum_{k=1}^{n} \left( [L]_k^T \{F^e\}_k \right) \end{aligned} \tag{6.63}$$

In equation (6.63), it can be seen

- the $n$ layer element mass matrix $\rightarrow [M^e]_n = \sum_{k=1}^{n} \left( [L]_k^T [M^e]_k [L]_k \right)$
- the $n$ layer element stiffness matrix $\rightarrow [K^e]_n = \sum_{k=1}^{n} \left( [L]_k^T [K^e]_k [L]_k \right)$
- the $n$ layer element nodal forces vector $\rightarrow \{F^e\}_n = \sum_{k=1}^{n} \left( [L]_k^T \{F^e\}_k \right)$

Equation (6.63) must be valid for any $\{\delta d_i^e\}_n$, resulting the multilayer element equation of motion

$$[M^e]_n \left\{ \ddot{d}^e \right\}_n + [K^e]_n \{d^e\}_n^T = \{F^e\}_n \tag{6.64}$$

The $n$ layer element is finally formulated, as it has been obtained its equation of motion and described its mass and stiffness matrices as well as its external forces vector.

### 6.10.3 Shear locking problem

While using a 4 node thick plate element using bi-linear interpolation functions, a common numerical problem known as shear locking is verified. This phenomena occurs because the consistent interpolation of the shear strains on the thick plate formulation are not null over the whole element domain when this is submitted to a pure bending state of deformation. Therefore, in this particular situation, the strain energy resultant from the shear strain assumes a more relevant role for the total strain energy than the other plain strain components.

To solve this problem many different solutions were proposed but the one that it is going to be used in the developed element is the the *Mixed Interpolation of Tensorial Components* (*MITC*) for the 4 node plate element. The *MITC* method is based on the correct evaluation of the shear stresses on the central points of the rectilinear sides of the element, represented by the letters A, B, C and D in figure 6.6. This means that a correction of the shear strain deformation matrix $[B]^S$ is performed in order to compute the shear strain at those points (A, B, C and D),

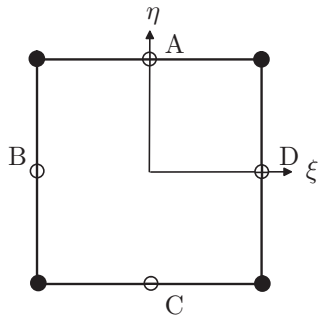


**Figure 6.6:** Element *MITC4*.

which are called *tying points*, instead of using regular sample points for the numeric integration (*Gauss* points). This corrected strain field is then interpolated within the element using a new set of interpolation functions used according to the coordinates of the tying points.

Considering the formulated 4 node plate element over its natural coordinates ($\xi$,$\eta$), the shear strain can be evaluated at any point within the element domain with a linear interpolation between the points A, B, C and D such as

$$\gamma\xi\zeta_k = N_i^A \gamma\xi\zeta_k^A + N_i^C \gamma\xi\zeta_k^C \tag{6.65a}$$

$$\gamma\eta\zeta_k = N_i^D \gamma\eta\zeta_k^D + N_i^B \gamma\eta\zeta_k^B \tag{6.65b}$$

where the interpolation functions are defined as:

$$\begin{aligned} N_i^A &= \frac{1+\eta}{2} \qquad & N_i^B &= \frac{1-\xi}{2} \\ N_i^C &= \frac{1-\eta}{2} \qquad & N_i^D &= \frac{1+\xi}{2} \end{aligned} \tag{6.66}$$

The shear strain vectors in A, B, C and D can then be computed using the interpolation functions $N_i$ from equation (6.48). Therefore, the shear strain $\gamma\xi\zeta_k$ are as follows

$$\gamma\xi\zeta_k = \sum_{i=1}^{4} \frac{\partial N_i}{\partial \xi} w_i + \sum_{i=1}^{4} N_i \frac{u_{t\,ki}^{\xi}}{h_k} - \sum_{i=1}^{4} N_i \frac{u_{b\,ki}^{\xi}}{h_k} \tag{6.67}$$

For point A ($\xi = 0$, $\eta = -1$), the shear strain vector is defined by

$$\gamma\xi\zeta_k^A = \sum_{i=1}^{4} \frac{1}{4}\xi_i \left(1+\eta_i\right) w_i + \sum_{i=1}^{4} \frac{1}{4}\left(1+\eta_i\right) \frac{u_{t\,ki}^{\xi}}{h_k} - \sum_{i=1}^{4} \frac{1}{4}\left(1+\eta_i\right) \frac{u_{b\,ki}^{\xi}}{h_k} \tag{6.68}$$

to point C ($\xi = 0$, $\eta = 1$), the shear strain deformation vector is given by:

$$\gamma\xi\zeta_k^C = \sum_{i=1}^{4} \frac{1}{4}\xi_i \left(1-\eta_i\right) w_i + \sum_{i=1}^{4} \frac{1}{4}\left(1-\eta_i\right) \frac{u_{t\,ki}^{\xi}}{h_k} - \sum_{i=1}^{4} \frac{1}{4}\left(1-\eta_i\right) \frac{u_{b\,ki}^{\xi}}{h_k} \tag{6.69}$$

Similarly, the shear strain $\gamma\eta\zeta_k^B$ and $\gamma\eta\zeta_k^D$ can be computed. Therefore, the shear strain $\gamma\eta\zeta_k$ can be defined by

$$\gamma\eta\zeta_k = \sum_{i=1}^{4} \frac{\partial N_i}{\partial \xi} w_i + \sum_{i=1}^{4} N_i \frac{v_{t\,ki}^{\eta}}{h_k} - \sum_{i=1}^{4} N_i \frac{v_{b\,ki}^{\eta}}{h_k} \tag{6.70}$$

the shear strain vectors can be computed in points B and D as

$$\gamma\eta\zeta_k^B = \sum_{i=1}^{4} \frac{1}{4}\eta_i \left(1+\xi_i\right) w_i + \sum_{i=1}^{4} \frac{1}{4}\left(1+\xi_i\right) \frac{v_{t\,ki}^{\eta}}{h_k} - \sum_{i=1}^{4} \frac{1}{4}\left(1+\xi_i\right) \frac{v_{b\,ki}^{\eta}}{h_k} \tag{6.71}$$

$$\gamma\eta\zeta_k^D = \sum_{i=1}^{4} \frac{1}{4}\eta_i \left(1-\xi_i\right) w_i + \sum_{i=1}^{4} \frac{1}{4}\left(1-\xi_i\right) \frac{v_{t\,ki}^{\eta}}{h_k} - \sum_{i=1}^{4} \frac{1}{4}\left(1-\xi_i\right) \frac{v_{b\,ki}^{\eta}}{h_k} \tag{6.72}$$

Substituting equations (6.68) and (6.69) into expression (6.65a) allows obtaining the component $\gamma\xi\zeta_k$ of the assumed shear strain vector

$$\begin{aligned}\gamma\xi\zeta_k &= \sum_{i=1}^{4} \frac{1}{4}\xi_i \left(1+\eta_i\eta\right) w_i + \sum_{i=1}^{4} \frac{1}{4}\left(1+\eta_i\eta\right) \frac{u_{t\,ki}^{\xi}}{h_k} - \sum_{i=1}^{4} \frac{1}{4}\left(1+\eta_i\eta\right) \frac{u_{b\,ki}^{\xi}}{h_k} \\ &= \sum_{i=1}^{4} \frac{\partial N_i}{\partial \xi} w_i + \sum_{i=1}^{4} \frac{1}{\xi_i}\frac{\partial N_i}{\partial \xi} \frac{u_{t\,ki}^{\xi}}{h_k} - \sum_{i=1}^{4} \frac{1}{\xi_i}\frac{\partial N_i}{\partial \xi} \frac{u_{b\,ki}^{\xi}}{h_k}\end{aligned} \tag{6.73}$$

Equally, substituting equations (6.71) and (6.72) into expression (6.65b) allows obtaining the component $\gamma\eta\zeta_k$ of the assumed shear strain vector

$$\begin{aligned}\gamma\eta\zeta_k &= \sum_{i=1}^{4} \frac{1}{4}\eta_i \left(1+\xi_i\xi\right) w_i + \sum_{i=1}^{4} \frac{1}{4}\left(1+\xi_i\xi\right) \frac{u_{t\,ki}^{\eta}}{h_k} - \sum_{i=1}^{4} \frac{1}{4}\left(1+\xi_i\xi\right) \frac{u_{b\,ki}^{\eta}}{h_k} \\ &= \sum_{i=1}^{4} \frac{\partial N_i}{\partial \eta} w_i + \sum_{i=1}^{4} \frac{1}{\eta_i}\frac{\partial N_i}{\partial \eta} \frac{u_{t\,ki}^{\eta}}{h_k} - \sum_{i=1}^{4} \frac{1}{\eta_i}\frac{\partial N_i}{\partial \eta} \frac{u_{b\,ki}^{\eta}}{h_k}\end{aligned} \tag{6.74}$$

## 6.11 Global assembly of the finite elements

Having defined the equation of motion of a multilayer plate element, equation (6.64), the global assembly of the elements to model a multilayer plate structure can now be made using a standard element assembly procedure widely documented and described [41, 42]. The equation of motion for the global multilayer plate structure will be obtained assembling each element equations of motion resulting

$$[M]\left\{\ddot{d}\right\} + [K(\omega)]\{d\} = \{F\} \tag{6.75}$$

## 6.12 Direct frequency analysis procedure

With the system of equations of motion of a multilayer plate finite element model obtained and described, the generation of Frequency Response Functions (FRFs) with the finite element model is now possible. To obtain the referred FRFs, the Direct Frequency Analysis (DFA) procedure will be used, similarly to what has been done and described in section 3.11, chapter 3, to the beam finite elements.

# Chapter 7

# Sandwich Plates with Cork Compound Cores: Experimental Results

## 7.1 Introduction

The experimental study hereby presented consists of modal analysis to characterize the dynamic behavior of sandwich plates with two aluminum faces and a cork compound core. The main purpose is to determine the cork compound influence on the structure dynamic response, namely its influence in its structural damping, as well as to obtain its characteristic natural frequencies. To verify the influence of cork compound formulation parameters, several sandwich plates with different cork compound cores have been tested and its results were compared. The measurement of several frequency response functions on the plates will also, further on, allow to compare experimental measurements with predicted ones permitting to validate the formulated plate element.

## 7.2 Characterization of the test samples

In this section, the sandwich plates are characterized as well as the properties of the different cork compounds used to make them are described.

### 7.2.1 Description of the test samples

The test samples analyzed are sandwich plates with a cork compound core and two aluminum faces as schematically depicted in figure 7.1.Where the cork compound thickness is represented by $e$ and the dimensions of the aluminum faces, as depicted in figure 7.1, are :

- length $\ell$: 400 mm
- width $b$: 100 mm
- thickness $h$: 1 mm

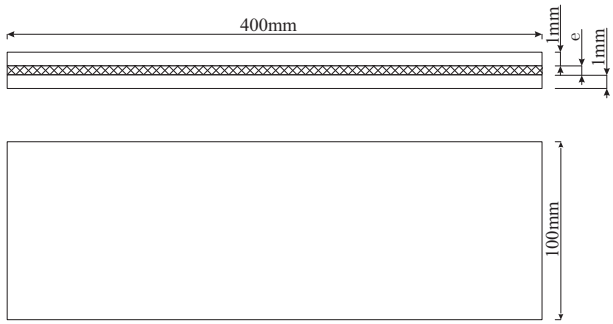


**Figure 7.1:** Schematic drawing of the test samples.

Three test samples were prepared, each with a different cork compound core. In the table 7.1 a short description of the test samples is presented and the relation between the properties identified in chapter 2 and the cork compounds used in each test sample is given.

### 7.2.2 Preparation of the test samples

The test sample preparation process involves the gluing of its constitutive parts in order to obtain the referred sandwich plate depicted in figure 7.1. The preparation steps of each test sample were:

1. The two aluminum plates were sandpapered in order to obtain a better gluing surface;
2. The two plates were cleaned with acetone to remove any dirt or grease on the gluing surfaces;
3. The cork compound was cut out with the plates width and length from a big sheet;
4. The cork compound was glued to the aluminum plates, using epoxy resin as glue, forming the sandwich plates.

## 7.3 Experimental modal analysis

To perform an experimental modal analysis of the test samples a set of frequency response functions was measured and from it the sandwich plates modal parameters were identified. To do this, the modal analysis functionality of the Matlab® toolbox SDT® was used.

### 7.3.1 Experimental setup

The experimental setup was prepared in order to impose to the sandwich plates free boundary conditions. To obtain these boundary conditions, each plate was suspended from a frame structure by two very thin nylon cables, while the electromechanical exciter was also suspended from another frame structure, independent from the one from which the test samples are suspended as depicted in figure 7.2. The chosen configuration restrains the plate in-plane motion while allowing it to move in the direction normal to the plates plane.

**Table 7.1:** Test samples characteristics.

| Sample Name | Sample Description | Core | Core Description | Equivalent Extensional Sample (Chapter 2) | Equivalent Shear Sample (Chapter 2) | Thickness $e$ $[mm]$ |
|---|---|---|---|---|---|---|
| PLT8003 | Two aluminium plates with with a cork compound core. | 8003 | • small grain<br>• low density | Sample A | Sample P2 | 1.2 |
| PLT8123 | Two aluminium plates with with a cork compound core. | 8123 | • small grain<br>• high density | Sample B | Sample P1 | 1.2 |
| PLT8303 | Two aluminium plates with with a cork compound core. | 8303 | • coarse grain<br>• high density | Sample C | Sample P3 | 1.2 |

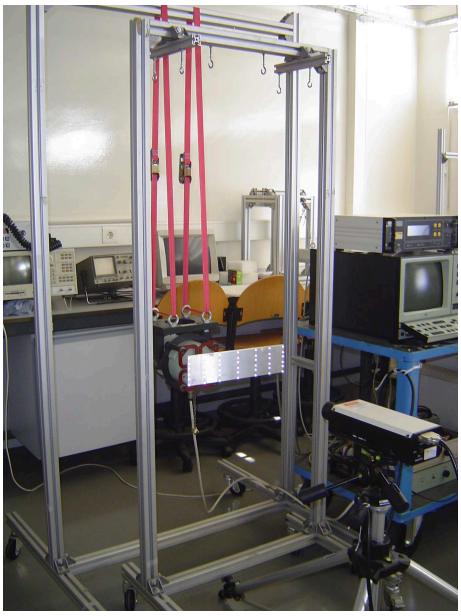

**Figure 7.2:** Fully assembled experimental setup.

The plate sample was excited with an electromagnetic shaker (LDS-401) at one point, being at that same point measured the exciting force with a piezoelectric force transducer (B&K-8203). The exciter was connected to the structure by a thin rod made out of steel, allowing an high axial stiffness but a low bending stiffness connection, assuring a good directional control of the excitation force. This connection can be seen in figure 7.3.

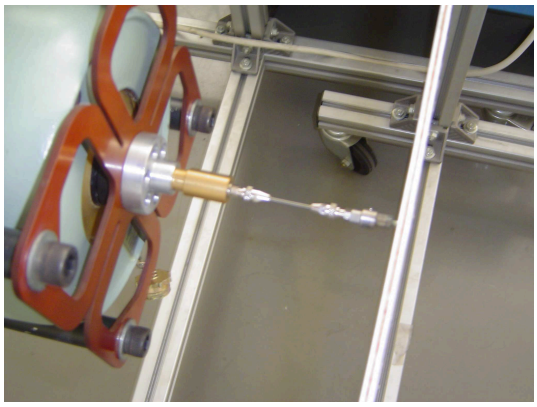

**Figure 7.3:** Connection between the test plate and the shaker through a stinger.

The shaker (LDS-401) was suspended from a frame structure separated to the one where was suspended the test sample in order to assure that no reaction force was transmitted to the testing structure.

The excitation force signal was generated by a signal generator integrated into the spectral analyzer (B&K-2035) and sent to the power amplifier (LDS-PA100E) which finally actuates the electromagnetic shaker. The generated excitation was a random one.

The response was measured in velocity on each point of the measuring mesh, by the laser vibrometer (Polytec-OFV303) using the vibrometer controller (Polytec-OFV3001), as depicted in figure 7.4.

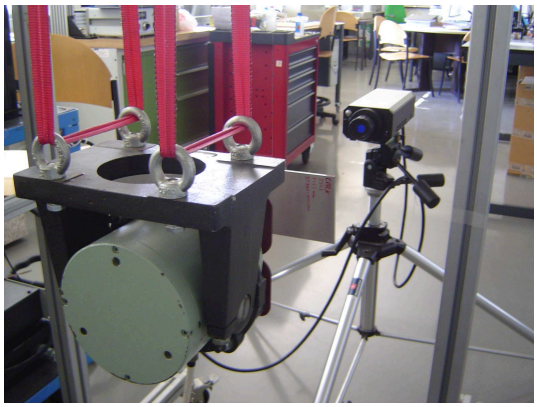

**Figure 7.4:** Measurement of plate response in velocity using the laser vibrometer.

The responses were measured on 42 points distributed along each test sample where reflective stickers were placed to allow the response measurement with the laser head vibrometer (Polytec-OFV303), as schematically depicted in figure 7.5.

The excitation force was applied at the point number 17 also represented in the measurement mesh depicted by figure 7.5.

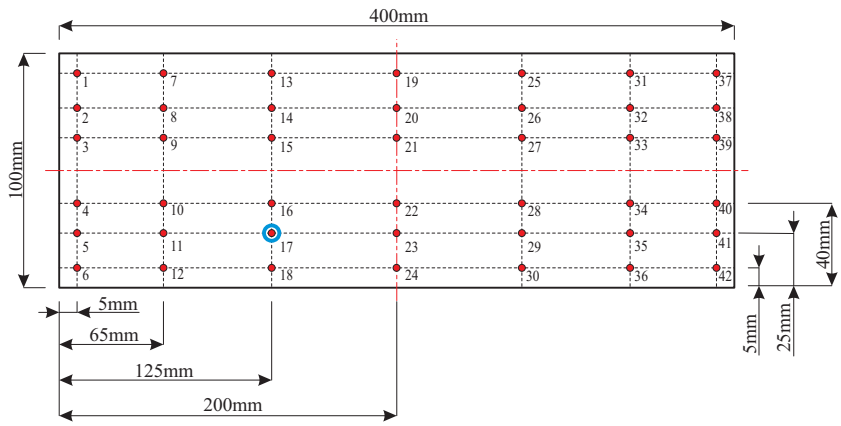


**Figure 7.5:** Schematic drawing with the position of the 42 points of the measurement mesh.

To measure the response, the excitation and estimate the frequency response functions (FRFs) between the excitation point and the measuring points, a FFT analyzer (B&K-2035) was used. The measurements were made in a frequency range between 0 Hz and 400 Hz.

From the measured FRFs, a multi degree of freedom (MDOF) technique was used to estimate the modal parameters. An algorithm in the time domain, the "Least Squares Complex Exponential" was used to identify the poles (values of the natural frequencies and damping), being the residues determined afterwords using the "Least Squares Frequency Domain" algorithm.

Finally, a set of modes were obtained, which include estimations for the natural frequencies, loss factors and mode shapes. These modes constitute the modal model for the analyzed frequency range. The software used to obtain the referred modal parameters was the Matlab® toolbox , SDT®.

### 7.3.2 Measured FRFs

For each test sample a set of 42 mobility FRFs were measured corresponding to each measuring point. In this section, are shown the direct FRF, obtained at the excitation point 17, as well as the FRFs measured at points 12, 27 and 37. In the representations depicted from figure 7.6 to figure 7.8, the mentioned FRFs of the three test samples are represented by the Bode diagram in the measured frequency range from 0 Hz to 400 Hz.

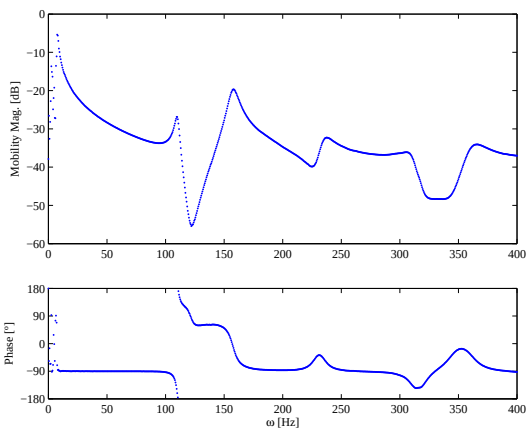


**(a)** Sample PLT8003: mobility 12-17

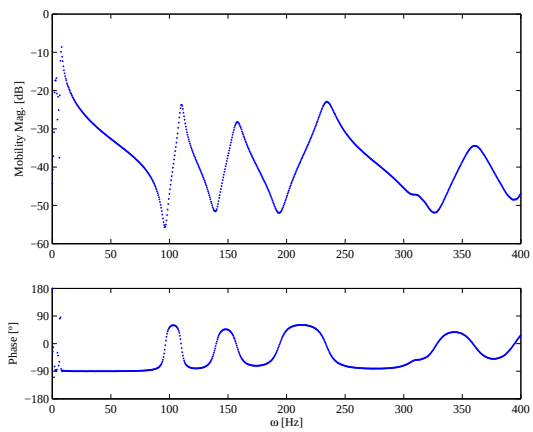


**(b)** Sample PLT8003: mobility 17-17

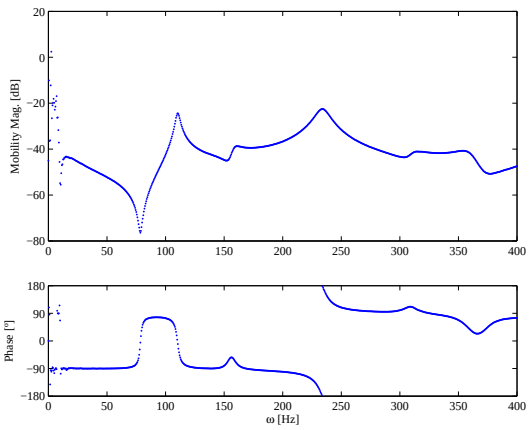


**(c)** Sample PLT8003: mobility 27-17

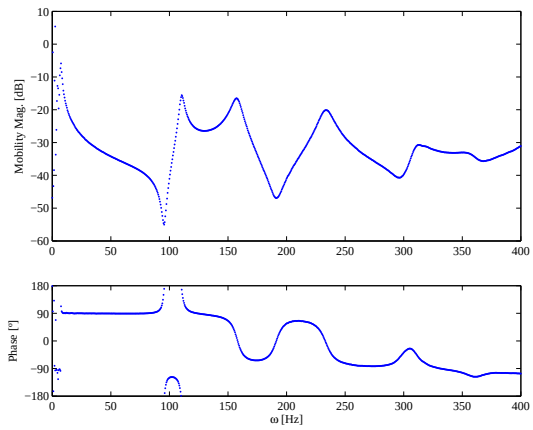


**(d)** Sample PLT8003: mobility 37-17

**Figure 7.6:** Measured mobilities of sample PLT8003 at points 12,17,27 and 37.

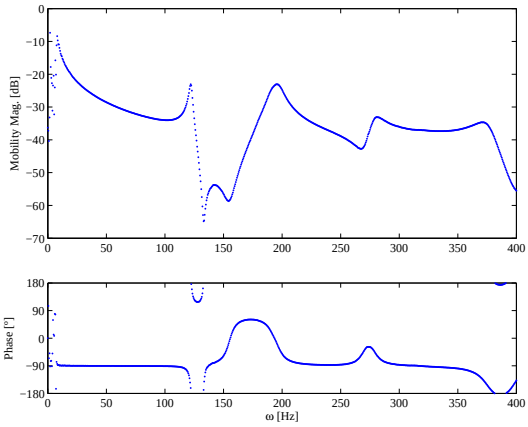


**(a)** Sample PLT8123: mobility 12-17

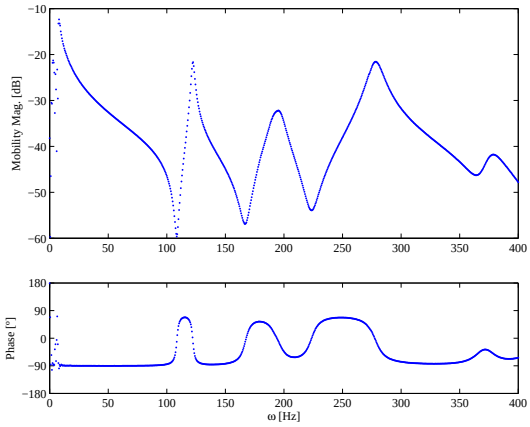


**(b)** Sample PLT8123: mobility 17-17

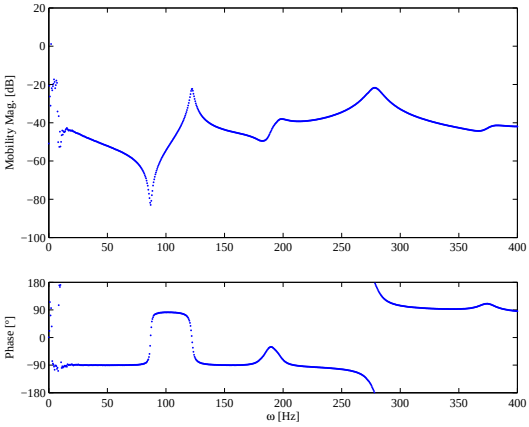


**(c)** Sample PLT8123: mobility 27-17

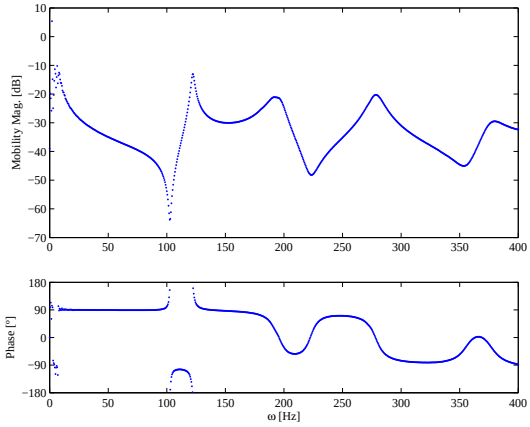


**(d)** Sample PLT8123: mobility 37-17

**Figure 7.7:** Measured mobilities of sample PLT8123 at points 12,17,27 and 37.

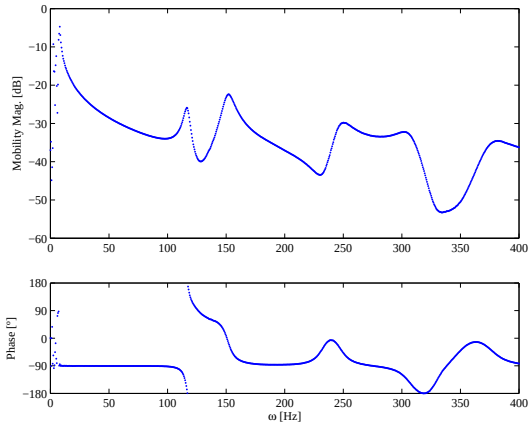


**(a)** Sample PLT8303: mobility 12-17

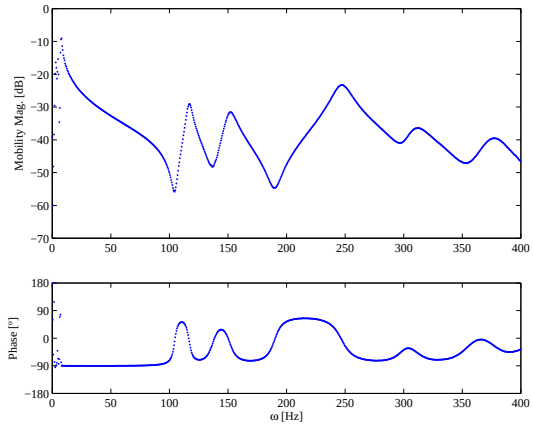


**(b)** Sample PLT8303: mobility 17-17

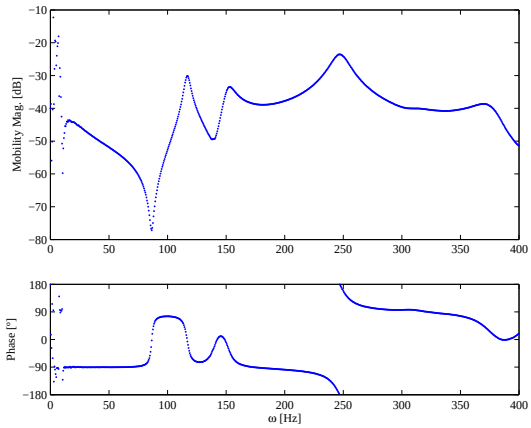


**(c)** Sample PLT8303: mobility 27-17

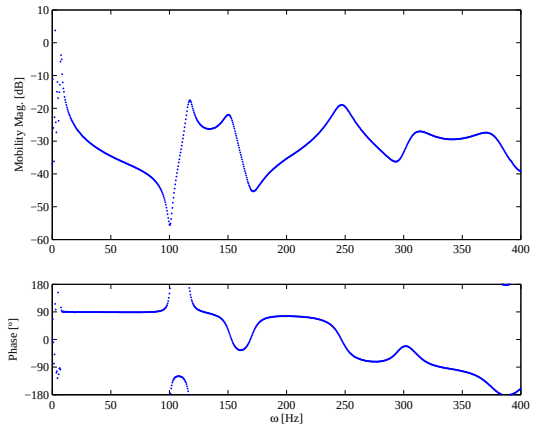


**(d)** Sample PLT8303: mobility 37-17

**Figure 7.8:** Measured mobilities of sample PLT8303 at points 12,17,27 and 37.

### 7.3.3 Discussion of the measurements

Performing a simple visual inspection of the measured FRFs, it is possible to verify that the cork compound layer introduced a damping effect on the plates. Such fact is evidenced by the rounded peaks verified in the proximity of the natural frequencies of all three test samples. The measured FRFs also evidence the presence of five modes, in the analyzed frequency range, for test samples PLT8003 and PLT8303, while showing the presence of four modes for test sample PLT8123.

### 7.3.4 Modal identification

With a set of measured frequency response functions (FRFs), a modal model can be defined in order to describe the acquired information. To obtain the modal parameters of the system, similarly to what has been done in chapter 4, it is necessary to use estimation techniques like curve fitting to approximate the modal model to the acquired information. In the identification

process, the Modal Indicator Functions (MIF) and Sum (SUM) were computed.

To perform the identification process a multi degree of freedom (MDOF) technique was applied, as previously described in chapter 4 in order to determine the natural frequencies and damping values for each mode.

In figure 7.9 to figure 7.11 the obtained SUM, MIF and the synthesized direct mobility of each one of the three test samples are shown.

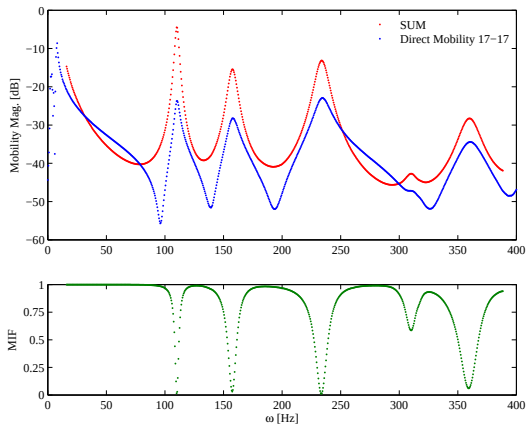


**(a)** Sample PLT8003: SUM MIF and direct mobility

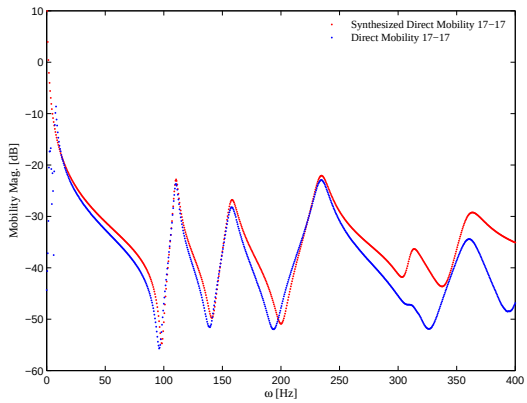


**(b)** Sample PLT8003: Synthesized and direct mobility

**Figure 7.9:** Sample PLT8003 functions obtained from modal analysis.

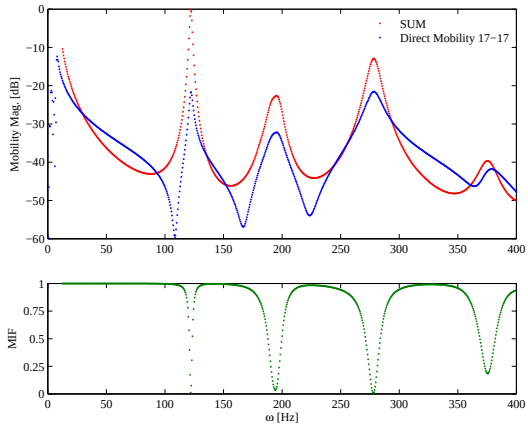


**(a)** Sample PLT8123: SUM MIF and direct mobility

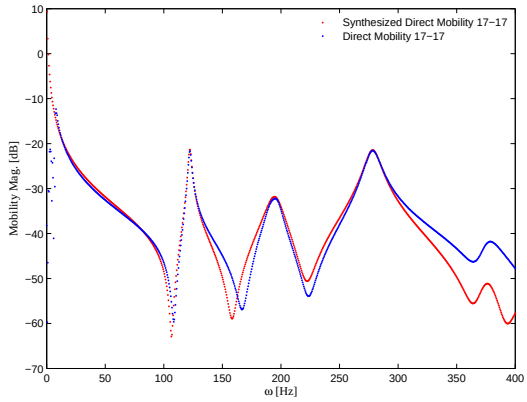


**(b)** Sample PLT8123: Synthesized and direct mobility

**Figure 7.10:** Sample PLT8003 functions obtained from modal analysis.

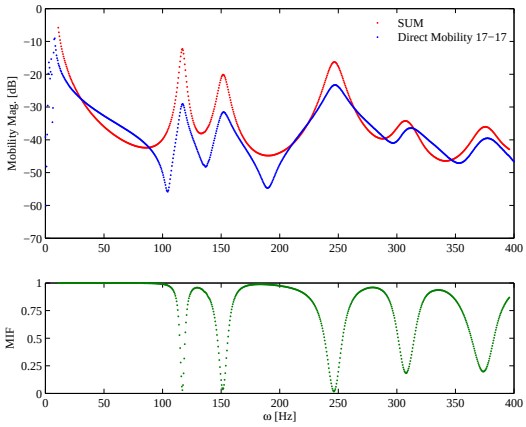


**(a)** Sample PLT8303: SUM MIF and direct mobility

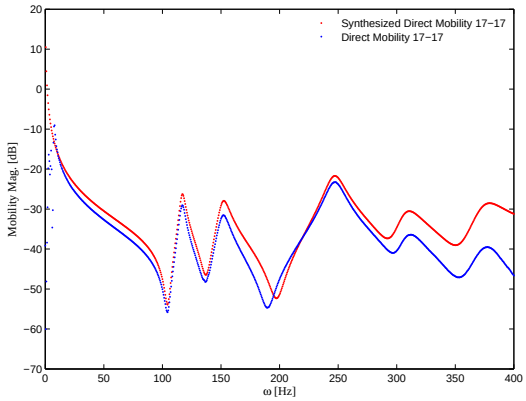


**(b)** Sample PLT8303: Synthesized and direct mobility

**Figure 7.11:** Sample PLT8303 functions obtained from modal analysis.

In Appendix C can be found the determined mode shapes for the three test samples.

The experimental analysis has been made for the three different test samples in the frequency range between 0 Hz and 400 Hz, being obtained the natural frequencies and loss factors, as previously described, and now summarized in table 7.2 and table 7.3.

**Table 7.2:** Natural frequencies of all test samples.

| Sample Name | Natural Frequencies [Hz] | | | | |
|---|---|---|---|---|---|
| | $1^{st}$ mode | $2^{nd}$ mode | $3^{rd}$ mode | $4^{th}$ mode | $5^{th}$ mode |
| PLT8003 | 110.27 | 157.70 | 233.96 | 311.36 | 360.22 |
| PLT8123 | 122.19 | 194.95 | 278.32 | 375.98 | - |
| PLT8303 | 116.91 | 151.66 | 246.84 | 307.40 | 374.41 |

**Table 7.3:** Loss factors of all test samples.

| Sample Name | Loss Factor $\eta$[%] | | | | |
|---|---|---|---|---|---|
| | $1^{st}$ mode | $2^{nd}$ mode | $3^{rd}$ mode | $4^{th}$ mode | $5^{th}$ mode |
| PLT8003 | 3.46 | 5.50 | 5.24 | 3.76 | 5.52 |
| PLT8123 | 2.24 | 7.78 | 4.56 | 4.98 | - |
| PLT8303 | 4.20 | 6.36 | 6.38 | 6.90 | 7.14 |

In figure 7.12 and figure 7.13 are respectively represented the three test samples natural frequencies and loss factors described in the previous table.

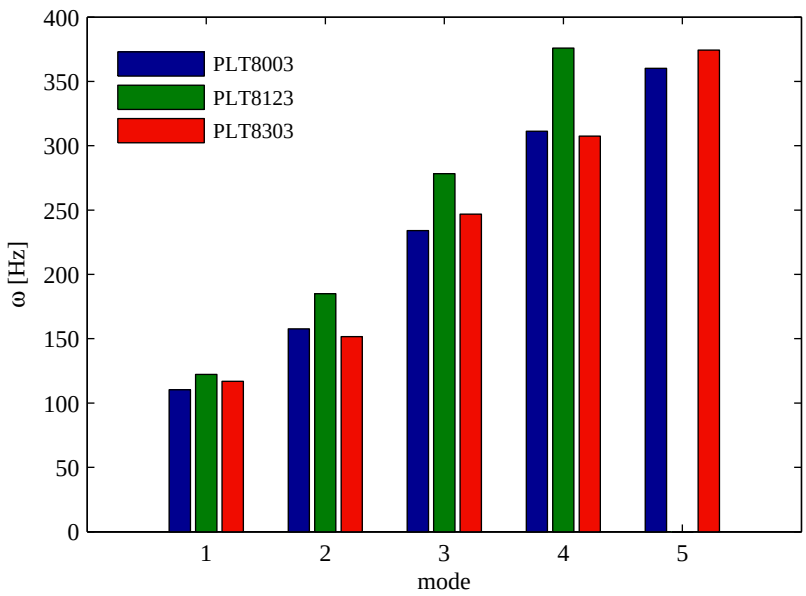


**Figure 7.12:** Natural frequencies of the three plate test samples.

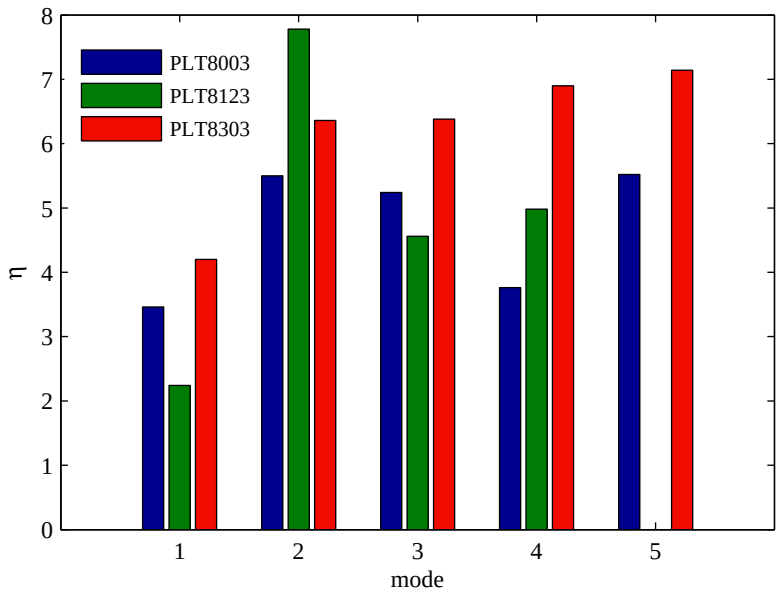


**Figure 7.13:** Loss factors of the three plate test samples.

### 7.3.5 Discussion of the modal identification results

From the results presented on the previous section it can be said that:

- as it can be seen in figure 7.9 the test sample PLT8003 presents five mode in the analysis frequency range, these modes can be clearly seen from both the dropping of the MIF

function and the peaks of SUM function; the same can be seen for sample PLT8123 (figure 7.10) presenting this sample four modes and for sample PLT8303 (figure 7.11), being in this case visible five modes;

- comparing the natural frequencies of sample PLT8003 and sample PLT8123, it can be seen that the second ones are higher than the first ones; this fact is due to the higher density of the cork used in PLT8123 which makes the plate structure stiffer than if it was used the same cork compound as used in sample PLT8003 (figure 7.12);
- the grain size also influences directly the sample stiffness, as it can be seen in figure 7.12; the natural frequencies of sample PLT8303, which has a coarse grain size cork compound, are lower than the ones presented for sample PLT8003 and PLT8123 evidencing that a coarse grain size mandatory reduces the structure stiffness;
- in all the test samples is evident that the introduction of a cork compound layer in the structures improves its damping capability (figure 7.13);
- when comparing the loss factors of sample PLT8003(small grain, low density) with sample PLT8123(small grain, high density), as it can be seen in figure 7.13, it is evident that sample PLT8123 presents a lower loss factor than the ones obtained for sample PLT8003 for modes 1 and 3 which represent the predominantly flexural plate modes (refer to Appendix C). The opposite happens for modes 2 and 4, which are predominantly torsional plate modes (Appendix C), being the loss factors of PLT8123 higher than the ones of PLT8003, suggesting that high densities cork compound should provide a better damping capability when summited to shear strains, at predominantly torsional modes, while low densities should provide a better structural damping for predominantly flexural modes;
- it is also suggested from figure 7.13 that a coarse grain size introduces a bigger structural damping than small grain size which can be seen when comparing loss factors from sample PLT8303 with the ones from samples PLT8003 and PLT8123; again, the only observed exception occurs at the second mode.

# Chapter 8

# Sandwich Plates with Cork Compound Cores: Numerical Results

## 8.1 Introduction

In this chapter, using the finite element method with the plate element formulated in chapter 6, the plates analyzed in chapter 7 are hereby simulated. To achieve this, the measured direct FRFs of each test sample, presented in the previous chapter, are compared to the predicted ones using the finite element method through a direct frequency analysis procedure. For all the simulations performed along this chapter, using the formulated element, the biharmonic interpolation functions were used, as well as the MITC formulation in order to avoid shear locking problems while the membrane and bending components of the element stiffness were integrated by the Gauss method using four $(2 \times 2)$ integration points .

## 8.2 Direct frequency analysis

To generate the numerical FRFs presented in the following sections of this chapter, the formulated plate finite element was used as well as the Direct Frequency Analysis (DFA) procedure. This procedure was also used to generate the numerical FRFs presented in chapter 5 for the sandwich beams. Refer to chapter 5, section 3.11, for a detailed description of the hereby used DFA procedure.

## 8.3 Element verification

One crucial step in building a numerical model is to verify its consistency and its ability to reproduce reality. In this section, to verify it, an aluminum plate is studied as reference. For this plate, several FRFs are measured and a modal analysis procedure is applied in order to characterize experimentally the dynamic behavior of the plate, namely to determine its natural frequencies and mode shapes. Additionally, the same plate is simulated numerically using the finite element method with the plate finite element formulated in chapter 6, being the natural

frequencies, mode shapes and the driving point FRF obtained by numerical simulation compared to the ones measured experimentally.

The plate structure hereby used for this element verification study is an aluminum plate with a *Young's* modulus of $E = 69$MPa, *Poisson's* ratio of $\nu = 0.32$ and density of $\rho = 2710$Kg/m$^3$, having the dimensions depicted in figure 8.1.

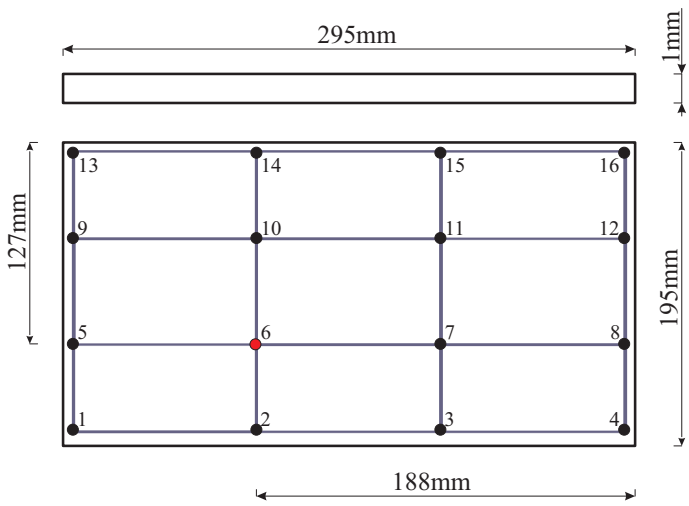


**Figure 8.1:** Reference plate dimensions and measurement mesh.

For this aluminum plate, several FRFs have been measured in order to allow an experimental characterization of the dynamic behavior of the structure. The aluminum plate was suspended from a frame structure by two very thin nylon cables, simulating the free boundary condition, and the excitation was applied at point 6 (figure 8.1) by an electromagnetic shaker. A set of 16 mobility frequency response functions(FRFs) were measured at the points depicted in the measurement mesh shown in figure 8.1, allowing a further experimental modal analysis of the plate to determine its natural frequencies and mode shapes.

To inspect the representativity of the numerical results produced by the finite element method using the formulated plate element, a numerical model of the plate structure was generated containing 600 elements (30 on the side with length 295mm and 20 on the side with length 195mm) using the plate element formulated in chapter 6 in a single layer configuration using the referred aluminum properties. The plate was simulated for free boundary conditions in order to reproduce the experimental measurements obtained from the tested plate and allow a further comparison between experimental measurements and numerical results.

In table 8.1 the obtained natural frequencies through experimental modal analysis and using the finite element method are represented. Additionally, the percent relative difference between the measured and determined natural frequencies is shown.

**Table 8.1:** Plate natural frequencies obtained with FEM and modal analysis.

| | Natural Frequencies [Hz] | | | | | |
|---|---|---|---|---|---|---|
| | $1^{st}$ mode | $2^{nd}$ mode | $3^{rd}$ mode | $4^{th}$ mode | $5^{th}$ mode | $6^{th}$ mode |
| FEM | 54.30 | 58.04 | 125.58 | 138.61 | 156.46 | 185.22 |
| Modal Analysis | 53.41 | 59.03 | 123.13 | 139.42 | 157.51 | 182.45 |
| % difference | 1.67 | 1.68 | 1.98 | 0.58 | 0.67 | 1.52 |

As it can be seen in table 8.1 the predicted natural frequencies show a good accordance to the ones measured experimentally, as it can be seen when inspecting the percent relative difference between them, which does not exceeds 2 %.

Additionally, in figure 8.3, the first three mode shapes of this reference plate are represented, being possible to compare the mode shapes obtained from modal analysis and from the FEM numerical prediction. As it can be seen, both appear to be in accordance, also sustaining the representativity of the numerical model.

Applying the DFA procedure, referred in the previous section and fully described in chapter 5, section 3.11, the driving point mobility FRF can be computed using the finite element method with the formulated plate element and compared to the measured mobility at point 6 (figure 8.1). Figure 8.2 shows both driving point mobilities, the predicted and the measured one.

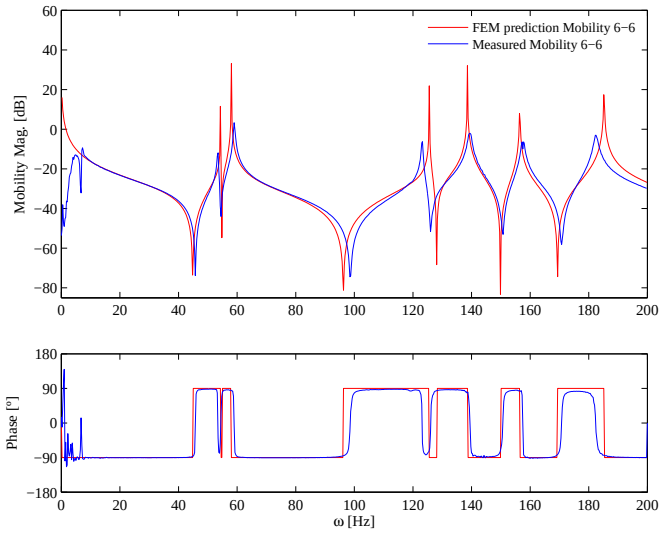


**Figure 8.2:** Comparison of measured and predicted mobility.

By visual inspection of figure 8.2 it is possible to verify a good accordance of the numerically predicted FRF to the measured one, revealing a good representativity of the numerical procedure, as it has also been suggested when the natural frequencies and mode shapes were analyzed.

Until now, the representativity of the plate element has been inspected using a single layer configuration. To analyze the convergence as well as the correction of the multilayer element formulation, some other tests have to be performed. To achieve this, the reference plate was analyzed using different element meshes in a single layer configuration with a thickness of 1 mm. The natural frequencies of the first six modes are presented in table 8.2 and from them

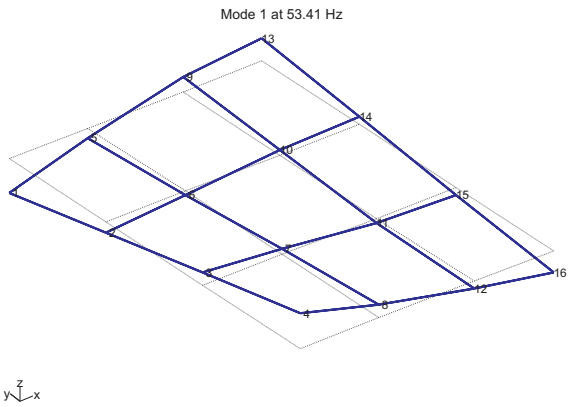


**(a)** $1^{st}$ mode from modal analysis

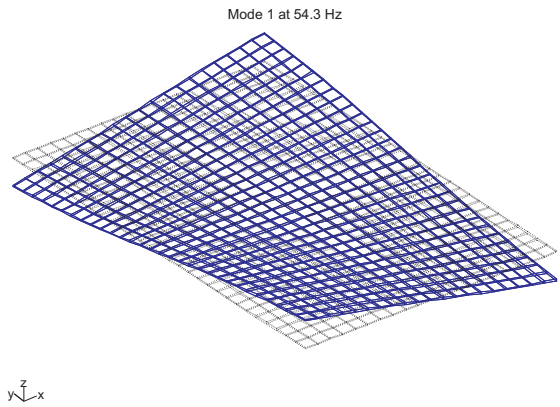


**(b)** $1^{st}$ mode from FEM

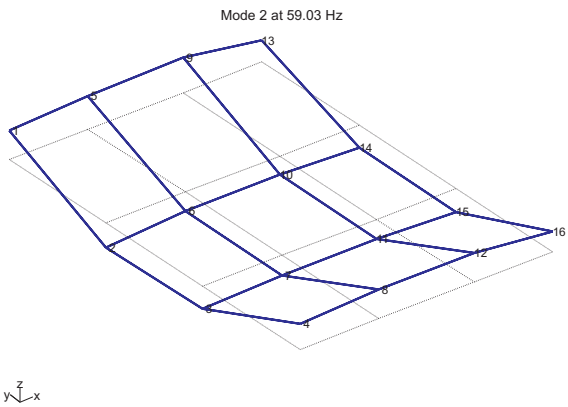


**(c)** $2^{nd}$ mode from modal analysis

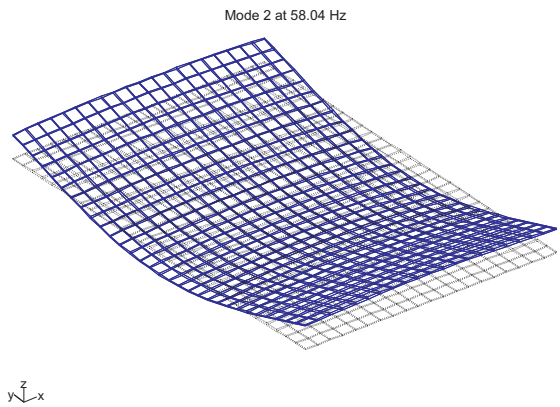


**(d)** $2^{nd}$ mode from FEM

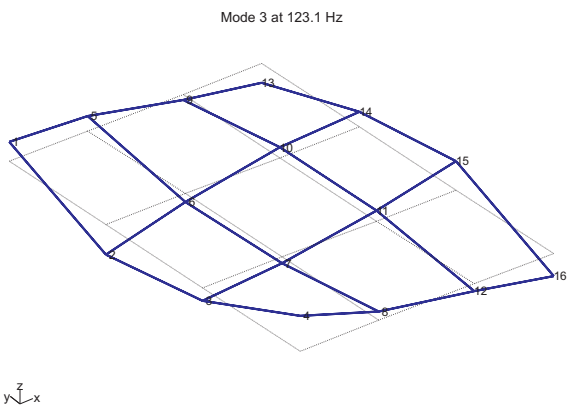


**(e)** $3^{rd}$ mode from modal analysis

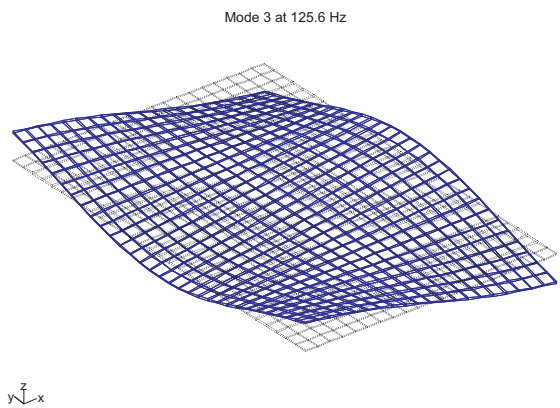


**(f)** $3^{rd}$ mode from FEM

**Figure 8.3:** Reference plate modes obtained from modal analaysis and FEM.

one can clearly see that, as mesh tightness increases the natural frequency values converge. To test the multilayer element configuration the reference plate spatial model was built with plate elements in a two layer configuration, each layer with a thickness that is half of the 1 mm original thickness. The computed natural frequencies with this configuration are shown in table 8.3, showing not only the convergence of the natural frequency values but also its coherence to the ones obtained for a single layer configuration. In table 8.4 the same natural frequencies were computed in a three layer configuration each layer with a thickness that is one third of the original thickness.

**Table 8.2:** Plate natural frequencies obtained with FEM in a single layer model.

| | **1 layer** | | | | | | | |
|---|---|---|---|---|---|---|---|---|
| mesh (lxw) | 3x2 | 6x4 | 12x8 | 15x10 | 18x12 | 21x14 | 27x18 | 30x20 |
| mode 1 | 49.89 | 53.47 | 54.14 | 54.21 | 54.25 | 54.27 | 54.29 | 54.30 |
| mode 2 | 55.24 | 57.55 | 57.95 | 57.99 | 58.01 | 58.02 | 58.03 | 58.04 |
| mode 3 | 112.14 | 124.46 | 125.52 | 125.56 | 125.58 | 125.58 | 125.58 | 125.58 |
| mode 4 | 130.32 | 136.89 | 138.46 | 138.55 | 138.58 | 138.59 | 138.61 | 138.61 |
| mode 5 | 146.14 | 155.67 | 156.77 | 156.68 | 156.61 | 156.55 | 156.48 | 156.46 |
| mode 6 | 216.89 | 189.99 | 186.48 | 185.96 | 185.66 | 185.48 | 185.28 | 185.22 |

**Table 8.3:** Plate natural frequencies obtained with FEM in a two layer model.

| | **2 layers** | | | | | | | |
|---|---|---|---|---|---|---|---|---|
| mesh (lxw) | 3x2 | 6x4 | 12x8 | 15x10 | 18x12 | 21x14 | 27x18 | 30x20 |
| mode 1 | 49.90 | 53.47 | 54.14 | 54.22 | 54.25 | 54.28 | 54.29 | 54.30 |
| mode 2 | 55.24 | 57.55 | 57.96 | 57.99 | 58.01 | 58.02 | 58.03 | 58.04 |
| mode 3 | 112.14 | 124.46 | 125.53 | 125.57 | 125.59 | 125.59 | 125.59 | 125.59 |
| mode 4 | 130.32 | 136.89 | 138.46 | 138.55 | 138.58 | 138.60 | 138.61 | 138.62 |
| mode 5 | 146.15 | 155.68 | 156.77 | 156.69 | 156.61 | 156.56 | 156.49 | 156.47 |
| mode 6 | 216.91 | 189.99 | 186.48 | 185.98 | 185.67 | 185.49 | 185.29 | 185.22 |

**Table 8.4:** Plate natural frequencies obtained with FEM in a three layer model.

| | **3 layers** | | | | | | | |
|---|---|---|---|---|---|---|---|---|
| mesh (lxw) | 3x2 | 6x4 | 12x8 | 15x10 | 18x12 | 21x14 | 27x18 | 30x20 |
| mode 1 | 49.89 | 53.47 | 54.14 | 54.22 | 54.25 | 54.28 | 54.29 | 54.31 |
| mode 2 | 55.24 | 57.55 | 57.96 | 57.99 | 58.01 | 58.02 | 58.03 | 58.04 |
| mode 3 | 112.14 | 124.46 | 125.53 | 125.57 | 125.59 | 125.59 | 125.59 | 125.59 |
| mode 4 | 130.32 | 136.89 | 138.46 | 138.55 | 138.58 | 138.59 | 138.61 | 138.62 |
| mode 5 | 146.15 | 155.67 | 156.77 | 156.68 | 156.61 | 156.56 | 156.49 | 156.47 |
| mode 6 | 216.91 | 189.99 | 186.48 | 185.97 | 185.67 | 185.49 | 185.29 | 185.23 |

## 8.4 Numerical simulation of plates used in experimental tests

For the numerical simulation of the plate test samples experimentally analyzed in chapter 7, the multilayer, layerwise plate element formulated in chapter 6 was included in a finite element routine, written in Matlab® programming language which included the DFA procedure to include the viscoelastic properties of cork compound which were determined using CMA in chapter 2. To verify the physical representativity of the developed finite element as well as the accuracy of the measured cork properties, a numerical spatial model was generated to simulate the sandwich plate analyzed experimentally which schematic drawing is recalled in figure 8.4

In the experimental tests, the FRF mobilities were measured in a set of 42 points on the plate, which are represented in figure 8.4, that recalls the measuring mesh of the test samples.

The excitation force was applied in point number 17, and the FRFs were measured for all 42 points. The comparison hereby presented is made between the driving point FRF (obtained at the excitation point 17) measured experimentally and the one obtained using the finite element method, with the multilayer layerwise plate element previously formulated.

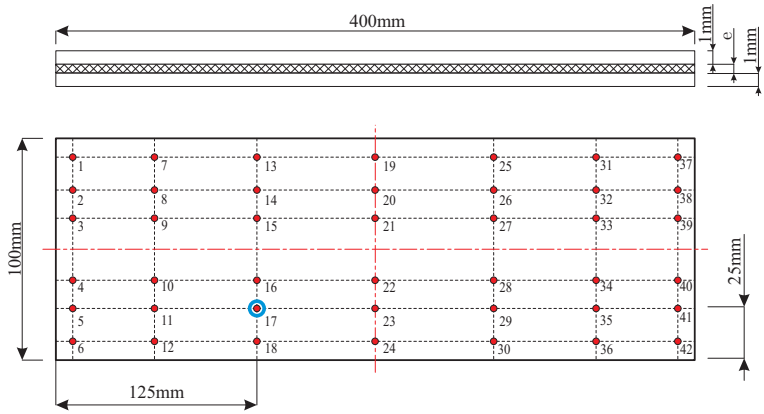


**Figure 8.4:** Schematic drawing of the plate test samples.

To obtain the driving point FRF, a spatial model with 600 plate elements was used, being used a 30 by 20 element mesh which allows a mesh node to be coincident to the location of point 17 depicted in figure 8.4.

In the DFA procedure, used to generate the numerical FRFs, the cork compound dynamic properties determined in chapter 2 were introduced in the finite element model. Therefore, as the cork types used in the plate test samples tested were the 8123, 8303 and 8003, the extensional properties obtained for these cork compounds were used, corresponding to samples A, B and C.

In figure 8.5 to figure 8.7, a comparison between the numerical results obtained with FEM and the experimental measurements of the direct mobility is shown for the plates test samples PLT8003, PLT8123 and PLT8303.

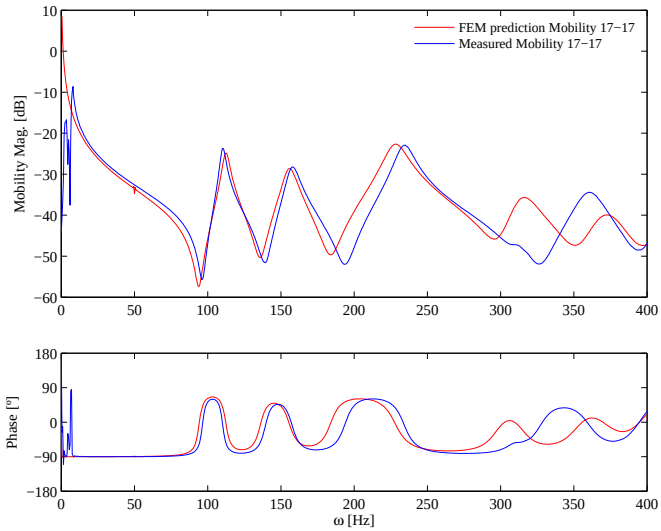


**Figure 8.5:** Comparison between FEM and experimental direct mobility of PLT8003.

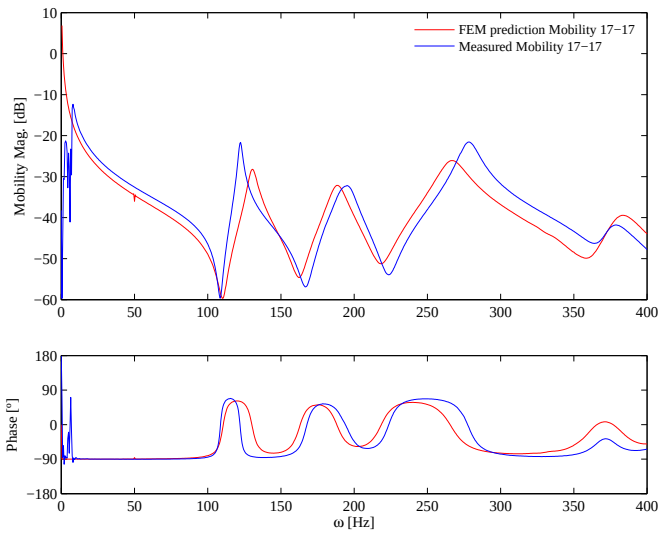


**Figure 8.6:** Comparison between FEM and experimental direct mobility of PLT8123.

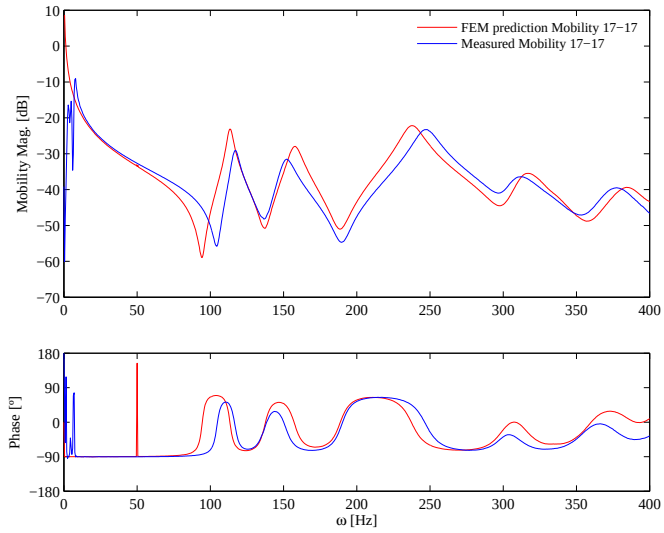


**Figure 8.7:** Comparison between FEM and experimental direct mobility of PLT8303.

Additionally, in table 8.5 and 8.6, the natural frequencies and modal loss factors obtained by the circular curve fitting method applied to the FEM predicted FRFs are compared to the ones previously obtained by experimental modal analysis (EMA) in chapter 7, table 7.2.

**Table 8.5:** Natural frequencies [Hz] of the plate test samples.

| | $\omega_1$ | | $\omega_2$ | | $\omega_3$ | | $\omega_4$ | | $\omega_5$ | |
|---|---|---|---|---|---|---|---|---|---|---|
| Sample | EMA | FEM | EMA | FEM | EMA | FEM | EMA | FEM | EMA | FEM |
| PLT8003 | 110.27 | 113.50 | 157.70 | 156.25 | 233.96 | 228.75 | 311.36 | 315.50 | 360.22 | 372.75 |
| PLT8123 | 122.19 | 130.25 | 194.95 | 188.75 | 278.32 | 267.50 | 375.98 | 382.25 | - | - |
| PLT8303 | 116.91 | 114.50 | 151.66 | 156.25 | 246.84 | 239.25 | 307.40 | 316.50 | 374.41 | 384.50 |

**Table 8.6:** Modal loss factors [%] of the plate test samples.

| | $\eta_1$ | | $\eta_2$ | | $\eta_3$ | | $\eta_4$ | | $\eta_5$ | |
|---|---|---|---|---|---|---|---|---|---|---|
| Sample | EMA | FEM | EMA | FEM | EMA | FEM | EMA | FEM | EMA | FEM |
| PLT8003 | 3.46 | 4.47 | 5.50 | 5.78 | 5.24 | 6.55 | 3.76 | 5.32 | 5.52 | 4.98 |
| PLT8123 | 2.24 | 4.63 | 7.78 | 5.87 | 4.56 | 6.73 | 4.98 | 5.17 | - | - |
| PLT8303 | 4.20 | 3.56 | 6.36 | 5.74 | 6.38 | 6.04 | 6.90 | 5.44 | 6.14 | 4.32 |

### 8.4.1 Discussion of the numerical results

As it can be seen in figure 8.5 the five modes identified experimentally, for sample PLT8003, are also visible in the FEM predicted mobility. For the first three modes, the predicted mobility is quite close to the experimentally measured suggesting that for this frequency range, from 0 Hz to 250 Hz, the cork properties determined and the plate FE correctly describe the physical system. In frequencies above 250 Hz, apparently the predicted mobility does not follows the

experimental one but the natural frequencies predicted for the fourth and fifth mode are not very far from the identified experimentally, despite the fact of the FRF amplitude difference.

In figure 8.6, as it can be seen, the four modes of sample PLT8123 identified experimentally can also be found in the FEM predicted mobility. In this case, the predicted mobility reproduces quite well the experimental one but, the increasing of difference while the mode frequencies increases suggests that the material properties at high frequencies might not be as accurate as at low frequencies.

For sample PLT8303, figure 8.7, the predicted mobility presents all five modes identified experimentally and the predicted FRF reproduced quite well the measured one, suggesting that the accuracy of the cork compound properties determined for sample C (Chapter 2) is very good and the spatial numerical FEM model is representative of the physical structure.

# Chapter 9

# Spectral Beam Finite Element

## 9.1 Introduction

The finite element method (FEM) has been used extensively in structural dynamics. The finite element model may provide accurate dynamic characteristics of a structure if the wavelength is large compared to the mesh size. However, the finite element solutions become increasingly inaccurate as the frequency increases. Although the accuracy can be improved by refining the mesh, this is sometimes prohibitively expensive in computational time and capacity. Alternatively, the dynamic stiffness matrix method, where the dynamic stiffness matrix is formulated from frequency dependent shape functions that are exact solutions of the governing differential equations. This frequency dependent matrix has both mass and stiffness properties of the structure embedded in it. Because the dynamic stiffness matrix method does not require subdivision of the structure into finite elements, it may eliminate discretization errors and is capable of predicting an infinite number of eigensolutionsby means of a minimum number of degrees of freedom (DOF). This improves the solution accuracy and lowers computational cost significantly. Additionally, as the dynamic stiffness matrix is frequency dependent, this approach seems to be advantageous in modeling sandwich or multilayer structures which properties are frequency dependent.

To develop a spectral approach to beam type structures and investigate the flexural waves phenomena, a first approach is made using the *Euler-Bernoulli* beam theory. Although it is well known, the derivation of the *Euler-Bernoulli* thin beam equation of flexural motion will be hereby presented to describe all the formulation steps of the spectral approach presented in this chapter. The equations of motion are derived using the energetic Hamilton's principle, allowing to obtain the equations of motion for the beam. Then, the differential equations of motion are stated in terms of the frequency domain, being therefore adapted to the establishing of an approximate waveguide theory.

## 9.2 Euler-Bernoulli beam equation of motion

Considering a long, thin beam with the loads applied as represented in figure 9.1, the *Euler-Bernoulli* beam model assumes that the deflection of the centerline $w(x,t)$ is small and only transverse. While this theory assumes the presence of a transverse shear force, it neglects any shear deformation due to it.

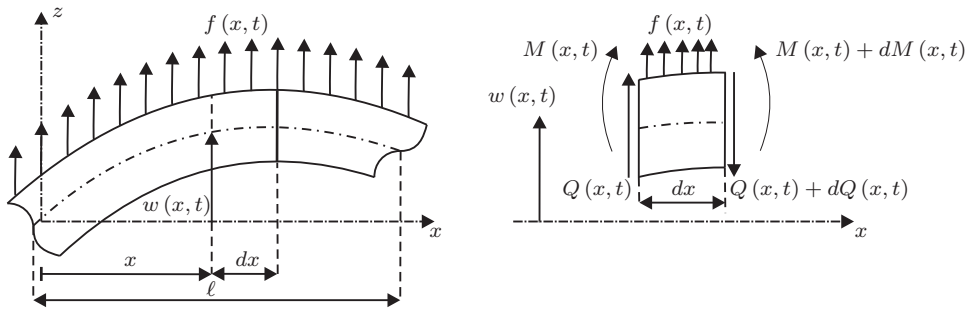


**Figure 9.1:** *Euler-Bernoulli* beam infinitesimal element.

Therefore, the centerline vertical displacement can be related to the section rotation $\theta$ as

$$\theta\left(x,t\right)=\frac{\partial w}{\partial x} \tag{9.1}$$

The horizontal displacement and velocity will be given by

$$u\left(x,t\right)=z\theta \quad \Rightarrow \quad u\left(x,t\right)=z\frac{\partial w}{\partial x} \quad \Rightarrow \quad \frac{\partial u\left(x,t\right)}{\partial t}=z\frac{\partial^2 w}{\partial x\partial t} \tag{9.2}$$

According to the constitutive law, the beam strain and stresses will be given by

$$\epsilon_{xx}=\frac{\partial u}{\partial x}=z\frac{\partial^2 w}{\partial x^2} \tag{9.3a}$$

$$\sigma_{xx}=E\epsilon_{xx}=Ez\frac{\partial^2 w}{\partial x^2} \tag{9.3b}$$

Then, the potential strain energy of the beam in a domain $\Omega$ will be given by

$$\Pi^P=\frac{1}{2}\int_{\Omega}\epsilon_{xx}\sigma_{xx}d\Omega \tag{9.4}$$

Substituting the strain and stresses expressions from (9.3a) (9.3b) into equation (9.4) will result in

$$\Pi^P=\frac{1}{2}\int_{\Omega}Ez^2\left(\frac{\partial^2 w}{\partial x^2}\right)^2 d\Omega \tag{9.5}$$

The domain $\Omega$ is defined in the $x$ $y$ $z$ coordinates. Considering $b$ as the beam width in the $y$ direction and $h$ as the beam thickness in the $z$ direction, then, integrating expression (9.5) in $y$ and $z$ will result into

$$\Pi^P=\frac{1}{2}\int_{\ell}E\frac{bh^3}{12}\left(\frac{\partial^2 w}{\partial x^2}\right)^2 dx \tag{9.6}$$

Considering the section area moment as being $I=\frac{bh^3}{12}$, expression (9.6) can be rewritten as

$$\Pi^P=\frac{1}{2}EI\int_{\ell}\left(\frac{\partial^2 w}{\partial x^2}\right)^2 dx \tag{9.7}$$

The kinetic energy of the beam will then be given by

$$\Pi^K = \frac{1}{2}\int_{\Omega} \rho \left(\frac{\partial w}{\partial t}\right)^2 d\Omega \tag{9.8}$$

Similarly to what as been done to the potential energy, an integration is performed in the $y$ and $z$ directions resulting

$$\Pi^K = \frac{1}{2}\int_{\ell} \rho bh \left(\frac{\partial w}{\partial t}\right)^2 dx \tag{9.9}$$

Having the section area represented by $A = bh$, expression (9.9) can be rewritten as

$$\Pi^K = \frac{1}{2}\rho A \int_{\ell} \left(\frac{\partial w}{\partial t}\right)^2 dx \tag{9.10}$$

With the potential and kinetic energy expressions defined, the Hamilton's principle can be used to derive the beam equation of motion. The Hamilton's principle states that

$$\int_{t_1}^{t_2} \delta\left(\Pi^K - \Pi^P\right) dt = 0 \tag{9.11}$$

Substituting the potential and kinetic energy expressions from (9.7) and (9.10) into (9.11) will result

$$\int_{t_1}^{t_2} \delta\left(\frac{1}{2}\rho A \int_{\ell} \left(\frac{\partial w}{\partial t}\right)^2 dx - \frac{1}{2}EI \int_{\ell} \left(\frac{\partial^2 w}{\partial x^2}\right)^2 dx\right) dt = 0 \tag{9.12}$$

The previous expression variational operation can now be perform resulting

$$\int_{t_1}^{t_2} \left(\frac{1}{2}\rho A \int_{\ell} 2\frac{\partial w}{\partial t}\delta\left(\frac{\partial w}{\partial t}\right) dx - \frac{1}{2}EI \int_{\ell} 2\frac{\partial^2 w}{\partial x^2}\delta\left(\frac{\partial^2 w}{\partial x^2}\right) dx\right) dt = 0 \tag{9.13}$$

Integrating expression (9.13) by parts in order to time and space,

$$\begin{aligned}
&\int_{\ell} \left[\rho A \frac{\partial w}{\partial t}\delta w\right]_{t_1}^{t_2} dx - \int_{t_1}^{t_2}\int_{\ell} \rho A \frac{\partial^2 w}{\partial t^2}\delta w dx dt \\
&\quad - \int_{t_1}^{t_2} \left[EI\frac{\partial^2 w}{\partial x^2}\delta\left(\frac{\partial w}{\partial x}\right)\right]_0^{\ell} dt + \int_{t_1}^{t_2}\int_{\ell} EI\frac{\partial^3 w}{\partial x^3}\delta\left(\frac{\partial w}{\partial x}\right) dx dt = 0
\end{aligned} \tag{9.14}$$

Integrating again by parts the last integral term of expression (9.14)

$$\begin{aligned}
&\int_{\ell} \left[\rho A \frac{\partial w}{\partial t}\delta w\right]_{t_1}^{t_2} dx - \int_{t_1}^{t_2}\int_{\ell} \rho A \frac{\partial^2 w}{\partial t^2}\delta w dx dt \\
&\quad - \int_{t_1}^{t_2} \left[EI\frac{\partial^2 w}{\partial x^2}\delta\left(\frac{\partial w}{\partial x}\right)\right]_0^{\ell} dt + \int_{t_1}^{t_2} \left[EI\frac{\partial^3 w}{\partial x^3}\delta w\right]_0^{\ell} dt - \int_{t_1}^{t_2}\int_{\ell} EI\frac{\partial^4 w}{\partial x^4}\delta w dx dt = 0
\end{aligned} \tag{9.15}$$

Expression (9.15) can now be rearranged as

$$\int_{\ell} \underbrace{\left[\rho A \frac{\partial w}{\partial t} \delta w\right]_{t_1}^{t_2}}_{=0} dx \quad + \quad \int_{t_1}^{t_2} \underbrace{\underbrace{\left[EI \frac{\partial^2 w}{\partial x^2} \delta \left(\frac{\partial w}{\partial x}\right)\right]_0^{\ell}}_{bending\ moment} - \underbrace{\left[EI \frac{\partial^3 w}{\partial x^3} \delta w\right]_0^{\ell}}_{shear force}}_{boundary\ conditions} dt$$

$$- \int_{t_1}^{t_2} \int_{\ell} \underbrace{\left[EI \frac{\partial^4 w}{\partial x^4} + \rho A \frac{\partial^2 w}{\partial t^2}\right]}_{equation\ of\ motion} \delta w dx dt = 0 \tag{9.16}$$

The differential equation of motion for the beam without external forces can now be written as

$$EI \frac{\partial^4 w}{\partial x^4} + \rho A \frac{\partial^2 w}{\partial t^2} = 0 \tag{9.17}$$

## 9.3 Spectral solution

The time and space dependent vertical displacement $w(x,t)$ can be written as the sum of a number of $n$ harmonic functions as

$$w(x,t) = \sum_{i=1}^{n} \hat{w}_i(x) e^{j\omega_i t} \tag{9.18}$$

To simplify the notation the sum will from now on be removed, being understood that

$$w(x,t) = \sum_{i=1}^{n} \hat{w}_i(x) e^{j\omega_i t} \quad \Leftrightarrow \quad w(x,t) = \hat{w}_n(x) e^{j\omega_n t} \tag{9.19}$$

Expression (9.19) can now be inserted into the equation of motion (9.17) resulting

$$EI \frac{d^4 \hat{w}}{dx^4} e^{j\omega_n t} - \rho A \omega_n^2 \hat{w} e^{j\omega_n t} = 0 \tag{9.20}$$

being rearranged as

$$EI \frac{d^4 \hat{w}}{dx^4} = \rho A \omega_n^2 \hat{w} \tag{9.21}$$

The differential equation (9.21) is now an ordinary, homogeneous differential equation having as a possible solution one sum of harmonic functions, dependent to $x$, as referred on the next expression

$$\hat{w}(x) = \sum_{m=1}^{p} A_m e^{jk_m x} \tag{9.22}$$

where the coefficients $A_m$ are constant values to be determined according to the boundary conditions applied to the beam and $k_m$ is the commonly known "wave number" [10, 35].

Then, inserting expression (9.22) into (9.21) and performing the necessary derivatives, one obtains

$$EIk_m^4 \sum_{m=1}^{p} A_m e^{jk_m x} = \rho A \omega_n^2 \sum_{m=1}^{p} A_m e^{jk_m x} \tag{9.23}$$

which can be simplified resulting into

$$EIk_m^4 = \rho A \omega_n^2 \tag{9.24}$$

From expression (9.24) four different wave numbers can be determined

$$k_m = \sqrt[4]{\frac{\rho A}{EI}\omega_n^2} \;\vee\; k_m = j\sqrt[4]{\frac{\rho A}{EI}\omega_n^2} \;\vee\; k_m = -\sqrt[4]{\frac{\rho A}{EI}\omega_n^2} \;\vee\; k_m = -j\sqrt[4]{\frac{\rho A}{EI}\omega_n^2} \tag{9.25}$$

Therefore, the solution (9.22) is a sum of four harmonic functions, which was expectable because the differential equation (9.21) has a fourth derivative respecting to $x$. Then, considering $k = \sqrt[4]{\frac{\rho A}{EI}\omega_n^2}$, expression (9.22) can be written as

$$\hat{w}(x) = A_1 e^{kx} + A_2 e^{jkx} + A_3 e^{-kx} + A_4 e^{-jkx} \tag{9.26}$$

Equation (9.26) is the solution for the differential equation of the beam, needing only to be determined the constant amplitudes of the four waves which are dependent of the beam boundary conditions.

The solution is therefore obtained by the combination of four waves, two near-field waves traveling in the positive and negative direction ($e^{-kx}$ and $e^{kx}$) and two propagating waves also traveling in the positive and negative direction ($e^{-jkx}$ and $e^{jkx}$). The near-field waves are evanescent components of the final response because they tend to disappear as the wave travels along the waveguide structure. Propagating waves are harmonic functions which play an important role in boundary reflections. A general representation of these waves for a generic amplitude is given in figure 9.2

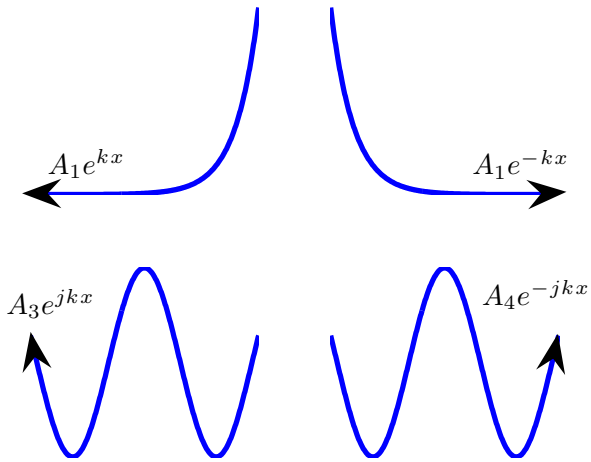


**Figure 9.2:** Generic representations of the waves in the beam.

### 9.3.1 Infinite beam

In this section, it will be obtained a solution for the case of an infinite beam. The beam then extends to minus and plus infinity, being an harmonic force applied at the center point of the beam which is the same to say at point $x = 0$. The described structure is represented in figure 9.3.

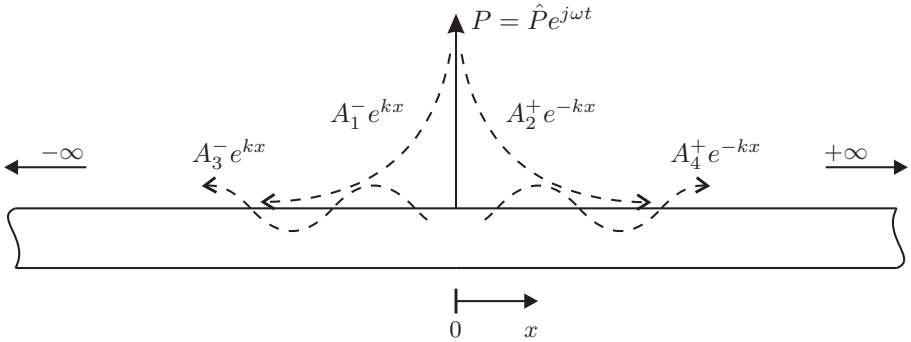


**Figure 9.3:** Infinite beam traveling waves generated by a load at $x = 0$.

According to the geometry of the problem the waves should propagate from the point where the load is applied to infinity. As a consequence, no wave reflections will occur. Then, considering a rigid joint at the harmonic loading point, the solution for this type of beam shall be

$$\hat{w}_-(x) = A_1 e^{kx} + A_3 e^{jkx} \qquad \text{with} \quad x \leq 0 \tag{9.27a}$$

$$\hat{w}_+(x) = A_2 e^{-kx} + A_4 e^{-jkx} \qquad \text{with} \quad x \geq 0 \tag{9.27b}$$

According to the described problem, the displacements continuity about the point $x = 0$ has to be assured. Therefore the following conditions shall be fulfilled:

- displacement continuity

$$\hat{w}_-(0) = \hat{w}_+(0) \quad \Rightarrow \quad A_1 + A_3 = A_2 + A_4 \tag{9.28}$$

- rotation continuity

$$\frac{d\hat{w}_-(0)}{dx} = \frac{d\hat{w}_+(0)}{dx} \quad \Rightarrow \quad kA_1 + jkA_3 = -kA_2 - jkA_4 \tag{9.29}$$

- moment equilibrium

$$EI\frac{d^2\hat{w}_-(0)}{dx^2} = EI\frac{d^2\hat{w}_+(0)}{dx^2} \quad \Rightarrow \quad EI\left(k^2A_1 - k^2A_3\right) = EI\left(k^2A_2 - k^2A_4\right) \tag{9.30}$$

- force equilibrium

$$EI\frac{d^3\hat{w}_+(0)}{dx^3} = \frac{\hat{P}}{2} \quad \Rightarrow \quad EI\left(-k^3A_2 + jk^3A_4\right) = \frac{\hat{P}}{2} \tag{9.31}$$

Equations from (9.28) to (9.31) form a system of four equations, making it possible to obtain the four unknowns $A_1$, $A_2$, $A_3$, $A_4$. Therefore, after manipulating the equations, the system will be

$$\begin{cases} A_1 + A_3 = A_2 + A_4 \\ A_1 + jA_3 = -A_2 - jA_4 \\ A_1 - A_3 = A_2 - A_4 \\ -A_2 + jA_4 = \frac{\hat{P}}{2EIk^3} \end{cases} \tag{9.32}$$

Combining the first and third equations of the system (9.32) leads to

$$\begin{cases} A_1 = A_2 \\ A_1 + jA_3 = -A_2 - jA_4 \\ A_3 = A_4 \\ -A_2 + jA_4 = \frac{\hat{P}}{2EIk^3} \end{cases} \tag{9.33}$$

Then, substituting $A_1$ and $A_3$ into the second equation of system (9.33)

$$\begin{cases} A_1 = A_2 \\ A_2 = -jA_4 \\ A_3 = A_4 \\ -A_2 + jA_4 = \frac{\hat{P}}{2EIk^3} \end{cases} \tag{9.34}$$

Now, substituting $A_2$ into the fourth equation of system (9.34) one obtains

$$\begin{cases} A_1 = A_2 \\ A_2 = -jA_4 \\ A_3 = A_4 \\ jA_4 + jA_4 = \frac{\hat{P}}{2EIk^3} \end{cases} \tag{9.35}$$

Therefore, the obtained values for the constants will be

$$\begin{cases} A_1 = -\frac{\hat{P}}{2EIk^3} \\ A_2 = -\frac{\hat{P}}{2EIk^3} \\ A_3 = -\frac{j\hat{P}}{2EIk^3} \\ A_4 = -\frac{j\hat{P}}{2EIk^3} \end{cases} \tag{9.36}$$

Finally, the solution for the infinite beam treated here will be

$$\hat{w}_-(x) = -\frac{\hat{P}}{2EIk^3}\left(e^{kx} + je^{jkx}\right) \qquad with \quad x \leq 0 \tag{9.37a}$$

$$\hat{w}_+(x) = -\frac{\hat{P}}{2EIk^3}\left(e^{-kx} + je^{-jkx}\right) \qquad with \quad x \geq 0 \tag{9.37b}$$

being $k = \sqrt[4]{\frac{\rho A}{EI}\omega^2}$ the wave number, and the wave speed will then be given by $c = \frac{\omega}{k}$.

In figure 9.4 the wave propagation along time of an infinite beam is represented. In this figure, a beam with $\rho A = 60$kg/m and $EI = 6.42$ N·m$^2$ characteristics, and with a load applied at point $x = 0$ m with unit amplitude $\hat{P} = 1$ N and frequency $\omega = 0.15$ rad/s, was considered.

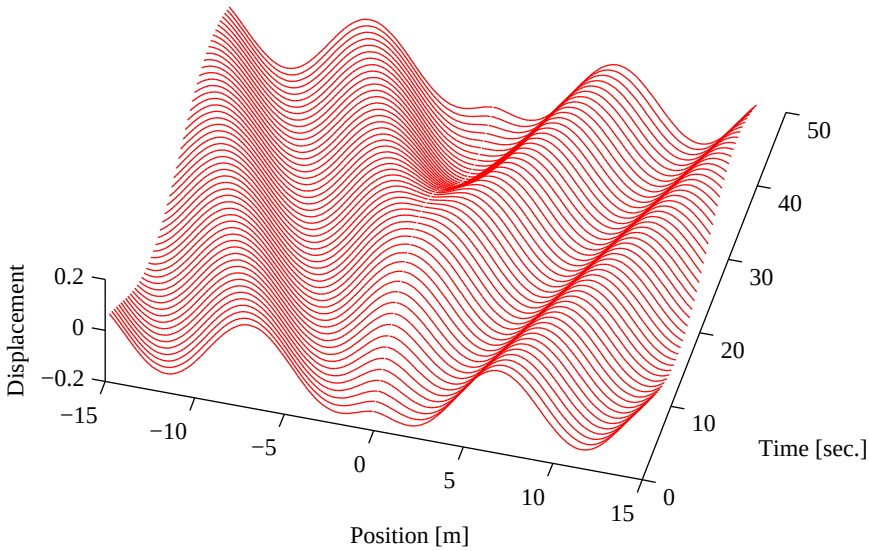


**Figure 9.4:** Infinite free beam traveling waves generated by an harmonic load at $x = 0$.

### 9.3.2 Infinite clamped beam

A different problem will now be solved using the obtained solution in equation (9.26) for the equation of motion of a beam in the frequency domain. The subject structure is now a beam which extends to minus infinity, has an harmonic force applied at point $x = 0$ and is clamped at distance $\ell$, as depicted in figure 9.5.

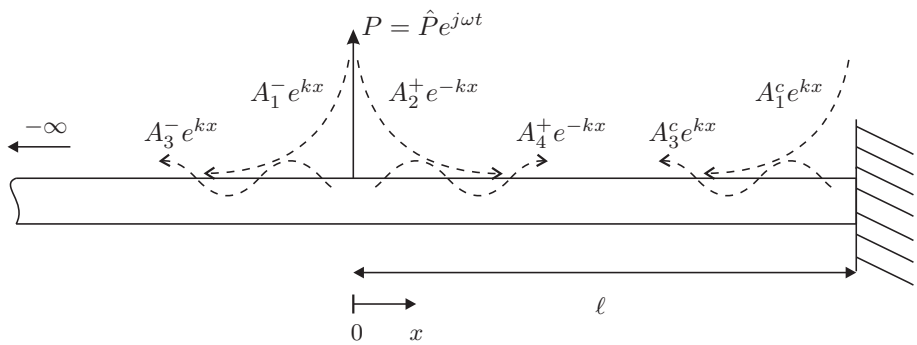


**Figure 9.5:** Infinite clamped beam traveling waves generated by a load at $x = 0$.

Now, considering the problem loading, propagating and near-field waves have to be generated by the applied harmonic load. Those waves are represented in figure 9.5 and have amplitudes $A_1^-$, $A_3^-$, $A_2^+$ and $A_4^+$. Waves traveling in the negative direction from the loading point will never be reflected because they are heading to minus infinity. On the contrary, waves traveling in the positive direction from the loading point will have to be reflected when they find the clamping boundary condition, being therefore, at point $x = \ell$, generated the reflected waves

with amplitudes $A_1^c$ and $A_3^c$. The solution of the equations of motion for this problem will then be

$$\hat{w}_-(x) = A_1^- e^{kx} + A_3^- e^{jkx} \qquad \text{with} \quad x \leq 0 \tag{9.38a}$$

$$\hat{w}_+(x) = A_1^c e^{kx} + A_3^c e^{jkx} + A_2^+ e^{-kx} + A_4^+ e^{-jkx} \qquad \text{with} \quad 0 \leq x \leq \ell \tag{9.38b}$$

According to the described problem, the following boundary conditions have to be respected:

- displacement continuity at $x = 0$

$$\hat{w}_-(0) = \hat{w}_+(0) \quad \Rightarrow \quad A_1^- + A_3^- = A_1^c + A_3^c + A_2^+ + A_4^+ \tag{9.39}$$

- rotation continuity at $x = 0$

$$\frac{d\hat{w}_-(0)}{dx} = \frac{d\hat{w}_+(0)}{dx} \quad \Rightarrow \quad kA_1^- + jkA_3^- = kA_1^c + jkA_3^c - kA_2^+ - jkA_4^+ \tag{9.40}$$

- moment equilibrium at $x = 0$

$$EI\frac{d^2\hat{w}_-(0)}{dx^2} = EI\frac{d^2\hat{w}_+(0)}{dx^2} \quad \Rightarrow \quad k^2A_1^- - k^2A_3^- = k^2A_1^c - k^2A_3^c + k^2A_2^+ - k^2A_4^+ \tag{9.41}$$

- force equilibrium at $x = 0$

$$EI\frac{d^3\hat{w}_-(0)}{dx^3} = \frac{\hat{P}}{2} \quad \Rightarrow \quad EI\left(k^3A_1^- - jk^3A_3^-\right) = \frac{\hat{P}}{2} \tag{9.42}$$

- displacement at $x = \ell$

$$\hat{w}_+(\ell) = 0 \quad \Rightarrow \quad A_1^c e^{k\ell} + A_3^c e^{jk\ell} + A_2^+ e^{-k\ell} + A_4^+ e^{-jk\ell} = 0 \tag{9.43}$$

- rotation at $x = \ell$

$$\frac{d\hat{w}_+(\ell)}{dx} = 0 \quad \Rightarrow \quad ke^{k\ell}A_1^c + jke^{jk\ell}A_3^c - ke^{-k\ell}A_2^+ - jke^{-jk\ell}A_4^+ = 0 \tag{9.44}$$

Equations (9.39) to (9.44) can be arranged as a system of equations as follows

$$\begin{cases} A_1^- + A_3^- - A_1^c - A_3^c - A_2^+ - A_4^+ = 0 \\ A_1^- + jA_3^- - A_1^c - jA_3^c + A_2^+ - jA_4^+ = 0 \\ A_1^- - A_3^- - A_1^c + A_3^c - A_2^+ + A_4^+ = 0 \\ A_1^- - jA_3^- = \frac{\hat{P}}{2EIk^3} \\ A_1^c e^{k\ell} + A_3^c e^{jk\ell} + A_2^+ e^{-k\ell} + A_4^+ e^{-jk\ell} = 0 \\ e^{k\ell}A_1^c + je^{jk\ell}A_3^c - e^{-k\ell}A_2^+ - je^{-jk\ell}A_4^+ = 0 \end{cases} \tag{9.45}$$

The system of equations (9.45) is a linear system of equations and it can be represented in a matrix form

$$\begin{bmatrix} 1 & 1 & -1 & -1 & -1 & -1 \\ 1 & j & -1 & -j & 1 & j \\ 1 & -1 & -1 & 1 & -1 & 1 \\ 1 & -j & 0 & 0 & 0 & 0 \\ 0 & 0 & e^{k\ell} & e^{jk\ell} & e^{-k\ell} & e^{-jk\ell} \\ 0 & 0 & e^{k\ell} & je^{jk\ell} & -e^{-k\ell} & -je^{-jk\ell} \end{bmatrix} \begin{Bmatrix} A_1^- \\ A_3^- \\ A_1^c \\ A_3^c \\ A_2^+ \\ A_4^+ \end{Bmatrix} = \begin{Bmatrix} 0 \\ 0 \\ 0 \\ \frac{\hat{P}}{2EIk^3} \\ 0 \\ 0 \end{Bmatrix} \tag{9.46}$$

The unknown amplitudes from (9.46) can now be determined solving the system of equations. To obtain the referred amplitudes, a Matlab® program was created to compute them and generate the time response.

In figure 9.6 the wave propagation along time of an infinite beam with an harmonic excitation force applied at point $x = 0$ m and clamped at $x = 10$ m is represented. To obtain this wave propagation, a beam with $\rho A = 60$ kg/m and $EI = 6.42$ N·m$^2$ was considered, with the harmonic load having a unit amplitude $\hat{P} = 1$ N and frequency $\omega = 0.15$ rad/s.

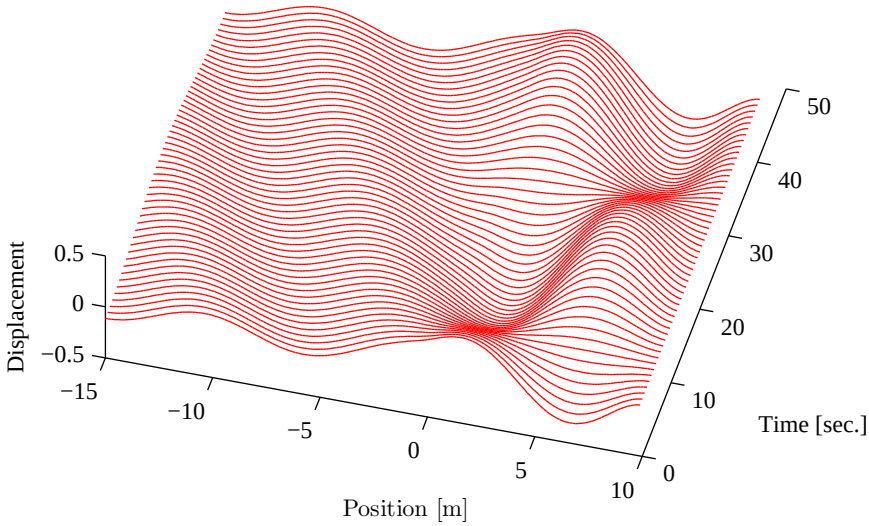


**Figure 9.6:** Infinite clamped beam traveling waves generated by an harmonic load at $x = 0$.

### 9.3.3 Finite free beam

In this section a finite beam with free boundary conditions will be studied, being applied at point with coordinate $x = 0$ an harmonic force $P = \hat{P}e^{jwt}$ as represented in figure 9.7.

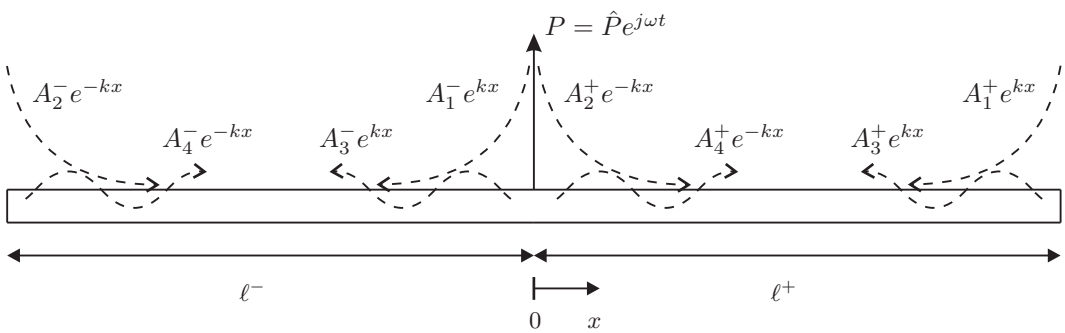


**Figure 9.7:** Finite free beam traveling waves generated by a load at $x = 0$.

Recalling once more equation (9.26), which represents the general solution for the transversal displacement of a *Euler-Bernoulli* beam in the frequency domain, for this section case, the solution will, according to figure 9.7, be

$$\hat{w}_-(x) = A_1^- e^{kx} + A_3^- e^{jkx} + A_2^- e^{-kx} + A_4^- e^{-jkx} \qquad \text{with} \quad -\ell^- \leq x \leq 0 \tag{9.47a}$$

$$\hat{w}_+(x) = A_1^+ e^{kx} + A_3^+ e^{jkx} + A_2^+ e^{-kx} + A_4^+ e^{-jkx} \qquad \text{with} \quad 0 \leq x \leq \ell^+ \tag{9.47b}$$

The applied harmonic force is therefore considered as a discontinuity on the beam length. Therefore, besides the natural boundary conditions, continuity must be assured on the loading point. The boundary conditions considered, have been:

- moment equilibrium at $x = -\ell^-$

$$EI\frac{d^2\hat{w}_-(-\ell^-)}{dx^2} = 0$$

$$\Rightarrow \quad EI\left[k^2 e^{-k\ell^-} A_1^- - k^2 e^{-jk\ell^-} A_3^- + k^2 e^{k\ell^-} A_2^- - k^2 e^{jk\ell^-} A_4^-\right] = 0 \tag{9.48}$$

- force equilibrium at $x = -\ell^-$

$$EI\frac{d^3\hat{w}_-(-\ell^-)}{dx^3} = 0$$

$$\Rightarrow \quad EI\left[k^3 e^{-k\ell^-} A_1^- - jk^3 e^{-jk\ell^-} A_3^- - k^3 e^{k\ell^-} A_2^- + jk^3 e^{jk\ell^-} A_4^-\right] = 0 \tag{9.49}$$

- moment equilibrium at $x = \ell^+$

$$EI\frac{d^2\hat{w}_+(\ell^+)}{dx^2} = 0$$

$$\Rightarrow \quad EI\left[k^2 e^{k\ell^+} A_1^+ - e^{jk\ell^+} k^2 A_3^+ + k^2 e^{-k\ell^+} A_2^- - k^2 e^{-jk\ell^+} A_4^+\right] = 0 \tag{9.50}$$

- force equilibrium at $x = \ell^+$

$$EI\frac{d^3\hat{w}_+(\ell^+)}{dx^3} = 0$$

$$\Rightarrow \quad EI\left[k^3 e^{k\ell^+} A_1^+ - jk^3 e^{jk\ell^+} A_3^+ - k^3 e^{-k\ell^+} A_2^+ + jk^3 e^{-jk\ell^+} A_4^+\right] = 0 \tag{9.51}$$

- displacement continuity at $x = 0$

$$\hat{w}_-(0) = \hat{w}_+(0)$$

$$\Rightarrow \quad A_1^- + A_3^- + A_2^- + A_4^- = A_1^+ + A_3^+ + A_2^+ + A_4^+ \tag{9.52}$$

- rotation continuity at $x = 0$

$$\frac{d\hat{w}_-(0)}{dx} = \frac{\partial\hat{w}_+(0)}{\partial x}$$

$$\Rightarrow \quad kA_1^- + jkA_3^- - kA_2^- - jkA_4^- = kA_1^+ + jkA_3^+ - kA_2^+ - jkA_4^+ \tag{9.53}$$

- moment equilibrium at $x = 0$

$$EI\frac{d^2\hat{w}_-(0)}{dx^2} = EI\frac{d^2\hat{w}_+(0)}{dx^2}$$
$$\Rightarrow \quad k^2A_1^- - k^2A_3^- + k^2A_2^- - k^2A_4^- = k^2A_1^+ - k^2A_3^+ + k^2A_2^+ - k^2A_4^+ \tag{9.54}$$

- force equilibrium at $x = 0$

$$EI\frac{d^3\hat{w}_-(0)}{dx^3} = \frac{\hat{P}}{2}$$
$$\Rightarrow \quad EI\left[k^3A_1^- - k^3A_3^- - k^3A_2^- + k^3A_4^-\right] = \frac{\hat{P}}{2} \tag{9.55}$$

After some modifications, equations from (9.48) to (9.55) are a system of eight equations with eight unknowns,

$$\begin{cases} e^{-k\ell^-}A_1^- - e^{-jk\ell^-}A_3^- + e^{k\ell^-}A_2^- - e^{jk\ell^-}A_4^- = 0 \\ e^{-k\ell^-}A_1^- - je^{-jk\ell^-}A_3^- - e^{k\ell^-}A_2^- + je^{jk\ell^-}A_4^- = 0 \\ e^{k\ell^+}A_1^+ - e^{jk\ell^+}A_3^+ + e^{-k\ell^+}A_2^+ - e^{-jk\ell^+}A_4^+ = 0 \\ e^{k\ell^+}A_1^+ - je^{jk\ell^+}A_3^+ - e^{-k\ell^+}A_2^+ + je^{-jk\ell^+}A_4^+ = 0 \\ A_1^- + A_3^- + A_2^- + A_4^- - A_1^+ - A_3^+ - A_2^+ - A_4^+ = 0 \\ A_1^- + jA_3^- - A_2^- - jA_4^- - A_1^+ - jA_3^+ + A_2^+ + jA_4^+ = 0 \\ A_1^- - A_3^- + A_2^- - A_4^- - A_1^+ + A_3^+ - A_2^+ + A_4^+ = 0 \\ A_1^- - jA_3^- - A_2^- + jA_4^- = \frac{\hat{P}}{2EIk^3} \end{cases} \tag{9.56}$$

The system of equations from (9.56) can be expressed in matrix form becoming

$$\begin{bmatrix} e^{-k\ell^-} & -e^{-jk\ell^-} & e^{k\ell^-} & -e^{jk\ell^-} & 0 & 0 & 0 & 0 \\ e^{-k\ell^-} & -je^{-jk\ell^-} & -e^{k\ell^-} & je^{jk\ell^-} & 0 & 0 & 0 & 0 \\ 0 & 0 & 0 & 0 & e^{k\ell^+} & -e^{jk\ell^+} & e^{-k\ell^+} & -e^{-jk\ell^+} \\ 0 & 0 & 0 & 0 & e^{k\ell^+} & -je^{jk\ell^+} & -e^{-k\ell^+} & je^{-jk\ell^+} \\ 1 & 1 & 1 & 1 & -1 & -1 & -1 & -1 \\ 1 & j & -1 & -j & -1 & -j & 1 & j \\ 1 & -1 & 1 & -1 & -1 & 1 & -1 & 1 \\ 1 & -j & -1 & j & 0 & 0 & 0 & 0 \end{bmatrix} \begin{Bmatrix} A_1^- \\ A_3^- \\ A_2^- \\ A_4^- \\ A_1^+ \\ A_3^+ \\ A_2^+ \\ A_4^+ \end{Bmatrix} = \begin{Bmatrix} 0 \\ 0 \\ 0 \\ 0 \\ 0 \\ 0 \\ 0 \\ \frac{\hat{P}}{2EIk^3} \end{Bmatrix}$$

The unknown amplitudes from the system above can now be determined solving the system of algebraic equations. To obtain them, a Matlab® program was created to compute them and afterward generate the time response.

To generate the time response depicted in figure 9.8 and 9.9, an ordinary aluminum beam with a Young's modulus of $E = 70$ GPa and a Poisson's ratio of $\nu = 0.3$ and having a thickness of $h = 6$ mm, a length of $l = 745$ mm and a width of $b = 40$ mm.

The time responses presented in figures 9.8 and 9.9 were computed considering an excitation force with a unitary amplitude $\hat{P} = 1$ N and a frequency identical to the first two natural frequencies which were obtained using the classical expression from a *Euler-Bernoulli* beam [44, 45].

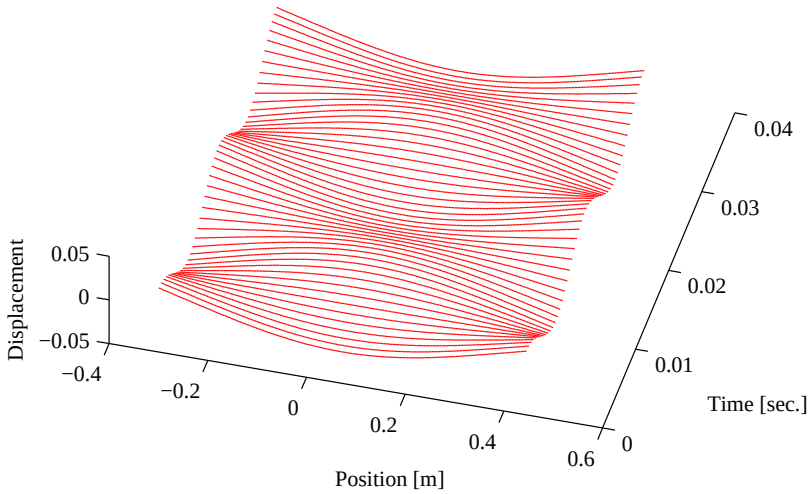


**Figure 9.8:** Finite free beams wave propagation at the first mode.

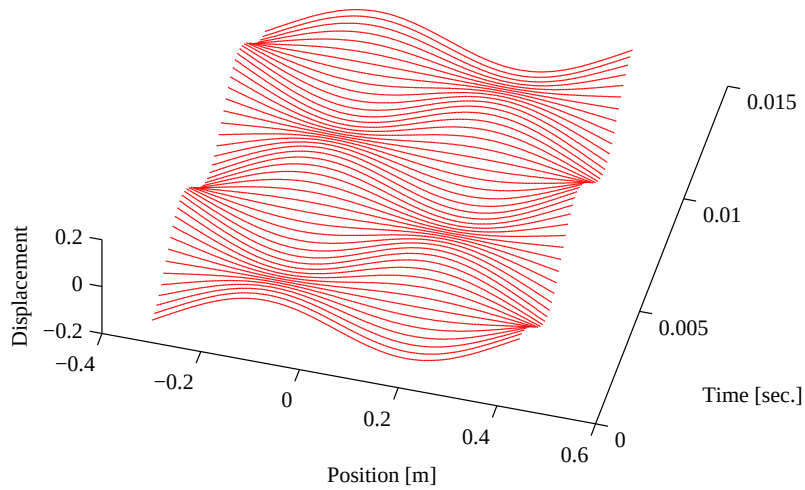


**Figure 9.9:** Finite free beams wave propagation at the second mode.

## 9.4 Spectral finite element

In this section, an approach to the spectral beam finite element formulation, according to *Euler-Bernoulli* theory will be made using the dynamic stiffness matrix concept. The generic element is depicted in figure 9.10.

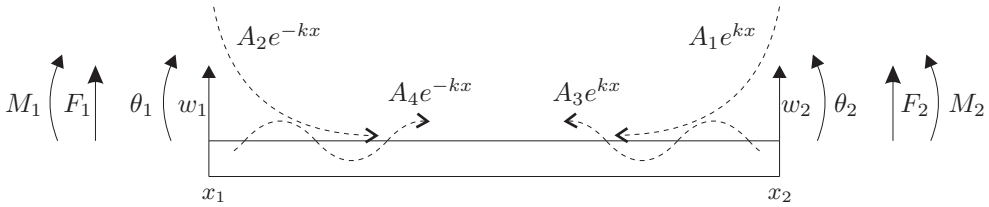


**Figure 9.10:** Spectral beam finite element.

### 9.4.1 *Euler-Bernoulli* theory

The general solution of the differential equation of motion of a *Euler-Bernoulli* beam has already been determined and is now recalled as

$$\hat{w}(x) = A_1e^{kx} + A_3e^{jkx} + A_2e^{-kx} + A_4e^{-jkx} \tag{9.57}$$

where $A_1$, $A_2$, $A_3$ and $A_4$ are constants to be determined according to the boundary conditions and $k$ is the wave number, which for a *Euler-Bernoulli* beam is given by $k = \sqrt[4]{\frac{\rho A}{EI}\omega_n^2}$.

According to the boundary displacement conditions for a length $\ell$ element that starts at $x = x_1$ and ends at $x = x_2$, as the ones depicted in figure 9.10, it can be stated that:

$$\hat{w}_1 = \hat{w}(x_1) = A_1e^{kx_1} + A_3e^{jkx_1} + A_2e^{-kx_1} + A_4e^{-jkx_1} \tag{9.58}$$

$$\hat{\theta}_1 = \frac{d\hat{w}(x_1)}{dx} = A_1ke^{kx_1} + A_3jke^{jkx_1} - A_2ke^{-kx_1} - A_4jke^{-jkx_1} \tag{9.59}$$

$$\hat{w}_2 = \hat{w}(x_2) = A_1e^{kx_2} + A_3e^{jkx_2} + A_2e^{-kx_2} + A_4e^{-jkx_2} \tag{9.60}$$

$$\hat{\theta}_2 = \frac{d\hat{w}(x_2)}{dx} = A_1ke^{kx_2} + A_3jke^{jkx_2} - A_2ke^{-kx_2} - A_4jke^{-jkx_2} \tag{9.61}$$

Expressions from (9.58) to (9.61) can be expressed in a matrix form becoming

$$\begin{Bmatrix} \hat{w}_1 \\ \hat{\theta}_1 \\ \hat{w}_2 \\ \hat{\theta}_2 \end{Bmatrix} = \begin{bmatrix} e^{kx_1} & e^{jkx_1} & e^{-kx_1} & e^{-jkx_1} \\ ke^{kx_1} & jke^{jkx_1} & -ke^{-kx_1} & -jke^{-jkx_1} \\ e^{kx_2} & e^{jkx_2} & e^{-kx_2} & e^{-jkx_2} \\ ke^{kx_2} & jke^{jkx_2} & -ke^{-kx_2} & -jke^{-jkx_2} \end{bmatrix} \begin{Bmatrix} A_1 \\ A_3 \\ A_2 \\ A_4 \end{Bmatrix} \tag{9.62}$$

The matrix multiplication expressed in (9.62) can be simply expressed by

$$\{d\} = [P_d]\{A\} \tag{9.63}$$

where $\{d\}$ is the element displacements vector, $\{A\}$ is a vector of constants and $[P_d]$ is a matrix which relates the displacements with the constants to be determined.

Next, as it has been done for the displacements, the same can be done for the forces at the edges of the element leading to

$$F_1 = EI\frac{d^3\hat{w}\left(x_1\right)}{dx^3} = EIk^3\left(A_1e^{kx_1} - A_3je^{jkx_1} - A_2e^{-kx_1} + A_4je^{-jkx_1}\right) \tag{9.64}$$

$$M_1 = EI\frac{d^2\hat{w}\left(x_1\right)}{dx^2} = EIk^2\left(A_1ke^{kx_1} - A_3ke^{jkx_1} + A_2ke^{-kx_1} - A_4ke^{-jkx_1}\right) \tag{9.65}$$

$$F_2 = -EI\frac{d^3\hat{w}\left(x_2\right)}{dx^3} = -EIk^3\left(A_1e^{kx_2} - A_3je^{jkx_2} - A_2e^{-kx_2} + A_4je^{-jkx_2}\right) \tag{9.66}$$

$$M_2 = -EI\frac{d^2\hat{w}\left(x_2\right)}{dx^2} = -EIk^2\left(A_1ke^{kx_2} - A_3ke^{jkx_2} + A_2ke^{-kx_2} - A_4ke^{-jkx_2}\right) \tag{9.67}$$

Expressions from (9.64) to (9.67) can also be expressed in a matrix form becoming

$$\left\{\begin{array}{c} F_1 \\ M_1 \\ F_2 \\ M_2 \end{array}\right\} = EIk^2\left[\begin{array}{cccc} ke^{kx_1} & -jke^{jkx_1} & -ke^{-kx_1} & jke^{-jkx_1} \\ e^{kx_1} & -e^{jkx_1} & e^{-kx_1} & -e^{-jkx_1} \\ -ke^{kx_2} & jke^{jkx_2} & ke^{-kx_2} & -jke^{-jkx_2} \\ -e^{kx_2} & e^{jkx_2} & -e^{-kx_2} & e^{-jkx_2} \end{array}\right]\left\{\begin{array}{c} A_1 \\ A_3 \\ A_2 \\ A_4 \end{array}\right\} \tag{9.68}$$

The matrix multiplication expressed in (9.68) can be simply expressed by

$$\{f\} = [P_f]\{A\} \tag{9.69}$$

where $\{f\}$ is the element nodal forces vector, $\{A\}$ is a vector of constants already present at (9.63) and $[P_f]$ is a matrix which relates the forces with the constants to be determined.

Expressions (9.63) and (9.69) can now be combined due to having both the vector of constants $\{A\}$, resulting therefore into

$$\{f\} = [P_f]\left[P_d\right]^{-1}\{d\} \tag{9.70}$$

Expression (9.70) can be simplified into

$$[D_k]\{d\} = \{f\} \tag{9.71}$$

where matrix $[D_k]$ represents the dynamic stiffness of the *Euler-Bernoulli* spectral beam element. From this point the relation between forces and displacements can be treated similarly to what is done in the conventional FEM, assembling the beam elements to generate a finite element model of a beam type structure.

### 9.4.2 Layerwise theory

The degrees of freedom for this modified beam element are represented in figure 9.11 and are the following:

- $w$ is the out-of-plane displacement along the beam centerline;
- $u_b$ is the in-plane displacement on the beam lower surface;
- $u_t$ is the in-plane displacement on the beam upper surface;

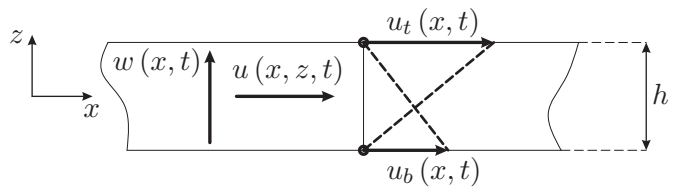


**Figure 9.11:** Single layer beam displacements.

Therefore, the beam in-plane displacement is given by the sum of two effects, one due to the translational effects and other due to the rotational effects, both originated by the two in-plane displacements. Then, the displacement field of this modified beam will be

$$\left\{ \begin{array}{c} u(x,t) \\ w(x,t) \end{array} \right\} = \left\{ \begin{array}{c} \frac{u_t+u_b}{2} + z\frac{u_t-u_b}{h} \\ w \end{array} \right\} \tag{9.72}$$

The strain field can therefore be expressed as

$$\begin{aligned} \{\epsilon\} = \left\{ \begin{array}{c} \epsilon_{xx} \\ \gamma_{xz} \end{array} \right\} &= \left\{ \begin{array}{c} \frac{\partial u}{\partial x} \\ \frac{\partial u}{\partial z} + \frac{\partial w}{\partial x} \end{array} \right\} \\ &= \left\{ \begin{array}{c} \left(\frac{1}{2} + \frac{z}{h}\right)\frac{\partial u_t}{\partial x} + \left(\frac{1}{2} - \frac{z}{h}\right)\frac{\partial u_b}{\partial x} \\ \frac{u_t-u_b}{h} + \frac{\partial w}{\partial x} \end{array} \right\} \end{aligned} \tag{9.73}$$

Considering the beam constitutive law, the stresses will come as

$$\{\sigma\} = \left\{ \begin{array}{c} E\epsilon_{xx} \\ G\gamma_{xz} \end{array} \right\} = \left\{ \begin{array}{c} E\left(\frac{1}{2} + \frac{z}{h}\right)\frac{\partial u_t}{\partial x} + E\left(\frac{1}{2} - \frac{z}{h}\right)\frac{\partial u_b}{\partial x} \\ G\frac{u_t-u_b}{h} + G\frac{\partial w}{\partial x} \end{array} \right\} \tag{9.74}$$

#### Extensional potential energy

By definition, the extensional potential energy for the modified element over the general domain $\Omega$ described shall come as

$$\Pi^{P_\epsilon} = \frac{1}{2}\int_\Omega \sigma_{xx}\epsilon_{xx} d\Omega \tag{9.75}$$

Substituting the stress $\sigma_{xx}$ from expression (9.74) and the strain $\epsilon_{xx}$ from (9.73) into equation (9.75) will result in

$$\Pi^{P_\epsilon} = \frac{1}{2}\int_{\Omega}\left[\left(\frac{1}{2}+\frac{z}{h}\right)\frac{\partial u_t}{\partial x}+\left(\frac{1}{2}-\frac{z}{h}\right)\frac{\partial u_b}{\partial x}\right]E\left[\left(\frac{1}{2}+\frac{z}{h}\right)\frac{\partial u_t}{\partial x}+\left(\frac{1}{2}-\frac{z}{h}\right)\frac{\partial u_b}{\partial x}\right]d\Omega \quad (9.76)$$

The domain $\Omega$ is the beam general domain that can be expressed in terms of $x$, $y$ and $z$. Therefore, expanding expression (9.76) and considering $h$ the beam thickness, $b$ the beam width, and $\ell$ the beam element length defined between the coordinates $x_1$ and $x_2$, will result into

$$\Pi^{P_\epsilon} = \frac{Eb}{2}\int_{\ell}\int_{-h/2}^{h/2}\left(\frac{1}{2}+\frac{z}{h}\right)^2\left(\frac{\partial u_t}{\partial x}\right)^2 + \left(\frac{1}{2}-\frac{z}{h}\right)^2\left(\frac{\partial u_b}{\partial x}\right)^2 + 2\left(\frac{1}{2}+\frac{z}{h}\right)\left(\frac{1}{2}-\frac{z}{h}\right)\frac{\partial u_t}{\partial x}\frac{\partial u_b}{\partial x}dzdx \quad (9.77)$$

Integrating expression (9.77) in order to $z$ will lead to

$$\Pi^{P_\epsilon} = \frac{Eb}{2}\int_{\ell}\frac{h}{3}\left(\frac{\partial u_t}{\partial x}\right)^2+\frac{h}{3}\left(\frac{\partial u_b}{\partial x}\right)^2+\frac{h}{3}\frac{\partial u_t}{\partial x}\frac{\partial u_b}{\partial x}dx \quad (9.78)$$

Expression (9.78) represents then the beam extensional potential energy.

**Shear potential energy**

By definition, the shear potential energy for the modified element described shall come as

$$\Pi^{P_\gamma} = \frac{1}{2}\int_{\Omega}\tau_{xz}\gamma_{xz}d\Omega \quad (9.79)$$

Substituting the stress $\tau_{xz}$ from expression (9.74) and the strain $\gamma_{xz}$ from (9.73) into equation (9.79) will result in to

$$\Pi^{P_\gamma} = \frac{1}{2}\int_{\Omega}\left(\frac{u_t-u_b}{h}+\frac{\partial w}{\partial x}\right)G\left(\frac{u_t-u_b}{h}+\frac{\partial w}{\partial x}\right)d\Omega \quad (9.80)$$

Expanding expression (9.80) and considering $h$ the beam thickness, $b$ the beam width, and $\ell$ the beam element length defined between the coordinates $x_1$ and $x_2$, will result into

$$\Pi^{P_\gamma} = \frac{Gb}{2}\int_{\ell}\int_{-h/2}^{h/2}\left(\frac{\partial w}{\partial x}\right)^2+2\frac{u_t}{h}\frac{\partial w}{\partial x}-2\frac{u_b}{h}\frac{\partial w}{\partial x}+\frac{u_t^2}{h^2}-2\frac{u_tu_b}{h^2}+\frac{u_b^2}{h^2}dzdx \quad (9.81)$$

Integrating expression (9.81) in order to $z$ will lead to

$$\Pi^{P_\gamma} = \frac{Gb}{2}\int_{\ell}h\left(\frac{\partial w}{\partial x}\right)^2+2u_t\frac{\partial w}{\partial x}-2u_b\frac{\partial w}{\partial x}+\frac{u_t^2}{h}-2\frac{u_tu_b}{h}+\frac{u_b^2}{h}dx \quad (9.82)$$

Expression (9.82) represents then the beam shear potential energy.

**Kinetic energy**

By definition, the kinetic energy will come as

$$\Pi^K = \frac{1}{2}\int_{\Omega} \dot{u}\left(x,t\right)\rho\dot{u}\left(x,t\right) + \dot{w}\left(x,t\right)\rho\dot{w}\left(x,t\right)d\Omega \tag{9.83}$$

According to the previously defined displacement field (9.72), the beam velocity field is

$$\begin{aligned}\left\{\begin{array}{c}\dot{u}(x,t)\\ \dot{w}(x,t)\end{array}\right\} = \left\{\begin{array}{c}\frac{\partial u(x,t)}{\partial t}\\ \frac{\partial w(x,t)}{\partial t}\end{array}\right\} &= \left\{\begin{array}{c}\frac{\dot{u}_t+\dot{u}_b}{2} + z\frac{\dot{u}_t-\dot{u}_b}{h}\\ \dot{w}\end{array}\right\}\\ &= \left\{\begin{array}{c}\left(\frac{1}{2}+\frac{z}{h}\right)\dot{u}_t + \left(\frac{1}{2}-\frac{z}{h}\right)\dot{u}_b\\ \dot{w}\end{array}\right\}\end{aligned} \tag{9.84}$$

Substituting the velocity field from (9.84) into (9.83) one obtains

$$\Pi^K = \frac{1}{2}\int_{\Omega}\left[\left(\frac{1}{2}+\frac{z}{h}\right)\dot{u}_t + \left(\frac{1}{2}-\frac{z}{h}\right)\dot{u}_b\right]\rho\left[\left(\frac{1}{2}+\frac{z}{h}\right)\dot{u}_t + \left(\frac{1}{2}-\frac{z}{h}\right)\dot{u}_b\right] + \dot{w}\rho\dot{w}d\Omega \tag{9.85}$$

Integrating expression (9.85) in order to $y$ results into

$$\Pi^K = \frac{\rho b}{2}\int_{\ell}\int_{-h/2}^{h/2}\left(\frac{1}{2}+\frac{z}{h}\right)^2\dot{u}_t^2 + \left(\frac{1}{2}-\frac{z}{h}\right)^2\dot{u}_b^2 + 2\left(\frac{1}{2}+\frac{z}{h}\right)\left(\frac{1}{2}-\frac{z}{h}\right)\dot{u}_t\dot{u}_b + \dot{w}^2 dxdz \tag{9.86}$$

Finally, integrating expression (9.86) in order to $z$ leads to

$$\Pi^K = \frac{\rho b}{2}\int_{\ell}\frac{h}{3}\dot{u}_t^2 + \frac{h}{3}\dot{u}_b^2 + \frac{h}{3}\dot{u}_t\dot{u}_b + h\dot{w}^2 dx \tag{9.87}$$

**Work of external forces**

Considering as being applied a distributed force $q\left(x\right)$ along the beam surface and the applied external forces at the beam element nodes located at $x_1$ and $x_2$, referring each one to the generalized displacements previously described. The work done by external forces on the element is given by

$$\begin{aligned}W^e = &\int_{\ell} q\left(x\right)wdx + F_b\left(x_1\right)u_b\left(x_1\right) + F_b\left(x_2\right)u_b\left(x_2\right)\\ &+F_t\left(x_1\right)u_t\left(x_1\right) + F_t\left(x_2\right)u_t\left(x_2\right) + F_w\left(x_1\right)w\left(x_1\right) + F_w\left(x_2\right)w\left(x_2\right)\end{aligned} \tag{9.88}$$

**Hamilton's principle**

The Hamilton's principle states that

$$\int_{t_1}^{t_2}\left[\delta\left(\Pi^K - \Pi^P + W^e\right)\right]dt = 0 \tag{9.89}$$

where $\Pi^K$ is the beam kinetic energy from (9.87), $\Pi^P$ is the beam total potential energy which means that $\Pi^P = \Pi^{P_\epsilon} + \Pi^{P_\gamma}$ and $W^e$ is the work done by external forces expressed in (9.88).

Substituting the energy expressions into equation (9.89) will lead to

$$\begin{aligned}
\int_{t_1}^{t_2} \Bigg[ \delta \Bigg( & \frac{\rho b}{2} \int_\ell \frac{h}{3}\dot{u}_t^2 + \frac{h}{3}\dot{u}_b^2 + \frac{h}{3}\dot{u}_t\dot{u}_b + h\dot{w}^2 dx \\
& - \frac{Eb}{2} \int_\ell \frac{h}{3}\left(\frac{\partial u_t}{\partial x}\right)^2 + \frac{h}{3}\left(\frac{\partial u_b}{\partial x}\right)^2 + \frac{h}{3}\left(\frac{\partial u_t}{\partial x}\right)\left(\frac{\partial u_b}{\partial x}\right) dx \\
& - \frac{Gb}{2} \int_\ell h\left(\frac{\partial w}{\partial x}\right)^2 + 2u_t\frac{\partial w}{\partial x} - 2u_b\frac{\partial w}{\partial x} + \frac{u_t^2}{h} - 2\frac{u_t u_b}{h} + \frac{u_b^2}{h} dx \Bigg) + \delta W^e \Bigg] dt = 0 \quad (9.90)
\end{aligned}$$

where the variational of the work of the external forces $\delta W^e$ shall be given, according to (9.88), by

$$\begin{aligned}
\delta W^e = & \int_\ell q(x)\,\delta w dx + F_b(x_1)\,\delta u_b(x_1) + F_b(x_2)\,\delta u_b(x_2) \\
& + F_t(x_1)\,\delta u_t(x_1) + F_t(x_2)\,\delta u_t(x_2) + F_w(x_1)\,\delta w(x_1) + F_w(x_2)\,\delta w(x_2) \qquad (9.91)
\end{aligned}$$

Applying the variational $\delta$ to the expression inside the parenthesis in equation (9.90), it will be obtained

$$\begin{aligned}
& \frac{\rho b}{2} \int_{t_1}^{t_2}\int_\ell \frac{2h}{3}\dot{u}_t\delta\dot{u}_t + \frac{2h}{3}\dot{u}_b\delta\dot{u}_b + \frac{h}{3}\dot{u}_t\delta\dot{u}_b + \frac{h}{3}\dot{u}_b\delta\dot{u}_t + 2h\dot{w}\delta\dot{w} dx dt \\
& - \frac{Eb}{2} \int_{t_1}^{t_2}\int_\ell \frac{2h}{3}\frac{\partial u_t}{\partial x}\delta\left(\frac{\partial u_t}{\partial x}\right) + \frac{2h}{3}\frac{\partial u_b}{\partial x}\delta\left(\frac{\partial u_b}{\partial x}\right) + \frac{h}{3}\frac{\partial u_t}{\partial x}\delta\left(\frac{\partial u_b}{\partial x}\right) + \frac{h}{3}\frac{\partial u_b}{\partial x}\delta\left(\frac{\partial u_t}{\partial x}\right) dx dt \\
& - \frac{Gb}{2} \int_{t_1}^{t_2}\int_\ell 2h\frac{\partial w}{\partial x}\delta\left(\frac{\partial w}{\partial x}\right) + 2u_t\delta\left(\frac{\partial w}{\partial x}\right) + 2\frac{\partial w}{\partial x}\delta u_t - 2u_b\delta\left(\frac{\partial w}{\partial x}\right) - 2\frac{\partial w}{\partial x}\delta u_b \\
& + 2\frac{u_t}{h}\delta u_t - 2\frac{u_t}{h}\delta u_b - 2\frac{u_b}{h}\delta u_t + 2\frac{u_b}{h}\delta u_b dx dt + \int_{t_1}^{t_2} \delta W^e dt = 0 \qquad (9.92)
\end{aligned}$$

Integrating by parts the first integral on expression (9.92) in order to $t$ and the second in

order to $x$, and rearranging the third integral results in

$$
\begin{aligned}
&\left[\frac{\rho b}{2}\int_{\ell}\frac{2h}{3}\dot{u}_t\delta u_t+\frac{2h}{3}\dot{u}_b\delta u_b+\frac{h}{3}\dot{u}_t\delta u_b+\frac{h}{3}\dot{u}_b\delta u_t+2h\dot{w}\delta w dx\right]_{t_1}^{t_2}\\
&\quad-\frac{\rho b}{2}\int_{t_1}^{t_2}\int_{\ell}\frac{2h}{3}\ddot{u}_t\delta u_t+\frac{2h}{3}\ddot{u}_b\delta u_b+\frac{h}{3}\ddot{u}_t\delta u_b+\frac{h}{3}\ddot{u}_b\delta u_t+2h\ddot{w}\delta w dxdt\\
&\quad-\left[\frac{Eb}{2}\int_{t_1}^{t_2}\frac{2h}{3}\frac{\partial u_t}{\partial x}\delta u_t+\frac{2h}{3}\frac{\partial u_b}{\partial x}\delta u_b+\frac{h}{3}\frac{\partial u_t}{\partial x}\delta u_b+\frac{h}{3}\frac{\partial u_b}{\partial x}\delta u_t dt\right]_{x_1}^{x_2}\\
&\quad+\frac{Eb}{2}\int_{t_1}^{t_2}\int_{\ell}\frac{2h}{3}\frac{\partial^2 u_t}{\partial x^2}\delta u_t+\frac{2h}{3}\frac{\partial^2 u_b}{\partial x^2}\delta u_b+\frac{h}{3}\frac{\partial^2 u_t}{\partial x^2}\delta u_b+\frac{h}{3}\frac{\partial^2 u_b}{\partial x^2}\delta u_t dxdt\\
&\quad-\frac{Gb}{2}\int_{t_1}^{t_2}\int_{\ell}2\frac{\partial w}{\partial x}\delta u_t-2\frac{\partial w}{\partial x}\delta u_b+2\frac{u_t}{h}\delta u_t-2\frac{u_t}{h}\delta u_b-2\frac{u_b}{h}\delta u_t+2\frac{u_b}{h}\delta u_b dxdt\\
&\quad-\frac{Gb}{2}\int_{t_1}^{t_2}\int_{\ell}2h\frac{\partial w}{\partial x}\delta\left(\frac{\partial w}{\partial x}\right)+2u_t\delta\left(\frac{\partial w}{\partial x}\right)-2u_b\delta\left(\frac{\partial w}{\partial x}\right)dxdt+\int_{t_1}^{t_2}\delta W^e dt=0 \qquad (9.93)
\end{aligned}
$$

Now, integrating by parts in order to $x$ the last double integral from expression (9.93), and replacing the variational of the work of the external forces given in (9.91) will result on the

following expression;

$$
\begin{aligned}
&\left[\frac{\rho b}{2}\int_{\ell}\frac{2h}{3}\dot{u}_t\delta u_t+\frac{2h}{3}\dot{u}_b\delta u_b+\frac{h}{3}\dot{u}_t\delta u_b+\frac{h}{3}\dot{u}_b\delta u_t+2h\dot{w}\delta w dx\right]_{t_1}^{t_2}\\
&\quad-\frac{\rho b}{2}\int_{t_1}^{t_2}\int_{\ell}\frac{2h}{3}\ddot{u}_t\delta u_t+\frac{2h}{3}\ddot{u}_b\delta u_b+\frac{h}{3}\ddot{u}_t\delta u_b+\frac{h}{3}\ddot{u}_b\delta u_t+2h\ddot{w}\delta w dxdt\\
&\quad-\left[\frac{Eb}{2}\int_{t_1}^{t_2}\frac{2h}{3}\frac{\partial u_t}{\partial x}\delta u_t+\frac{2h}{3}\frac{\partial u_b}{\partial x}\delta u_b+\frac{h}{3}\frac{\partial u_t}{\partial x}\delta u_b+\frac{h}{3}\frac{\partial u_b}{\partial x}\delta u_t dt\right]_{x_1}^{x_2}\\
&\quad+\frac{Eb}{2}\int_{t_1}^{t_2}\int_{\ell}\frac{2h}{3}\frac{\partial^2 u_t}{\partial x^2}\delta u_t+\frac{2h}{3}\frac{\partial^2 u_b}{\partial x^2}\delta u_b+\frac{h}{3}\frac{\partial^2 u_t}{\partial x^2}\delta u_b+\frac{h}{3}\frac{\partial^2 u_b}{\partial x^2}\delta u_t dxdt\\
&\quad-\frac{Gb}{2}\int_{t_1}^{t_2}\int_{\ell}2\frac{\partial w}{\partial x}\delta u_t-2\frac{\partial w}{\partial x}\delta u_b+2\frac{u_t}{h}\delta u_t-2\frac{u_t}{h}\delta u_b-2\frac{u_b}{h}\delta u_t+2\frac{u_b}{h}\delta u_b dxdt\\
&\quad-\left[\frac{Gb}{2}\int_{t_1}^{t_2}2h\frac{\partial w}{\partial x}\delta w+2u_t\delta w-2u_b\delta w dt\right]_{x_1}^{x_2}+\frac{Gb}{2}\int_{t_1}^{t_2}\int_{\ell}2h\frac{\partial^2 w}{\partial x^2}\delta w+2\frac{\partial u_t}{\partial x}\delta w-2\frac{\partial u_b}{\partial x}\delta w dxdt\\
&\quad+\int_{t_1}^{t_2}\int_{\ell}q\left(x\right)\delta w dxdt+\int_{t_1}^{t_2}F_b\left(x_1\right)\delta u_b\left(x_1\right)+F_b\left(x_2\right)\delta u_b\left(x_2\right)dt\\
&\quad+\int_{t_1}^{t_2}F_t\left(x_1\right)\delta u_t\left(x_1\right)+F_t\left(x_2\right)\delta u_t\left(x_2\right)dt+\int_{t_1}^{t_2}F_w\left(x_1\right)\delta w\left(x_1\right)+F_w\left(x_2\right)\delta w\left(x_2\right)dt=0 \quad (9.94)
\end{aligned}
$$

The first term between square brackets in expression (9.94) is zero. But, besides that, there are some important explanations and descriptions that have to be done for a better understanding of the following formulation steps.

The other terms between square brackets refer to definite integrals evaluated between $x_1$ and $x_2$, therefore the terms inside the brackets have to be evaluated on those two points. As it can be seen, the terms in the last two lines refer to the forces applied on the element, and for the particular case of the forces applied on the nodes, the terms are already evaluated on points $x_1$ and $x_2$. Therefore, on the next equation the referred terms in equation (9.94) were rearranged

in order to be grouped according to the degrees of freedom to which it is referred.

$$
\begin{aligned}
&\left[\frac{\rho b}{2}\int_{\ell}\frac{2h}{3}\dot{u}_t\delta u_t+\frac{2h}{3}\dot{u}_b\delta u_b+\frac{h}{3}\dot{u}_t\delta u_b+\frac{h}{3}\dot{u}_b\delta u_t+2h\dot{w}\delta w dx\right]_{t_1}^{t_2}\\
&\quad+\int_{t_1}^{t_2}F_w\left(x_1\right)\delta w\left(x_1\right)+F_w\left(x_2\right)\delta w\left(x_2\right)dt+\left[\int_{t_1}^{t_2}\left(-Gbh\frac{\partial w}{\partial x}-Gbu_t+Gbu_b\right)\delta w dt\right]_{x_1}^{x_2}\\
&\quad+\int_{t_1}^{t_2}F_b\left(x_1\right)\delta u_b\left(x_1\right)+F_b\left(x_2\right)\delta u_b\left(x_2\right)dt+\left[\int_{t_1}^{t_2}\left(-\frac{Ebh}{6}\frac{\partial u_t}{\partial x}-\frac{Ebh}{3}\frac{\partial u_b}{\partial x}\right)\delta u_b dt\right]_{x_1}^{x_2}\\
&\quad+\int_{t_1}^{t_2}F_t\left(x_1\right)\delta u_t\left(x_1\right)+F_t\left(x_2\right)\delta u_t\left(x_2\right)dt+\left[\int_{t_1}^{t_2}\left(-\frac{Ebh}{3}\frac{\partial u_t}{\partial x}-\frac{Ebh}{6}\frac{\partial u_b}{\partial x}\right)\delta u_t dt\right]_{x_1}^{x_2}\\
&\quad+\int_{t_1}^{t_2}\int_{\ell}\left[-\frac{\rho b}{2}\left(\frac{2h}{3}\ddot{u}_t+\frac{h}{3}\ddot{u}_b\right)+\frac{Eb}{2}\left(\frac{2h}{3}\frac{\partial^2 u_t}{\partial x^2}+\frac{h}{3}\frac{\partial^2 u_b}{\partial x^2}\right)-\frac{Gb}{2}\left(2\frac{\partial w}{\partial x}+2\frac{u_t}{h}-2\frac{u_b}{h}\right)\right]\delta u_t\\
&\quad+\left[-\frac{\rho b}{2}\left(\frac{2h}{3}\ddot{u}_b+\frac{h}{3}\ddot{u}_t\right)+\frac{Eb}{2}\left(\frac{2h}{3}\frac{\partial^2 u_b}{\partial x^2}+\frac{h}{3}\frac{\partial^2 u_t}{\partial x^2}\right)-\frac{Gb}{2}\left(-2\frac{\partial w}{\partial x}-2\frac{u_t}{h}+2\frac{u_b}{h}\right)\right]\delta u_b\\
&\quad+\left[-\frac{\rho b}{2}\left(2h\ddot{w}\right)+\frac{Gb}{2}\left(2h\frac{\partial^2 w}{\partial x^2}+2\frac{\partial u_t}{\partial x}-2\frac{\partial u_b}{\partial x}\right)+q\left(x\right)\right]\delta w dx dt=0
\end{aligned}
\tag{9.95}
$$

The equations of motion in the time domain can now be extracted from the last three lines of equation (9.95)

$$
\begin{cases}
-\frac{\rho b}{2}\left(\frac{2h}{3}\ddot{u}_t+\frac{h}{3}\ddot{u}_b\right)+\frac{Eb}{2}\left(\frac{2h}{3}\frac{\partial^2 u_t}{\partial x^2}+\frac{h}{3}\frac{\partial^2 u_b}{\partial x^2}\right)-\frac{Gb}{2}\left(2\frac{\partial w}{\partial x}+2\frac{u_t}{h}-2\frac{u_b}{h}\right)=0\\
-\frac{\rho b}{2}\left(\frac{2h}{3}\ddot{u}_b+\frac{h}{3}\ddot{u}_t\right)+\frac{Eb}{2}\left(\frac{2h}{3}\frac{\partial^2 u_b}{\partial x^2}+\frac{h}{3}\frac{\partial^2 u_t}{\partial x^2}\right)-\frac{Gb}{2}\left(-2\frac{\partial w}{\partial x}-2\frac{u_t}{h}+2\frac{u_b}{h}\right)=0\\
-\frac{\rho b}{2}\left(2h\ddot{w}\right)+\frac{Gb}{2}\left(2h\frac{\partial^2 w}{\partial x^2}+2\frac{\partial u_t}{\partial x}-2\frac{\partial u_b}{\partial x}\right)+q\left(x\right)=0
\end{cases}
\tag{9.96}
$$

The associated boundary conditions at each end of the beam are obtained expanding the expressions corresponding to the second, third and fourth line of equation (9.95). The boundary conditions can then be grouped by degree of freedom and position where are applied, as follows

$$w \quad : \quad x=x_1 \quad \Rightarrow \quad F_w=-Gbh\frac{\partial w}{\partial x}-Gbu_t+Gbu_b \tag{9.97a}$$

$$u_b \quad : \quad x=x_1 \quad \Rightarrow \quad F_{u_b}=-\frac{Ebh}{6}\frac{\partial u_t}{\partial x}-\frac{Ebh}{3}\frac{\partial u_b}{\partial x} \tag{9.97b}$$

$$u_t \quad : \quad x=x_1 \quad \Rightarrow \quad F_{u_t}=-\frac{Ebh}{3}\frac{\partial u_t}{\partial x}-\frac{Ebh}{6}\frac{\partial u_b}{\partial x} \tag{9.97c}$$

$$w \quad : \quad x=x_2 \quad \Rightarrow \quad F_w=Gbh\frac{\partial w}{\partial x}+Gbu_t-Gbu_b \tag{9.97d}$$

$$u_b \quad : \quad x = x_2 \quad \Rightarrow \quad F_{u_b} = \frac{Ebh}{6}\frac{\partial u_t}{\partial x} + \frac{Ebh}{3}\frac{\partial u_b}{\partial x} \tag{9.97e}$$

$$u_t \quad : \quad x = x_2 \quad \Rightarrow \quad F_{u_t} = \frac{Ebh}{3}\frac{\partial u_t}{\partial x} + \frac{Ebh}{6}\frac{\partial u_b}{\partial x} \tag{9.97f}$$

Similarly to what has been done to the *Euler-Bernoulli* beam, the degrees of freedom $w$, $u_b$ and $u_t$ can be expressed as a sum of harmonic functions that are frequency dependent, being expressed as

$$w = \hat{w}e^{j\omega t} \quad (9.98a) \qquad u_b = \hat{u}_b e^{j\omega t} \quad (9.98b) \qquad u_t = \hat{u}_t e^{j\omega t} \quad (9.98c)$$

Substituting expressions (9.98a) to (9.98c) into (9.96) and expanding the terms of this expression will result in

$$\begin{cases} \rho\frac{bh}{3}\omega^2\hat{u}_t + \rho\frac{bh}{6}\omega^2\hat{u}_b + E\frac{bh}{3}\frac{d^2\hat{u}_t}{dx^2} + E\frac{bh}{6}\frac{d^2\hat{u}_b}{dx^2} - Gb\frac{d\hat{w}}{dx} - \frac{Gb}{h}\hat{u}_t + \frac{Gb}{h}\hat{u}_b = 0 \\ \rho\frac{bh}{6}\omega^2\hat{u}_t + \rho\frac{bh}{3}\omega^2\hat{u}_b + E\frac{bh}{6}\frac{d^2\hat{u}_t}{dx^2} + E\frac{bh}{3}\frac{d^2\hat{u}_b}{dx^2} + Gb\frac{d\hat{w}}{dx} + \frac{Gb}{h}\hat{u}_t - \frac{Gb}{h}\hat{u}_b = 0 \\ \rho bh\omega^2\hat{w} + Gbh\frac{d^2\hat{w}}{dx^2} + Gb\frac{d\hat{u}_t}{dx} - Gb\frac{d\hat{u}_b}{dx} = 0 \end{cases} \tag{9.99}$$

Expanding the degrees of freedom as a sum of harmonics throughout the length as

$$\hat{w} = \mathbf{A}e^{-jkx} \quad (9.100a) \qquad \hat{u}_b = \mathbf{B}e^{-jkx} \quad (9.100b) \qquad \hat{u}_t = \mathbf{C}e^{-jkx} \quad (9.100c)$$

and inserting equations (9.100a) to (9.100c) into (9.99) will lead to

$$\begin{cases} \rho\frac{bh}{3}\omega^2\mathbf{C} + \rho\frac{bh}{6}\omega^2\mathbf{B} - E\frac{bh}{3}k^2\mathbf{C} - E\frac{bh}{6}k^2\mathbf{B} + jGbk\mathbf{A} - \frac{Gb}{h}\mathbf{C} + \frac{Gb}{h}\mathbf{B} = 0 \\ \rho\frac{bh}{6}\omega^2\mathbf{C} + \rho\frac{bh}{3}\omega^2\mathbf{B} - E\frac{bh}{6}k^2\mathbf{C} - E\frac{bh}{3}k^2\mathbf{B} - jGbk\mathbf{A} + \frac{Gb}{h}\mathbf{C} - \frac{Gb}{h}\mathbf{B} = 0 \\ \rho bh\omega^2\mathbf{A} - Gbhk^2\mathbf{A} - jGbk\mathbf{C} + jGbk\mathbf{B} = 0 \end{cases} \tag{9.101}$$

The system of equations (9.101) can be rearranged into

$$\begin{cases} (jGbk)\,\mathbf{A} + \left(\rho\frac{bh}{6}\omega^2 - E\frac{bh}{6}k^2 + \frac{Gb}{h}\right)\mathbf{B} + \left(\rho\frac{bh}{3}\omega^2 - E\frac{bh}{3}k^2 - \frac{Gb}{h}\right)\mathbf{C} = 0 \\ (-jGbk)\,\mathbf{A} + \left(\rho\frac{bh}{3}\omega^2 - E\frac{bh}{3}k^2 - \frac{Gb}{h}\right)\mathbf{B} + \left(\rho\frac{bh}{6}\omega^2 - E\frac{bh}{6}k^2 + \frac{Gb}{h}\right)\mathbf{C} = 0 \\ \left(\rho bh\omega^2 - Gbhk^2\right)\mathbf{A} + (jGbk)\,\mathbf{B} + (-jGbk)\,\mathbf{C} = 0 \end{cases} \tag{9.102}$$

The system of equations (9.102) can now be expressed in a matrix form

$$\begin{bmatrix} (jGbk) & \left(\rho\frac{bh}{6}\omega^2 - E\frac{bh}{6}k^2 + \frac{Gb}{h}\right) & \left(\rho\frac{bh}{3}\omega^2 - E\frac{bh}{3}k^2 - \frac{Gb}{h}\right) \\ (-jGbk) & \left(\rho\frac{bh}{3}\omega^2 - E\frac{bh}{3}k^2 - \frac{Gb}{h}\right) & \left(\rho\frac{bh}{6}\omega^2 - E\frac{bh}{6}k^2 + \frac{Gb}{h}\right) \\ \left(\rho bh\omega^2 - Gbhk^2\right) & (jGbk) & (-jGbk) \end{bmatrix} \begin{Bmatrix} \mathbf{A} \\ \mathbf{B} \\ \mathbf{C} \end{Bmatrix} = \begin{Bmatrix} 0 \\ 0 \\ 0 \end{Bmatrix} \tag{9.103}$$

The characteristic equation of the system (9.103) shall be a polynomial equation in order to the wave number $k$, as follows

$$\mathbf{Y}_6 k^6 + \mathbf{Y}_4 k^4 + \mathbf{Y}_2 k^2 + \mathbf{Y}_0 = 0 \tag{9.104}$$

where $\mathbf{Y}_6$, $\mathbf{Y}_4$, $\mathbf{Y}_2$ and $\mathbf{Y}_0$ are terms not dependent of $k$. Solving equation (9.104) will lead to six wave numbers or three pairs of negative/positive wave numbers. From now on the wave numbers will be considered by its indexes, from 1 to 6. Therefore, the solutions in the frequency domain for the three degrees of freedom will be

$$\hat{w} = \sum_{i=1}^{6} \mathbf{A}_i e^{-jk_i x} \quad (9.105a) \qquad \hat{u}_b = \sum_{i=1}^{6} \mathbf{B}_i e^{-jk_i x} \quad (9.105b) \qquad \hat{u}_t = \sum_{i=1}^{6} \mathbf{C}_i e^{-jk_i x} \quad (9.105c)$$

Now, from the system of equations (9.102) one can obtain a relation between each constant associated with each wave number. Then, adding the second equation of system (9.102) to the first will lead to

$$\begin{cases} \left(\rho\frac{bh}{2}\omega^2 - E\frac{bh}{2}k^2\right)\mathbf{B}_i + \left(\rho\frac{bh}{2}\omega^2 - E\frac{bh}{2}k^2\right)\mathbf{C}_i = 0 \\ (-jGbk)\,\mathbf{A}_i + \left(\rho\frac{bh}{3}\omega^2 - E\frac{bh}{3}k^2 - \frac{Gb}{h}\right)\mathbf{B}_i + \left(\rho\frac{bh}{6}\omega^2 - E\frac{bh}{6}k^2 + \frac{Gb}{h}\right)\mathbf{C}_i = 0 \\ \left(-\rho bh - Gbhk^2\omega^2\right)\mathbf{A}_i + (jGbk)\,\mathbf{B}_i + (-jGbk)\,\mathbf{C}_i = 0 \end{cases} \tag{9.106}$$

From the first equation of expression (9.106) it can be seen that $\mathbf{B}_i = -\mathbf{C}_i$. Substituting this relation into the second and third equations of the system

$$\begin{cases} \mathbf{B}_i = -\mathbf{C}_i \\ (-jGbk)\,\mathbf{A}_i + \left(\rho\frac{bh}{6}\omega^2 - E\frac{bh}{6}k^2 - 2\frac{Gb}{h}\right)\mathbf{B}_i = 0 \\ \left(-\rho bh - Gbhk^2\omega^2\right)\mathbf{A}_i - 2jGbk\mathbf{C}_i = 0 \end{cases} \tag{9.107}$$

The final relation between constants will be

$$\begin{cases} \mathbf{B}_i = -\mathbf{C}_i \\ \mathbf{B}_i = \frac{jGbk}{\rho\frac{bh}{6}\omega^2 - E\frac{bh}{6}k^2 - 2\frac{Gb}{h}}\mathbf{A}_i \\ \mathbf{C}_i = \frac{\rho bh - Gbhk^2\omega^2}{2jGbk}\mathbf{A}_i \end{cases} \tag{9.108}$$

Considering then that

$$\lambda_i = \frac{jGbk}{\rho\frac{bh}{6}\omega^2 - E\frac{bh}{6}k^2 - 2\frac{Gb}{h}} \tag{9.109}$$

and

$$\mu_i = \frac{\rho bh - Gbhk^2\omega^2}{2jGbk} \tag{9.110}$$

The system of equations (9.108) can be expressed as

$$\begin{cases} \mathbf{B}_i = -\mathbf{C}_i \\ \mathbf{B}_i = \lambda_i \mathbf{A}_i \\ \mathbf{C}_i = \mu_i \mathbf{A}_i \end{cases} \tag{9.111}$$

For notation convenience, the solutions written in the form of a sum in (9.105a) to (9.105c) can be expressed as a vector multiplication

$$\hat{w} = \{\phi\}^{\mathbf{T}} \{\mathbf{A}\} \quad (9.112a) \qquad \hat{u}_b = \{\phi\}^{\mathbf{T}} \{\mathbf{B}\} \quad (9.112b) \qquad \hat{u}_t = \{\phi\}^{\mathbf{T}} \{\mathbf{C}\} \quad (9.112c)$$

where

$$\{\phi\} = \left\{ \begin{array}{cccccc} e^{jk_1x} & e^{jk_2x} & e^{jk_3x} & e^{jk_4x} & e^{jk_5x} & e^{jk_6x} \end{array} \right\}^{\mathbf{T}} \tag{9.113}$$

$$\{\mathbf{A}\} = \left\{ \begin{array}{cccccc} \mathbf{A}_1 & \mathbf{A}_2 & \mathbf{A}_3 & \mathbf{A}_4 & \mathbf{A}_5 & \mathbf{A}_6 \end{array} \right\}^{\mathbf{T}} \tag{9.114}$$

$$\{\mathbf{B}\} = \left\{ \begin{array}{cccccc} \mathbf{B}_1 & \mathbf{B}_2 & \mathbf{B}_3 & \mathbf{B}_4 & \mathbf{B}_5 & \mathbf{B}_6 \end{array} \right\}^{\mathbf{T}} \tag{9.115}$$

$$\{\mathbf{C}\} = \left\{ \begin{array}{cccccc} \mathbf{C}_1 & \mathbf{C}_2 & \mathbf{C}_3 & \mathbf{C}_4 & \mathbf{C}_5 & \mathbf{C}_6 \end{array} \right\}^{\mathbf{T}} \tag{9.116}$$

Taking into account the relations from (9.111), the solutions from (9.112a) to (9.112c) can be written as

$$\hat{w} = \{\phi\}^{\mathbf{T}} \{\mathbf{A}\} \quad (9.117a) \qquad \hat{u}_b = \{\phi\}^{\mathbf{T}} \lceil \lambda_i \rfloor \{\mathbf{A}\} \quad (9.117b) \qquad \hat{u}_t = \{\phi\}^{\mathbf{T}} \lceil \mu_i \rfloor \{\mathbf{A}\} \quad (9.117c)$$

where the matrices $\lceil \lambda_i \rfloor$ and $\lceil \mu_i \rfloor$ only have values in the diagonal and those values are respectively $\lambda_i$ and $\mu_i$. Therefore, the displacements at the nodes of the element can be found in order to the constants $\{\mathbf{A}\}$ as follows

$$\{d\} = [P_d] \{\mathbf{A}\} \tag{9.118}$$

where the nodal displacements are

$$\{d\} = \left\{ \begin{array}{cccccc} \hat{w}^1 & \hat{u}_b^1 & \hat{u}_t^1 & \hat{w}^2 & \hat{u}_b^2 & \hat{u}_t^2 \end{array} \right\}^{\mathbf{T}} \tag{9.119}$$

and the matrix $[P_d]$, which is a $6 \times 6$ matrix, relates the nodal displacements and the constants

is given by

$$[P_d] = \begin{bmatrix} \{\phi(x_1)\}^{\mathrm{T}} \\ \{\phi(x_1)\}^{\mathbf{T}} \lceil \lambda_i \rfloor \\ \{\phi(x_1)\}^{\mathbf{T}} \lceil \mu_i \rfloor \\ \{\phi(x_2)\}^{\mathbf{T}} \\ \{\phi(x_2)\}^{\mathbf{T}} \lceil \lambda_i \rfloor \\ \{\phi(x_2)\}^{\mathbf{T}} \lceil \mu_i \rfloor \end{bmatrix}_{6\times 6} \tag{9.120}$$

The forces at the nodes of the element can also be found in order to the constants $\{\mathbf{A}\}$ as follows

$$\{F\} = [P_f]\{\mathbf{A}\} \tag{9.121}$$

where the nodal forces shall be given by

$$\{F\} = \left\{ \begin{array}{cccccc} \hat{F}_v^1 & \hat{F}_{u_b}^1 & \hat{F}_{u_t}^1 & \hat{F}_v^2 & \hat{F}_{u_b}^2 & \hat{F}_{u_t}^2 \end{array} \right\}^{\mathbf{T}} \tag{9.122}$$

and the matrix $[P_f]$, which is a $6 \times 6$ matrix, relates the nodal forces and the constants. This matrix can be derived from expressions (9.97a)-(9.97f) and is represented as

$$[P_f] = \begin{bmatrix} -Gh\left\{\frac{\partial\phi(x_1)}{\partial x}\right\}^{\mathrm{T}} - G\{\phi(x_1)\}^{\mathbf{T}} \lceil \lambda_i \rfloor + G\{\phi(x_1)\}^{\mathbf{T}} \lceil \mu_i \rfloor \\ -\frac{Ebh}{6}\left\{\frac{\partial\phi(x_1)}{\partial x}\right\}^{\mathrm{T}} \lceil \lambda_i \rfloor - \frac{Ebh}{3}\left\{\frac{\partial\phi(x_1)}{\partial x}\right\}^{\mathrm{T}} \lceil \mu_i \rfloor \\ -\frac{Ebh}{3}\left\{\frac{\partial\phi(x_1)}{\partial x}\right\}^{\mathrm{T}} \lceil \lambda_i \rfloor - \frac{Ebh}{6}\left\{\frac{\partial\phi(x_1)}{\partial x}\right\}^{\mathrm{T}} \lceil \mu_i \rfloor \\ Gh\left\{\frac{\partial\phi(x_2)}{\partial x}\right\}^{\mathrm{T}} + G\{\phi(x_2)\}^{\mathbf{T}} \lceil \lambda_i \rfloor - G\{\phi(x_2)\}^{\mathbf{T}} \lceil \mu_i \rfloor \\ \frac{Ebh}{6}\left\{\frac{\partial\phi(x_2)}{\partial x}\right\}^{\mathrm{T}} \lceil \lambda_i \rfloor + \frac{Ebh}{3}\left\{\frac{\partial\phi(x_2)}{\partial x}\right\}^{\mathrm{T}} \lceil \mu_i \rfloor \\ \frac{Ebh}{3}\left\{\frac{\partial\phi(x_2)}{\partial x}\right\}^{\mathrm{T}} \lceil \lambda_i \rfloor + \frac{Ebh}{6}\left\{\frac{\partial\phi(x_2)}{\partial x}\right\}^{\mathrm{T}} \lceil \mu_i \rfloor \end{bmatrix}_{6\times 6} \tag{9.123}$$

Finally, similarly to what has been done in the *Euler-Bernoulli* spectral element, expressions (9.118) and (9.121) can now be combined due to having both the vector of constants $\{A\}$, resulting therefore into

$$\{f\} = [P_f][P_d]^{-1}\{d\} \tag{9.124}$$

Expression (9.124) can be simplified into

$$\{f\} = [D_k]\{d\} \tag{9.125}$$

where matrix $[D_k]$ represents the dynamic stiffness of the new, modified beam element. From this point the relation between forces and displacements can be treated similarly to what is done in the conventional FEM, being now possible to assemble the layerwise spectral beam elements to model a beam type structure.

### 9.4.3 Results

The main advantage of the spectral element method, when compared to the conventional finite element method, resides in the frequency domain formulation of the element. Such fact allows the spectral element to obtain accurate simulation results for high frequencies with fewer elements than with with the finite element method which, for high frequencies requires a high number of elements, due to the short wave length of propagating waves, to provide accurate results.

To verify that, several driving point frequency response functions of a free aluminum beam with the characteristics referred in table 9.1, were predicted with the finite element method, using the beam finite element formulated in this manuscript with a single layer configuration, and the spectral element method, using the formulated layerwise spectral beam element.

**Table 9.1:** Characteristics of the aluminum beam.

| Aluminum properties | | Beam geometry | |
|---|---|---|---|
| *Young's* modulus | $E = 69.5$ GPa | Thickness | $h = 3$ mm |
| *Poisson's* ratio | $\nu = 0.3$ | Width | $b = 40$ mm |
| Mass density | $\rho = 2700$ Kg/m$^3$ | Length | $\ell = 745$ mm |

In figure 9.12 the predicted FRFs are presented as well as one additional FRF measured experimentally (red dots) in the frequency range from 0 to 2800 Hz. The FRF predicted with the spectral element method was obtained using two elements (black line), wile the FRFs predicted with the finite element method were obtained using a 25 (blue dots), 50 (green dots), 100 (cyan dots) and 150 (magenta dots) elements mesh.

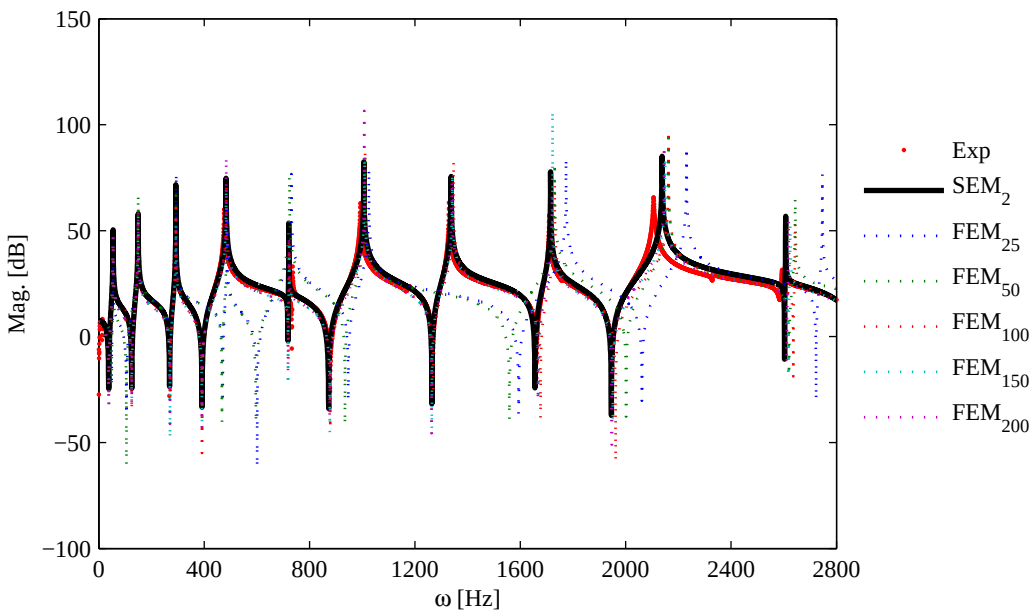


**Figure 9.12:** Comparison between the Spectral Element Method with FEM.

Figure 9.13 is a zoom of figure 9.12 in the frequency range from 1600 to 2800 Hz, allowing a higher detail of results depicted in figure 9.12 for the higher frequencies.

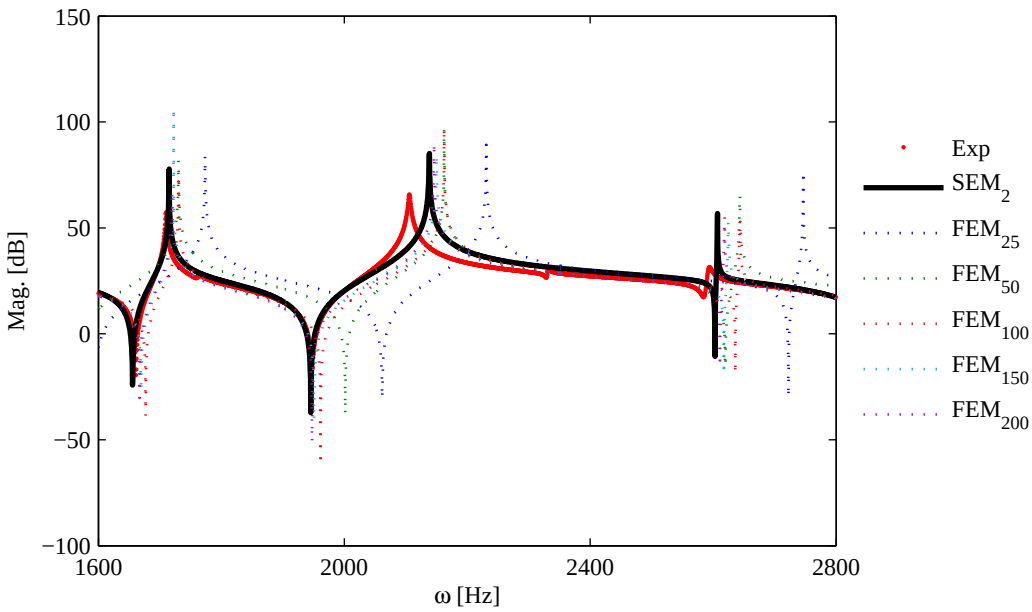


**Figure 9.13:** Zoom of figure 9.12 in the bandwidth from 1600 to 2800 Hz.

From figure 9.12 and figure 9.13 it is possible to verify that, for the given frequency range, the FRF predicted with the layerwise spectral beam element, using only two elements, provides a good approximation to the experimental FRF, as it can be inspected visually. Additionally, when comparing the FRF obtained with the layerwise spectral element method with the ones predicted with the finite element method, it is possible to verify that the spectral element method allows achieving more accurate results with a coarse element mesh and lower computational cost. The finite element method requires 150 elements or more, in the given frequency range, to provide results as accurate as the spectral element method does with only two elements.

As a concluding remark, it is worth to mention that the layerwise spectral beam finite element hereby formulates has revealed a reliable and numerically efficient tool in modeling multilayer or sandwich structures and it can become even more interesting if the material properties are frequency dependent. Nevertheless, more work needs to be done in order to validate this layerwise spectral beam finite element formulation when modeling multilayer structures.

# Chapter 10

# Conclusion

## 10.1 Conclusions

Accordingly to the established objectives, the viscoelastic dynamic properties of cork compound have been investigated using two different methodologies based in a *Complex Modulus Analysis*. The influence of cork compound in the dynamic behavior of sandwich beams and plates has also been investigated, both experimentally and numerically. The experimental tests consisted in characterizing the modal properties of sandwich beams and plates using experimental modal analysis. The numerical simulations of the dynamic behavior of sandwich beams and plates were made using the finite element method with a multi-layer layerwise beam element and a multi-layer layerwise plate element.

### 10.1.1 Characterization of cork compound dynamic properties

Determining the dynamic properties of cork compounds, namely its complex modulus, is an important step in demonstrating this material efficiency when used as a damping treatment. The cork compound properties were hereby determined using two different procedures, one allowing to determine the shear complex modulus properties of the material and another to determine the extensional complex modulus of cork compound.

To determine the shear complex modulus of cork compound an experimental methodology was implemented in order to efficiently obtain the referred properties. The experimental setup efficiently reproduces a single degree of freedom system simplifying the identification procedure of the cork compound dynamic properties. Throughout the steel blades, an elastic guiding system was implemented avoiding the appearance of spurious degrees of freedom. The effect of the boundary conditions on the experimental setup were avoided by clamping the setup to a granite block. The shear dynamic properties were determined from the measured accelerances and receptances.

The extensional dynamic properties of cork compound have been determined using an experimental setup which reproduces a discrete two degrees of freedom semi-definite system which allowed an efficient and simple determination of the extensional dynamic properties of several commercially available cork compounds. The experimental setup revealed very efficient in the determination of the cork compound dynamic properties, avoiding the presence of spurious modes of the setup from appearing in the measured frequency response functions from the system. The properties were identified from both measured transmissibilities and accelerances of

the two degree of freedom system.

### 10.1.2 Layerwise finite elements

A multilayer beam element and a multilayer plate element have been developed. Both elements are based in a partial layerwise theory complying a multi-layer configuration. The finite elements were formulated using the discrete layer theory being imposed directly the continuity of the displacement field between the layers of the element, the transverse displacement was considered constant through the layers. The finite elements present a generalized formulation allowing an arbitrary number of layers, in both elements the formulation has been done for a generic layer using a location matrix to derive the element matrices for the desired number of layers. Both elements complied viscoelastic layers, being the frequency dependent properties, the complex modulus, included in the finite element routine using the *Direct Frequency Analysis* (DFA) procedure which revealed to be a simple and efficient process to simulate the frequency dependent damping in layered structures.

For the layerwise plate element the bi-harmonic interpolation functions were used to obtain more accurate results. In the plate element a *Mixed Interpolation of Tensorial Components* (MITC) formulation was used to avoid shear locking phenomena, being in the element formulation procedure separated the membrane, bending and shear components of the plate element stiffness.

The physical representativity and validation of the formulated beam and plate elements was made by comparing the driving point FRFs measured in test samples with the FEM predicted ones. Applying the DFA procedure and using the determined complex modulus properties of cork compound, the driving point FRFs were predicted, using the formulated finite elements, for all layered beam and layered plate test samples. The predicted driving point FRFs were graphically compared to the correspondent measured ones being verified a good correlation between them.

In sum, both beam and plate elements, can efficiently represent multi-layer and multi-material passive damping treatments.

### 10.1.3 Sandwich structures with cork compound cores

To evaluate the increase in structural damping achieved with the use of cork compound layers in beam and plate structures, several sandwich beams and sandwich plates with cork compound cores and aluminum plies were analyzed in a free boundary configuration. Using experimental modal analysis, the dynamic response of the sandwich beams and sandwich plates was characterized in a free boundary configuration and the modal damping ratios, natural frequencies and mode shapes were identified for both beams and plates.

The obtained modal damping ratios revealed that the use of cork compound as an integrated damping treatment effectively introduces structural damping. The measured experimental results were used to verify the physical representativity of the numerical finite element model and the accuracy of the measured properties of cork compound.

## 10.2 Contribution of the thesis

The determination of cork compound dynamic properties, namely its storage modulus and loss factor in extension and shear and the investigation of their frequency dependence is one of the main contributions of this thesis since this information is scarcely known.

The development of a multilayer beam and multilayer plate layerwise finite elements using a formulation which allows an easy implementation of an arbitrary number of layers and the inclusion of viscoelastic layers was also one of this thesis contribution.

The experimental measurements made on sandwich structures with cork compounds allowed verifying the effectiveness of this natural and easy to recycle material as a passive damping treatment in a integrated/sandwich plate and beam configuration.

## 10.3 Future work

Throughout the preparation of this thesis it was clear that the information on the cork compound dynamic properties is still very scarce. Since the cork compound properties identification was hereby performed at a constant temperature, it is natural to be suggested as a future work the identification of the cork compound properties in a controlled environment which will allow a deeper and more complete knowledge of the variation of the dynamic properties of cork compound with parameters such as temperature and humidity.

Due to the fact that both beam and plate finite elements are multi-material, multi-layer elements, different layered structures can be studied. It can be investigated the performance of cork compound in a free layer damping treatment or in a constrained layer damping treatment.

Different damping models like GHM and ADF can be used to verify if they are more representative of the damping added by the cork compound inclusion in a layered structure.

Improvement of the spectral beam layerwise finite element, namely its implementation and testing of its dynamical behavior for different configurations needs to be pursued.

# Appendix A

# Measured FRFs and Identified Properties of Cork Compound

## A.1 FRFs and Properties of Sample P1

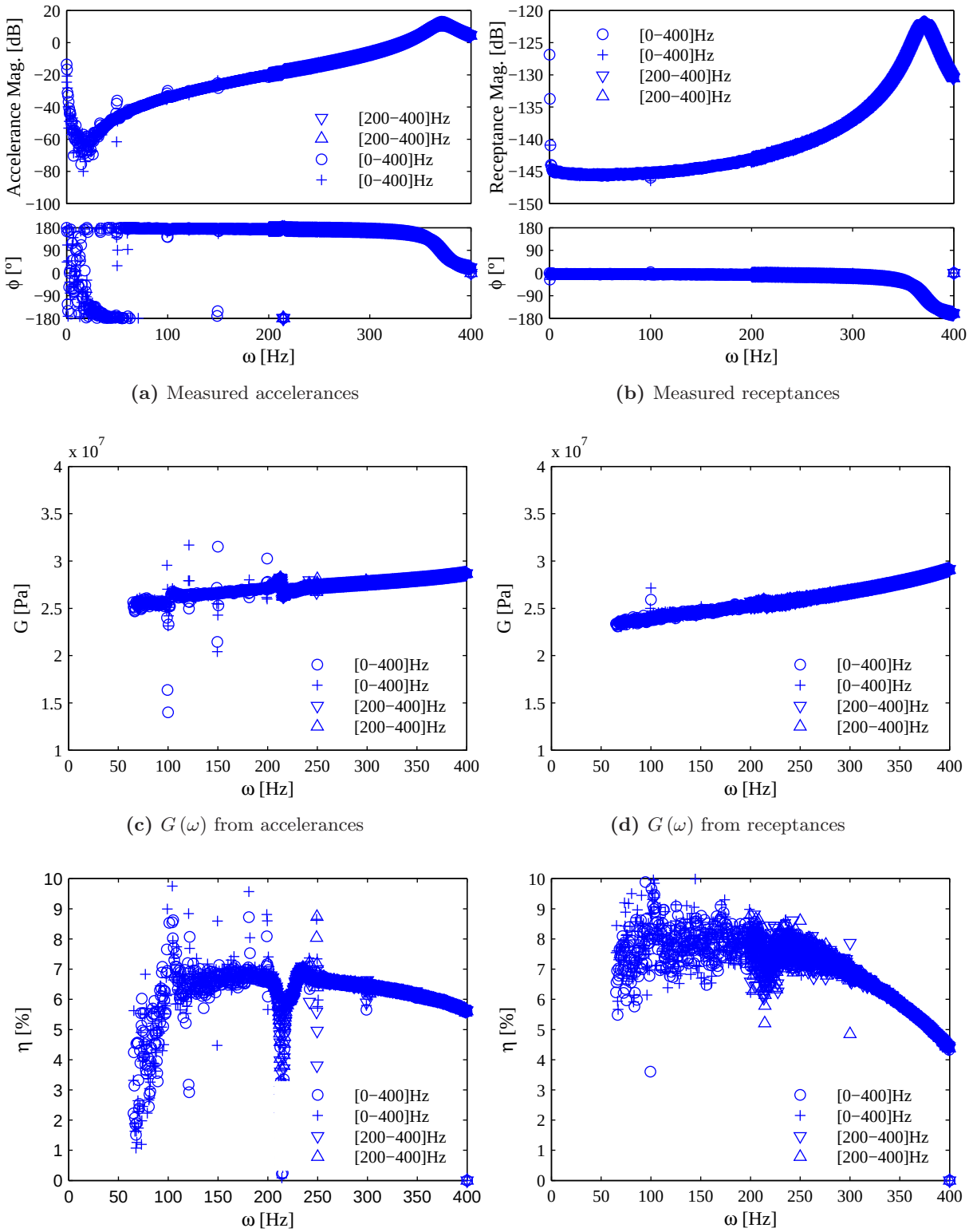


**(a)** Measured accelerances

**(b)** Measured receptances

**(c)** $G(\omega)$ from accelerances

**(d)** $G(\omega)$ from receptances

**(e)** $\eta(\omega)$ from accelerances

**(f)** $\eta(\omega)$ from receptances

**Figure A.1:** Measured FRFs and identified properties of Sample P1.

## A.2 FRFs and Properties of Sample P2

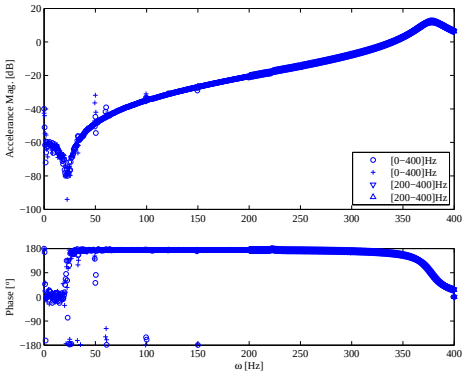


**(a)** Measured accelerances

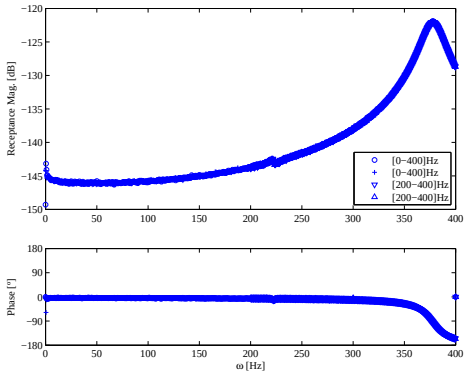


**(b)** Measured receptances

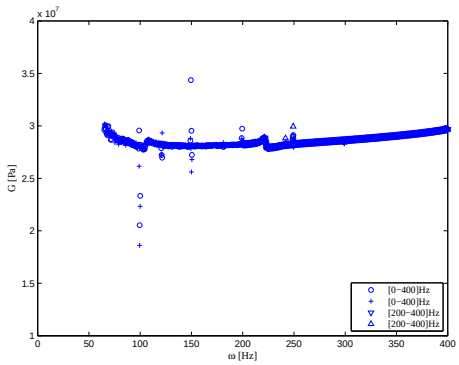


**(c)** $G(\omega)$ from accelerances

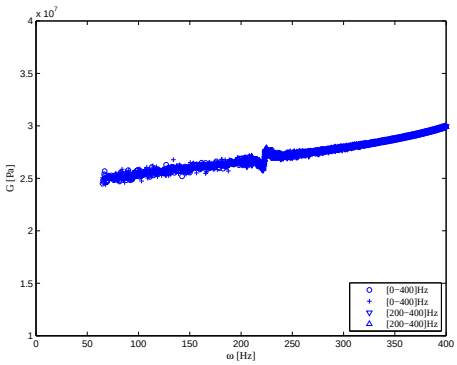


**(d)** $G(\omega)$ from receptances

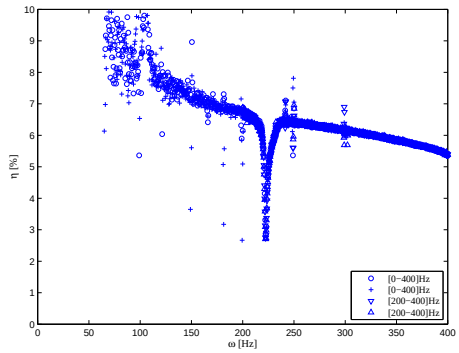


**(e)** $\eta(\omega)$ from accelerances

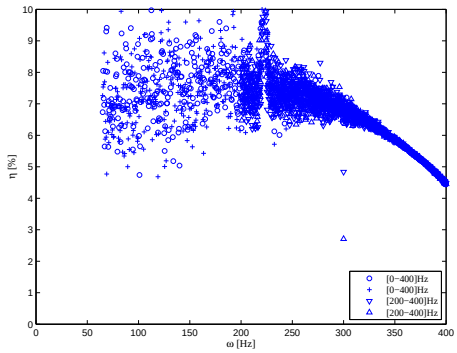


**(f)** $\eta(\omega)$ from receptances

**Figure A.2:** Measured FRFs and identified properties of Sample P2.

## A.3 FRFs and Properties of Sample P3

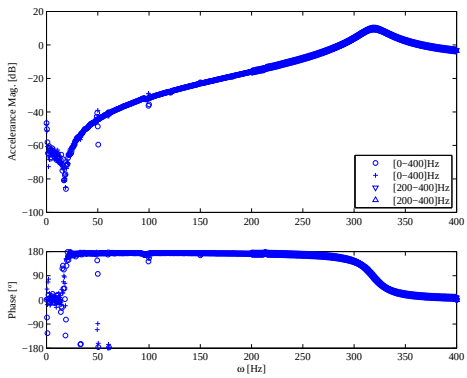


**(a)** Measured accelerances

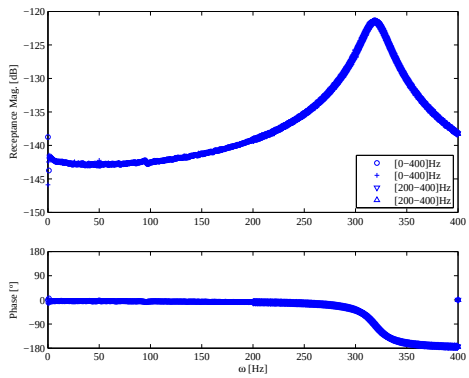


**(b)** Measured receptances

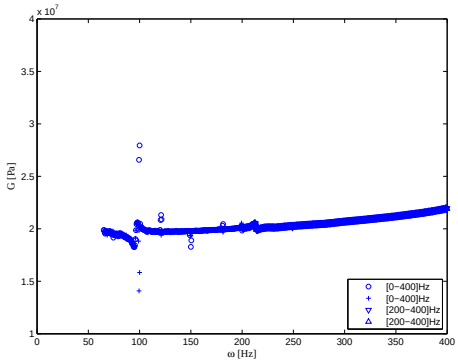


**(c)** $G(\omega)$ from accelerances

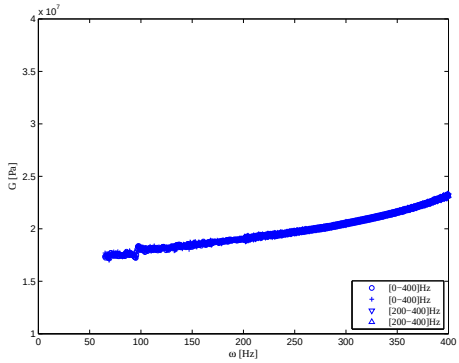


**(d)** $G(\omega)$ from receptances

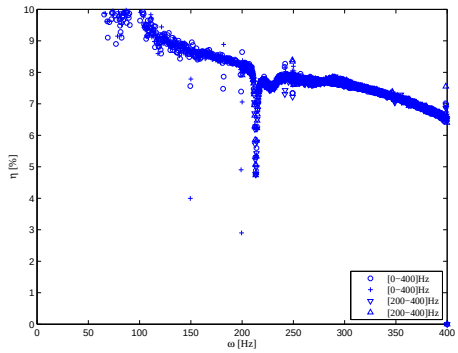


**(e)** $\eta(\omega)$ from accelerances

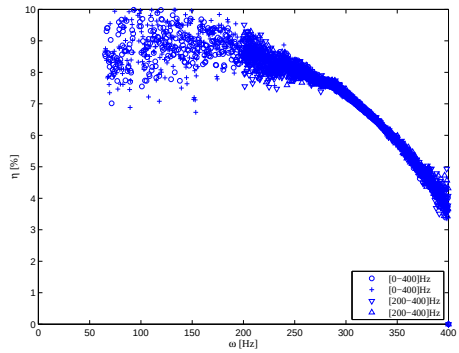


**(f)** $\eta(\omega)$ from receptances

**Figure A.3:** Measured FRFs and identified properties of Sample P3.

# Appendix B

# Measured FRFs of all test samples

## B.1 FRFs of Beam 0 test sample

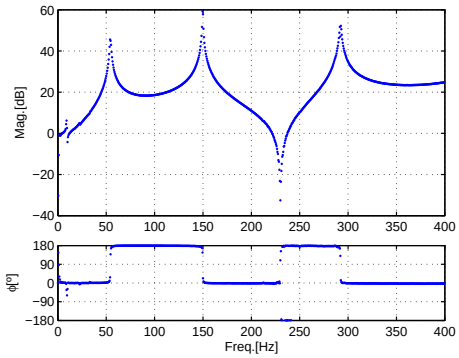


**(a)** FRF measured at point 1

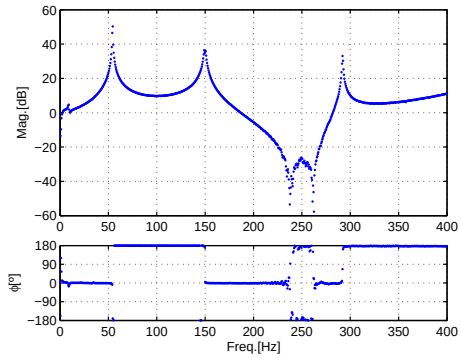


**(b)** FRF measured at point 2

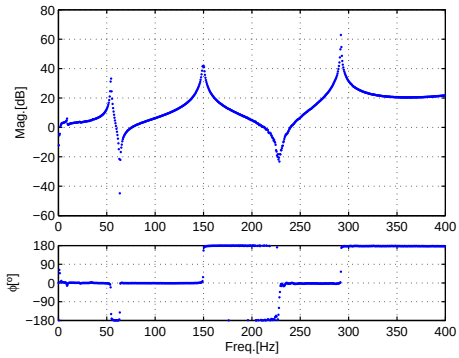


**(c)** FRF measured at point 3

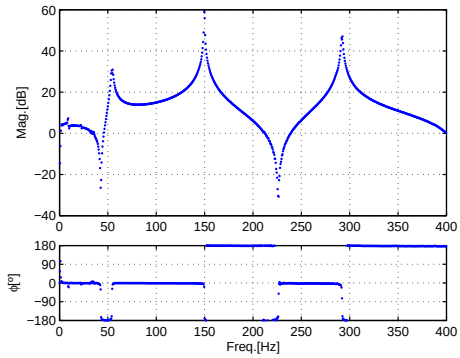


**(d)** FRF measured at point 4

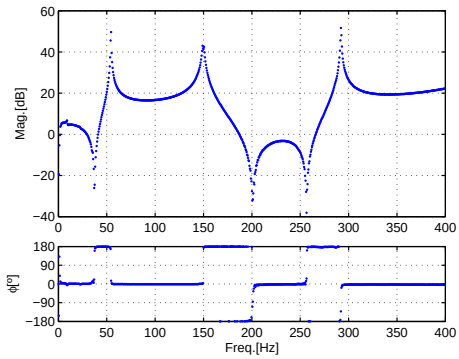


**(e)** FRF measured at point 5

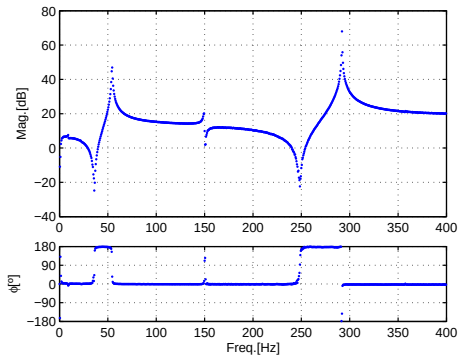


**(f)** FRF measured at point 6

**Figure B.1:** Measured FRFs of Beam 0 for points from 1 to 6, excitation on point 7.

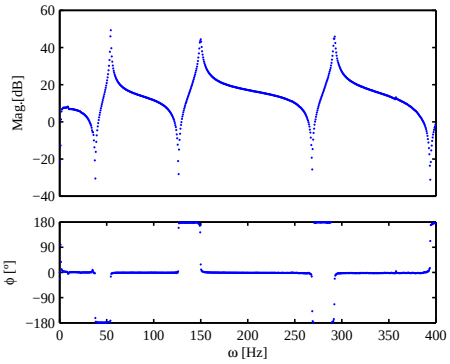


**(a)** FRF measured at point 7

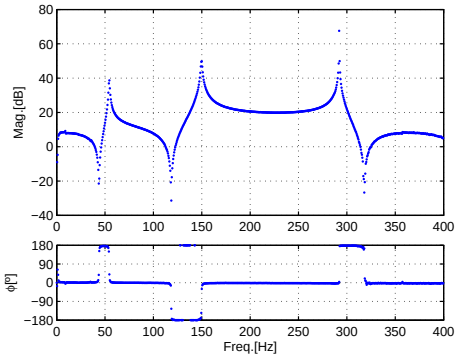


**(b)** FRF measured at point 8

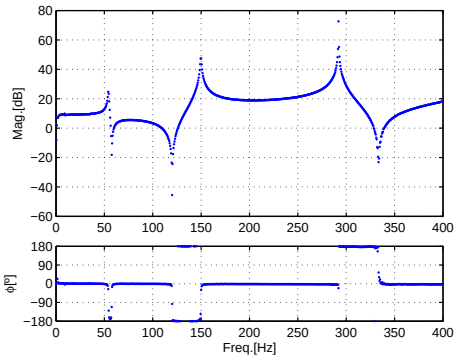


**(c)** FRF measured at point 9

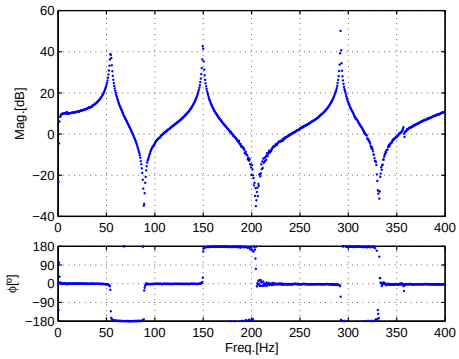


**(d)** FRF measured at point 10

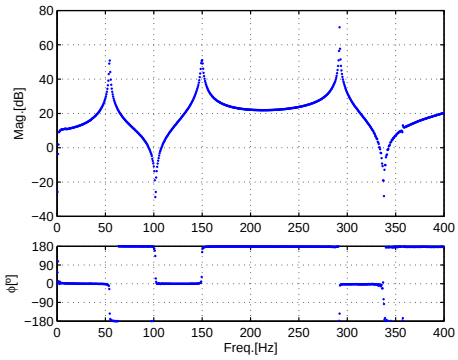


**(e)** FRF measured at point 11

**Figure B.2:** Measured FRFs of Beam 0 for points from 7 to 11, excitation on point 7.

## B.2 FRFs of Beam 1 test sample

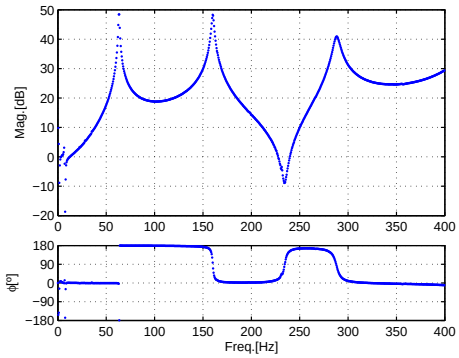


**(a)** FRF measured at point 1

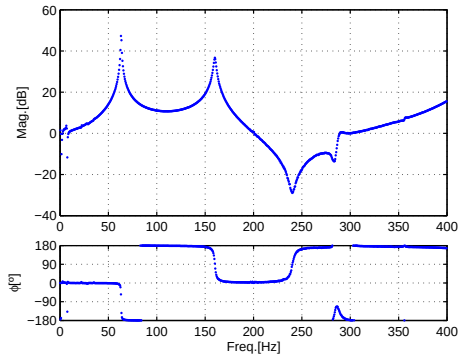


**(b)** FRF measured at point 2

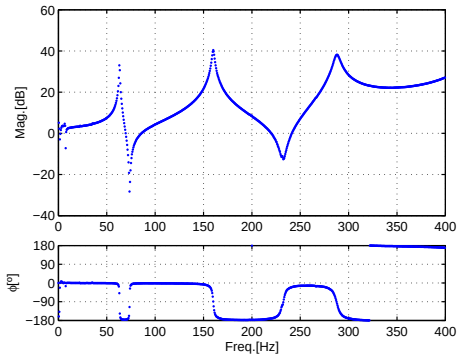


**(c)** FRF measured at point 3

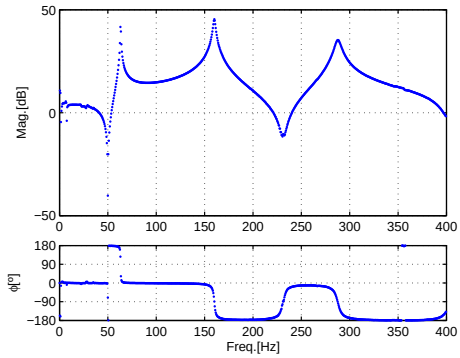


**(d)** FRF measured at point 4

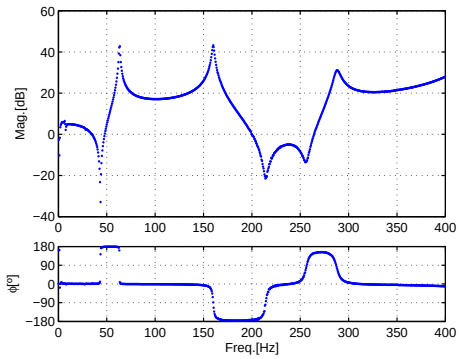


**(e)** FRF measured at point 5

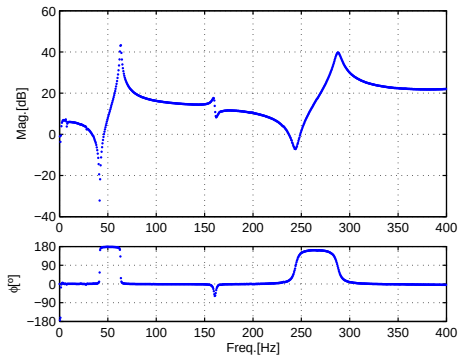


**(f)** FRF measured at point 6

**Figure B.3:** Measured FRFs of Beam 1 for points from 1 to 6, excitation on point 7.

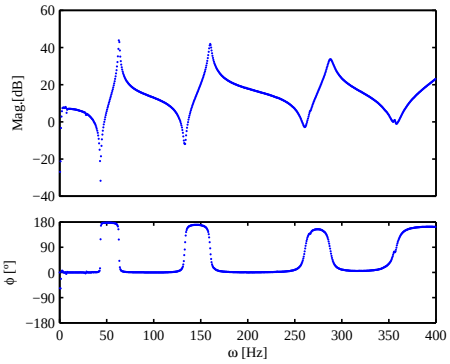


(a) FRF measured at point 7

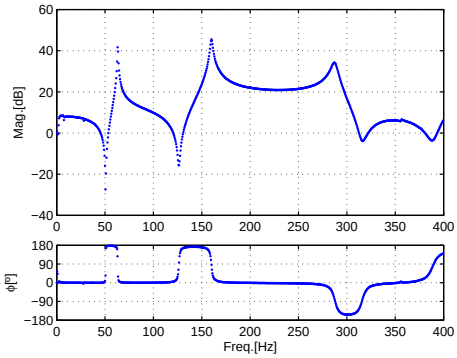


(b) FRF measured at point 8

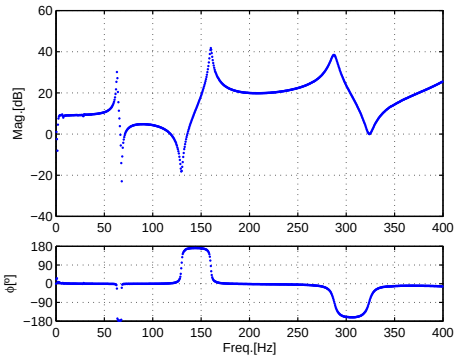


(c) FRF measured at point 9

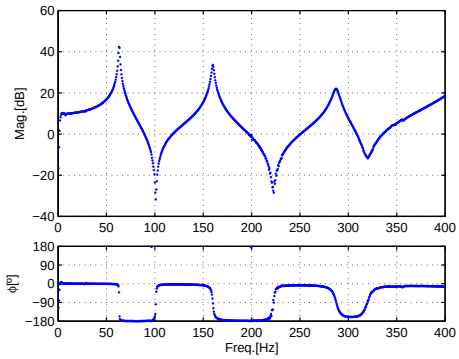


(d) FRF measured at point 10

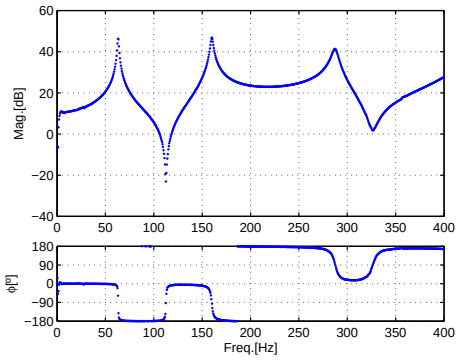


(e) FRF measured at point 11

**Figure B.4:** Measured FRFs of Beam 1 for points from 7 to 11, excitation on point 7.

## B.3 FRFs of Beam 2 test sample

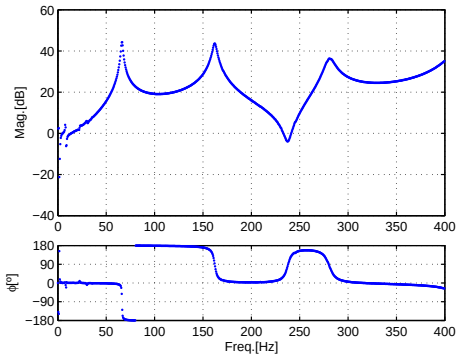


**(a)** FRF measured at point 1

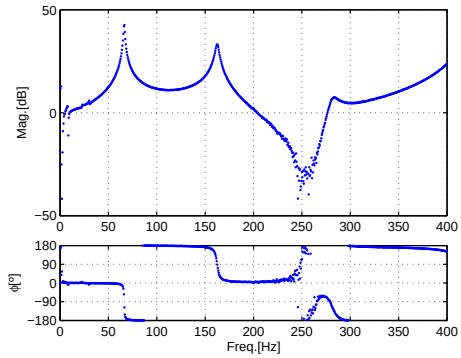


**(b)** FRF measured at point 2

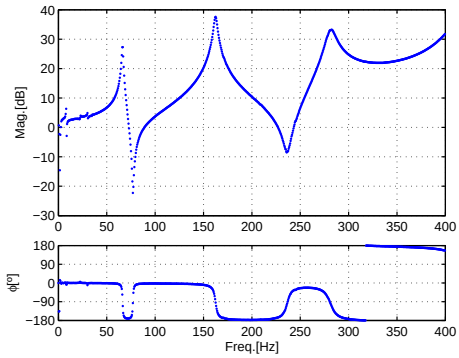


**(c)** FRF measured at point 3

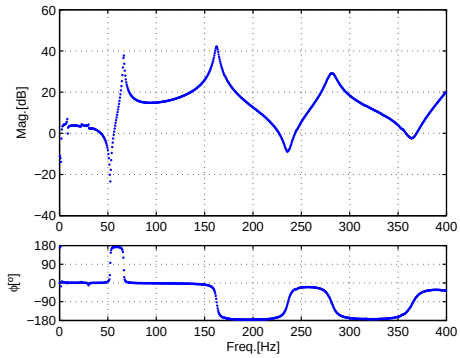


**(d)** FRF measured at point 4

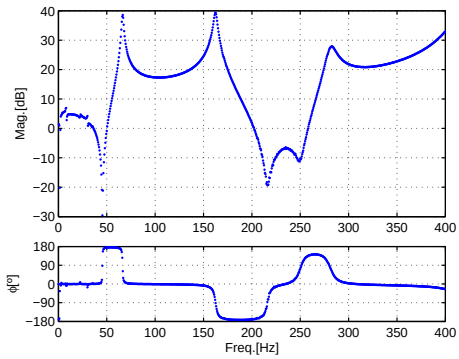


**(e)** FRF measured at point 5

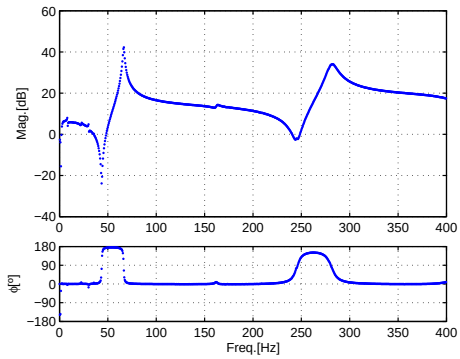


**(f)** FRF measured at point 6

**Figure B.5:** Measured FRFs of Beam 2 for points from 1 to 6, excitation on point 7.

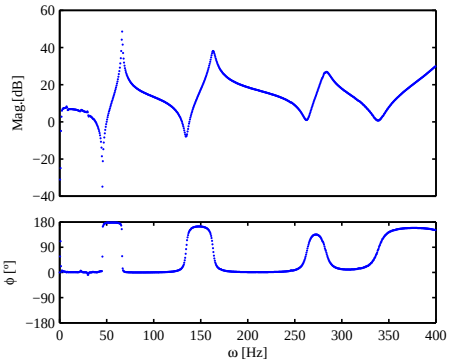


(a) FRF measured at point 7

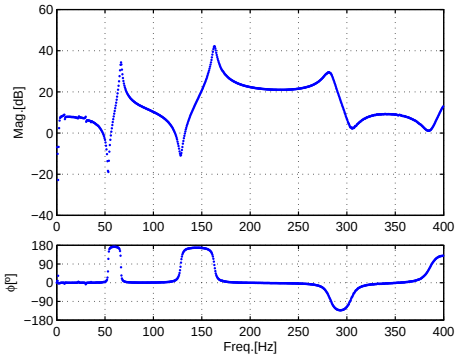


(b) FRF measured at point 8

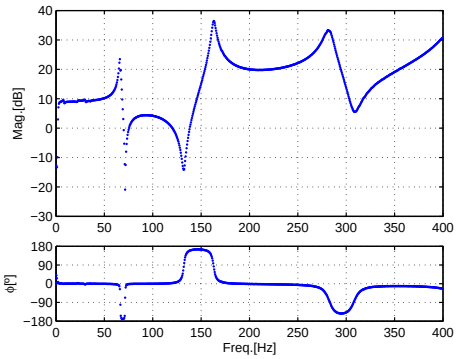


(c) FRF measured at point 9

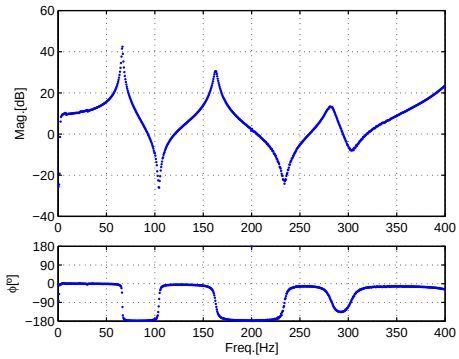


(d) FRF measured at point 10

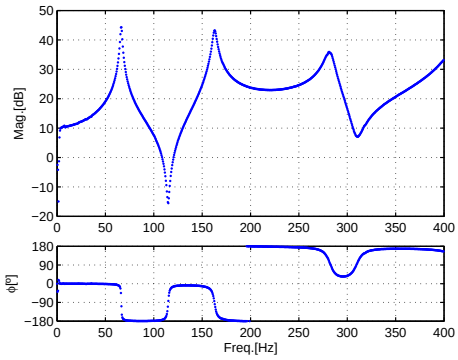


(e) FRF measured at point 11

**Figure B.6:** Measured FRFs of Beam 2 for points from 7 to 11, excitation on point 7.

## B.4 FRFs of Beam 3 test sample

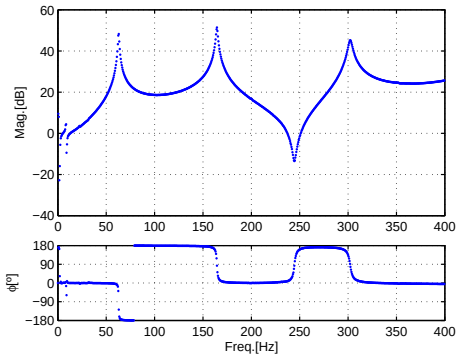


**(a)** FRF measured at point 1

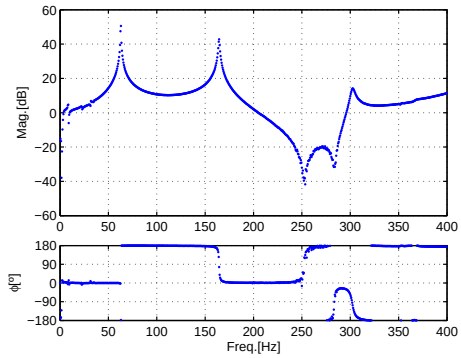


**(b)** FRF measured at point 2

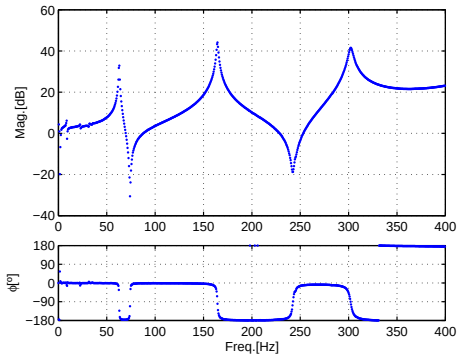


**(c)** FRF measured at point 3

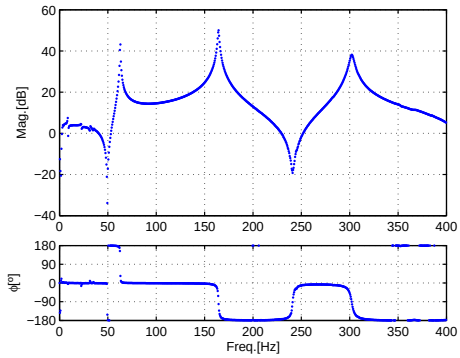


**(d)** FRF measured at point 4

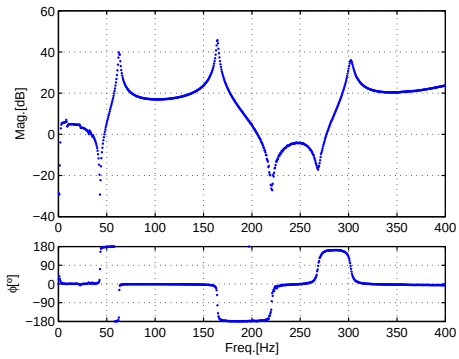


**(e)** FRF measured at point 5

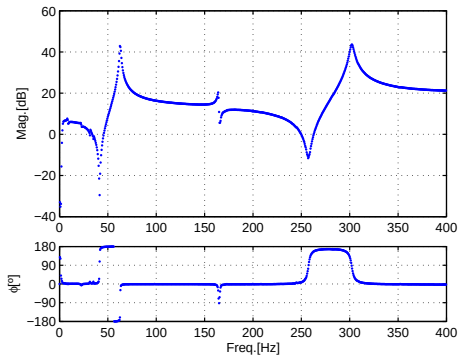


**(f)** FRF measured at point 6

**Figure B.7:** Measured FRFs of Beam 3 for points from 1 to 6, excitation on point 7.

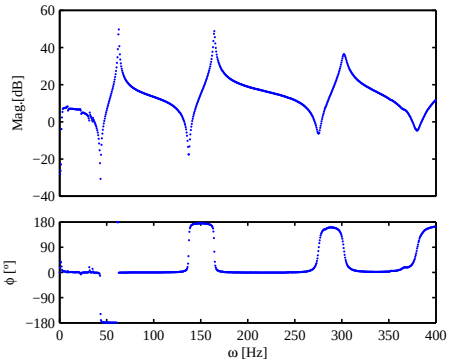


**(a)** FRF measured at point 7

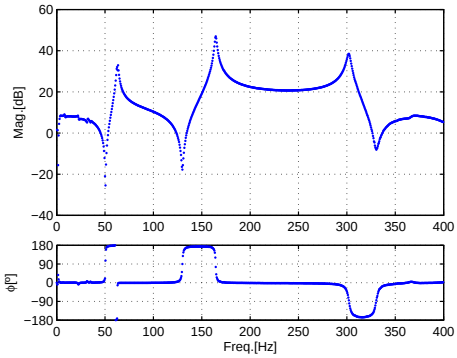


**(b)** FRF measured at point 8

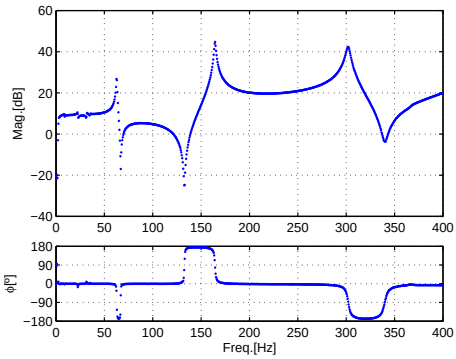


**(c)** FRF measured at point 9

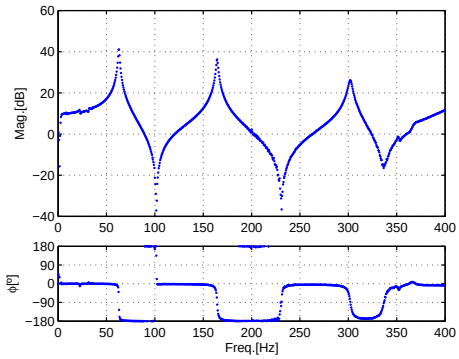


**(d)** FRF measured at point 10

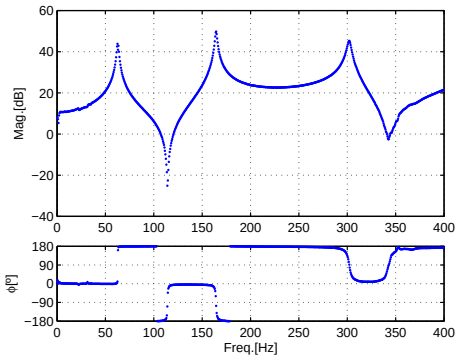


**(e)** FRF measured at point 11

**Figure B.8:** Measured FRFs of Beam 3 for points from 7 to 11, excitation on point 7.

## B.5 FRFs of Beam 4 test sample

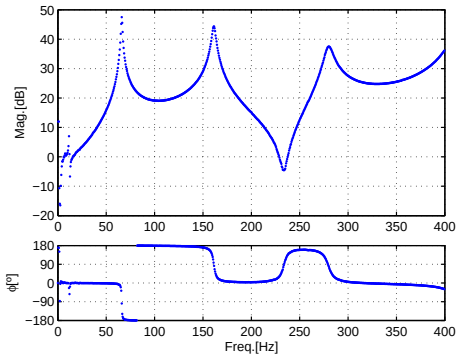


**(a)** FRF measured at point 1

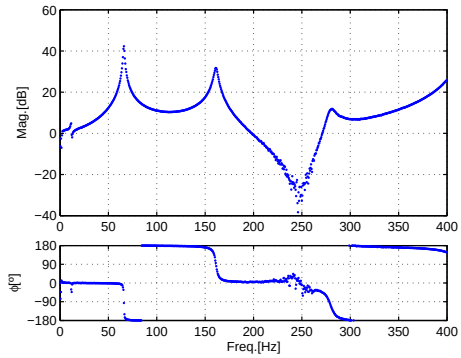


**(b)** FRF measured at point 2

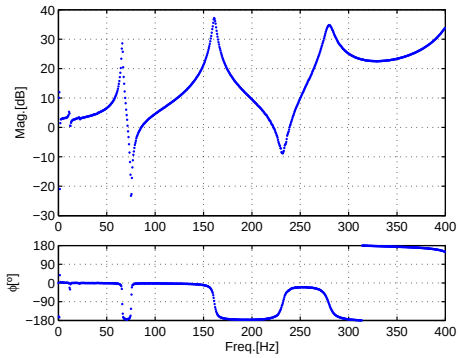


**(c)** FRF measured at point 3

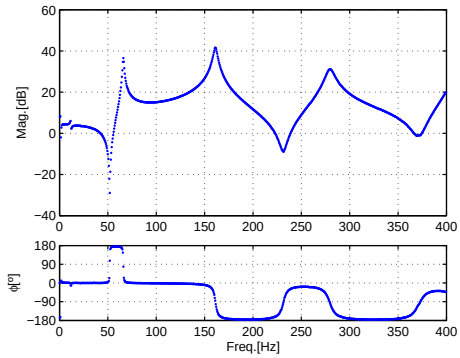


**(d)** FRF measured at point 4

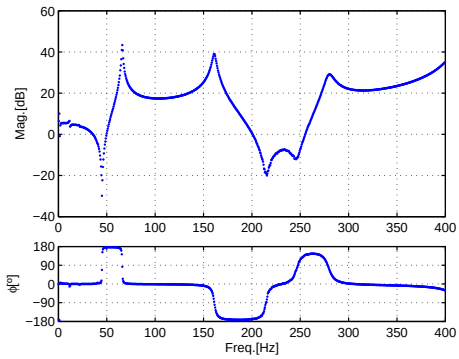


**(e)** FRF measured at point 5

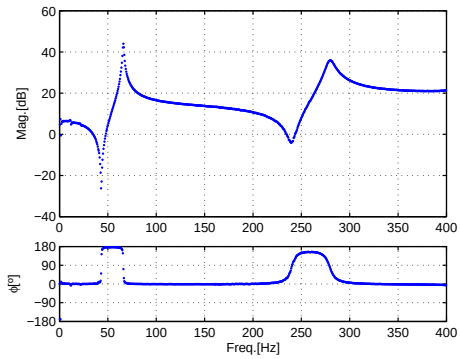


**(f)** FRF measured at point 6

**Figure B.9:** Measured FRFs of Beam 4 for points from 1 to 6, excitation on point 7.

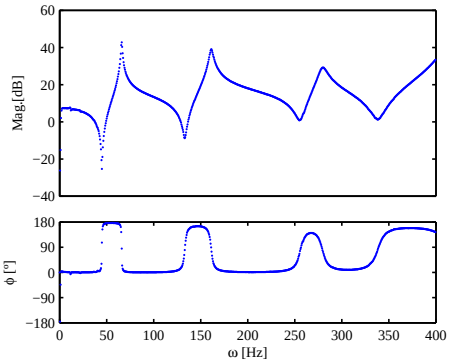


(a) FRF measured at point 7

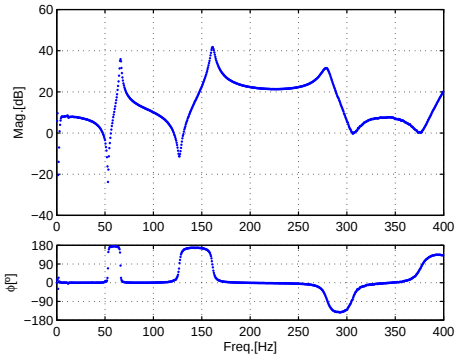


(b) FRF measured at point 8

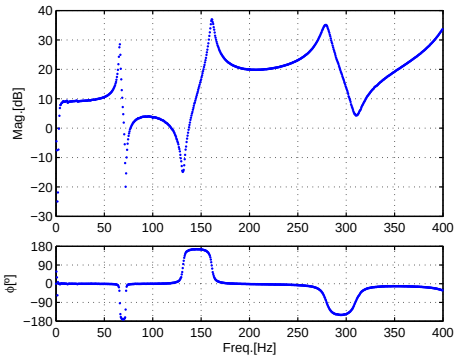


(c) FRF measured at point 9

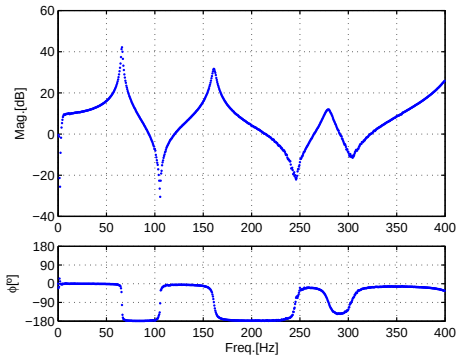


(d) FRF measured at point 10

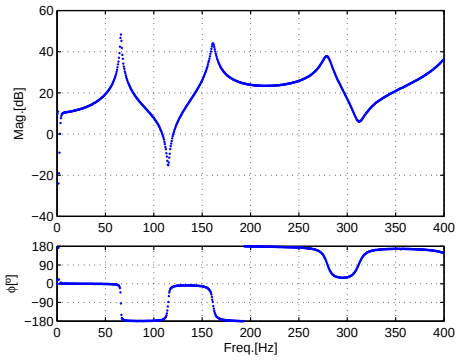


(e) FRF measured at point 11

**Figure B.10:** Measured FRFs of Beam 4 for points from 7 to 11, excitation on point 7.

## B.6 FRFs of Beam 5 test sample

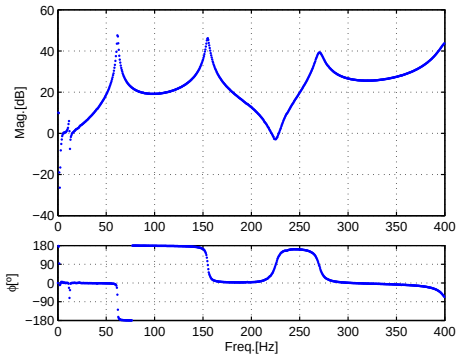


**(a)** FRF measured at point 1

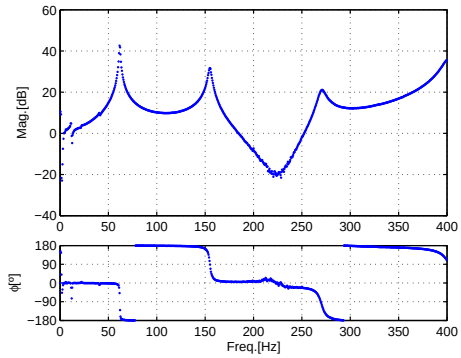


**(b)** FRF measured at point 2

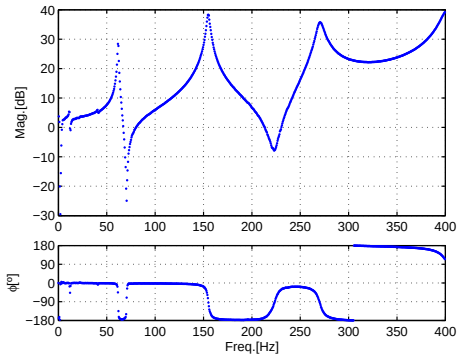


**(c)** FRF measured at point 3

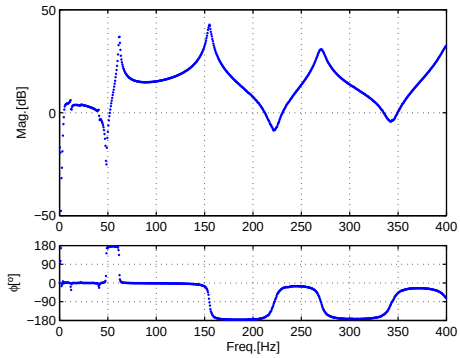


**(d)** FRF measured at point 4

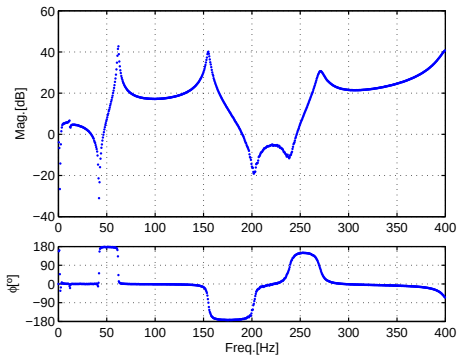


**(e)** FRF measured at point 5

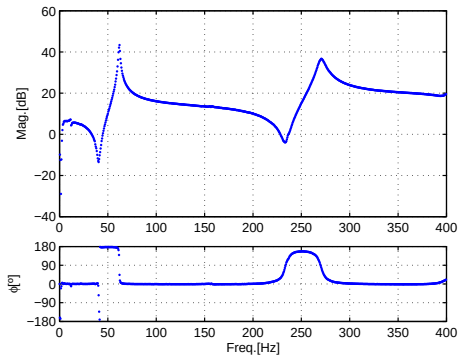


**(f)** FRF measured at point 6

**Figure B.11:** Measured FRFs of Beam 5 for points from 1 to 6, excitation on point 7.

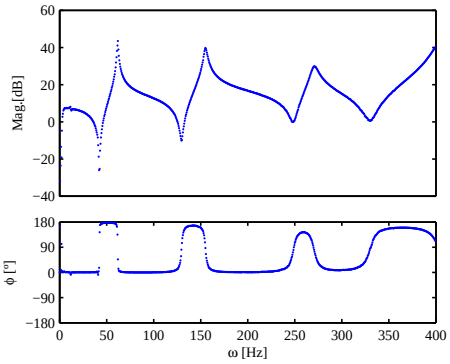


(a) FRF measured at point 7

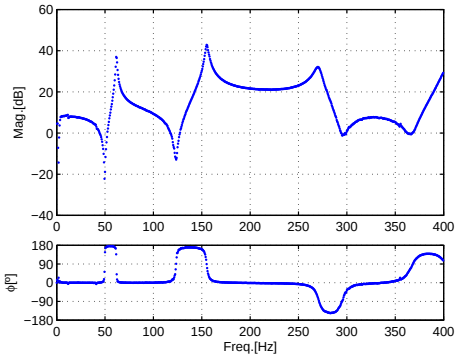


(b) FRF measured at point 8

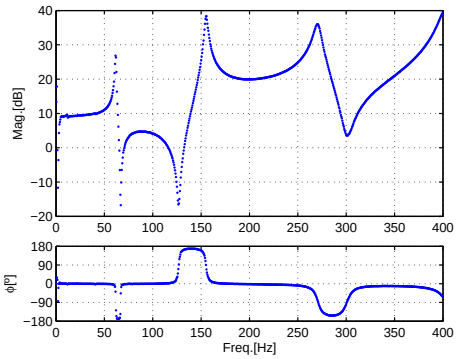


(c) FRF measured at point 9

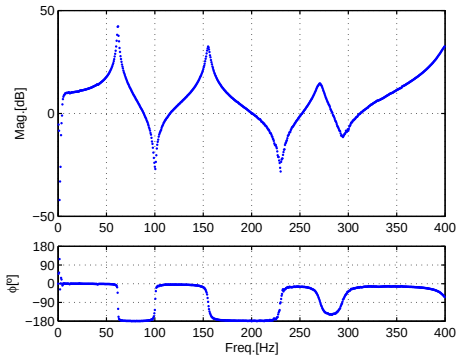


(d) FRF measured at point 10

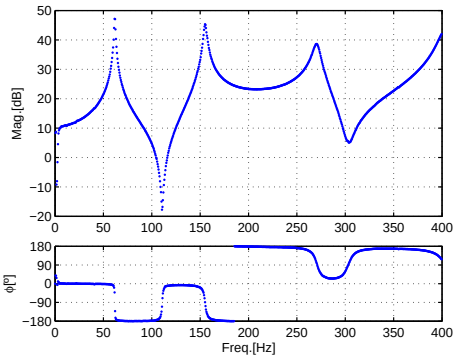


(e) FRF measured at point 11

**Figure B.12:** Measured FRFs of Beam 5 for points from 7 to 11, excitation on point 7.

## B.7 FRFs of Beam 6 test sample

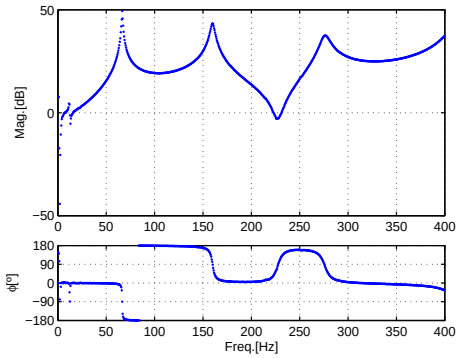


**(a)** FRF measured at point 1

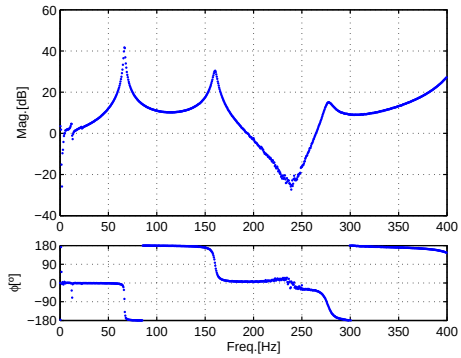


**(b)** FRF measured at point 2

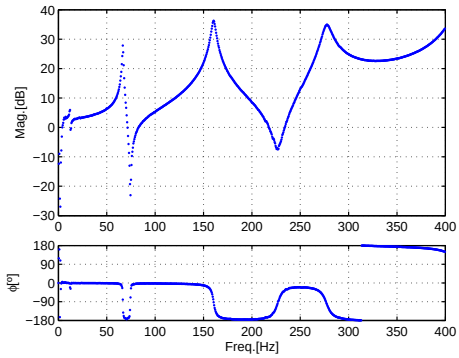


**(c)** FRF measured at point 3

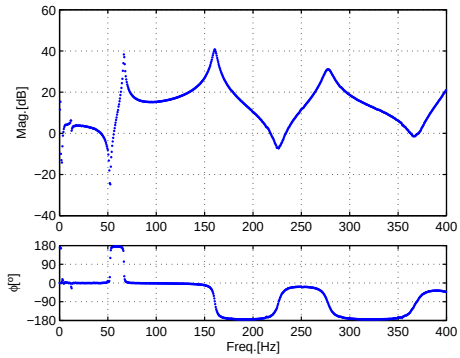


**(d)** FRF measured at point 4

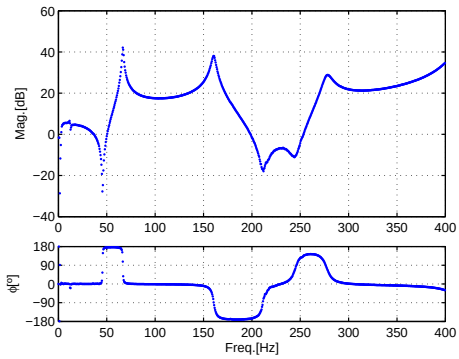


**(e)** FRF measured at point 5

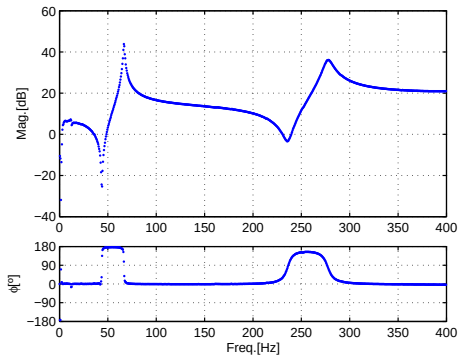


**(f)** FRF measured at point 6

**Figure B.13:** Measured FRFs of Beam 6 for points from 1 to 6, excitation on point 7.

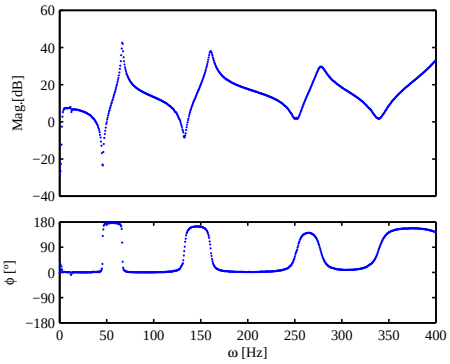


(a) FRF measured at point 7

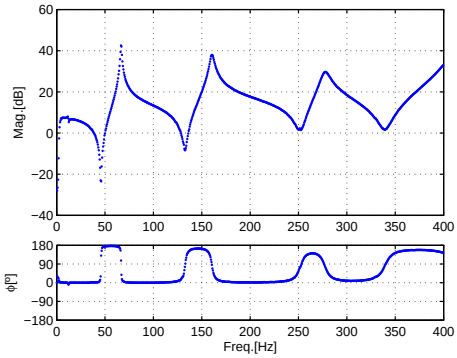


(b) FRF measured at point 8

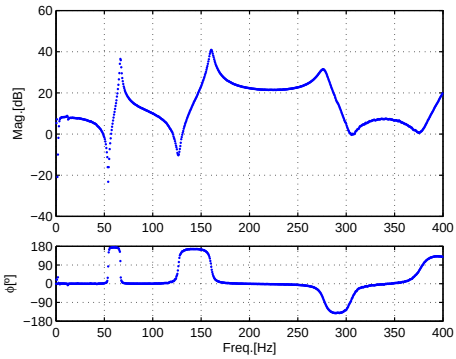


(c) FRF measured at point 9

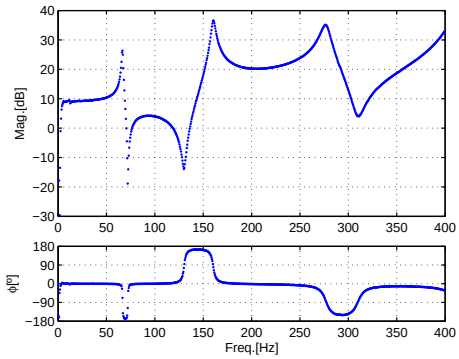


(d) FRF measured at point 10

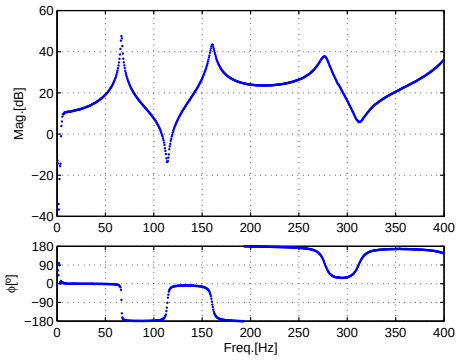


(e) FRF measured at point 11

**Figure B.14:** Measured FRFs of Beam 6 for points from 7 to 11, excitation on point 7.

## B.8 FRFs of Beam 7 test sample

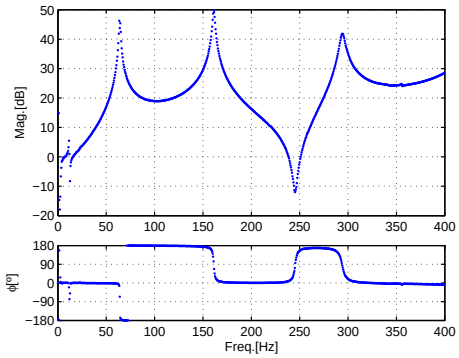


**(a)** FRF measured at point 1

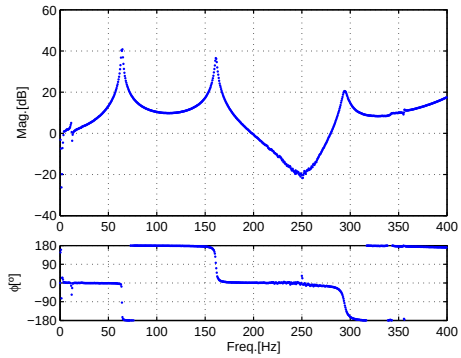


**(b)** FRF measured at point 2

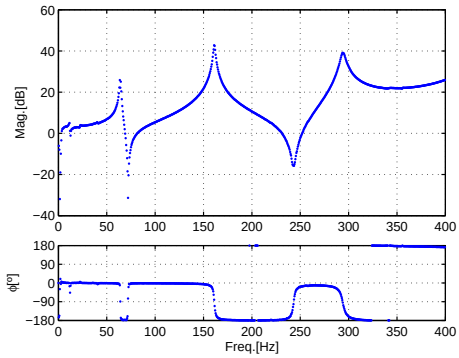


**(c)** FRF measured at point 3

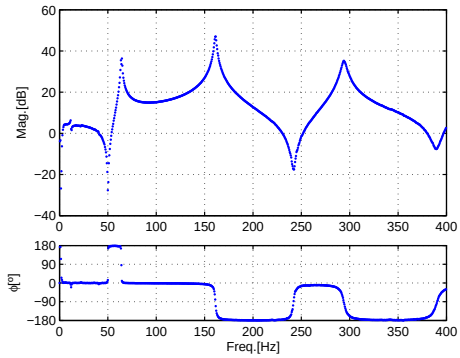


**(d)** FRF measured at point 4

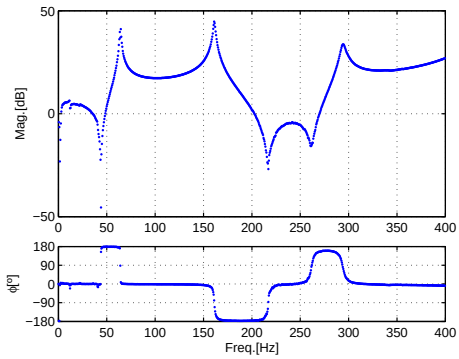


**(e)** FRF measured at point 5

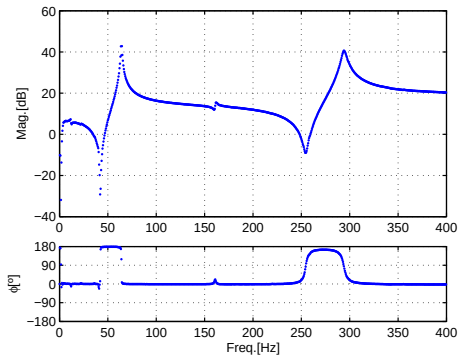


**(f)** FRF measured at point 6

**Figure B.15:** Measured FRFs of Beam 7 for points from 1 to 6, excitation on point 7.

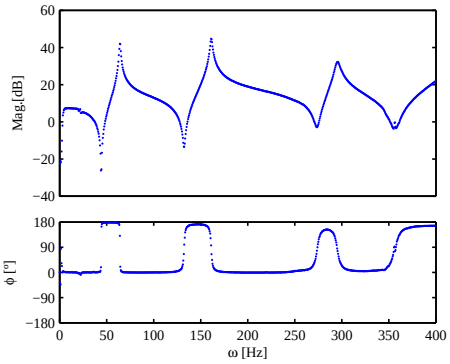


(a) FRF measured at point 7

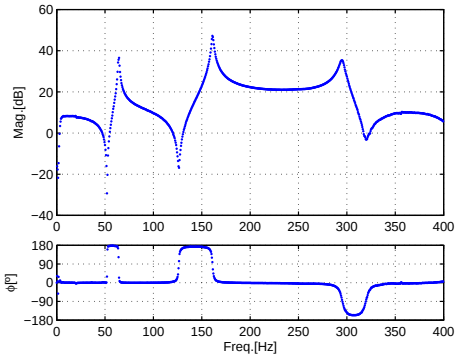


(b) FRF measured at point 8

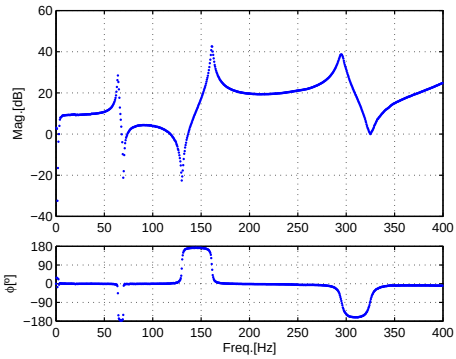


(c) FRF measured at point 9

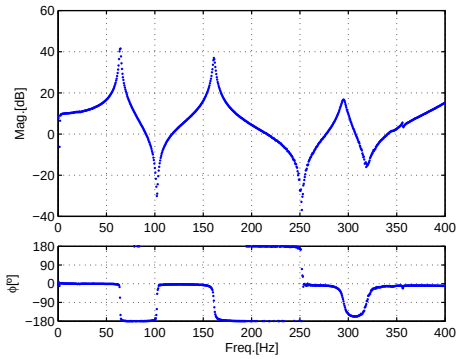


(d) FRF measured at point 10

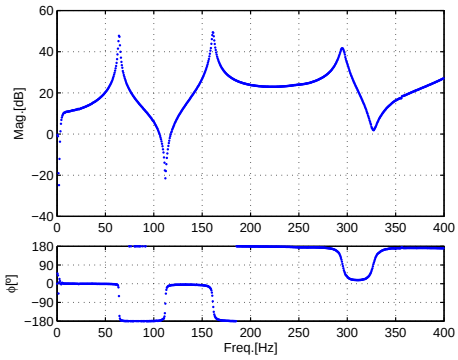


(e) FRF measured at point 11

**Figure B.16:** Measured FRFs of Beam 7 for points from 7 to 11, excitation on point 7.

## B.9 FRFs of Beam 8 test sample

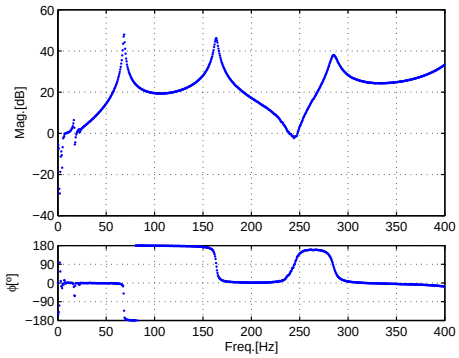


**(a)** FRF measured at point 1

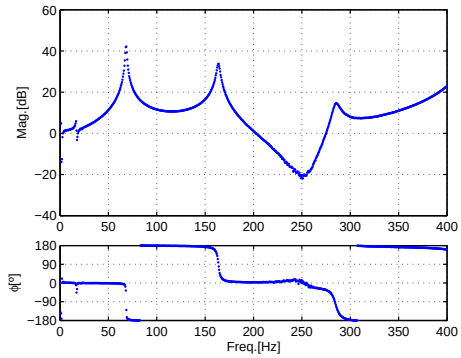


**(b)** FRF measured at point 2

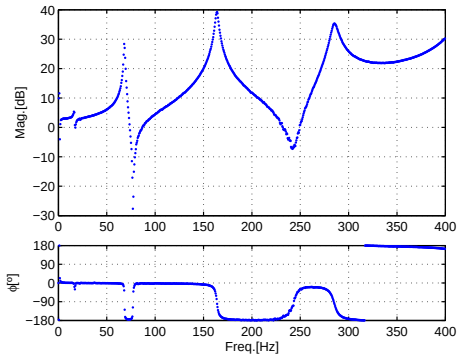


**(c)** FRF measured at point 3

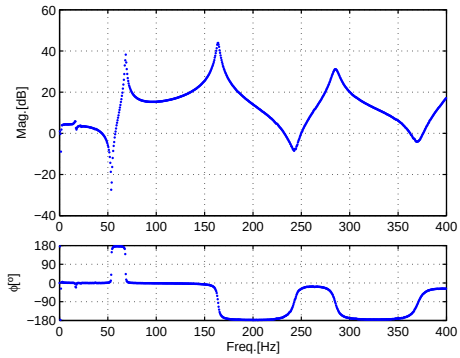


**(d)** FRF measured at point 4

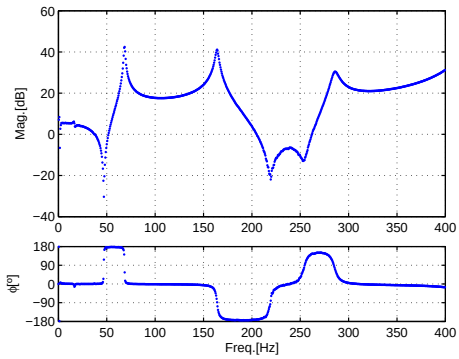


**(e)** FRF measured at point 5

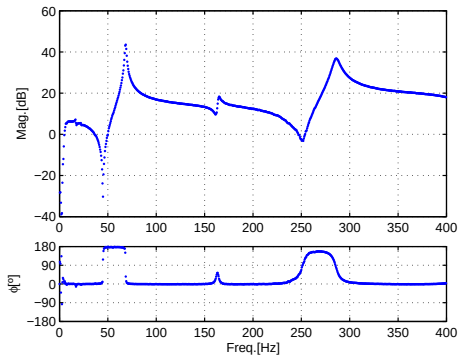


**(f)** FRF measured at point 6

**Figure B.17:** Measured FRFs of Beam 8 for points from 1 to 6, excitation on point 7.

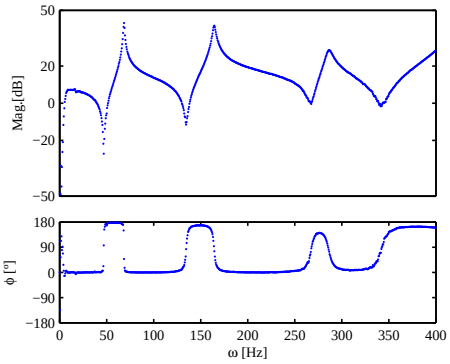


(a) FRF measured at point 7

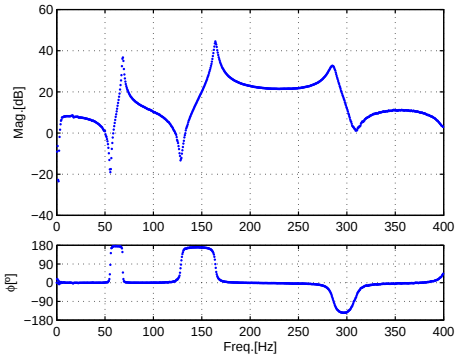


(b) FRF measured at point 8

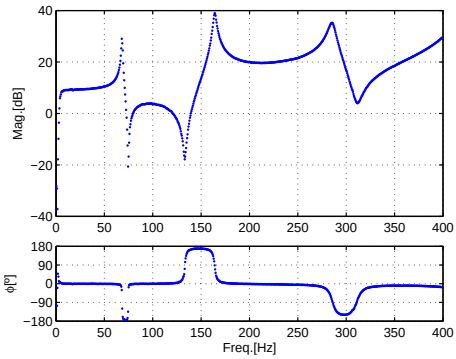


(c) FRF measured at point 9

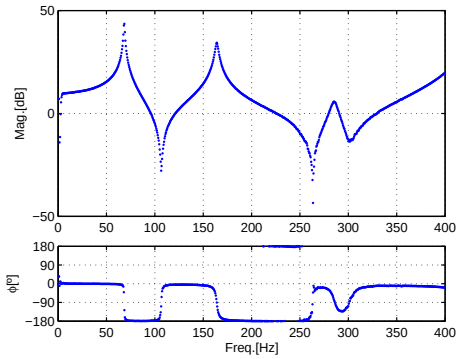


(d) FRF measured at point 10

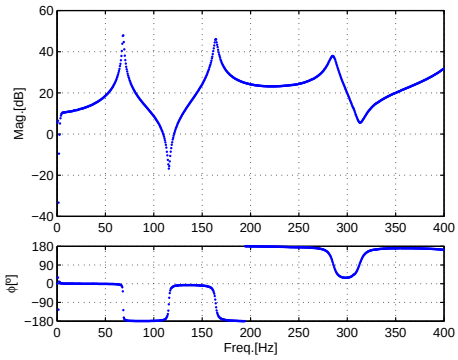


(e) FRF measured at point 11

**Figure B.18:** Measured FRFs of Beam 8 for points from 7 to 11, excitation on point 7.

# Appendix C

# Plate test samples mode shapes

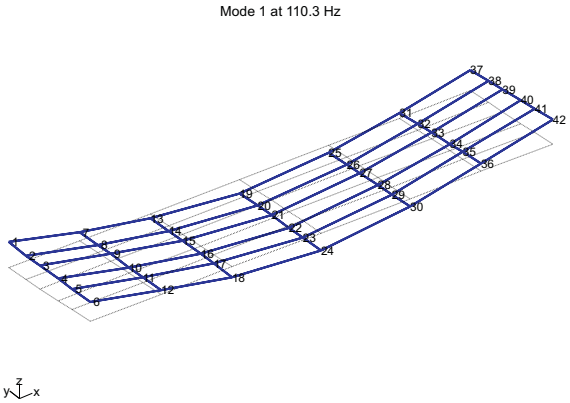


**(a)** $1^{st}$ mode shape

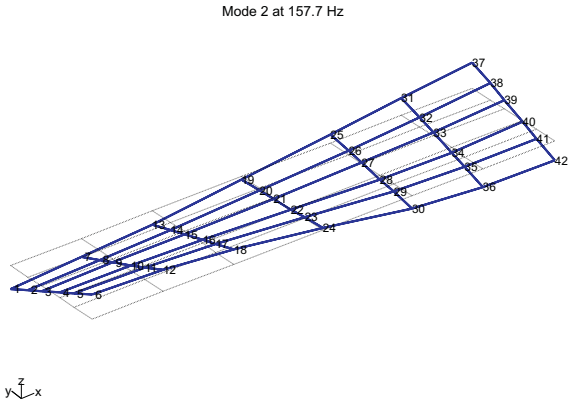


**(b)** $2^{nd}$ mode shape

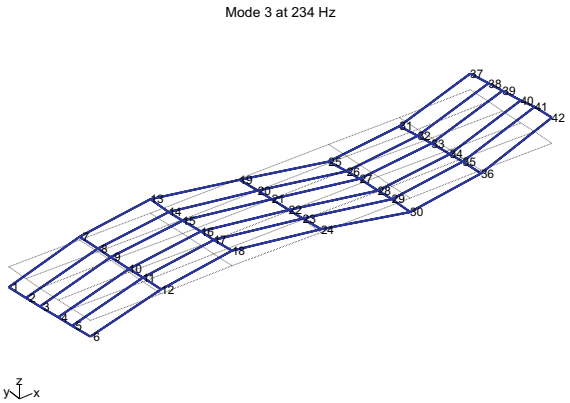


**(c)** $3^{rd}$ mode shape

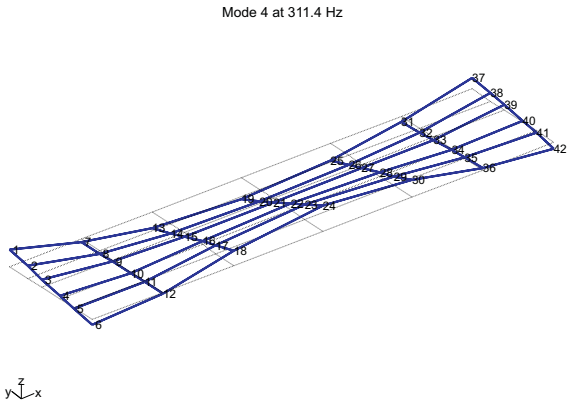


**(d)** $4^{th}$ mode shape

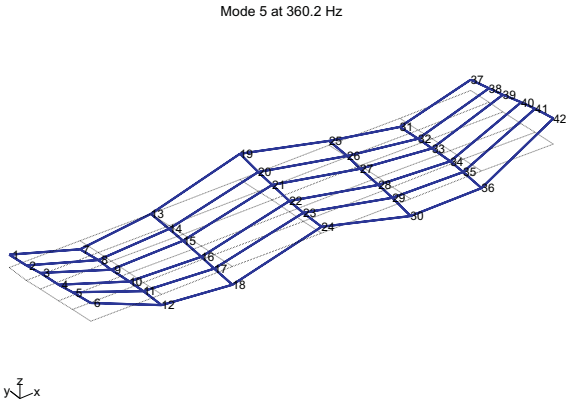


**(e)** $5^{th}$ mode shape of Sample PLT8003

**Figure C.1:** Mode shapes of test sample PLT8003.

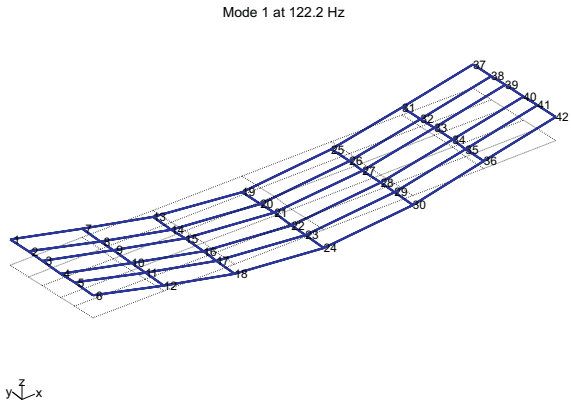


**(a)** $1^{st}$ mode shape

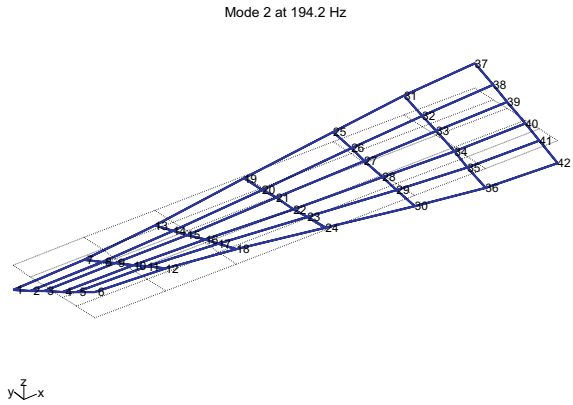


**(b)** $2^{nd}$ mode shape

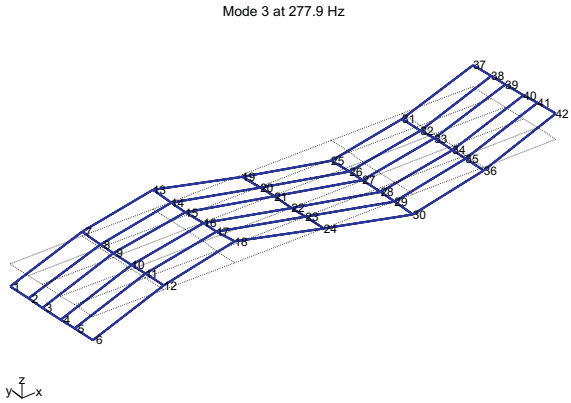


**(c)** $3^{rd}$ mode shape

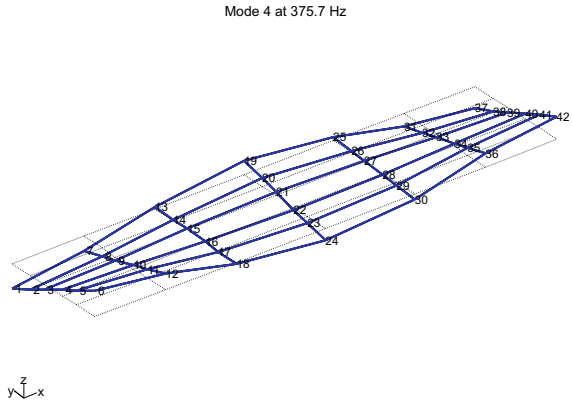


**(d)** $4^{th}$ mode shape

**Figure C.2:** Mode shapes of test sample PLT8123.

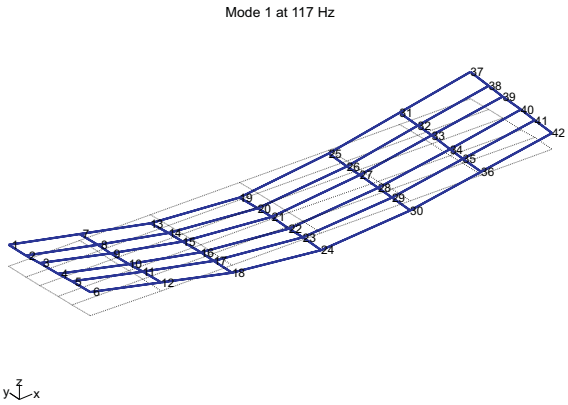


**(a)** $1^{st}$ mode shape

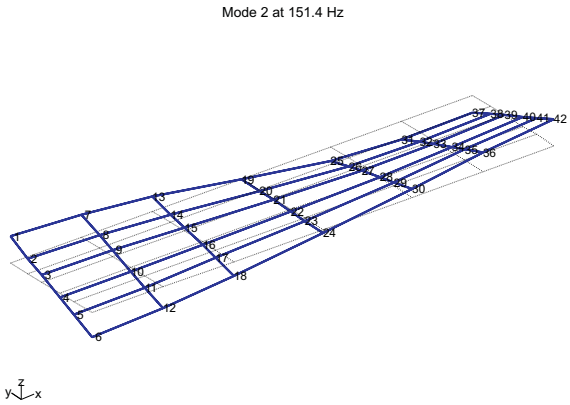


**(b)** $2^{nd}$ mode shape

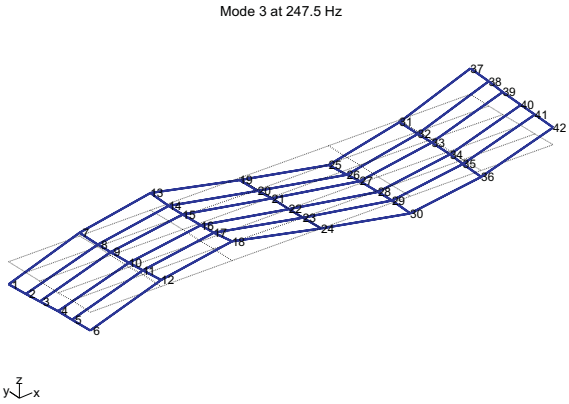


**(c)** $3^{rd}$ mode shape

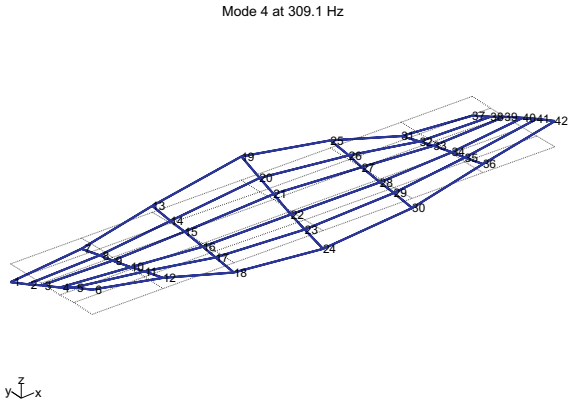


**(d)** $4^{th}$ mode shape

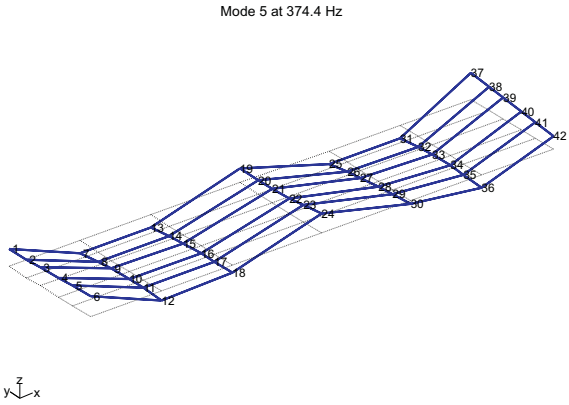


**(e)** $5^{th}$ mode shape of Sample PLT8303

**Figure C.3:** Mode shapes of test sample PLT8303.

# Appendix D

# Experimental equipment list

| **Spectral analyzer** | |
|---|---|
| Brandt/Model: | Brüel&Kjær / 2035 |
| Input modules: | 2x3019 (25 kHz) |
| Output modules: | 1x3106 (25 kHz) |

| **Electrodynamic shaker LDS201** | |
|---|---|
| Brandt/Model: | Ling Dynamic Systems (LDS) / V401 |
| Range: | 17.8 N / 5-13000 Hz |
| Total mass(with trunnion): | 1.81 kg (3.17 kg) |

| **Power amplifier PA25E** | |
|---|---|
| Brandt/Model: | Ling Dynamic Systems (LDS) / PA25E |

| **Force transducer BK8203** | |
|---|---|
| Brandt/Model: | Brüel&Kjær / 8203 / 10118 |
| Sensivity: | 3.3 $pC/N$ |
| Mass: | 3.2 g |

| **Laser vibrometer** | |
|---|---|
| Brandt/Model: | Polytec / OFV 303 |
| Sensivity: | 0.025 $ms^{-1}/V$ |

| **Laser vibrometer controler** | |
|---|---|
| Brandt/Model: | Polytec / OFV 3001 |

# References


[1] K.K. Denoyer and C.D. Johnson. Recent achievements in vibration isolation systems for space launch and on-orbit applications. In *Proceedings of 52nd International Aeronautical Congress (AIAA)*, Toulouse, France, 2001.

[2] B.C. Nakra. Vibration control in machines and structures using viscoelastic damping. *Journal of Sound and Vibration*, 221(3):449–465, 1998.

[3] D.I.G. Jones. Reflections on damping technology at the end of the twentieth century. *Journal of Sound and Vibration*, 190(3):449–462, 1996.

[4] C.D. Johnson. Design of passive damping systems. *Journal of Vibration and Acoustics (Special 50th Anniversary Design Issue)*, 117:171–176, 1995.

[5] A.D. Nashif, D.I.G. Jones, and J.P. Henderson. *Vibration Damping*. John Wiley & Sons, 1st edition, 1985.

[6] Z.A. Momin, D.J. Nefske, and S.H. Sung. Evaluation of vibration damping treatments using a vehicle structural-acoustic analysis. In *Proceedings of 5th International Modal Analysis Conference (IMAC V)*, pages 330–335, London, UK, 1987.

[7] D. Battazzo and O. McDaniel. Prediction of acoustical power using modal analysis: A case study on a plate treated with constrained layer damping. In *Proceedings of 8th International Modal Analysis Conference (IMAC VIII)*, pages 263–269, Kissimmee, FL, USA, 1990.

[8] L. Garibaldi, L.G. Liang, and B. Piombo. Acoustical emission control of metal plates using modal analysis to distribute visco-elastic materials. In *Proceedings of 8th International Modal Analysis Conference (IMAC VIII)*, pages 275–278, Kissimmee, FL, USA, 1990.

[9] R.A.S. Moreira. *Modelação e análise de tratamentos viscoelásticos multi-camada para controlo passivo de vibrações*. PhD thesis, Faculdade de Engenharia da Universidade do Porto, 2004.

[10] D.J. Mead. *Passive vibration control*. John Wiley & Sons, 1st edition, 1998.

[11] D.I.G. Jones. *Handbook of viscoelastic vibration damping*. John Wiley & Sons, 2001.

[12] M.A. Fortes, M.E. Rosa, and H. Pereira. *A Cortiça*. IST Press, 2004.

[13] J.F. Mano. The viscoelastic properties of cork. *Journal Material Sciences*, 37:257–263, 2002.

[14] J.D. Ferry. *Viscoelastic Properties of Polymers*. John Wiley & Sons, 1st edition, 1961.

[15] M.L. Williams. Structural analysis of viscoelastic materials. *AIAA Journal*, 2(5):785–808, 1964.

[16] R.L. Bagley and P.J. Torvik. Fractional calculus - a different approach to the analysis of viscoelastically damped structures. *AIAA Journal*, 21(5):741–748, 1983.

[17] R.L. Bagley and P.J. Torvik. Fractional calculus in the transient analysis of viscoelastically damped structures. *AIAA Journal*, 23(6):918–925, 1985.

[18] G.A. Lesieutre and E. Bianchini. Time domain modeling of linear viscoelastic using anelastic displacement fields. *Journal of Vibration and Acoustics - Transactions of the ASME*, 117: 424–430, 1995.

[19] G.A. Lesieutre and K. Govindswamy. Finite element modeling of frequency-dependent and temperature-dependent dynamic behavior of viscoelastic materials in simple shear. *International Journal of Solids and Structures*, 33(3):419–432, 1996.

[20] D.J. McTavish and P.C. Hughes. Modeling of linear viscoelastic space structures. *Journal of Vibration and Acoustics - Transactions of the ASME*, 115:103–110, 1993.

[21] N. Wagner and S. Adhikari. Symmetric state-space method for a class of nonviscously damped systems. *AIAA Journal*, 41(5):951–956, 2003.

[22] A. Plouin and E. Balmés. A test validated model of plates with constrained viscoelastic materials. In *IMAC XVII*, Kissimee, FL, USA, 1999.

[23] C.D. Johnson and D.A. Kienholz. Finite element prediction of damping in structures with constrained viscoelastic layers. *AIAA Journal*, 20(9):1284–1290, 1982.

[24] Y.P. Lu, J.W. Killian, and G.C. Evertine. Vibrations of three layered damped sandwich plate composites. *Journal of Sound and Vibration*, 64(1):63–71, 1979.

[25] J.W. Killian and Y.P. Lu. A finite element modeling approximation for damping material used in constrained damped structures. *Journal of Sound and Vibration*, 97(2):352–354, 1984.

[26] J.N. Reddy. *Mechanics of Laminated Composite Plates: Theory and Analysis*. CRC Press, 1997.

[27] E. Carrera. Theories and finite elements for multilayered anisotropic, composite plates and shells. *Arch Comput Meth Eng*, 10(3):87–140, 2002.

[28] E. Carrera. Theories and finite elements for multilayered plates and shells: a unified compact formulation with numerical assessment and benchmarking. *Arch Comput Meth Eng*, 179 (4):591–602, 2003.

[29] A. Bhimaraddi. Sandwich beam theory and analysis of constrained layer damping. *Journal of Sound and Vibration*, 179(4):591–602, 1995.

[30] D.A. Saravanos and J.M. Pereira. Dynamic characteristics of specialty composite structures with embedded damping layers. *Journal of Vibration Acoustics*, 117:62–69, 1995.

[31] P. Cupial and J. Niziol. Vibration and damping analysis of a three-layered composite plate with a viscoelastic mid-layer. *Journal of Sound and Vibration*, 183(1):99–114, 1995.

[32] K. Suzuki, K. Kageyama, I. Kimpara, S. Hotta, T. Ozawa, S. Kabashima, and T. Ozaki. Vibration and damping prediction of laminates with constrained viscoelastic layers - numerical analysis by a multilayer higher-order-deformable finite element and experimental observations. *Mech Adv Mat Strucu*, 10:359–378, 2003.

[33] H.J. Pain. *The physics of vibrations and waves.* John Wiley & Sons, 4th edition, 1993.

[34] R.H. Lyon and R.G. DeJong. *Theory and application of statistical energy analysis.* Butterworth-Heinemann, 2nd edition, 1995.

[35] J.F. Doyle. *Wave Propagation in Structures.* Springer, 2nd edition, 1997.

[36] R.A.S. Moreira and J. Dias Rodrigues. An efficient experimental methodology for viscoelastic complex modulus identification. In *II ECCOMAS Thematic Conference on Smart Structures and Materials*, Lisbon, Portugal, 2005.

[37] ASTM. D4092-908 standard terminology relating to dynamic mechanical measurements on plastics, 1990.

[38] D.J. Ewins. *Modal Testing: Theory and Practice.* Baldock: Research Studies press LTD., 2nd edition, 2000.

[39] B.R. Allen. A direct complex stiffness test system for viscoelastic material properties. In *Proceedings of 3th Smart Structures and Materials Conference (SPIE)*, San Diego, CA, USA, 1996.

[40] G. Kergourlay and E. Balmés. Caractérisation des films viscoélastiques en fréquence, température et précontrainte. In *GIENS*, France, 2003.

[41] K.J. Bathe. *Finite element procedures.* CRC, 1996.

[42] Zienkiewicz O.C. and R.L. Taylor. *The finite element method*, volume 1: The basis. Butterworth-Heinemann, 5th edition, 1997.

[43] CADA-PC. *Modal Identification Software User Manual.* LMS International, Leuven, Belgium, 1993.

[44] J. Dias Rodrigues. *Apontamentos de Vibrações de Sistemas Mecânicos.* Faculdade de Engenharia da Universidade do Porto, Edição 2007.

[45] S.S. Rao. *Mechanical Vibrations.* Pearson Prentice Hall, 2004.